Binns, R.A., Barriga, F.J.A.S., Miller, D.J., et al., 2002
Proceedings of the Ocean Drilling Program, Initial Reports Volume 193

4. Site 1189[1]

Shipboard Scientific Party[2]

INTRODUCTION

Principal Results

Site 1189 is located at the Roman Ruins hydrothermal site, the largest development of active sulfide-sulfate chimneys at the PACMANUS hydrothermal field and one that has been surveyed and sampled in considerable detail by towed-camera video traverses and submersible dives. Chimneys as high as 20 m, but more commonly 3 m or less tall, include both simple and compound gray smokers and pillars, as well as cones that vent shimmering fluid through typically ribbed surfaces with a veneer of white material, presumed to be bacterial mat or surficial anhydrite coatings. At the fringes of the field, chimneys rise directly from the jagged surfaces of somewhat mafic dacite lavas (~65 wt% SiO_2 on an anhydrous basis), whereas on the northeastern side there is a low mound, 10 to 15 m high, of chimney debris and Fe oxyhydroxide deposits topped by standing and fallen chimneys.

Two cored holes and one resistivity-at-the-bit (RAB) hole were drilled at Site 1189. Hole 1189A, tagged on the seafloor at 1690 m water depth, was sited near the center of the field in a shallow trough between chimneys, aimed at the mound crest but proving to be on its southwestern side. This was drilled to a depth of 125.8 meters below seafloor (mbsf), with modest core recovery, but was not logged because of the need to sever the pipe. Hole 1189B, placed ~35 m east-northeast from Hole 1189A, tagged bottom 6 m higher at 1684 m water depth, so it was evidently closer to the crest of the mound. This was drilled to 206.0 mbsf, having been cased to 31 mbsf using the new hard-rock reentry system (HRRS). With a free-fall funnel (FFF) installed, the hole was reentered and successfully logged, the remarkable imagery returned from the Formation MicroScanner (FMS) tool being one of the leg highlights. Recovery was very low to ~120 mbsf and then improved dramatically. Hole

[1]Examples of how to reference the whole or part of this volume.
[2]Shipboard Scientific Party addresses.

Ms 193IR-104

1189C, the second logging-while-drilling (LWD) deployment of Leg 193, was drilled and logged to 166.0 mbsf at a site 30 m east-southeast of Hole 1189B. Placed at the foot of a 3- to 4-m-high active chimney encrusted by fauna near its crest, this tagged bottom at the deeper level of 1689 m water depth toward the eastern edge of the Roman Ruins hydrothermal site. The higher section of this hole was also logged by wireline tools, providing a valuable comparison of the two methods.

Despite their proximity, the sequences penetrated by Holes 1189A and 1189B differ significantly. After recovering samples of fresh black dacite in its first core at <10 mbsf, Hole 1189A passed rapidly into intensely altered rocks that continued to the end of hole. These contain disseminated pyrite, but apart from a 5-cm interval of semimassive sulfide in a volcaniclastic unit near 115 mbsf, there were no significant intersections of mineralization. By contrast, Hole 1189B appears to have intersected the mineralized stockwork that was expected from land-based orebody analogs to underlie the sulfide chimneys at Roman Ruins hydrothermal site. While casing the first 31 m, the rate of penetration (ROP) was initially fast, but then became difficult from 7 to 15 mbsf. Possibly the initial interval represented the hydrothermal mound, whereas the harder rocks were fresh lava corresponding to the near-seabed intersection in Hole 1189A. Below 15 mbsf, the ROP again became very rapid, a situation that continued when coring started at 31 mbsf and continued to ~120 mbsf with poor but exciting recoveries of the stockwork mineralized zone. Around 120 mbsf, there was a rapid change to more typical drilling conditions and better core recovery. This corresponds to a major lithologic break, passing into a darker, differently altered sequence of former felsic volcanic rocks containing only trace to minor amounts of sulfide minerals. The break also corresponds to a substantial change in FMS imagery, from conspicuous coarse-scale fracturing below to a more complex pattern above of resistive and conductive layers and pods presumed to denote and, indeed, amplify structure of the stockwork zone where core recovery was poor. Resistivity logging and FMS imagery delineated an interval from 65 to 70 mbsf, where significantly higher conductivity implies a marked increase in sulfide content. Unfortunately, this corresponds to an interval of no core recovery.

Resistivity logging and imagery in Hole 1189C delineated a similar break between coarsely fractured rocks below and a sequence with more complex, possibly veined structure above. Here the boundary is slightly deeper, at ~150 m. No particularly conductive layers were logged that might correspond to massive sulfide intersections.

Site 1189, especially the lower part of Hole 1189B, provides a clear picture of the volcanic construction of Pual Ridge for 200 m below the Roman Ruins hydrothermal site at the PACMANUS hydrothermal field. The only fresh rocks recovered are aphyric dacite at the top of Hole 1189A. These contain 64 wt% SiO_2 and are equivalent to dredged surface exposures in this vicinity. Although all other cores from this site show moderate to complete alteration, abundant preservation of textures (such as vesicles and, in less-altered intervals, phenocrysts and microlites) and of structures (such as perlite, spherulites, and flow banding) shows that the whole sequence penetrated is either volcanic or volcaniclastic in origin. Shipboard chemical determinations of the key immobile element indicator ratio Zr/TiO_2 fall within the range from mafic dacite to rhyodacite throughout the entire sequence, with rhyodacites dominating the lower part of Hole 1189B.

The well-preserved lower part of Hole 1189B shows particularly well the same alternation of coherent and fragmental flows, with occasional volcaniclastic horizons, that we infer for the more altered parts where evidence is at times equivocal because of alteration. Many coherent volcanic units from Site 1189 are vesicular, with the degree of vesicularity ranging up to ~20 vol%. Fragmental flows tend to be conspicuously flow banded. Autoclastic textures and even contacts between coherent and fragmental sectors of the same flow have been observed. Confidently identified volcaniclastic units, including polymict breccias and volcaniclastic sandstone, define paleoseafloor horizons. Five such units were logged in Hole 1189B, but only one in 1189A. It is clear that Pual Ridge was not built in a single eruption. A maximum thickness of ~50 m is estimated for individual flow units, but a minimum figure cannot be set. One coherent unit in Hole 1189B shows consistent vertically oriented stretched vesicles over some 10 m of core. There is speculation that this might be a dike or alternatively a flow that has cascaded over a precipice. Some deeper coherent lavas contain a greater abundance of somewhat larger plagioclase microcrysts or pseudomorphs in their groundmass than those closer to the seabed, which might indicate slower cooling. However, as at Site 1188, there is no evidence for major intrusive bodies of hypabyssal or plutonic character.

Although very close together, Holes 1189A and 1189B show rather different alteration features. The assemblages and fabrics in Hole 1189A are similar to those at Site 1188, but the mineralogical profile is telescoped with cristobalite being restricted to the upper 25 mbsf. Below the cristobalite-bearing interval of this hole, quartz generally increases in abundance with depth. Quartz is patchily developed, overprinting early greenish silica-clay alteration and pale gray to white silica-clay bleaching that occasionally contains anhydrite. Illite and chlorite dominate the phyllosilicate mineral assemblages. Disseminated pyrite is present at the 1%–5% abundance range in all assemblages.

As expected, cristobalite was not found in the upper succession of Hole 1189B, which did not core the interval where it would be present based on the profile of Hole 1189A. The stockwork zone is characterized by quartz-bearing greenish silica-clay alteration of former volcanic wall rocks, with silicification increasing downhole. Illite and chlorite again dominate the phyllosilicate component, but smectite, chlorite-smectite, or illite-bearing mixed-layer clays, and possible kaolinite were also detected. Potassium feldspar was also identified by X-ray diffraction (XRD) in several samples. Although likely, it is uncertain whether this is a hydrothermal phase rather than an igneous relic.

The lower sequence of Hole 1189B, below ~120 mbsf, shows pervasive but rarely complete hydrothermal alteration, relict igneous plagioclase microlites and phenocrysts having commonly survived. Potassium feldspar of either hydrothermal or relict igneous origin is also present. The sequence is characterized by repeated alternations from cristobalite-bearing to quartz-bearing rocks and by a less abundant but very complex and variable clay mineral assemblage. Relative to the upper sequence in Hole 1189B and to Hole 1189A, as well as to the alteration profiles at Site 1188, the lower sequence is an interval subjected to less interaction between rock and hydrothermal fluids. Fragmental units tend to be more altered than their coherent associates.

Analyses were performed on board on altered rocks from Site 1189, and these generally reflect the alteration mineralogy. In Hole 1189A, green silica-clay altered rocks have high water and sulfur contents, and increases in Fe and Mg correspond to increases in reported chlorite, clay

minerals, and pyrite. In Hole 1189B, SiO_2, CaO, and Na_2O increase in the lower sequence, in agreement with the observed increase in plagioclase content.

As at Site 1188, pyrite is the dominant sulfide at Site 1189. It is disseminated throughout the altered volcanic rocks, is present within quartz-anhydrite veins, and occurs as linings and cores to vesicle fill. Sphalerite and chalcopyrite are noticeably more abundant in Hole 1189B than in Hole 1189A, whereas chalcopyrite in the lower levels of Hole 1189A is more common than at Site 1188. Marcasite, galena, tennantite, and covellite are rare, and the latter three have only been identified in cores from Hole 1189B. The relationships between the accessory sulfides and pyrite provide evidence for at least two generations of pyrite-quartz precipitation at Site 1189. In addition, the oxides magnetite and hematite are present.

Semimassive sulfide mineralization comprising ~50% sulfides was recovered in Hole 1189B by the first core below casing. Besides pyrite, this contains substantial chalcopyrite and subordinate sphalerite. The gangue is mainly coarse anhydrite, in part replaced by gypsum. Ovoid features tentatively interpreted to be mineralized worm casings are present. This interpretation, if correct, would imply an exhalative seafloor origin and burial by the lava presumed to be present from drilling characteristics during the casing operation, but numerous small fragments of altered wallrock in this sample suggest the occurrence is basically related to the underlying stockwork. The stockwork grades into breccia, and extends to the discontinuity in Hole 1189B at ~120 mbsf, with sulfide veins becoming less abundant downward in the limited material recovered. Nevertheless, the overall sulfide content of this zone is low and should be considered as only a very weakly mineralized stockwork sequence.

The structures identified in Holes 1189A and 1189B were primary volcanic layering, brecciation of volcanic rocks, orientation of veins, and age relationship between veins. There are several interesting similarities and differences between the two holes with respect to vein structures.

The brecciated rocks in the two holes are very similar, consisting of variably altered volcanic fragments, crosscut by vein networks of quartz with pyrite and minor anhydrite. However, the volcanic rocks recovered from Hole 1189B are more brecciated than the rocks from Hole 1189A. Additionally, the vein intensity is higher and intervals of vein network (stockwork) are thicker in Hole 1189B. In contrast to Hole 1189A, in Hole 1189B magnetite and hematite are present in the networks as minor components, whereas sphalerite and chalcopyrite are trace minerals. In both holes, late coarse-grained anhydrite veins crosscut vein networks and brecciated rocks.

Bacteria were not detected by direct count below 50 mbsf in cores from Hole 1189A, or below 31 mbsf in Hole 1189B. Enrichment cultivations of samples from Hole 1189A showed growth of bacteria in aerobic conditions to 25°C, and as high as 90°C in anaerobic conditions. Samples from Hole 1189B exhibit growth of bacteria in anaerobic cultures from as deep as 130 mbsf, and at temperatures to 90°C.

Magnetic susceptibility decreases from top to bottom in the cored section from Hole 1189A. A similar pattern is expressed in data from the lower part of Hole 1189B, although the overall susceptibility is distinctly higher. Compressional wave velocity averages 4.4 km/s at ambient pressure. Thermal conductivity is relatively constant at ~2 W/(m·K), with the exception of one pyrite-rich sample that has a value of >5 W/

(m·K). Solid-rock density varies little in all samples measured from both holes, averaging 2.7 g/cm³. As in samples from Site 1188, porosity is highly variable, from 15% to nearly 70%.

In terms of rock magnetic behavior, Site 1189 shares many common features with Site 1188. The uppermost part of the section at both sites is characterized by high susceptibility and high remanent intensity caused by abundant magnetite and titanomagnetite. At both sites, the upper few tens of meters are underlain by an interval of low remanent intensity. Below this is a zone of high susceptibility and high remanent intensity. Inasmuch as the maximum remanent intensity is in this lowermost interval, it is conceivable that this lower zone is equally important, if not more so, as the source of the magnetic anomalies measured from the sea surface. Some significant differences also exist between Sites 1188 and 1189 in terms of magnetic behavior. The highest measured magnetization intensity is deeper at Site 1189 than it is at Site 1188. However, susceptibility and remanent intensity are both generally lower at Site 1189. This may reflect more intense high-temperature alteration at Site 1189.

Site 1189 will likely turn out to be the highlight of downhole measurements for Leg 193. Continuous wireline logs were collected in Hole 1189B, with excellent tool response as a result of good borehole condition. FMS data are particularly striking, imaging different patterns of faulting and local dissemination of sulfide minerals. A second LWD/RAB hole, Hole 1189C, was drilled to 166 mbsf, past a distinct change in the fracturing pattern probably equivalent to the lithology change described in the cores of Hole 1189B and potentially imaged in Hole 1189B wireline logging data. Following completion of RAB drilling, we dropped a FFF and conducted wireline logging of Hole 1189C. This marks the first time in the history of the Ocean Drilling Program (ODP) that we have the opportunity to correlate directly between wireline logging and RAB data from the same drilled interval in hard rock.

Site Objectives

The geological objectives at Site 1189 were to delineate the vertical profile of alteration and mineralization patterns, and their variation with depth, beneath an area of focused, high-temperature venting—the Roman Ruins hydrothermal site. The data obtained on cored samples and by logging will allow assessments of the chemical and hydrological processes at this "end-member" location, just as comparison of this site with Site 1188 at the low-temperature diffuse vent field at Snowcap hydrothermal site would provide an understanding of lateral variations.

In addition, Site 1189 was designed as a test of the nature and extent of microbial life, particularly hyperthermophilic bacteria, at such a high-temperature hydrothermal site, together with delineation of the conditions conducive to the presence of a deep biomass.

Operations Summary

Hole 1189A

After severing the pipe at Hole 1188A, a new rotary core barrel (RCB) bottom-hole assembly (BHA) was assembled, and the drill string and vibration-isolated television (VIT)/subsea camera were run to bottom at Site 1189. The precision depth recorder depth reading for this site was 1693.4 meters below rig floor (mbrf) corrected to the dual elevator

stool. As at the previous site, a positioning beacon was attached to the VIT frame rather than being deployed from the surface. This was to allow a more accurate placement of the beacon relative to the actual hole location. At 1310 hr on 22 November 2000, while positioning off of a Global Positioning System (GPS) signal, a load shed occurred in the ship's hotel structure. Power to lighting and air conditioning services was cut; however, the regulated power to all computer systems remained on. All services were restored within 5 min. The cause of the power outage was an abrupt 15-m shift in the GPS signal position. This caused all thrusters to rapidly ramp up to full power as the vessel appeared to be off location. The resultant abrupt call for electrical power from the main electrical service bus overloaded the three engines on line at the time. This failure was attributed to attempting to position on a GPS signal alone without a seafloor beacon as a fixed reference.

The seafloor TV survey at this site began at 1515 hr on 22 November 2000. The beacon was released from the VIT frame at 1516 hr, and the survey continued until 1545 hr. Tall sulfide chimneys were readily apparent in the video images, many of which were active black/gray smokers. Once a candidate site was identified, a 3.0-m jet-in test was conducted to determine the viability of deploying a FFF should it be required. Hole 1189A (Fig. **F1;** Table **T1**) was spudded at 1615 hr on 22 November 2000, and the VIT frame was recovered while the driller maintained weight on the bit. We initiated RCB coring and deployed a Whirl-Pak microbiology core contamination tracer on Core 193-1189A-4R and maximum reading thermometers in the drill string accelerator (DSA) pressure housing on Cores 193-1189A-8R and 12R. Recorded circulating temperatures were 37° and 39°C, respectively. Core 193-1189A-13R was cut to a depth of 1817.1 mbrf (125.8 mbsf), but while running in with the sinker bars to recover Core 193-1189A-13R, the pipe stuck in the borehole. Despite our attempts to wrest the pipe free, the pipe remained immobile. Core 193-1189A-13R was recovered and the shifting tool was deployed to release the bit; however, the pipe remained firmly planted at 120 mbsf. Since shooting off the pipe was inevitable, the DSA tool housing was deployed one last time with the maximum reading thermometers. Recorded temperature at the bottom of the hole was 34°C with the circulating pumps shut down for 10 min. The driller continued to work the pipe while the third severing charge of the leg was deployed. The drill string was severed at a depth of 1708.0 mbrf (7.0 mbsf) in the third joint of the 5.5-in transition drill pipe. The remaining drill string was recovered and the severed pipe cleared the rotary table at 2045 hr on 23 November 2000. This concluded operations in Hole 1189A.

F1. Hole locations for Sites 1189 and 1190, p. 67.

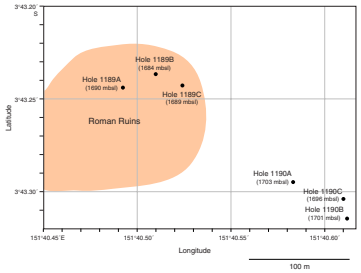

T1. Coring summary, Site 1189, p. 231.

Hole 1189B

Hole 1189B is unique in that it represents the first complete deployment of the HRRS. After the conclusion of coring and logging operations at Hole 1188F, 33.6 m of 13.375-in flush joint casing were assembled with the HRRS casing hanger and the fluid hammer with a spline drive ring bit welded to the bottom of the shoe joint. In design, this would result in >30 m of cased hole, with ±2 m of casing above the seafloor for deployment of a free-fall reentry cone.

The HRRS running tool and release assembly, as well as the hammer, were tested before deployment. At 0015 hr on 23 December 2000, we began a brief camera survey and jetted in 1 m once an acceptable location was selected in the middle of a chimney field. The ROP was vari-

able at first, but after only ~1 hr, the casing had advanced 7 m. The next meter (7–8 mbsf) required 1 hr of hammering before the ROP sped up again to between 8 and 10 mbsf. The interval between 10 and 15 mbsf appeared to be very hard, as it took more than 6 hr to advance. Speculation regarding potential failure of some part of the system was proven groundless when the hammer broke through the hard layer and drilled the next 15 m in <30 min, including a pipe connection. General hammer-drilling parameters were 5–20 klb weight on bit, top drive 10–40 revolutions per min, one pump at 40 strokes per min (spm) to two pumps at 50 spm held pump pressures of ~750 psi to as high as ~2000 psi. Average ROP was 3.0 m/hr for the 10.0 hr of operation. The running tool released without complication and, after recovering the subsea camera and rigging the HRRS reentry cone, the cone was deployed through the moonpool. The entire operation, from rigging the tools to recovery of the hammer, was complete in only 33 hr.

An RCB BHA was assembled with all available drill collars to maximize our potential depth of penetration. RCB coring commenced at 0815 hr on 24 December 2000. Although recovery was again poor (~8%), coring continued without incident through Core 193-1189B-18R to a depth of 1899.0 mbrf (206.0 mbsf). Hole conditions began to deteriorate, and because we were within 2 m of the maximum depth we could achieve without placing the top of the drill collars below the bottom of the casing, we decided to terminate operations in this hole. Wireline logging commenced at 2015 hr on 25 December 2000, and was complete by early afternoon on 26 December 2000, ending operations in this hole.

Hole 1189C

Following the temperature measurement and water sample recovery at Hole 1188F, we embarked on our second LWD/RAB experiment. Because the core recovery in Hole 1189B indicated a lithologic change at ~120 mbsf coincident with an increase in resistivity noted in the wireline log from that hole, we planned to attempt a total depth of at least 160 m with this operation. After a quick camera survey, Hole 1189C was spudded at the base of a spectacular chimney at 1700 hr on 27 December 2000. The RAB experiment proceeded flawlessly, reaching 166 mbsf in <26 hr. Before pulling free of the seafloor, we decided to drop a FFF to allow us to reenter Hole 1189C, measure a temperature profile, and if conditions allowed, run wireline logs and collect a water sample. The successful completion of the logging (albeit only to a depth of 67 mbsf because of a blockage in the hole) will provide the first direct comparison between LWD/RAB and wireline logging data in the same borehole spudded in volcanic rock in the history of ODP. The planned water sample was abandoned because of the low temperature measured in the borehole (~30°C) and our desire to collect another water sample from Hole 1188F before we were required to leave our operations area.

Site Survey

The entire survey for Hole 1189A (1500 to 1617 hr on 20 November 2000) occurred on target within an area 25 m east of where the beacon was dropped, across a field of standing and fallen chimneys and fine debris covering the basal mound. Sonar indicated we were in a low, elongate trough between two walls of high-standing chimneys. During the survey, the VIT passed close by the base of two large chimneys ~5 m

across, over a 2- to 3-m-long fallen chimney, and across finer chimney rubble with occasional small chimneys (including two parasitic examples on the pediment of one large chimney). Shimmering water was seen at several places, and on one side of the field there were clouds of gray smoke. The jet-in test (3 m achieved in 50 strokes) and the final spud site (achieved after raising to add pipe) were both at sites of fine chimney debris with minor sediment cover (metalliferous ooze?).

The survey for Hole 1189B commenced as the bit and VIT descended close to the Hole 1189A site through a billowing smoke plume to a field of chimneys with rubbly debris below. The pipe was then moved east-northeast for 30 m, passing fallen chimneys, small chimneys, and rubble. With the overall seafloor gently rising, we concluded we were near the crest of the Roman Ruins mound. We stayed at the new site while twice raising to add pipe, then spudded Hole 1189B in rubble, including chimney fragments, on a gentle slope at the foot of a tall, active (white tipped) multi-spired chimney, between this and a small simple conical-tipped white chimney. The rubble moved after pumping started, so was not coherent.

Prior to spudding Hole 1189C, the bit and VIT descended over a large, active chimney encrusted with fauna. With minimal maneuvering of the pipe required, drilling commenced on apparently coherent hydrothermal deposit at the foot of this chimney.

IGNEOUS PETROLOGY

Site 1189 is located at the high-temperature Roman Ruins hydrothermal site within the PACMANUS hydrothermal field on Pual Ridge. Core was recovered from two drill holes. Hole 1189A was placed in a shallow trough stretching ~5 m across between a group of active chimneys encrusted by fauna and was established to investigate the style of hydrothermal alteration underlying this high-temperature vent field. The hole was cored with the RCB system to a depth of 125.8 mbsf, with an average recovery of 6.8%.

The rocks recovered from Hole 1189A included very little material with significant sulfide mineralization. Partly for this reason, Hole 1189B was placed higher on the mound ~30 m northeast, again among the active high-temperature smokers at the Roman Ruins hydrothermal site. Hole 1189B was RCB cored from 31.0 to 206.0 mbsf with an average recovery of 7.8%. Rocks from the upper part of Hole 1189B include samples of semimassive sulfide and stockwork veining, whereas those from the lower part represent altered volcanic rocks with many similarities to those from Hole 1189A.

This chapter contains documentation of the igneous-rock types and igneous features observed in core from Holes 1189A and 1189B based upon hand specimen and thin section descriptions and supplemented with the results of XRD analyses. In the following sections, the two holes are described in turn.

Hole 1189A

The first core recovered from the uppermost part of Hole 1189A consists of unaltered, black, moderately vesicular aphyric dacite with a glassy to microcrystalline groundmass (Unit 1). The felsic composition of the unit has been confirmed by measurements of the refractive index

of the glass, which indicates a SiO_2 content of 66 wt%, and by shipboard chemical analysis (see "Geochemistry," p. 46).

Below the first core (Core 193-1189A-1R), alteration intensity increases rapidly. Unit 2 in Core 193-1189A-2R is lithologically very similar to Unit 1 except for a gradual change in the color of the groundmass from dark gray to white with depth, indicating increasing pervasive bleaching (see "Hydrothermal Alteration," p. 23). The vesicles in Unit 2 are lined or partially filled by silica, anhydrite, and minor pyrite.

Below Unit 2, alteration is complete and identification of primary lithology is commonly difficult. However, remnant volcanic features including vesicles, flow banding, and perlitic groundmass textures have been recognized in most units.

Several units show fragmental textures that have been logged as hydrothermal breccia because conclusive evidence for a volcaniclastic origin (e.g., grading, layering, rounding, and polymict composition) is lacking. These units typically contain flow-banded clasts (Units 9, 11, 13, and 16), and locally, textural evidence indicates clast movement prior to, or as a result of, hydrothermal activity. Some units contain perlitic fragments that consisted of volcanic glass prior to alteration. Clasts with well-preserved vesicles are absent in hydrothermal breccia units.

Volcaniclastic breccias have been identified in the lower portion of Hole 1189A. The altered and mineralized Unit 21 contains abundant tube pumice and nonvesicular aphyric volcanic clasts with angular, blocky to shardlike shapes. Unit 23 is a polymict volcaniclastic breccia with aphyric clasts showing substantial differences in alteration mineralogy. These units mark paleoseafloor positions in the Pual Ridge stratigraphy.

Units with well-preserved vesicles typically show pervasive bleaching and/or silicification along quartz veins. Any brecciation associated with fracturing during alteration generated perfect jigsaw-fit textures. These features indicate that these units originally were coherent parts of lava flows that locally developed pseudoclastic textures caused by hydrothermal activity.

Hole 1189A intersected a silica-Fe-oxide-pyrite-rich jasperoidal rock with altered volcanic clasts (Unit 14) and sulfide-rich breccia (Units 18 and 21). These units are described in more detail in "Sulfide and Oxide Petrology," p. 34.

A full description of the various units, including lithologic characteristics and alteration mineral assemblages, is provided in Table T2. A graphic log of Hole 1189A summarizes the distribution of units and their lithologic and alteration characteristics (Fig. F2). Detailed hand specimen descriptions of individual pieces and thin-section descriptions are available (see "Site 1189 Thin Sections," p. 59).

T2. Lithology and alteration of Units 1 to 24, Hole 1189A, p. 233.

F2. Graphic summary log for Hole 1189A showing the lithologic characteristics of the various units including alteration, p. 68.

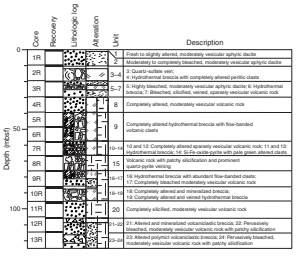

Unit Summaries

The following is a brief summary of the lithologic units from Hole 1189A that have either well-preserved or remnant igneous features. Note that Units 3, 14, and 18 have no such features.

Unit 1 is black, aphyric, moderately vesicular, microlite-bearing, glassy dacite. Most of the vesicles are flattened as a result of flow during eruption and cooling. It is similar in appearance to fresh rhyodacite recovered from the top of Hole 1188A at the Snowcap hydrothermal site, except for the lack of phenocrysts.

Unit 2 is lithologically similar to Unit 1 but shows a gradual increase in pervasive silica-clay bleaching, which is reflected by a change in the

color of the groundmass from gray to light gray to white with increasing depth.

Unit 3 is a single piece of a coarse-grained quartz-sulfate vein.

Unit 4 is a hydrothermal breccia with completely altered, green, angular perlitic volcanic clasts with a coarse, white to gray anhydrite-silica-pyrite stockwork matrix (Fig. F3). Some clasts have minor (1–2 vol%) vesicles (<1–1 mm across), which may be filled by anhydrite and/or traces of pyrite. The perlitic texture of some clasts is locally well preserved, indicating that the clasts were originally glassy volcanic fragments (Fig. F4).

Unit 5 is a highly to completely bleached, aphyric, moderately vesicular volcanic rock similar to Unit 2. Vesicles may be lined or filled by silica, zeolite, or anhydrite (Fig. F5). Locally, these minerals grow preferentially on the footwall side of the vesicles, indicating that they may be used as geopetal structures.

Unit 6 is a single piece of hydrothermal breccia, which consists of white, sulfate-rich volcanic clasts in a bluish green, clay-rich quartz-anhydrite-pyrite stockwork matrix.

Unit 7 is a pervasively bleached, light gray, sparsely vesicular volcanic rock with abundant anhydrite-quartz-pyrite veins and partially quartz-filled vesicles. Jigsaw breccia textures are prominent and clearly related to fracturing and vein formation.

Unit 8 is a light green-gray pervasively green silica-chlorite altered, moderately vesicular volcanic rock. The vesicles are generally at least partially filled by silica, which can also be observed in the groundmass, and the rock is veined by quartz-anhydrite-pyrite.

Unit 9 is a completely altered hydrothermal breccia with flow-banded volcanic clasts showing patchy to pervasive multiphase alteration (Fig. F6). The volcanic fragments are bleached but locally preserve the flow banding. This alteration is overprinted by gray-green chlorite-smectite alteration, and the last stage was quartz-pyrite veining locally forming a stockwork matrix.

Unit 10 is pervasively silica-clay altered, variably vesicular volcanic rock that has been overprinted by silicification, which is concentrated in halos along quartz-pyrite veins.

Unit 11 is a hydrothermal breccia with bluish green, silica-chlorite altered, flow-banded volcanic fragments that are cemented by fine-grained, gray silica. Textural evidence indicates that flow-banded fragments have been rotated relative to each other.

Unit 12 is pervasively silicified, sparsely vesicular volcanic rock, essentially identical to Unit 10.

Unit 13 is a hydrothermal breccia with silica-chlorite altered, flow-banded clasts in a fine-grained, gray silica stockwork matrix. This unit is very similar to Unit 11 and also shows textural evidence for relative movement of volcanic fragments.

Unit 15 is a white-tan massive volcanic rock with a fine network of silica-pyrite veins. Some pieces show relict perlitic groundmass texture in hand specimen. Minor plagioclase phenocrysts (<1 vol%) in a trachytic groundmass have been observed in thin section. The unit is intensely veined and fractured (Fig. F7). In addition, two specimens (Samples 193-1189A-8R-1 [Pieces 4 and 17]) each contain a black patch, both a few centimeters across, that exhibit an unusual coarse bladed texture. These patches may represent xenoliths of quenched mafic rock or an unusual alteration style (see below).

Unit 16 is a hydrothermal breccia with green, silica-clay altered, flow-banded volcanic fragments in a stockwork matrix of quartz and

F3. Hydrothermal breccia with completely altered volcanic fragments in an anhydrite-silica-pyrite stockwork matrix, p. 69.

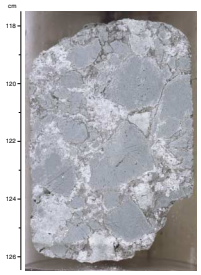

F4. Volcanic fragments with perlitic groundmass texture, p. 70.

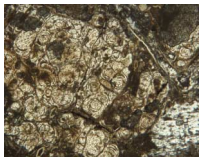

F5. Vesicle with secondary minerals and pilotaxitic groundmass texture from Unit 5, p. 71.

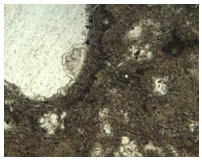

F6. Flow banding preserved in fragments within hydrothermal breccia, Unit 9, p. 72.

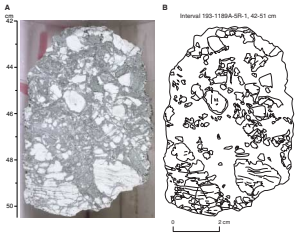

pyrite veins, which have silicified halos. Textural evidence indicates that some flow-banded fragments have been rotated and/or moved relative to each other (Figs. F8, F9). This unit is very similar to Units 11 and 13.

Unit 17 is a completely bleached, moderately vesicular volcanic rock.

Unit 19 is a completely altered and veined hydrothermal breccia with abundant jigsaw-fit textures (Fig. F10). In thin section, this unit is slightly plagioclase-phyric with a trachytic groundmass, and the veins consist of quartz-anhydrite-pyrite.

Unit 20 is a completely silicified, moderately vesicular volcanic rock. Vesicles are typically lined with quartz and pyrite. Remnant microlites in the groundmass are altered to illite and are set in a chlorite or clay matrix.

Unit 21 consists of a single piece of semimassive sulfide with abundant, white to light green, silica- and/or chlorite-altered, aphyric volcanic clasts (Fig. F11). They have angular (blocky, wispy, or polygonal) shapes and maximum diameters are in the range of 0.5–1 cm. In thin section, many of these clasts show laminar, fibrous textures, which are interpreted as the remnants of tube vesicles sufficiently abundant to warrant calling them tube pumice (Fig. F12). In addition, there are nonvesicular volcanic clasts that are about equally abundant as the tube pumice clasts. Sulfide-poor domains show a densely packed, clast-supported texture indicating that this unit is a volcaniclastic breccia or hycloclastite (Fig. F13).

Unit 22 is a pervasively bleached, moderately vesicular volcanic rock with patchy silicification. Vesicles are commonly lined with pyrite crystals.

Unit 23 is a polymict volcaniclastic breccia with aphyric, nonvesicular volcanic clasts distinguished by different styles of alteration. Green clasts are pervasively clay altered, whereas gray clasts are silicified or bleached.

Unit 24 is a pervasively bleached, moderately vesicular volcanic rock showing patchy silicification.

Volcanic Textures

Primary volcanic features have been recognized in many units of Hole 1189A, despite the hydrothermal alteration. These include vesicles, phenocrysts, perlitic texture, flow banding, and tube pumice clasts. Point counts of the thin sections of several fresh and altered volcanic rocks, which have identifiable phenocrysts and vesicles (or remnant vesicles), are given in Table T3.

Vesicles

Vesicles are common in the rock units from Hole 1189A. They are present in the fresh dacite of Unit 1 as well as in many of the altered volcanic rock units (including Units 2, 5, 7, 8, 10, 12, 15, 17, 20, 22, 23, and 24). The vesicularity of individual specimens varies from 0 to 20 vol%. The vesicle size varies from as small as several tenths of a millimeter in diameter to several centimeters (maximum dimension) in large, stretched or coalesced, vesicles. Commonly, the majority of vesicles are aligned, oblate, and tube shaped, 1 or 2 mm across, and 1 or 2 cm long. These reflect stretching and/or flattening of originally spherical vesicles in the lava as it flowed and cooled. An extreme example of stretched vesicles is represented by pumiceous volcanic clasts with abundant tube vesicles in Unit 21 (Fig. F12).

F7. A massive volcanic rock with quartz-pyrite veining and associated jigsaw-fit breccia textures, p. 73.

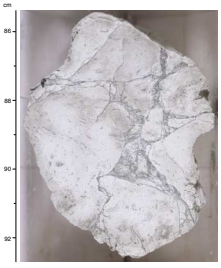

F8. Rotated volcanic fragments in hydrothermal breccia, p. 74.

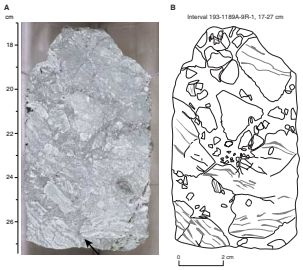

F9. Rotated volcanic fragments in hydrothermal breccia, p. 75.

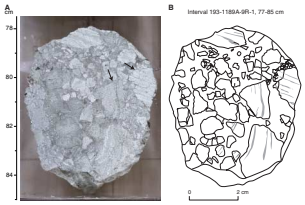

F10. Jigsaw-fit texture in hydrothermal breccia with pervasively silica-clay alteration overprinted by silicification, p. 76.

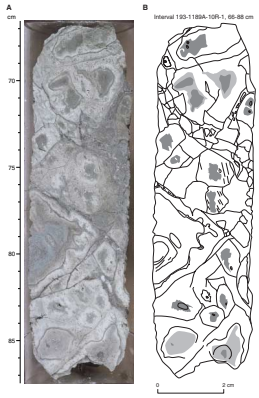

Vesicles are commonly lined with secondary minerals or completely filled to form amygdules. In one notable example, vesicles are decorated with small (0.1–0.2 mm) blocky zeolite crystals and crystal clusters (Fig. F5). Most of these zeolite crystals are on the same side of the vesicles and may define a geopetal reference. Similar features have been observed in oriented pieces from Hole 1191A, suggesting that the zeolites preferentially occupy the floor or footwall of individual vesicles.

Phenocrysts

All of the rocks sampled from Hole 1189A are aphyric, with no phenocrysts noted in hand specimen. One thin section of the fresh aphyric dacite of Unit 1 in Section 193-1189A-1R-1 is completely aphyric, whereas a thin section of bleached aphyric volcanic rock from Unit 5 in Section 193-1189A-3R-1 has just one phenocryst of plagioclase and one altered phenocryst of clinopyroxene. Thin sections also reveal very scarce phenocrysts in Units 10, 12, and 15 (Table T3).

Perlitic Texture

Volcanic clasts with well-preserved perlitic texture are hosted within an anhydrite-silica-pyrite stockwork matrix in Unit 4 (hydrothermal breccia). This texture indicates that these originally glassy fragments were hydrated prior to hydrothermal alteration. In thin section, perlitic domains are arranged in a jigsaw-fit pattern and separated from each other by linear to irregular fractures (Fig. F4). This indicates that hydrothermal fluid flow was largely independent of the fracture pattern provided by the perlitic cracks and probably more focused along fractures generated during hydrothermal activity. In contrast to Site 1188, altered volcanic rocks showing pseudoclastic textures with round to lensoidal apparent clasts (perlite kernels?; cf. Figs. F6, p. 104, F7, p. 106, both in the "Site 1188" chapter) have not been observed in the recovered rocks from Hole 1189A.

Flow Banding

Flow-banded volcanic fragments are common in most units consisting of hydrothermal breccia in Hole 1189A. In general, these units have been overprinted by several stages of alteration, and remnant flow-banding textures are preserved as alternating white to light gray and gray-green linear to wavy domains (Figs. F8, F9). In thin section, flow-banded clasts consist of micro- to cryptocrystalline minerals with low birefringence (silica, sulfate, zeolites, fine clay?), and the dark domains are enriched in a dark mineral that is too fine to be resolved under the microscope (Fig. F14). The boundaries between light and dark groundmass are poorly defined, and in detail dark domains consist of irregular, black patches that are loosely aligned. We infer that hydrothermal alteration preserved the flow banding because of primary textural and/or mineralogical differences between the bands, whose original nature remains uncertain.

Volcaniclastic Textures

Fragmental textures are abundant in the altered volcanic rocks recovered from Hole 1189A. However, because of the textural and mineralogical overprint of alteration, it is difficult to discriminate between hydrothermal breccia and rocks that consisted of volcanic clasts prior to alteration. In the absence of observations regarding contact relationships or internal organization (such as grading) caused by limited recovery, most fragmental units with monomict composition have been logged as hydrothermal breccia. However, several hydrothermal breccia

F11. Semimassive sulfide with abundant blocky to wispy volcanic clasts, Unit 21, p. 78.

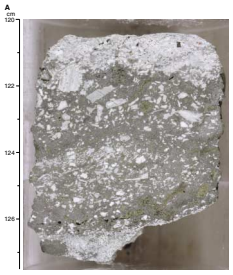

F12. Volcanic clasts with tube pumice texture within semimassive sulfide, Unit 21, p. 80.

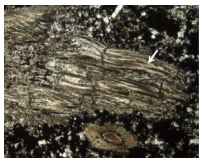

F13. Vesicular and nonvesicular volcanic clasts forming a clast-supported texture in sulfide-poor domains, Unit 21, p. 81.

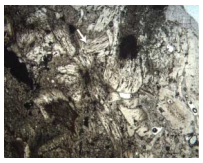

T3. Results of point counts on volcanic rock thin sections, Hole 1189A, p. 235.

F14. Remnant flow banding in volcanic fragments of hydrothermal breccia, p. 82.

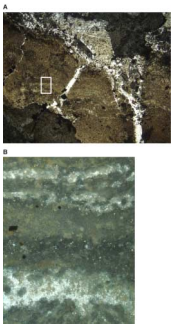

units contain flow-banded volcanic fragments and show textural evidence for relative movement of individual clasts (see below). Despite these limitations, two volcaniclastic breccia units have been recognized in Hole 1189A marking paleoseafloor positions.

Altered and Mineralized (Tube Pumice-Bearing) Volcaniclastic Breccia

Unit 21 is a semimassive sulfide with abundant silica and/or chlorite altered volcanic clasts. There are about equal proportions of nonvesicular clasts and tube pumice with abundant fibrous laminar textures representing the former tube vesicles (Fig. **F12**). These delicate features have been preserved by an early (diagenetic?) stage of alteration, which generated a fine, dark brown lining on the inner vesicle walls. The central parts of the vesicles are filled with the same material (silica and/or chlorite) that replaced the originally glassy groundmass. The volcaniclastic origin of this unit is indicated by the polymict composition of the clast population and the chaotic, densely packed, clast-supported texture in sulfide-poor domains. The angular, platy to wispy shapes of the volcanic clasts suggest that they were generated by quench fragmentation and deposited by settling or mass-flow processes not far from their source.

Polymict Volcaniclastic Breccia

Unit 23 consists of densely packed, aphyric, nonvesicular clasts that are clay-altered, silicified, or bleached. Because individual clasts show distinctive types of alteration, it is inferred that they were derived from different source areas and mixed together during mass flow transport.

Hydrothermal Breccia with Evidence for Clast Movement

Several units with abundant flow-banded volcanic fragments have been logged as hydrothermal breccias (Units 9, 11, 13, and 16). These units experienced several stages of pervasive to vein-controlled alteration causing complex mineralogical and textural modifications. In general, most remnant volcanic fragments are arranged in a jigsaw-fit pattern and, therefore, may have been generated during hydrothermal activity. However, textural observations indicate that at least some differential movement occurred in these units, because adjacent clasts show internal flow banding with random orientations (Figs. **F8, F9**). This observation may be interpreted as evidence for a volcaniclastic origin of these units or for brecciation and clast movement in void fractures during hydrothermal activity.

Hydrothermal Breccia with Pseudoclastic Textures

In several units logged as hydrothermal breccia, the volcanic fragments are separated by <<1-cm-wide veins and are arranged in a jigsaw-fit pattern (Figs. **F7, F10**). This indicates that this fragmental texture is related to fracturing and alteration of coherent volcanic rocks during hydrothermal activity generating pseudoclastic textures. In several units it has been observed that alteration (typically silicification) is concentrated in halos along the veins. Locally, remnants of groundmass encircled by these halos may be misinterpreted as angular to irregular clasts if not carefully examined (Fig. **F10**). Similar textures have also been commonly observed at Site 1188 (Snowcap hydrothermal site), suggesting that pseudoclastic textures are a common product of hydrothermal alteration processes.

Black Patches in Unit 15

Two black patches revealed after cutting core of Unit 15, each ~2–3 cm across, possess unusual textures. The patches are roughly equant and angular and appear to be xenoliths in a fine-grained volcanic unit with scant plagioclase phenocrysts. Their interiors contain long pseudomorphs (1–2 cm) after acicular crystals, whereas their rims comprise a millimeter-wide finer grained zone.

Thin sections show that the cores of the patches consist mainly of a chloritic groundmass hosting faint pseudomorphs of medium-grained acicular crystals, which are now altered to anhedral feldspar and/or quartz grains, and lineations of opaque material (now magnetite, hematite, and pyrite) (Fig. F15). There are also two medium-grained relict felsic phenocrysts in the thin section from Sample 193-1189A-8R-1 (Piece 17, 103–105 cm) (Fig. F16). The millimeter-scale rim zones of the patches contain slightly smaller altered acicular crystals and a groundmass of plumose, skeletal (hollow) feldspar crystals (Fig. F17). The microlites in the volcanic host material of Unit 15 conform to the edge of the patch (Fig. F17).

The patches contain significant sulfide mineralization, and they are cut by quartz veins. This alteration style is similar to that observed in the host felsic volcanic rock of Unit 15. The groundmass of the patches also contains a minor pleochroic green to yellow mineral with high-birefringence resembling either well-crystallized celadonite/glauconite or amphibole (actinolite or hornblende).

Interpretation

The volcanic rocks near the top of Hole 1189A are fresh dacites based upon the SiO_2 content of their glass. They are aphyric, containing only traces of small plagioclase and clinopyroxene phenocrysts. Altered volcanics deeper in the cored section are similar to the fresh ones in terms of their phenocryst content and are probably altered equivalents of dacite.

The dacites from Hole 1189A are distinguished from the rhyodacites of Hole 1188A by the silica concentration of their glasses and by the fact that the Hole 1188A rhyodacites are sparsely phyric, typically with 2%–3% plagioclase, 1% clinopyroxene, and 0.5% magnetite phenocrysts (see **"Igneous Petrology,"** p. 19, in the "Site 1188" chapter). This suggests that magma differentiation from 66 to 72 wt% SiO_2 (i.e., from dacite to rhyodacite) may have been accomplished by low-pressure fractional crystallization of plagioclase, clinopyroxene, and magnetite deeper within the crust.

Black patches occurring within felsic volcanic host rock of Unit 15 in Core 193-1189A-8R probably represent quenched, originally mafic material. The patches possibly represent xenoliths of mafic material ripped off the chilled margin of a dike or sill somewhere deeper within or beneath Pual Ridge.

Hole 1189B

The first 31.0 mbsf at Hole 1189B was not cored. Instead, the hole was spudded directly into a high-temperature chimney field using a hammer-in casing system. Two sources of information are relevant to the lithostratigraphy of this upper part of the hole. First, the hammer drill encountered very hard rock at depths of 7–8 mbsf and again at 10–15 mbsf (see **"Introduction,"** p. 1). These intervals probably correspond to volcanic rocks similar to the resistant volcanic units sampled

F15. A black patch with former acicular crystals replaced by feldspar/quartz and fine opaque grains, p. 83.

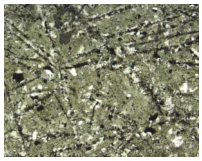

F16. Margin of a black patch showing a former plagioclase phenocryst, p. 84.

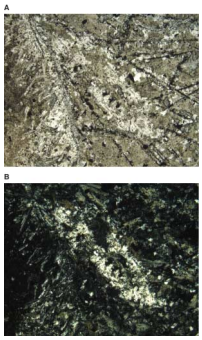

F17. Rim at the edge of a black patch with relict bladed crystals showing oriented microlites in the host rock, p. 85.

at Sites 1190 and 1191 or near the top of Site 1188 (recovered in Hole 1188A). Second, the uppermost 6 m, the material between 8 and 10 mbsf, and that between 15 and ~30 mbsf, was relatively soft and nonresistant. The suspicion that these intervals represent, at least in part, massive sulfide deposits was reinforced when the hammer drill tool was retrieved and found to have sand-sized sulfide debris stuck inside.

The first rock recovered by coring is semimassive sulfide with minor altered volcanic clasts (Unit 1 in Core 193-1189B-1R-1). This was followed by a succession of completely altered coherent volcanic rock units alternating with various types of brecciated units (Fig. **F18**). From ~31 to 128 mbsf (curated depth), lithologies alternate between vesicular (or amygdaloidal) volcanic rocks (Units 2, 7, 9, 11, 13, and 15) and hydrothermal breccias (Units 3–6, 8, 10, 12, 14, 16, and 17). The breccias, particularly in Units 3, 4, and 5, are altered volcanic rocks cut by stockwork veins with a structure transitional to breccia. In fact, these units are distinguished primarily on the basis of the stockwork mineralogy rather than the original igneous protolith.

Unit 18 at 128 mbsf is a polymict volcaniclastic breccia and is underlain by a sequence of highly altered vesicular volcanic rocks alternating with flow-banded and perlitic volcanic rocks that exhibit, to varying degrees, both pseudoclastic textures and poorly sorted, ungraded, true clastic textures. The latter are typically manifested as subangular, grain-supported, poorly sorted breccias of flow-banded clasts, rotated with respect to each other and, in at least one case, intruded by coherent, flow-banded lava. These rocks are interpreted as in situ and/or resedimented autoclastic breccias that formed on the margin of lava flows during extrusive eruptions on the seafloor.

Volcaniclastic sandstone with sedimentary grading and petrographically diverse rock fragments forms Unit 31 at 186 mbsf, and polymict volcaniclastic breccia forms Unit 35 at 197 mbsf. These units provide further evidence of paleoseafloor surfaces sampled by the drill core at Site 1189.

A full description of the various units including lithologic characteristics and alteration mineral assemblages is provided in Table **T4.** A graphic log of Hole 1189B summarizes the distribution of units and their lithologic and alteration characteristics (Fig. **F18**). Detailed hand specimen descriptions of individual pieces and thin-section descriptions are available (see **"Site 1189 Thin Sections,"** p. 59).

F18. Graphic summary log for Hole 1189B showing the lithologic characteristics of the various units including alteration, p. 86.

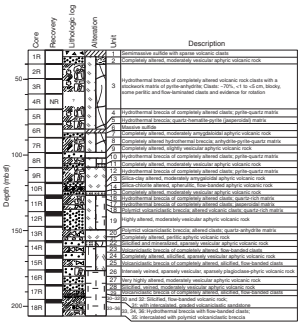

T4. Lithology and alteration of Units 1 to 36, Hole 1189B, p. 236.

Unit Summaries

Unit 1 is a semimassive sulfide with minor volcanic rock clasts. The matrix is fine-grained pyrite-chalcopyrite-anhydrite-quartz, whereas the sparsely vesicular volcanic clasts (2–3 mm in maximum dimension) are completely altered to clay, silica, and anhydrite.

Unit 2 is a completely altered (green clay and silica), moderately vesicular, aphyric volcanic rock with ~10% elongated and aligned vesicles that are lined by pyrite.

Units 3, 4, and 5 are matrix-supported hydrothermal breccias of completely altered (green clay and silica) volcanic clasts in a stockwork vein matrix. The angular to blocky clasts (up to 1 cm in maximum dimension) are generally arranged in a jigsaw-fit pattern, and some show preserved flow banding or perlitic groundmass texture. In Unit 3, the stockwork matrix consists of pyrite-anhydrite veins, which alternately cut and parallel the flow banding present in some clasts. In Unit 4, the vein matrix is pyrite-quartz, which forms a stockwork of semimassive

sulfide. Unit 5 has a stockwork that is jasperoidal (pyrite + hematite + quartz), which is distinct from the otherwise similar Unit 4. The perlitic clasts in Unit 5 have minor vesicles and rare plagioclase phenocrysts, which are locally truncated at the clast margin.

Unit 6 is a small piece of vuggy massive sulfide, composed of 90% very fine grained euhedral pyrite, 9% quartz, 1% anhydrite, and traces of chalcopyrite and red-brown sphalerite. This is possibly a fragment of stockwork vein.

Unit 7 is a completely altered, moderately amygdaloidal rock with soft clay-rich alteration and <1-mm-diameter quartz-filled amygdules.

Unit 8 is a hydrothermal breccia of completely altered, matrix-supported volcanic clasts in an anhydrite-pyrite-quartz stockwork vein matrix (Fig. F19). Rock clasts (up to 1 cm in maximum dimension) are generally green clay altered. Some are flow banded and some contain minor <1-mm-diameter quartz-filled amygdules. Unit 8 is very similar to Units 3, 4, and 5.

Unit 9 is a completely altered, slightly vesicular volcanic rock. The rock is completely altered (silica, clay, and sulfate bearing), with patchy silicification and both pyrite and anhydrite in vesicles.

Unit 10 is a hydrothermal breccia of completely altered volcanic clasts in a pyrite-quartz matrix. The altered fragments, up to 1 cm in size, are either green, soft, and clay-rich or tannish and silicified.

Unit 11 is a completely altered, silicified, moderately vesicular volcanic rock with between 1 and 8 vol% ovoid vesicles (up to 1 mm). Some vesicles are lined by quartz, which is overgrown by pyrite.

Unit 12 is a hydrothermal breccia of completely altered nonvesicular volcanic clasts, which locally show remnant flow banding, in a pyrite-quartz stockwork matrix. This unit is very similar to Unit 4.

Units 13 through 15 are coherent volcanic rocks. Unit 13 is a silica-clay altered, moderately amygdaloidal, aphyric volcanic rock (Fig. F20); Unit 14 is a silica-chlorite altered, spherulitic, and flow-banded aphyric volcanic rock (Fig. F21); and Unit 15 is a completely altered, silicified, moderately vesicular, aphyric volcanic rock.

Units 16 and 17 are hydrothermal breccias of completely altered volcanic rock clasts. In Unit 16, the 1-cm clasts are flow banded and exhibit random rotations with respect to each other. The breccia matrix is siliceous ± magnetite bearing. Unit 17 is distinguished by a jasperoidal matrix containing quartz and hematite ± magnetite.

Unit 18 is a polymict volcaniclastic breccia of completely altered, <1-cm volcanic clasts, which are green-clay altered (locally flow banded), white-clay altered, or gray and siliceous. The matrix is quartz ± pyrite and magnetite.

Unit 19 is highly altered, moderately vesicular, aphyric volcanic rock. Highly stretched, steeply oriented vesicles and abundant (25 to 40 vol%) plagioclase microlites, as seen in thin section, distinguish this unit. Furthermore, several black xenoliths (1–2 cm) have been observed.

Unit 20 is a volcaniclastic breccia with abundant, clay-altered volcanic clasts in a quartz-anhydrite ± pyrite matrix. Clasts are mainly perlitic or flow banded; however, locally amygdaloidal, trachytic, and pumiceous clasts have been observed in thin section.

Units 21 and 22 are aphyric volcanic rocks. Unit 21 is completely silica-clay altered, massive, and nonvesicular, whereas Unit 22 is silicified, mineralized, and sparsely vesicular.

Unit 23 is a volcaniclastic breccia of green- and white-clay altered, commonly flow-banded, volcanic clasts in a quartz-anhydrite matrix

F19. Hand specimen of matrix-supported breccia with green clay altered volcanic clasts in an anhydrite-pyrite-quartz cement, p. 87.

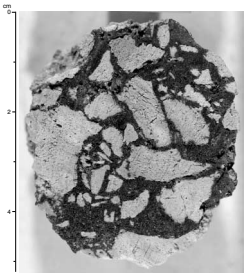

F20. Green silicified, moderately amygdaloidal, aphyric volcanic rock with hairline quartz-anhydrite-pyrite veins, p. 88.

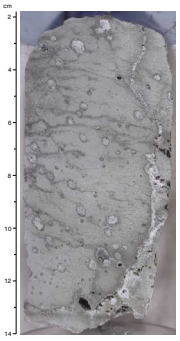

F21. Flow banding defined by alternating white bands of coalesced microspherulites and dark bands with isolated microspherulites, p. 89.

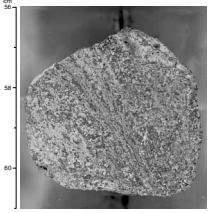

(Fig. F22). The clasts, commonly rotated with respect to each other, are in one specimen intruded by flow-banded lava (Fig. F23), which is interpreted as an exceptional example of a coherent lava intruding its own autoclastic breccia at the flow margin.

Unit 24 is a completely altered, highly silicified, sparsely vesicular, aphyric volcanic rock. Vesicles are elongated and lined with quartz and pyrite, followed by anhydrite.

Unit 25 is a poorly sorted, clast-supported, volcaniclastic breccia of completely altered (silicified and green- and white-clay altered), flow-banded volcanic rock. The unit is partly coherent and partly (auto)clastic with abundant rotated clasts (>5 cm in maximum dimension) (Fig. F24). Locally, alteration along, and outward from, a network of microfractures has overprinted the flow banding generating a nodular, pseudoclastic texture (Fig. F25). In one sample, flow banding wraps around a black, vesicular xenolith (Fig. F25).

Units 26 through 28 are variably vesicular, aphyric to sparsely plagioclase phyric volcanic rocks. Unit 26 is sparsely vesicular and sparsely porphyritic volcanic rock with up to 2 vol% of small (≤2 mm) plagioclase phenocrysts (laths or tabular to rounded shapes). It is silicified and contains a fine network of quartz (-pyrite-magnetite) veins that network imparts a pseudoclastic texture locally (Fig. F26). Unit 27 is very highly altered (silicified), moderately vesicular, and contains trace amounts of fresh plagioclase phenocrysts (up to 2 mm in maximum dimension, <1 vol%). Vesicles (up to 2 cm; round to lensoidal) are lined by quartz and anhydrite, and the groundmass has an alteration texture resembling hieroglyphics (Fig. F27). Unit 28 is intensely silicified and moderately vesicular aphyric volcanic rock. Vesicles are lined by quartz ± pyrite.

Unit 29 is a volcaniclastic breccia of completely altered (silicified and green-clay bearing), flow banded clasts. Some clasts show folded flow banding, and in one clast, flow banding is wrapped around a black xenolith.

Unit 30 is a silicified, flow-banded, aphyric volcanic rock. Flow banding is wrapped around a xenolith of black volcanic rock with a spinifex-like texture in one piece. Locally, fine, fresh plagioclase phenocrysts are present (up to 1 vol%).

Unit 31 is a graded volcaniclastic sandstone and represents a sedimentary unit deposited on a paleoseafloor. It contains a variety of volcanic fragments (generally <1 mm in maximum dimension) including porphyritic, perlitic, and glassy clasts, indicating that it was derived from a heterogeneous source area.

Unit 32 is a flow-banded and silicified aphyric volcanic rock with a fine network of quartz-pyrite veins.

Units 33 and 34 are completely altered hydrothermal breccia consisting of flow-banded volcanic rock with a quartz (-hematite-pyrite) matrix. The two units are nearly identical, except that Unit 33 contains fresh plagioclase phenocrysts (<1 vol%, up to 1 mm), whereas Unit 34 is aphyric and shows a prominent nodular pseudoclastic texture caused by alteration along fine veinlets.

Unit 35 is a completely altered (green clay and silica), poorly sorted, clast-supported polymict breccia with flow-banded, spherulitic, and perlitic clasts in a quartz (-hematite-pyrite) matrix. Clasts with folded flow banding truncated at the margin (Fig. F28) indicate abrasion of clasts during particle transport. This observation indicates that Unit 35 represents a resedimented volcaniclastic breccia deposit.

F22. Poorly sorted volcaniclastic breccia (Unit 23) with flow-banded clasts showing evidence for in situ fragmentation and rotation of clasts, p. 90.

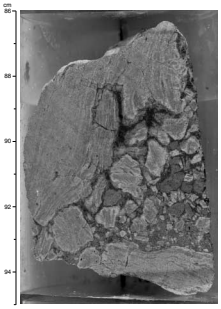

F23. Synvolcanic intrusion of molten lava into its own autoclastic breccia, Unit 23, p. 91.

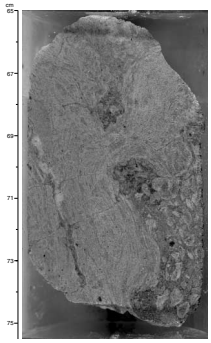

F24. Clast-supported volcaniclastic breccia with rotated fragments, p. 92.

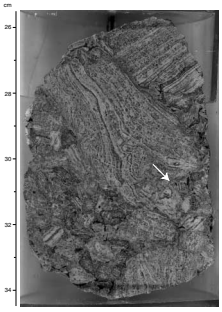

Unit 36 is a completely altered (green clay and silica) hydrothermal breccia consisting of flow-banded volcanic clasts with a quartz (-pyrite) matrix. Textural observations indicate that whereas most of the rock was fragmented in situ, some clasts have been rotated.

Volcanic Textures

Several primary volcanic features have been recognized from Hole 1189B. These include phenocrysts, vesicles and amygdules, perlite, flow banding, spherulites, and xenoliths. In addition, there are several types of clastic rocks (including monomict and polymict volcaniclastic breccia, volcaniclastic sandstone, and hydrothermal breccia) and units with pseudoclastic texture.

Phenocrysts

The dominant phenocryst type observed in rocks from Hole 1189B is plagioclase, as it is at Site 1188 and Hole 1189A. In Hole 1189B, plagioclase phenocrysts (<1–2 vol%; up to 2 mm) are present mainly below ~125 mbsf (Units 19, 21, 23, 26, 27, and 35). These units in the lower half of the hole are characteristically less altered than rocks in the upper part. However, there are also plagioclase phenocrysts (from trace to 2 vol%) in several altered clasts in the shallow stockwork Units 5 and 8 at around 80 and 90 mbsf.

The plagioclase phenocrysts reach ~2 mm in length and are typically lath-shaped with highly rounded edges (Fig. **F29**). This texture suggests that the crystals underwent a corrosive dissolution prior to eruption of the magma. In several cases, the rounded phenocrysts coexist with acicular phenocrysts that are less rounded and with microphenocrysts that are euhedral.

In addition to plagioclase, several rocks studied in thin section contain minor, altered clinopyroxene phenocrysts, partially or completely replaced by clay minerals (Fig. **F30**). Traces of clinopyroxene phenocrysts were noted in Units 19, 25, 26, and 27. Likewise, a very few magnetite phenocrysts were noted in Unit 26, where they reach 0.25 mm across and may be free-floating in groundmass or included inside plagioclase and clinopyroxene.

Vesicles and Amygdules

The maximum vesicularity observed in volcanic rocks from Hole 1189B is 20 vol% in Units 15 and 19, 15 vol% in Unit 27, and 10 vol% or less in Units 1–3, 9, 11, 13, 16, 18, 22–24, 26, and 30. Volcanic rocks exhibiting flow banding are generally not vesicular. Filled vesicles (amygdules) are common and are generally lined or filled by quartz (Fig. **F31**), followed frequently by pyrite, sphalerite (Fig. **F32**), or anhydrite.

Many vesicles and amygdules are nonspherical, reflecting stretching or flattening in response to plastic flow. The vesicles from Unit 19 are striking in this regard not only because they are highly stretched, but also because the stretching direction is uniformly steep (between 70° and 90°; see **"Structural Geology,"** p. 41), indicating subvertical laminar flow of the lava. Consequently, Unit 19 may represent a magma feeder zone within a syngenetic lava dome or older volcanic rocks.

Perlite

Well-preserved to remnant perlitic texture, indicating that the volcanic groundmass consisted of volcanic glass that became hydrated prior to hydrothermal alteration, has been observed in Units 3, 5, 20, 21, 23,

F25. Flow-banded, highly altered volcanic rock, crosscut by a feeble network of silica veins, surrounded by alteration halos of silica-clay minerals, p. 93.

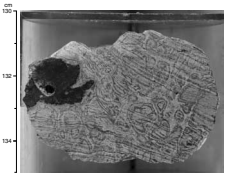

F26. Intensely veined, weakly vesicular and sparsely plagioclase phyric volcanic rock, p. 94.

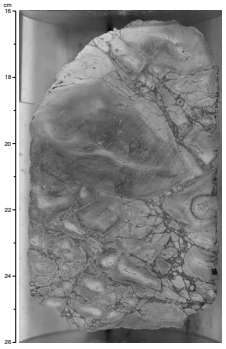

F27. Moderately vesicular aphyric volcanic rock with a hieroglyphic texture caused by incomplete hydrothermal alteration of groundmass, p. 95.

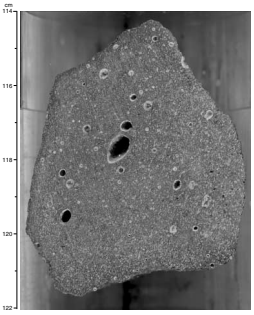

and 31. These units represent a spectrum of volcanic rock types including aphyric volcanic rock, hydrothermal breccia, volcaniclastic breccia, and volcaniclastic sandstone.

Remnant perlite is present in the altered groundmass of a completely altered, aphyric massive rock (Unit 21) where the arcuate cracks have been preserved despite the replacement of the glassy volcanic groundmass by quartz, chlorite, and clay minerals (Fig. F33).

Perlitic clasts are a common component of volcaniclastic breccia (Units 20 and 23). The originally glassy groundmass has been replaced dominantly by microcrystalline quartz, and the fine arcuate domains defining the perlitic cracks are occupied by chlorite and black cryptocrystalline material (Fig. F34). Perlitic clasts with very fine, stretched, and aligned chlorite amygdules are present in Unit 20 (Fig. F35). These clasts were initially glassy and vesicular and probably represent tube pumice fragments.

In hydrothermal breccia (Units 3 and 5), perlitic texture is preserved in the central parts of clay-rich volcanic clasts that are hosted in a stockwork matrix of variable mineralogy (jasperoidal in Fig. F36). In Unit 3, perlitic clasts are hosted in an anhydrite and gypsum-rich stockwork matrix. Textural evidence indicates that these clasts are locally consumed and replaced along their margins during hydrothermal alteration in this unit (Fig. F37).

In volcaniclastic sandstone (Unit 31), angular submillimeter perlitic clasts are also important components (see below).

Flow Banding

Flow banding is a common feature in many units of Hole 1189B (Units 3–5, 8, 10, 12, 14, 16–18, 20, 23, 25, and 29–36); however, it is best preserved in units below ~120 mbsf. Some of the flow-banded units appear to be coherent lava (Units 14, 30, and 32) (Fig. F21), whereas others are clearly of volcaniclastic origin (Units 18, 20, 23, 25, 29, and 35) (Figs. F22, F24). It seems most likely that there are gradational contacts between brecciated and nonbrecciated flow-banded rocks grading from coherent facies to brecciated facies with jigsaw-fit texture to chaotic, poorly sorted, monomict breccia facies. A synvolcanic intrusion of flow-banded lava into brecciated facies consisting of cogenetic flow-banded clasts has been observed in Unit 23 (Fig. F23). A mixture of gradational and synvolcanic intrusive contact relationships between coherent and clastic facies (autoclastic and/or hyaloclastic) is characteristic for felsic lavas and has been described from several submarine examples (see "Igneous Petrology," p. 4, in the "Explanatory Notes" chapter).

In most units, flow banding is defined by fine, linear, alternating bands (generally <1 to 2 mm in width and continuous for as much as 5 cm) of pale gray and light green color. In Unit 14 (Fig. F21) it is apparent from hand specimen inspection that the light gray bands consist of aligned, small, white concentric spherules. The dark groundmass contains isolated spherules or nodular groups of spherules. This observation is confirmed by thin-section examination. The spherules (0.2 to 0.3 mm in diameter) consist of light gray to brown clay and have coalesced to form linear structures with bulbous outer margins (Fig. F38). The central part of these necklacelike domains consists of very fine grained quartz. In other units, the flow banding is defined by similar structures; however, individual spherules are <0.1 mm and can only be resolved in thin section (Fig. F39). The dark bands between these linear

F28. Polymict breccia showing evidence for clast abrasion and fine sulfide veins that predate deposition, p. 96.

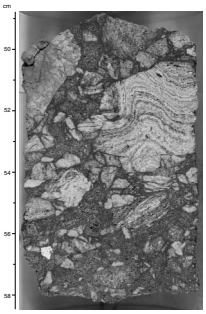

F29. Rounded, fresh plagioclase phenocrysts, typical of the lower sequence in Hole 1189B, p. 97.

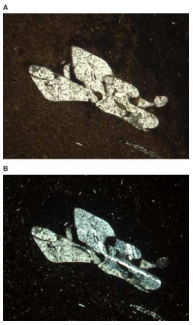

F30. Fresh plagioclase and altered clinopyroxene phenocrysts, Unit 25, p. 98.

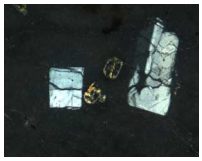

F31. Quartz ± pyrite amygdules within a completely altered volcanic rock, Unit 11, p. 99.

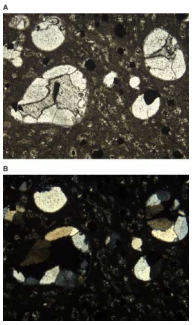

domains consist of chlorite and/or dark brown clay minerals and contain minor, isolated spherules.

This type of flow banding is best interpreted as a result of high-temperature devitrification of lava generating spherulites. However, they lack the typical, spherulitic internal texture of radiating quartz and feldspar needles. This might be caused by a subsequent recrystallization of the original material during alteration. The dark bands are interpreted to represent the remnant volcanic glass that was left between the devitrified bands. The glass has been completely altered to chlorite and other phyllosilicates.

Flow banding has also been observed in clasts of Unit 20, which, however, lack the banded texture defined by aligned and coalesced microspherulites. Instead, the clasts contain fibrous, wispy linear domains consisting of very fine grained black minerals (Fig. F40). Possibly, this type of banding is a result of Fe oxide precipitation in very fine, stretched vesicles during an early stage of alteration.

Spherulites

Well-preserved spherulites have been observed in several clasts of a polymict breccia (Unit 35). These consist of densely packed, radiating aggregates of quartz and feldspar, which are impinging on each other (Fig. F41). Individual spherulites have diameters between 0.2 and 0.3 mm and are locally replaced by patches of micropoikilitic quartz.

Xenoliths

Small centimeter-scale xenoliths have been noted infrequently in Units 11, 19, and 25–30. Some are completely altered soft green clay xenoliths of unknown origin. Others are dark gray, green, or black. The xenoliths are commonly rounded and exhibit a halo or reaction rim to the host rock in hand specimen. When the host rock is flow banded, the lamination wraps around the xenoliths. Some xenoliths have acicular crystals several millimeters long and arranged in plumose arrays, resembling a spinifex texture. Xenoliths similar to these were described from Site 1188.

In thin section, most xenoliths have fine-grained intergranular or intersertal textures, commonly with acicular, skeletal, plumose, or variolitic plagioclases suggesting a quench texture (Fig. F42). In one case, the variolitic plagioclase is concentrated at the margin of the xenolith and extends into the host volcanic matrix (Fig. F43). That same xenolith contains a talc(?) pseudomorph of a mafic phenocryst, possibly olivine, which has a euhedral brown spinel inclusion embedded within it.

The xenoliths are interpreted to represent fragments of rock entrained by moving magma or lava, either within the crustal plumbing system or during eruption at the seafloor, respectively. It may be significant that the unit with the most xenoliths (i.e., three xenoliths noted in the igneous logs) is Unit 19, which has the uniformly steeply oriented stretched vesicles and might be interpreted as a dike or part of a magma feeder system.

Clastic Textures

There are abundant units with fragmental textures in Hole 1189B, which represent a range from volcaniclastic breccia and sandstone to hydrothermal breccia and coherent volcanic rock with superimposed pseudoclastic texture caused by alteration. These features are similar to Hole 1189A; however, because of the lower intensity of hydrothermal alteration, discrimination of "true" clastic texture from alteration-related, apparent clastic texture was possible for most units in the lower

F32. Quartz-sphalerite amygdule within highly altered volcanic rock, Unit 26, p. 100.

F33. Remnant perlite texture in the altered groundmass of a completely altered, aphyric massive rock, p. 101.

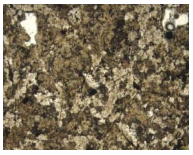

F34. Perlitic cracking preserved in altered volcanic rock, p. 102.

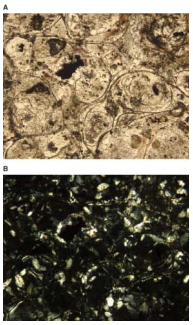

F35. Former tube pumice clast with perlitic structure and stretched chlorite-filled amygdules, p. 103.

F36. Perlitic texture preserved in altered volcanic clast, within a jasperoidal stockwork matrix, p. 104.

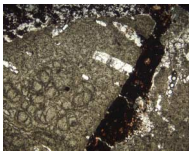

part of Hole 1189B. Textural evidence for a volcaniclastic origin includes polymict composition (Units 18, 20, and 30), abrasion of clasts (truncated phenocrysts, vesicles, amygdules, and flow banding; Units 18, 20, 23, 25, and 35) and rotation of large (>2 cm) flow-banded clasts (Units 18, 20, 23, 25, 29, and 35).

Polymict Volcaniclastic Breccia

Distinctive clast types have been recognized in Units 18, 20, and 35 (Table T4), indicating heterogeneous sources for these deposits. Distinctive, aphyric siliceous and clay-rich clasts in Unit 18 indicate that clasts were derived from source areas that were not only already altered, but which possessed different styles of alteration. Unit 35 contains aphyric, perlitic, flow-banded, and spherulitic clasts, and Unit 20 consists of a variety of clasts including perlitic, flow-banded, trachytic, amygdaloidal, and pumiceous fragments. Whereas Units 18 and 35 may have been derived from a single lava flow with variable groundmass textures and different styles of alteration, it is evident that clasts in Unit 20 are derived from a variety of parent rocks. Nevertheless, it is beyond any doubt that these units must have been emplaced by sedimentary, mass-flow processes and, therefore, represent paleoseafloor positions.

Graded Volcaniclastic Sandstone

Unit 31 is a thinly laminated, graded volcaniclastic sandstone and contains a variety of angular volcanic fragments including glassy, perlitic, and porphyritic clasts (Fig. F44). The maximum particle size is ~3 mm at the base of individual laminae, rapidly grading to <0.5 mm in the upper parts. The grading, if it is normal (the piece is unoriented), is evidence for deposition of the unit from dilute mass flows rather than by suspension settling, and therefore, it probably represents the distal equivalent of polymictic breccia units.

Monomict Volcaniclastic Breccia

Units 23, 25, and 29 are monomict, clast-supported, poorly sorted breccia with flow-banded clasts. There is abundant evidence for rotation of large (>5 cm) clasts (Fig. F24), and a synvolcanic intrusion of coherent flow-banded lava into the clastic facies has been observed in Unit 23 (Fig. F23). Based on these textural characteristics, we interpret these units as the clastic facies of lava (autobreccia and/or hyaloclastite) formed on the outer margin of the flow.

Hydrothermal Breccia

Clastic units with monomict composition, matrix-supported texture, and prominent jigsaw-fit arrangement of clasts are interpreted as hydrothermal breccia. Transport and rotation of clasts are also consistent with hydrothermal brecciation, however, only to limited degree because of the spatial constraints. Units 3–5, 8, 10, 12, 16, 17, 33, 34, and 36 have been logged as hydrothermal breccia in Hole 1189B. Unit 26 is an intensely veined volcanic rock and contains one zone were volcanic fragments (as much as 1 cm) were incorporated in an exceptionally large fracture (Fig. F45). These clasts are rotated with respect to each other and more intensely altered than the groundmass of the surrounding volcanic rock. This zone is an exceptional example of hydrothermal brecciation.

Pseudoclastic Texture

Prominent apparent clastic textures, which are clearly related to hydrothermal alteration yet do not result in clast rotation or relative

F37. Perlitic clasts hosted in an anhydrite and gypsum-rich stockwork matrix, p. 105.

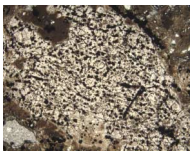

F38. Flow banding defined by aligned, coalesced spherulites forming "necklacelike" domains, p. 106.

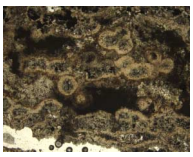

F39. Flow banding defined by alternating light gray bands of aligned and coalesced spherulites and brown to dark gray bands with only isolated spherulites, p. 107.

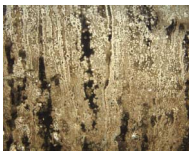

F40. Flow-banded clasts in Unit 20 showing wispy domains of black, very fine grained material, p. 108.

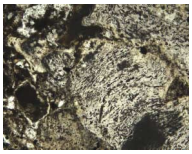

F41. Polymict volcaniclastic breccia with closely packed spherulites, p. 109.

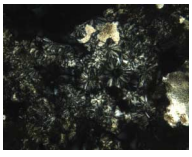

movement, have been observed in several units. Examples include Unit 26, which is intensely veined with some parts of the. volcanic rock showing a clastic texture with prominent jigsaw-fit arrangement of the fragments (Fig. F26). Also, alteration along and outward from an irregular network of fine veins has produced a nodular apparent clastic texture in Unit 25, which is overprinting the flow banding of the rock (Fig. F25). The hieroglyphic groundmass texture of Unit 27 may also be mistaken for a fine-grained, clastic texture because the white domains resemble shard-shaped fragments (Fig. F27). However, these domains are never in direct contact with each other and the abundant vesicles are unequivocal evidence that this unit is a coherent volcanic rock. It is inferred that this texture is caused by an incomplete pervasive alteration and that the white domains represent remnants of the unaltered (or less altered) volcanic groundmass.

Summary

Holes 1189A and 1189B provide a first-order understanding of the volcanic origin of the upper 200 m of Pual Ridge at the Roman Ruins high-temperature hydrothermal site. The only fresh rocks were recovered in the first core from Hole 1189A, which is located a short distance away from the focus of the high-temperature venting. These fresh rocks are dacite and are completely aphyric. All of the other samples from Site 1189 exhibit varying degrees of hydrothermal alteration, ranging from high (40%–80%) to complete (95%–100%). Nevertheless, abundant evidence for extrusive volcanic features shows that the whole sequence is either volcanic or volcaniclastic in origin.

Whereas the fresh dacite at the top of Hole 1189A is aphyric, many coherent volcanic units from both Hole 1189A and 1189B contain sparse phenocrysts, both fresh and replaced by secondary minerals. Plagioclase, or pseudomorphs thereof, represent the most common phenocryst type, whereas clinopyroxene (almost always replaced) and magnetite are only infrequently noted. Fresh plagioclases, especially in Hole 1189B, are characteristically rounded, suggesting a period of phenocryst instability and dissolution prior to or during eruption.

Many coherent volcanic units from Site 1189 are vesicular, with the degree of vesicularity ranging up to ~20 vol%. Hydrothermal alteration has commonly resulted in vesicle filling by secondary minerals, resulting in an amygdaloidal texture. Other coherent units contain spherulites, formed as a result of high-temperature devitrification of glass, and/or perlitic groundmass textures, formed during low-temperature hydration of volcanic glass.

One moderately vesicular rock unit from Hole 1189B (Unit 19, from ~138 mbsf) is noteworthy for its highly stretched vesicles, all of which have steep stretching orientations ranging from ~70° to 90°, indicative of subvertical flow. This unit represents ~10–12 m of coring and could have obtained its unusual oriented structure during eruption at the seafloor or alternatively by synvolcanic intrusive emplacement. The bounding lithologies (Units 18 and 20) are both polymict volcaniclastic breccias, which have been interpreted to represent paleoseafloor deposits. Consequently, one could envision a tectonically disrupted seafloor with a veneer of polymict breccia. A vesicular lava flow cascades over a 10-m fault scarp, and a new polymict breccia eventually develops on top of it. These units are subsequently covered by younger extrusive volcanic rocks. The alternative explanation requires a dikelike body with an average dip of 80° to have been sampled by the drill core. With

F42. Photomicrograph of a xenolith with intergranular texture and skeletal plagioclase, p. 110.

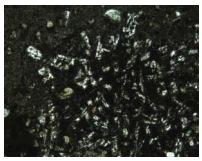

F43. Variolitic plagioclase concentrated at the margin of a xenolith, p. 111.

F44. The graded volcaniclastic sandstone contains a variety of submillimeter angular fragments including glassy, porphyritic, and perlitic clasts, p. 112.

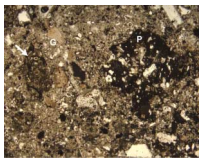

F45. Hydrothermal brecciation with a clastic zone within an exceptionally large vein in coherent volcanic rock, p. 113.

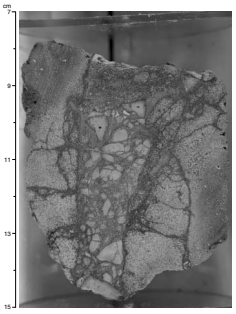

a 12-m vertical extent, the calculated dike width would be 2.08 m. Unfortunately, with no contacts recovered, these alternatives can not be tested simply.

The lithologic succession at Hole 1189A is composed of alternating coherent volcanic rock units and brecciated units. One obvious paleoseafloor position, a polymict volcaniclastic breccia, was sampled at a depth of ~125 mbsf.

The lithologic succession at Hole 1189B is more complicated. The first 31 m was drilled, not cored, yet it is reasonably certain that there are massive sulfides at the seafloor, hard-rock units at 7–8 and 10–15 mbsf, and either soft, highly altered rocks or massive sulfides from 0–7, 8–10, and 15–31 mbsf. In the cored part of Hole 1189B, below 31 mbsf, the rocks recovered alternate between coherent volcanic units and brecciated units. Above ~70 mbsf, many of the breccias have stockworklike veining. Below 70 mbsf, and particularly below 137 mbsf (beginning with Unit 19), the volcanic rocks are, on average, less altered and more plagioclase rich. Paleoseafloor positions are evident at ~135, 150, 193, and possibly 82 mbsf. This spacing places a broad upper limit on the thickness of eruptive units at Pual Ridge of ~50 m. Thus, the ridge was not built up in a single or even two or three very thick eruptions. No lower limit to the thickness of individual eruptive units emerges from the core data because all of the paleoseafloor indicators may not have been sampled in these fairly low recovery drill holes.

HYDROTHERMAL ALTERATION

Hydrothermally altered volcanic rocks were recovered at Site 1189 beneath the Roman Ruins hydrothermal site, a site of active, high-temperature (>240°C) (Douville et al., 1999) fluid outflow and sulfide chimney development at the PACMANUS hydrothermal field (Tables T2, T4; Figs. F2, F17, F46, F47). At Site 1189, two RCB holes, Hole 1189A and Hole 1189B, were cored over intervals of 0.0–125.8 and 31.0–206.0 mbsf, respectively. Although the two holes are located only 30 m apart within the chimney field, the exceptionally poor recovery in the upper cored portion of Hole 1189B makes it extremely difficult to effectively compare them (total recovered material in Cores 193-1189B-1R to 10R between 31.0 and 127.6 mbsf is 1.49 m, at an average recovery of 1.54%). Nevertheless, it is apparent that Hole 1189B intersected a much more strongly mineralized sequence than the equivalent interval in Hole 1189A, indicating rapid lateral variation in alteration style within the volcanic sequence below Roman Ruins hydrothermal site. This is not surprising, given the focused nature of hydrothermal outflow onto the seafloor at the site, although both holes were located near chimneys.

General Overview

The following detailed description of hydrothermal alteration in coherent volcanic rocks and breccias from beneath the Roman Ruins chimney site is based primarily on visual descriptions of cores from Hole 1189A and Hole 1189B and is supplemented by thin-section petrography (Fig. F48) and XRD analyses of bulk samples (Figs. F46, F47). The portable infrared mineral analyzer (PIMA) analyses were also conducted on a large number of core samples from Hole 1189A. However,

F46. Summary of lithostratigraphic units, alteration type, and distribution of alteration phases as indicated by XRD, Hole 1189A, p. 114.

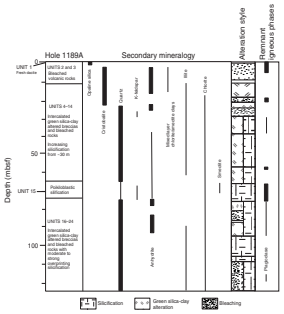

F47. Summary of lithostratigraphic units, alteration type, and distribution of alteration phases as indicated by XRD, Hole 1189B, p. 115.

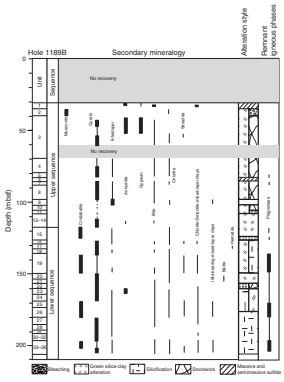

F48. Variation in abundance of minerals with depth as estimated from thin sections, Holes 1189A and 1189B, p. 117.

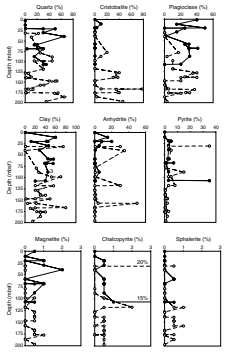

the spectra were not processed on board, and it was not possible to utilize PIMA results for this report.

Alteration was classified in the core primarily by the visual detection under binocular microscope of the following key minerals: soft green to bluish-green clay; soft white clay, and hard silica polymorphs. Sulfide and oxide mineralization are readily distinguished by the presence of abundant pyrite and other sulfides (principally chalcopyrite and sphalerite) and rare jasperoidal silica-iron oxide, respectively. These rocks are discussed more fully in **"Sulfide and Oxide Petrology,"** p. 34. Sulfides, predominantly pyrite, are also present as minor to trace phases within altered rocks throughout the drilled section.

Alteration Types and Relative Timing of Alteration Events

Whereas the lithology summaries (Tables **T2, T4**) reflect the dominant alteration type in any particular unit, it is common that multiple overprinting alteration styles can be distinguished in individual core pieces from Site 1189. Similar to Site 1188 (see **"Hydrothermal Alteration,"** p. 33, in the "Site 1188" chapter), alteration appears to be multistage, with a general evolution from early green silica-clay (GSC) alteration, followed by pale gray to white silica-white clay-anhydrite bleaching, and finally hard silicification. Late anhydrite ± quartz ± pyrite veins are present in cores from Site 1189. However, they were much less abundantly recovered than similar veins seen at Site 1188 and do not exhibit the bleached, banded alteration halos that are commonly developed around these veins at Snowcap hydrothermal site.

Variation of Alteration with Depth

Alteration at Site 1189 shows a similar variation with depth to that seen at Site 1188. However, a steeper temperature gradient is suggested, as equivalent transitions are developed at shallower depths. In Hole 1189A, only four pieces of fresh dacite, with alteration restricted to films of opaline silica and clay on fracture surfaces, were recovered before penetrating a sequence of bleached volcanic rocks with cristobalite, mixed-layer chlorite-smectite phases, and anhydrite as the principal secondary minerals (Fig. **F46;** Tables **T2, T5**). These variably bleached rocks extend to a curated depth of ~10 mbsf and are underlain by pervasively and completely altered, flow-banded, brecciated, GSC altered rocks, intercalated with more coherent, bleached, vesicular volcanic units. The mineralogy of this interval, which extends to a depth of 68 mbsf, is dominated by illite, chlorite, and either cristobalite (to 25 mbsf) or quartz (below 25 mbsf). In Hole 1189A, the transition between cristobalite and quartz is sharp and shallow, when compared to the similar transition at Site 1188, where it is gradual between 100 and 120 mbsf. Within the intercalated GSC altered and bleached rocks at Site 1189, patchy silicification is present and becomes more pronounced downhole, as indicated by the increasing quartz content and hardness of the rocks. A zone of poikiloblastic silicification is present between 68 and 78 mbsf in Hole 1189A, in which illite is rare and smectite and chlorite are the dominant phyllosilicates. Despite the common development of poikiloblastic quartz in this lithologic unit, the extent of alteration is not as high as in the overlying rocks, and the unit contains abundant fresh plagioclase microlites and phenocrysts. Similar units with poikiloblastic quartz and relict fresh plagioclase are also present in the deeper part of Hole 1189B (>120 mbsf). Potassium feldspar is also

T5. Minerals identified by X-ray diffraction analysis, Hole 1189A, p. 240.

present and is considered to be an alteration product, although this could not be confirmed unequivocally by thin-section petrography. Pervasive silicification (overprinting remnant GSC and bleached domains) is the dominant style of alteration in the remainder of Hole 1188A (78–117 mbsf). The alteration assemblage is dominated by quartz, illite, and chlorite with remnant igneous plagioclase commonly preserved.

In Hole 1189B, the upper 30 m was not cored. However, rapid fluctuations in the ROP suggest that a sequence of intercalated hard rocks (most likely fresh volcanic rock) and very soft rocks (highly altered or mineralized material, rich in sulfide, sulfate, and/or clay) occupy this cased interval. A sand sample recovered from the hammer bit used to drill this interval consists of pyrite, anhydrite, and gypsum. From 30 to ~120 mbsf, Hole 1189B intersected a sequence of strongly brecciated, stockwork veined, GSC altered rocks with patchy silicification, which increases in intensity downhole, together with narrow intervals of both sulfide mineralization (pyrite, with subsidiary chalcopyrite and sphalerite) and patches of jasperoidal quartz with pyrite (Fig. **F47**). The mineralized samples are discussed in more detail in **"Sulfide and Oxide Petrology,"** p. 34. Although clearly more sulfide rich than the equivalent interval in Hole 1189A, the dominant alteration assemblage of quartz, illite, and chlorite in Hole 1189B is similar, except for the common occurrence of potassium feldspar below 70 mbsf (Table **T6**). The extremely poor recovery in the upper part of Hole 1189B makes further correlation impractical between the holes.

T6. Minerals identified by X-ray diffraction analysis, Hole 1189B, p. 241.

The lower portion of Hole 1189B, between ~120 and 200 mbsf, comprises a sequence of highly silicified, massive vesicular lavas, which show little evidence of sulfide mineralization, and flow-banded, brecciated units with highly to completely developed silicification overprinting GSC alteration and with widespread development of quartz-pyrite ± anhydrite ± sphalerite ± hematite veining. This sequence shows varying mineralogy, with less strongly altered units dominated by cristobalite (primarily developed by devitrification of volcanic glass), whereas the completely altered rocks contain quartz. A range of phyllosilicate phases (illite, chlorite, smectite, chlorite-smectite mixed layer, and illite-bearing mixed layer) are found in both cristobalite- and quartz-bearing lithologies, as is potassium feldspar.

Detailed Description of Alteration

A detailed description of the significant features of hydrothermal alteration at Site 1189 is presented in the following pages. As discussed previously, attempts to correlate between the upper parts of the two holes cored at the site are hampered by the poor recovery in the upper portion of Hole 1189B, compounded by the more sulfidic nature of material intersected in it. Consequently, the alteration in Holes 1189A and 1189B will be described separately, before being discussed jointly at the conclusion of this section of the "Site 1189" chapter.

Hand specimen descriptions of the alteration of individual core pieces (see the **"Site 1189 Alteration Logs,"** p. 120) and descriptions of individual thin sections are presented in Figure **F48** and in the **"Site 1189 Thin Sections,"** p. 59. Additionally, Tables **T2** and **T4** present a summary of the hydrothermal alteration of the lithologic units in Holes 1189A and 1189B, whereas a summary of mineralogy as determined by XRD analysis is presented in Tables **T5** and **T6.**

Hole 1189A

Films on Fresh Aphyric Dacite

Fresh dacite (<2% alteration) was only recovered in the first core in Hole 1189A (Unit 1: interval 193-1189A-1R-1, 0–17 cm) (Table T2). Alteration is limited to the development of patchy coatings of grayish silica-clay ± sulfate and occasional films of Fe oxyhydroxide along cracks and on vesicle walls. Based on an XRD analysis of interval 193-1189A-1R-1, 0–4 cm, opaline silica is the dominant component of these films, with quartz as a minor phase.

Green Silica-Clay Alteration

The GSC alteration is the earliest style of pervasive hydrothermal alteration observed at Site 1189 and may be overprinted by patchy bleaching or, more commonly, silicification. As at Site 1188, GSC alteration may be pervasive, giving rocks an overall pale green to blue green color, or it may form remnant patches of greenish coloration within otherwise pale, silicified rocks. Pervasive GSC alteration is best developed in zones of strong hydrothermal brecciation in Hole 1189A (Unit 4: interval 193-1189A-2R-1, 101–137 cm; Unit 6: interval 193-1189A-3R-1, 56–63 cm; Unit 9: Cores 193-1189A-5R through 6R; Unit 11: interval 193-1189A-7R-1, 59–72 cm; Unit 13: interval 193-1189A-7R-1, 92–99 cm; Unit 16: Core 193-1189A-9R; and Unit 19: interval 193-1189A-10R-1, 4–135 cm), where fragments of GSC altered volcanic rocks are cut and/or enclosed by hairline to massive silica ± pyrite and, with increasing depth, quartz-(pyrite) vein networks. More coherent GSC altered units (Unit 8: Core 193-1189A-4R-1 and Unit 10: interval 193-1189A-7R-1, 0–59 cm) are intercalated with the breccias. GSC altered clasts are also present in a polymict volcaniclastic breccia near the base of the hole (Unit 23: interval 193-1189A-13R-1, 51–59 cm).

GSC alteration typically pseudomorphs primary igneous features, preserving perlitic textures and flow banding, even at the microscopic scale (Figs. F49, F50). Originally microlitic GSC altered rocks commonly contain domains in which remnant igneous plagioclase microlites are surrounded by microcrystalline silica-clay alteration. Very fine grained disseminated primary magnetite is also preserved in some samples, although these crystals commonly exhibit evidence of incipient alteration and breakdown to leucoxene.

In brecciated units, angular flow-laminated clasts hosted in a silica matrix commonly show evidence of rotation relative to each other (Fig. F49). It is often unclear whether this rotation is a result of hydrothermal brecciation or whether it reflects an initial volcaniclastic texture in the rock. Flow-top breccias commonly contain angular clasts, so the lack of rounding of fragments in the breccias is not a clear indication of a strictly hydrothermal origin (McPhie et al., 1993). Nevertheless, more coherent intervals of GSC alteration typically exhibit incipient veining and fracturing, and thin-section petrography records the presence of interlinked vein networks parallel to or cutting across flow lamination. These fractures could develop into broad veins, such as those seen in more strongly brecciated core intervals, allowing transportation and rotation of volcanic fragments. Consequently, on the weight of currently available evidence, a hydrothermal origin for most breccias is preferred.

In Hole 1189A, GSC altered breccia clasts are hosted by anhydrite-cristobalite-(pyrite) stockworks at shallow depths (Unit 4: 10.71–11.07 mbsf). However, with increasing depth, quartz is the dominant silica polymorph, instead of cristobalite, and anhydrite generally decreases in

F49. Brecciated, GSC altered rock with flow-banded, rotated volcanic clasts hosted in a silica-pyrite vein network, p. 118.

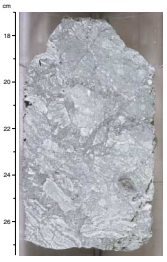

F50. A GSC altered volcanic rock with preserved flow-banded texture and late crosscutting silica veins, p. 119.

abundance. Clasts from Unit 6 (19.96–20.03 mbsf) are hosted by anhydrite-quartz-(pyrite) veins (Fig. F51), whereas in Units 9 (38.80–49.29 mbsf), 11 (58.89–59.02 mbsf), 13 (59.22–59.59 mbsf), 16 (77.70–78.56 mbsf), and 19 (87.41–88.72 mbsf) anhydrite is present only as late vug fill and quartz-(pyrite) veins form the stockwork (Fig. F50). These changes are similar to those seen at Site 1188 and are supported by thin-section descriptions and XRD analyses of GSC altered units from Hole 1189A (Table T5). Illite is present in all examples of GSC alteration chosen for XRD analysis. A disordered chlorite-smectite mixed-layer phase was detected only in Unit 4, whereas all other samples contain chlorite, which generally increases in abundance downhole.

Pyrite is present as the dominant sulfide phase in all intervals of GSC alteration. Traces of chalcopyrite, generally as a late phase in quartz veins and vug fill, are also present in most polished thin sections examined (Fig. F48). The petrography and temporal relationships between these sulfide phases are discussed in "Sulfide and Oxide Petrology," p. 34.

F51. Anhydrite-quartz-(pyrite) veining between GSC altered volcanic fragments, p. 120.

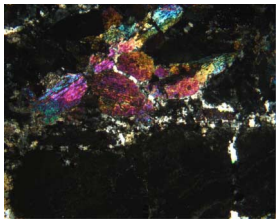

Bleaching

Pervasive bleaching is most common in the upper parts of Hole 1189A (Unit 2: intervals 193-1189A-1R-1, 17–34 cm, and 2R-1, 0–93 cm; Unit 5: interval 193-1189A-3R-1, 0–56 cm; and Unit 7: interval 193-1189A-3R-1, 63–96 cm). Intervals of bleaching are also present in the lower parts of the hole (Unit 17: intervals 193-1189A-9R-1, 86–89 cm, and 10R-1, 0–7 cm; Unit 22: intervals 193-1189A-12R-1, 128–138 cm, and 13R-1, 0–51 cm; Unit 23: interval 193-1189A-13R-1, 51–59 cm; and Unit 24: interval 193-1189A-13R-1, 59–72 cm), but these units are all silicified to some degree.

Bleached units are typically pale gray to white in appearance and may be distinguished from pervasively silicified rocks by their relative softness and from GSC altered rocks by color (GSC altered rocks are pale gray-green to blue-green). With the exception of vesicles (coated or filled with anhydrite, silica, and pyrite) and rare remnant perlitic textures, macroscopic igneous features are generally absent in these units. However, it appears that most of the pervasively bleached units represent massive, sparsely to moderately vesicular lavas, and thin sections of these units commonly display remnant domains of microlitic plagioclase (Figure F52).

F52. Remnant weakly aligned microlitic plagioclase in the groundmass of a bleached, sparsely vesicular volcanic rock, p. 121.

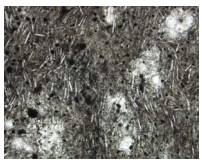

XRD analysis (Table T5) and thin-section observations of bleached units indicate that silica polymorphs, clays, and anhydrite are the main alteration minerals. Cristobalite is found in Units 2 and 5 (0.17–10.63 and 19.40–19.96 mbsf, respectively). As with the GSC altered rocks, quartz dominates in the remaining, deeper units. Chlorite and illite are also present in bleached units throughout the depth of the hole, but rarely comprise more than a few volume percent of the rock. Remnant igneous plagioclase and probable secondary potassium feldspar (Unit 7 only) may also be present. Silica-(pyrite) ± anhydrite veins with silica-clay altered halos are the most abundant vein type in the bleached rocks. Coarse-grained anhydrite is the final phase to precipitate in these veins (Fig. F53) and is also present as vuggy cavity fill. Fine-grained pyrite and traces of chalcopyrite are disseminated in the rocks and concentrated in vugs. The petrography and relationships between these sulfide phases are discussed in "Sulfide and Oxide Petrology," p. 34.

F53. Coarse-grained, bladed anhydrite filling the center of a quartz-pyrite vein in a bleached volcanic rock, p. 122.

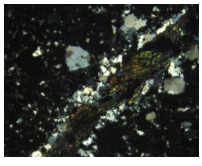

Silicification

As at Snowcap hydrothermal site (Site 1188), silicification is the dominant style of alteration for deeper lithologic units in Hole 1189A at Roman Ruins hydrothermal site. All rocks, irrespective of the dominant alteration style, host silica-(pyrite) bearing veins, and all lithologic units below Unit 7 (Cores 193-1189A-4R to 13R; 29.10–116.82 mbsf) are patchily to pervasively silicified (Table T2). In all cases, silicification is the final stage of pervasive alteration and may overprint either bleaching or GSC alteration. However, even later anhydrite-(silica-pyrite) veins locally overprint silicification.

In general, the degree of silicification increases with depth in Hole 1189A, as demonstrated by an increasing hardness of rocks in hand specimen. Granular microcrystalline to subhedral crystalline quartz replaces the groundmass and fills voids and vesicles of rocks, often preserving igneous textures. In many cases, volcanic features such as perlitic fractures or flow banding provide early fluid pathways, as indicated by the alteration halos commonly developed along these features. Anhydrite is not a major component of the silicified units in Hole 1189A but is found as late vesicle and vein fill in some instances.

Petrographic work confirms that quartz is the main alteration phase introduced to the rock during silicification (Figs. F48, F54). Typically, all vesicles in the rock are filled with crystalline quartz, and the groundmass is pervasively replaced by microcrystalline silica (identified as quartz by XRD analysis) intergrown with fine clay (illite and chlorite, again from XRD analyses) (Table T5). Quartz-pyrite veining is widespread and some veins contain late anhydrite infill. Remnant microlitic igneous plagioclase and very fine grained magnetite (partly replaced by leucoxene) are preserved in some sections. As well as pyrite, traces of chalcopyrite are present in all thin sections of silicified units from Hole 1189A. The petrography and relationships between these sulfide phases are discussed in "Sulfide and Oxide Petrology," p. 34.

Poikiloblastic Silicification

Unit 15 (Core 193-1189A-8-R; 68.00–69.28 mbsf) is a patchily silicified, sparsely vesicular, plagioclase-phyric volcanic rock with weakly to strongly developed quartz-pyrite (± anhydrite) veining. However, the poikiloblastic style of alteration observed in this rock is unique to Site 1189 and has not been intersected at any other site during Leg 193. Consequently, the unit is discussed separately here.

The core from Unit 15 is cream colored in hand specimen, preserving traces of an original vesicular texture and cut by a fine (mostly <0.5 mm wide) anastomosing to crosscutting network of pyrite veinlets with well-developed siliceous alteration halos (Fig. F55). Rare examples develop into very fine grained quartz-pyrite veins as wide as 5 mm. Pyrite-silica veining exhibits an overall increase in intensity toward the lower part of the unit. Rare rounded xenolithic fragments of a coarse grained dark gray-green silicified plagioclase-chlorite–bearing rock are also found within the unit.

In thin section, Unit 15 contains 1%–2% fresh plagioclase phenocrysts, as long as 1 mm, and rare quartz phenocrysts hosted in a moderately clay-silica altered groundmass, with abundant weakly oriented acicular plagioclase microlites. Vesicles are filled with coarse quartz crystals, which in some cases host euhedral pyrite or chalcopyrite crystals in their centers. Narrow granular quartz veins typically host pyrite and minor chalcopyrite. Silicification is present as coarse-grained poikiloblastic quartz crystals (Fig. F56), which grow in halos along quartz-

F54. A pervasively silicified volcanic rock with quartz amygdules and remnant plagioclase microlites, p. 123.

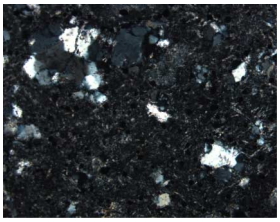

F55. A massive volcanic rock with quartz-pyrite veining and associated jigsaw-fit breccia textures, p. 124.

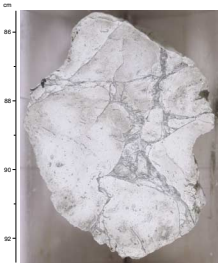

F56. Poikiloblastic silicification in Unit 15, p. 125.

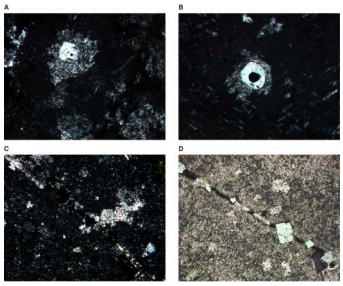

pyrite veins, quartz phenocrysts, quartz amygdules, and, where best developed (Sample 193-1189A-8R-1, 42–44 cm), within the groundmass of the rock. The poikiloblasts replace the formerly glassy groundmass of the rock, enclosing plagioclase microlites. When they overgrow quartz-bearing veins, or surround amygdules or quartz phenocrysts, the poikiloblasts are commonly optically continuous with the adjacent quartz in these structures.

The XRD spectra of Unit 15 are dominated by plagioclase, along with quartz in the lower, more strongly veined and silicified portion of the unit (Table T5). Quartz and pyrite are present throughout the unit, as is chlorite. Illite, smectite, and K-feldspar are also present as minor to trace phases in some samples.

Hole 1189B

The core from Hole 1189B is divided into an upper sequence (Units 1–14; 31–119 mbsf) roughly corresponding to the interval cored in Hole 1189A, but which is dominated by sulfide-rich, partly stockwork breccias, and a lower sequence (Units 15–36; 119–198 mbsf) comprising intercalated moderately to highly altered coherent units, highly to completely altered monomict breccias, and polymict volcaniclastic breccias and sandstones. The curated depth of the boundary (top of Unit 15) is at 118.53 mbsf. However, given the poor core recovery and the procedure for assigning sample depths (see **"Shipboard Scientific Procedures"**, p. 2, in the "Explanatory Notes" chapter), it likely corresponds to a downhole logging discontinuity at 123 mbsf.

Upper Sequence (31–119 mbsf)

Rocks recovered from the uppermost 119 m of Hole 1189B include fragments of massive to semimassive sulfides (described in **"Sulfide and Oxide Petrology,"** p. 34), completely GSC altered clasts of volcanic rocks embedded in vein networks variably rich in anhydrite, quartz, pyrite, and hematite, and rare GSC altered vesicular units. Core recovery across this interval is extremely poor, making it impossible to comment on the relationship between the different lithologies. However, the generally small size (<5 cm) of the individual core pieces and the widespread presence of veins within the recovered material implies a strongly veined and fractured sequence of rocks. Additionally, a very high ROP means that the missing intervals are exceptionally soft, suggesting sulfide, sulfate, and/or clay-rich lithologies.

Vesicular volcanic rocks in the upper sequence are restricted to Unit 2 (interval 193-1189B-1R-1, 29–39 cm; 31.29–31.39 mbsf), Unit 7 (interval 193-1189B-6R-1, 67–78 cm; 79.67–79.78 mbsf), Unit 9 (interval 193-1189B-8R-1, 0–24 cm; 98.40–98.64 mbsf), Unit 11 (interval 193-1189B-8R-1, 33–73 cm; 98.73–99.13 mbsf), and Unit 13 (interval 193-1189B-10R-1, 0–33 cm; 117.90–118.13 mbsf). Rocks from these units are completely and pervasively altered, predominantly to green clay (GSC alteration), but show an increasing extent of patchy silicification down the hole. The sample from Unit 2 is very soft and contains muscovite, chlorite, and pyrite, with only traces of quartz; Unit 7 exhibits millimeter-scale quartz-rich spots in the groundmass; Unit 9 is patchily silicified with silicified halos along pyrite veins; and Units 11 and 13 are pervasively silicified with quartz-pyrite–filled amygdules and variably developed quartz-pyrite veins (Figs. F57, F58). This progression in the extent of silicification is similar to that observed in Hole 1189A. With the exception of Unit 2, thin-section petrography and XRD analyses (Table T6)

F57. Quartz amygdules in a spotted quartz-clay altered groundmass with disseminated pyrite, p. 127.

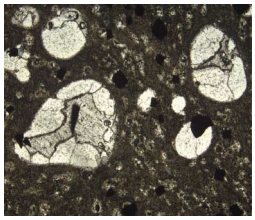

F58. Green silicified, moderately amygdaloidal, aphyric volcanic rock with hairline quartz-anhydrite-pyrite veins, p. 128.

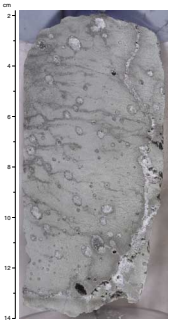

indicate that the major components of these units are quartz, illite, chlorite, and pyrite, along with potassium feldspar in some cases.

The remaining units of the upper sequence of Hole 1189B are breccias (partly stockwork breccias) with variable sulfide contents and gangue mineralogy. Unit 3 (Sections 193-1189B-2R-1 through 3R-1, 84 cm; 40.1–50.5 mbsf) consists of soft GSC altered rock fragments cemented in and cut by an anhydrite-pyrite stockwork. The XRD studies and thin-section observations indicate that gypsum is present in these rocks, replacing anhydrite, which, in turn appears to have replaced altered rock fragments (Fig. F59). Visual inspection of hand specimens from this interval suggests that individual samples contain up to 65% anhydrite, whereas others contain up to 60% pyrite and may also show significant concentrations of chalcopyrite. Unit 4 (Section 193-1189B-5R-1; 69.30–69.85 mbsf) is also a stockwork breccia with completely GSC altered perlitic clasts that, in thin section, show incipient silicification, indicated by poikiloblastic growth of quartz similar to that seen in Unit 15 of Hole 1189A. In contrast to Unit 3, the stockwork in Unit 4 is quartz-pyrite and the slight silicification of the clasts of Unit 4 may be related to the more siliceous breccia cement. Unit 5 (interval 193-1189B-6R-1, 0–56 cm; 79.00–79.56 mbsf) is characterized by its distinct red color, which is related to an abundance of hematite, accompanied by quartz and minor pyrite, in the quartz grains of the stockwork (Fig. F60). The volcanic clasts in Unit 5 are distinctly perlitic and contain K-feldspar, chlorite, illite, quartz, and disseminated pyrite. Two pieces of a breccia with anhydrite-quartz-pyrite stockwork and flow-banded, amygdaloidal clasts (Fig. F61) make up Unit 8 (interval 193-1189B-7R-1; 88.70–88.92 mbsf), whereas Unit 10 (interval 193-1189B-8R-1, 24–33 cm; 98.64–99.73 mbsf) and Unit 12 (interval 193-1189B-9R-1; 108.10–108.19 cm) consist of greenish gray, soft clasts embedded in a quartz-pyrite stockwork.

Lower Sequence (119–198 mbsf) - Coherent Units

The coherent units of the lower sequence of Hole 1189B are Unit 15 (interval 193-1189B-10R-1, 63–77 cm; 118.53–118.67 mbsf), Unit 19 (interval 193-1189B-11R-1, 43 cm, through 13R-1, 20 cm; 128.03–147.14 mbsf), and Units 26–28 (interval 193-1189B-15R-2, 37 cm, through 17R-1, 28 cm; 167.96–185.57 mbsf). These units are variably altered (25%–100% secondary phases in thin sections), vesicular to amygdaloidal volcanic rocks with rare quartz-pyrite ± magnetite or anhydrite veining. Alteration of these units is pervasive, but rarely complete. A marked feature of the coherent rocks is the development of large round to ovoid vesicles that are often filled or lined with quartz (Fig. F62). Moreover, they characteristically lack the flow banding and spherulitic textures that are characteristic of the brecciated units (see below).

With the exception of Unit 26, coherent units from the lower sequence of Hole 1189B rarely contain significant (>1%) sulfide. In Unit 26, a network of fine quartz-pyrite-magnetite veinlets with a magnetite-bearing alteration halo is developed (Fig. F63). These veins are moderately sulfide-rich (5%–20% contained pyrite) and in some cases coalesce to form brecciated zones with quartz-pyrite infill (refer to "Structural Geology," p. 41).

The mineralogy, revealed by XRD analysis (Table T6) and thin-section studies, of coherent volcanic rocks from the lower sequence of Hole 1189B may be grouped into two assemblages. In Units 15, 19, and 26, the dominant silica polymorph is cristobalite (occurring as ground-

F59. Relationship between volcanic fragments, anhydrite, and gypsum in Unit 3, p. 129.

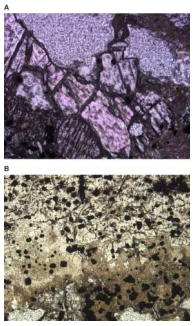

F60. Jasperoidal silica breccia cement from Unit 5, p. 130.

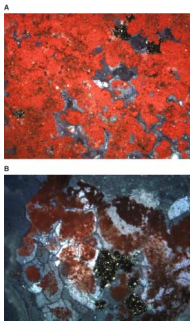

F61. Hand specimen of matrix-supported breccia with green clay altered volcanic clasts in an anhydrite-pyrite-quartz cement, p. 131.

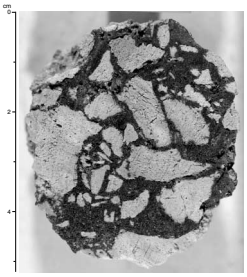

F62. Moderately vesicular aphyric volcanic rock with a hieroglyphic texture, p. 132.

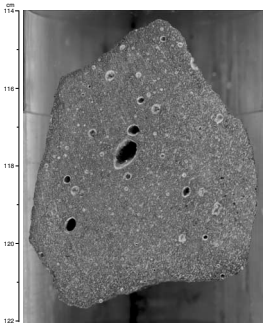

mass replacement and vesicle fill and interpreted to primarily be a product of devitrification of volcanic glass) with minor quartz (as vesicle fill, or more rarely in veins) and potassium feldspar, illite, and chlorite/illite-bearing mixed-layer phases. In contrast, Units 27 and 28 contain quartz in the groundmass and as vesicle fill, with potassium feldspar and chlorite or chlorite-smectite mixed-layer phases. Quartz also commonly forms irregular poikiloblasts, overgrowing clay-altered groundmass. Remnant microlites and less abundant phenocrysts of igneous plagioclase are present in both cristobalite- and quartz-bearing units, although thin-section studies (Fig. F48) indicate that the abundance of plagioclase in the latter (<20%) is generally lower than in the former (20%–40%). These observations indicate that quartz is the dominant silica polymorph in more extensively altered units, whereas cristobalite predominates in less altered rocks. This interpretation is consistent with the more complex phyllosilicate mineralogy of the cristobalite-bearing lithologies, which may be interpreted as disequilibrium assemblages that result from less intense fluid-rock interaction.

Lower Sequence (119–198 mbsf) - Monomict Breccias

A large proportion of the core recovered from the lower sequence of Hole 1189B is composed of monomict breccias (Units 16, 17, 21–25, 29, 30, 32–34, and 36) (see Table T4 for intervals). These brecciated rocks are composed of spherulitic, microlitic, and perlitic flow-banded volcanic fragments (refer to "Igneous Petrology," p. 8) hosted in quartz-pyrite and anhydrite-pyrite cements (Figs. F64, F65, F66). The degree of brecciation is highly variable, and individual core pieces may be coherent, with a pseudobrecciated texture provided by alteration to light greenish gray material along fracture networks, overprinting flow banding (Fig. F67). Both brecciated and coherent intervals commonly exhibit zoned alteration patterns, with less altered kernels (Figs. F64, F67). Despite the development of pseudoclastic textures caused by alteration, the widespread recognition of clast rotation, scattered examples of flow-banded domains intruding breccias (refer to "Igneous Petrology," p. 8), and intercalated polymict units (see below) indicate that many of these brecciated units are at least partially volcaniclastic in origin.

As for the coherent intervals, two distinct alteration assemblages are present in monomict breccias from the lower sequence of Hole 1189B (Table T6). The majority of units (Units 16, 17, 21–24, 30, and 32) are quartz-dominated, with clay (generally chlorite, chlorite/smectite mixed layer phases, and/or illite) and potassium feldspar (in most units). Anhydrite is abundant in the cement of some breccias, which are scattered throughout the sequence (refer to the "Site 1189 Alteration Log," p. 120). Minor remnant igneous plagioclase is present in some intervals. In contrast, Units 25, 33, and 34 contain cristobalite and remnant plagioclase as major phases, potassium feldspar, and a very complex clay assemblage (illite, chlorite, smectite, chlorite/smectite mixed-layer phases, and illite-bearing mixed-layer phases). Rare quartz veins are also present in some intervals. Unit 34 also may contain minor talc and actinolite. However, no thin section of the unit was cut and the XRD spectra are somewhat ambiguous, so this remains to be confirmed. It is apparent that, like the coherent units, quartz-dominated assemblages are developed in more strongly altered brecciated rocks, whereas cristobalite, most likely produced by the devitrification of volcanic glass, is confined to the less altered intervals.

F63. Intensely veined, weakly vesicular and sparsely plagioclase phyric volcanic rock, p. 133.

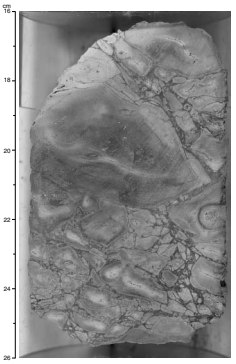

F64. Breccia, comprising flow-banded, volcanic clasts hosted in a quartz-rich cement with coarse anhydrite vug fill, p. 134.

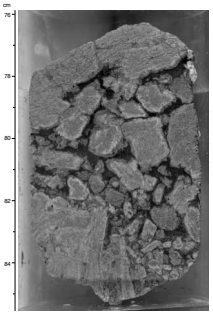

F65. Partly coherent, flow-banded jigsaw-fit breccia, dissected by a network of quartz-sphalerite-pyrite veins, p. 135.

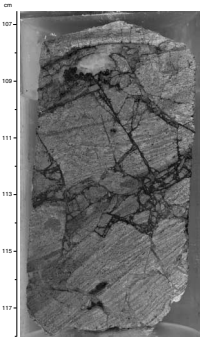

Lower Sequence (119–198 mbsf) - Polymict Volcaniclastic Breccias and Sandstones

Three intervals of polymict volcaniclastic breccia (Unit 18: 127.77–128.03 mbsf; Unit 20: 147.20–147.49 mbsf; and Unit 35: 196.78–197.16 mbsf) and a volcaniclastic sandstone (Unit 31: 186.26–186.34 mbsf) exhibiting graded bedding are present within the lower sequence of Hole 1189B. These rocks show a similar style of alteration to the monomict breccias. They contain a range of perlitic, flow-banded, and vesicular to vuggy clasts, which show moderate to complete GSC alteration and/or silicification and are hosted in a quartz-sulfide (dominantly pyrite) ± magnetite matrix (Fig. F68). In the breccias, some clasts contain narrow sulfide veinlets that are terminated by the matrix, implying that hydrothermal activity occurred prior to erosion and deposition of the units. Similarly, a glassy volcanic clast in the volcaniclastic sandstone contains chalcopyrite and sphalerite (Fig. F69), which are not found in the matrix of the rock, again implying preerosional hydrothermal activity. A thin section of a sample from Unit 35 (Sample 193-1189B-18R-2, 65–67 cm) contains minor amounts of acicular actinolite and possible epidote as inclusions in quartz. Actinolite was also provisionally identified by XRD analysis in one sample from Unit 34 and may be a common minor phase in rocks from the lowermost part of Hole 1189B.

Quartz is the only silica polymorph observed in the polymict volcaniclastic rocks of the lower sequence of Hole 1189B. Some or all of the clasts in all thin section (Fig. F48) and XRD samples (Table T6) also contain minor remnant plagioclase microlites, within a clay- (illite-chlorite) and quartz-rich groundmass. The clasts are hosted in a fine (for the sandstone) to coarsely crystalline quartz matrix, with 1%–3% pyrite. Minor anhydrite, which is partly replaced and overgrown by barite (Fig. F70), is also present in the matrix of Unit 20.

Discussion

Holes 1189A and 1189B were targeted in the midst of a zone of high-temperature focused fluid flow at the Roman Ruins sulfide chimney field. Despite this, the nature of alteration in Hole 1189A (cored interval 0–125.8 mbsf) is similar to that observed at Site 1188, a low-temperature diffuse vent field at Snowcap hydrothermal site (see **"Hydrothermal Alteration,"** p. 33, in the "Site 1188" chapter). The sequence once again shows a systematic change from cristobalite to quartz as the silica polymorph within alteration (Figs. F46, F53; Table T2), which broadly corresponds to a brecciated zone of GSC alteration, increasingly overprinted by silicification at depth. However, the transition from cristobalite to quartz, which takes place at 25 mbsf in Hole 1189A, is sharp and shallow when compared to the gradual transition over 100–120 mbsf at Site 1188. This is interpreted to reflect a higher temperature gradient at Site 1189.

The upper portion (31–~120 mbsf) of Hole 1189B, which is sited 30 m from Hole 1189A, is also represented by a sequence of dominantly brecciated, GSC altered volcanic rocks, with generally increasing silicification downhole. However, the rocks within Hole 1189B are much more sulfide-rich than those from Hole 1189A and contain intervals of polymetallic (pyrite-chalcopyrite-sphalerite) stockwork and semimassive to massive sulfide mineralization. As a result of the extremely poor recovery in this portion of Hole 1189B, it is not possible to determine the relationship of these units to other, less mineralized intervals within the sequence. However, it seems likely that this part of Hole

F66. Rotated flow-banded fragments set in a dark gray, soft vuggy matrix, and with spherulitic domains, p. 136.

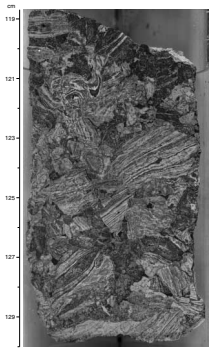

F67. Flow-banded, highly altered volcanic rock, p. 137.

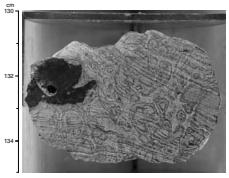

F68. Polymict breccia showing evidence for clast abrasion and fine sulfide veins that predate deposition, p. 138.

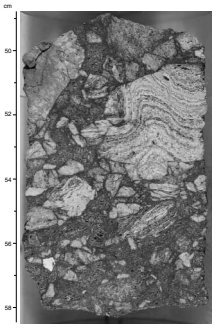

F69. Chalcopyrite-sphalerite bearing clast in volcaniclastic sandstone, p. 139.

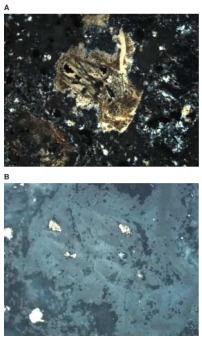

1189B successfully drilled a focused fluid discharge network (i.e., a mineralized stockwork). In contrast, Hole 1189A appears to have intersected a slightly peripheral alteration sequence that can be attributed to more diffusional fluid flow around the main conduits, similar to the system drilled at Site 1188. This rapid lateral variation in alteration style and intensity is not unexpected in a fracture-controlled fluid flow regime.

The lower sequence of altered volcanic rock recovered from Hole 1189B (~120–198 mbsf) is distinctly different in character to the upper sequence. It consists of highly silicified, massive vesicular lavas that show little evidence of sulfide mineralization, intercalated with flow-banded, brecciated units with highly to completely developed silicification that overprints GSC alteration, and widespread development of quartz-pyrite ± anhydrite ± sphalerite ± hematite veining. This sequence shows varying mineralogy. Less strongly altered units are dominated by cristobalite (primarily developed by devitrification of volcanic glass). In contrast, very highly to completely altered rocks contain quartz. The flow-banded, brecciated units are mostly quartz-bearing, whereas the vesicular lavas mostly contain cristobalite, although there are exceptions to this rule. This relationship suggests the possibility of lithologically controlled alteration zones at depth beneath Roman Ruins hydrothermal site. However, the lower sequence of Hole 1189B, where this relationship is developed, is almost entirely deeper than the bottom of Hole 1189A. Consequently, it is not possible to test this hypothesis by attempting to correlate units between the two holes at Site 1189.

Significance of the Cristobalite–Quartz Transition

Although cristobalite is a high-temperature silica polymorph, metastable low-temperature forms of the mineral are commonly found (Deer et al., 1992). These forms are widespread in devitrified acidic volcanic rocks (Williams et al., 1982) and shallow volcanic-hosted hydrothermal systems. In their review of southwestern Pacific Rim gold-copper deposits, Corbett and Leach (1998) find that cristobalite is a typical alteration mineral within low-temperature (<150°C), high crustal-level epithermal-style mineralization, whereas quartz becomes the dominant polymorph with increasing temperature and depth. Consequently, the change from cristobalite to quartz at Sites 1189 and 1188 is interpreted to be caused by an increase in temperature with depth. This hypothesis is supported by the generally decreased abundance of anhydrite in quartz-dominant alteration. Anhydrite becomes insoluble in seawater at temperatures >150°C (Bischoff and Seyfried, 1978), requiring that downwelling seawater would precipitate anhydrite at or around the 150°C isotherm. At deeper (and hotter) levels within the hydrothermal system, this would effectively confine anhydrite to open fractures that may allow sudden influxes of relatively cool water. The fluid entering these fractures would be conductively heated, precipitating anhydrite as fracture fill, as observed.

In contrast to Site 1188, where fresh volcanic rocks were recovered to a depth of 34 mbsf, moderately altered bleached volcanic rocks were encountered only in the first 9 m core of Hole 1189A. Other significant mineralogical differences, such as the change from cristobalite to quartz as principal silica polymorph and the decrease in the importance of anhydrite as an alteration mineral, also take place at much shallower depths at Site 1189. These differences imply a higher temperature gradient during subseafloor alteration for Roman Ruins hydrothermal site

F70. Barite replacing and overgrowing anhydrite in a quartz-breccia matrix, p. 140.

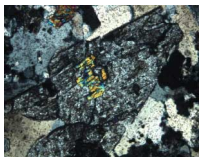

than for Snowcap hydrothermal site, which is presumably related to the higher temperature venting observed at the former site.

The contrasting temperature gradients at Snowcap hydrothermal site and Roman Ruins hydrothermal site may reflect differences between the hydrological properties of the subseafloor at the two hydrothermal sites. For instance, the local development of less permeable layers at Snowcap hydrothermal site may promote pooling and mixing of fluids in the subsurface, followed by a slow upward flow through a poorly connected fracture network, resulting in diffuse surface hydrothermal activity. In contrast, at Roman Ruins hydrothermal site, the permeability structure appears to allow more vigorous hydrothermal circulation and the development of efficient fluid conduits that permit focused venting of high-temperature hydrothermal fluids at the seafloor. However, at this early stage of investigation, it is not possible to provide a detailed discussion of the specific factors that influence fluid flow at the two sites.

Significance of the Sulfates

As outlined above, the presence of anhydrite in many samples indicates that the interacting fluids had temperatures >150°C. However, occasional replacement of anhydrite by gypsum and barite implies that anhydrite is no longer stable in these rocks and that conditions have changed after the anhydrite was deposited. The partial replacement of anhydrite by gypsum in Unit 3 (between 40 and 50 mbsf) suggests that the present-day temperature at this depth is below ~40°C, the temperature below which anhydrite transforms to gypsum (MacDonald, 1953). Moreover, the replacement of anhydrite by barite in Unit 20 (~150 mbsf) indicates that anhydrite was unstable. The presence of apparently unmodifed anhydrite in other sections of the cores from Site 1189, however, suggests that anhydrite is generally not unstable throughout the drilled sequence. This complexity in sulfate distribution may be attributed to temporal variations in fluid flow and fluid-rock interaction along a variably connected fracture network.

Evidence for Prior Hydrothermal Activity

The presence of apparent presedimentation sulfide veining in clasts from polymict volcaniclastic breccias and sulfide mineralization in a clast within the volcaniclastic sandstone at a depth approaching 200 mbsf implies that the hydrothermal system at Roman Ruins hydrothermal site has been active for an extended period of time. Similarly, the recognition of textures that indicate exhalative deposition of sulfides, which are now located subsurface (refer to **"Sulfide and Oxide Petrology,"** p. 34), also indicates that active seafloor venting is not unique to the present time. Rather, this evidence suggests that hydrothermal activity and felsic volcanism have been ongoing and intimately related over a period of time at the PACMANUS hydrothermal field.

SULFIDE AND OXIDE PETROLOGY

Two holes were cored 30 m apart at Site 1189. Both are close to sulfide chimneys in the Roman Ruins hydrothermal site as is LWD Hole 1189C. Because of the close proximity of the two cored holes, a similarity in their alteration and mineralization styles was anticipated.

Hole 1189A

Pyrite is the most common sulfide mineral within Hole 1189A, generally in trace amounts but infrequently with modes >10%. Other sulfide phases are sphalerite, chalcopyrite, marcasite, and galena. Magnetite is the major oxide phase, with trace amounts of hematite and possibly maghemite. The downhole distributions of pyrite, chalcopyrite, sphalerite, and magnetite are shown in Figure F48 (see "Hydrothermal Alteration," p. 23).

The style of mineralization includes disseminated pyrite (Type 1) (see Table T6, p. 66, in the "Explanatory Notes" chapter), pyrite within anhydrite-quartz veins (Type 2), and pyrite lining vesicles (Type 2a). Sulfide rocks, containing by definition >5% sulfide minerals (see "Sulfide and Oxide Petrology," p. 11, in the "Explanatory Notes" chapter), consist predominantly of Type 2 anhydrite—quartz veins containing pyrite with some trace chalcopyrite. These are present in seven of the 24 units in Hole 1189A. Examples are shown in Figures F71 and F72. The pyrite occurs as very fine to fine-grained granular euhedral and subhedral crystals. Chalcopyrite occurs as very fine grained anhedral grains.

In contrast to Site 1188, quartz is more abundant than anhydrite in the veins, and in some cases, such as Sample 193-1189A-11R-1 (Piece 5, 25–30 cm), the veins are monomineralic quartz. Others range from 7% to 65% quartz or other forms of silica. Figure F73, on the other hand, shows a vein with cockade structure that is entirely anhydrite with ~5% pyrite between some of the layers. Most of the veins are very narrow (<0.5 mm) although Sample 193-1189A-12R-1 (Piece 16, 120–127 cm) is 5 cm wide.

Semimassive sulfide mineralization (Unit 21 of the lithologic log), comprising ~50% sulfides, was recovered in Sample 193-1189A-12R-1, 120–128 cm (Fig. F74). Aggregates of pyrite and chalcopyrite are observed within a very fine grained quartz-pyrite (±clay) matrix, which envelops angular clasts of altered vesicular volcanic rock (Fig. F75). The complete enclosure of the angular clasts with sulfide mineralization running along fractures into the clasts suggests that this is a sulfide-rich Type 2 vein. Within the matrix of the sample, chalcopyrite is intergrown with quartz and partially to completely encloses pyrite. There are few sphalerite grains within the pyrite.

Pyrite

Type 1 disseminated pyrite is widespread within Hole 1189A (Fig. F76). In some samples, Type 1 euhedral pyrite is crowded with inclusions of microlites, which have a similar morphology and distribution as those in the surrounding groundmass (Fig. F77). This pyrite has grown within the groundmass at the expense of the very fine grained material that is the matrix for the microlites. The most spectacular example of pyrite replacing the preexisting volcanic groundmass is found in Sample 193-1189A-8R-1 (Piece 7, 103–105 cm), where the original elongate laths of plagioclase, probably representing an igneous quench texture, are replaced by quartz and pyrite. The pyrite tends to locate along the cores of the replaced laths (Fig. F78). However, the host rock is xenolithic, and the relation of the replacement phenomena with the alteration described for Hole 1189A is uncertain.

Pyrite is commonly associated with Type 2 quartz-anhydrite veins, with the pyrite tending to be located near the selvages of these veins. Where anhydrite is present in the veins, there is a suggestion that the

F71. Anhydrite-quartz-pyrite vein in altered breccia, p. 141.

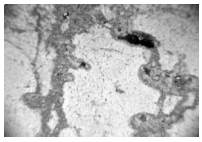

F72. Narrow anastomosing quartz-pyrite veins in altered rock, p. 142.

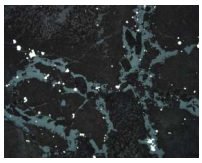

F73. Anhydrite-quartz-pyrite vein with cockade structure, p. 143.

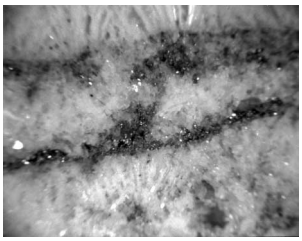

F74. Semimassive sulfide consisting of pyrite and chalcopyrite grains in a quartz-rich matrix, p. 144.

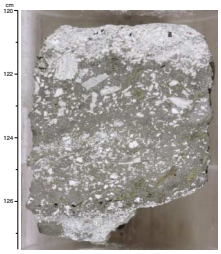

F75. Angular fragment of volcanic rock within a quartz-pyrite matrix, p. 145.

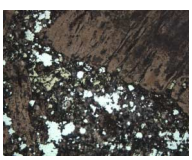

pyrite takes a coarser form. Pyrite grains within the veins commonly contain inclusions of magnetite.

Pyrite is also observed as vesicle fill associated with chalcopyrite (Type 2a). There are several examples in which quartz has coated the wall of a vesicle and pyrite has precipitated on the quartz (Fig. F79). Marcasite is found as a rare mineral enclosed in pyrite (Fig. F80). Framboids, assumed to be pyrite but too small to photograph at 0.006-mm diameter, are within quartz in Sample 193-1189A-2R-1 (Piece 15, 113–115 cm).

Chalcopyrite

Chalcopyrite is commonly present in trace amounts, especially in Section 193-1189B-12R-1, where it is typically located within the clay groundmass. Chalcopyrite is estimated to represent 15% of the semimassive sulfide in Sample 193-1189A-12R-1 (Piece 16, 122–125 cm) (Fig. F74).

Chalcopyrite is locally intergrown with pyrite within quartz veins and may occur as vesicle fill (e.g., interval 193-1189A-7R1-1, 72–92 cm), where chalcopyrite occurs in central cavities of quartz masses within small amygdules (Fig. F81). Where observed as cavity fill, chalcopyrite locally replaces pyrite.

Sphalerite

Sphalerite was seen sporadically in thin sections of Type 2 veins, where it is commonly associated with chalcopyrite, which partially replaces it. In such associations, the sphalerite typically develops a chalcopyrite disease texture (Figs. F82, F83).

Galena

One grain of galena was encountered, enclosed within pyrite in a Type 2 vein (Figs. F82, F83).

Iron Oxides

Magnetite is present as a primary igneous phase in the groundmass of fresh and some altered dacites, as scattered grains in Type 2 quartz-pyrite veins and Type 2a quartz-filled amygdules, and as fine inclusions in pyrite. Some of the magnetite has broken down to leucoxene, indicating that it was titanium bearing. A mineral tentatively identified as maghemite rims magnetite grains in Sample 193-1189A-8R-1 (Piece 17, 103–105 cm).

Hematite is found sporadically as an oxidation product (replacement) of magnetite and, in one instance, as a jasper. The bright red jasper or hematitic chert (Fig. F84) contains disseminated grains of pyrite and chalcopyrite. Because the sample is so small (~10 cm^3), it is not certain whether this is a vein or a cavity filling in the dacite.

Parageneses

Detailed study of polished thin sections has revealed a number of key sulfide and oxide mineral associations. There is evidence for at least two generations of pyrite, most likely within a continuous mineralizing process, rather than separated by a significant gap in time. In Sample 193-

F76. Disseminated pyrite in a microlite-rich groundmass of moderately altered rhyodacite, p. 146.

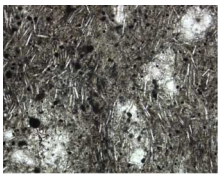

F77. Disseminated euhedral pyrite containing inclusions of groundmass microlites, p. 147.

F78. Pyrite and magnetite occupy the cores of former plagioclase crystals that have been replaced by quartz, p. 148.

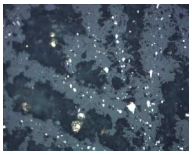

F79. Quartz and pyrite precipitated on the wall of a vesicle, p. 149.

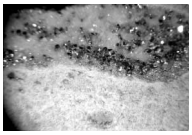

F80. Pyrite crystals nucleated around quartz and overgrown by marcasite crystals overgrown by more pyrite, p. 150.

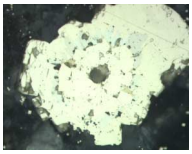

F81. Chalcopyrite in cavity within a quartz mass that fills an amygdule, p. 151.

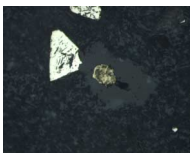

1189A-10R-1 (Piece 9, 75–77 cm), pyrite is present as tiny inclusions in rare magnetite and magnetite is included in anhedral pyrite. In Figure F85, tiny crystals of either sphalerite or magnetite (too small to identify with certainty) have precipitated on early pyrite and, in turn, are overgrown by younger pyrite. There is a rare example (Fig. F86) of sphalerite inclusions with chalcopyrite disease within the second-generation pyrite. In Figure F80, euhedral pyrite crystals are overgrown by marcasite that, in turn, is overgrown by more pyrite. The age relation of the framboids in Sample 193-1189A-2R-1 (Piece 15, 113–115 cm) to the other pyrite is not known.

Figure F87 shows a quartz vein with pyrite intergrown with chalcopyrite-diseased sphalerite and chalcopyrite. A close-up view of another area in this same thin section (Fig. F83) reveals a pyrite crystal containing an inclusion of galena.

Figure F88 shows a magnetite-hematite-pyrite assemblage. The magnetite appears to be partially replaced by both pyrite and hematite pseudomorphs.

A paragenetic sequence that is consistent with the microscopic observations is given in Figure F89. There are at least two generations of pyrite and possibly two generations of sphalerite with chalcopyrite disease. The origin of chalcopyrite disease is somewhat contentious, with both replacive and coprecipitative models supported. Current research suggests that both mechanisms may be important (Bortnikov et al., 1991; Nagase and Kojima, 1997). Textural features are sometimes useful in distinguishing between the two models, although these are strongly influenced by the Fe content of the sphalerite (Nagase and Kojima, 1997). The composition of the sphalerite from Hole 1189A is unknown; consequently, it was not possible to use textures to discriminate between replacement and coprecipitation. The following paragenetic sequence is based on the replacive model for chalcopyrite disease.

Early sphalerite is encapsulated in late pyrite, which would have protected this sphalerite from subsequent reaction, so its chalcopyrite disease is considered to have been caused by an earlier chalcopyrite for which there is no other evidence (i.e., this chalcopyrite has not been observed as a separate phase). The time of deposition of magnetite and quartz is poorly constrained, other than it followed the deposition of early pyrite. The timing of the oxidation of this magnetite to hematite is also not known, nor is the relationship of this hematite, if any, to the hematitic chert (jasper) in Figure F84. The framboids must have formed at low temperature (<100°C). Because they are encapsulated in quartz, their formation must have preceded the quartz that filled the amygdules.

Chalcopyrite in seafloor hydrothermal systems is deposited from fluids with temperatures generally >300°C. A similar temperature is required for the replacive formation of chalcopyrite disease in sphalerite, but sphalerite is typically deposited at much lower temperatures. The paragenetic interpretation presented in Figure F89 suggests a progressive increase in temperature of the hydrothermal system through time, and that this has occurred at least twice (Fig. F89).

Hole 1189B

Hole 1189B exhibits the widest range of sulfide phases encountered during Leg 193. Minerals recognized are pyrite, chalcopyrite, sphalerite, and rare tennantite and covellite (or bornite). In addition, the oxides magnetite, hematite, and possibly ilmenite (one example) are present.

F82. Sphalerite and chalcopyrite replacing pyrite, p. 152.

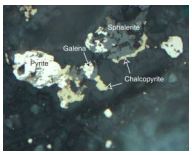

F83. Enlargement showing chalcopyrite inclusions in sphalerite, p. 153.

F84. Red hematitic chert with disseminated pyrite and chalcopyrite and fragments of highly altered rock, p. 154.

F85. Sphalerite or magnetite precipitated on early pyrite and overgrown by later pyrite, p. 155.

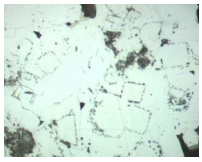

F86. Pyrite containing inclusions of quartz and sphalerite with chalcopyrite disease, p. 156.

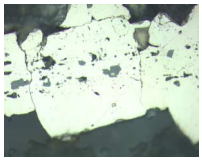

The majority of sulfide-bearing assemblages in Hole 1189B have trace to 5% sulfides, as disseminations in altered rock (Type 1; in Table T6, p. 66, in the "Explanatory Notes" chapter), in anhydrite-quartz veins (Type 2), as vesicle linings with quartz and anhydrite (Type 2a), and with magnetite in anhydrite-quartz veins (Type 3). Hole 1189B also has examples of semimassive sulfides (25%–75% sulfides) and an ~1-cm³ sample of massive sulfide (Sample 193-1189B-06R-1 [Piece 6]: 90% pyrite, trace chalcopyrite and sphalerite, 7% quartz, and 3% anhydrite). The latter, the only massive sulfide encountered on Leg 193, is sufficiently small that it is possible that it is a piece of sulfide from a Type 2 vein that has become separated from most of its quartz and anhydrite gangue during drilling. The samples of semimassive sulfide were observed in Samples 193-1189B-1R-1 (Piece 1), 3R-1 (Pieces 2 and 4), and 5R-1 (Pieces 1, 2, and 5). Additional samples from an unknown depth were recovered on the logging tool during wireline operations. See the "Site 1189 Sulfide Log," p. 144, for details of individual samples and Figure F48 for modal distributions of pyrite, chalcopyrite, sphalerite, and magnetite downhole. Overall, the uppermost sections of Hole 1189B show elevated sulfide (pyrite) concentrations, with modes commonly >5% in cores above Section 193-1189B-11R-1 (127.6 mbsf). Below 130 mbsf, the modal pyrite falls away to <5% and is commonly present in only trace amounts.

Oxides are present in trace amounts with the exception of Section 193-1189B-14R-1, which contains ~5% hematite. Magnetite first makes an appearance in Section 193-1189B-11R-1 at 127.74 mbsf and is present mostly in trace concentrations sporadically to the bottom of the hole.

Pyrite

Pyrite occurs as anhedral and subhedral discrete grains and as aggregates within the semimassive and massive sulfide samples. It typically is present within veins of anhydrite and quartz (Type 2) and disseminated within the clay-altered matrix of the volcanic protoliths (Type 1). Within the veins, the greatest concentrations of pyrite are commonly observed near the vein margins, where it is intergrown with quartz. The veins tend to show a pronounced "stockwork" texture, although their thickness rarely exceeds 5 mm. Pyrite commonly contains inclusions of silicates, chalcopyrite, and sphalerite.

Sample 193-1189B-1R-1 (Piece 1A) deserves special mention. In thin section, this semimassive sulfide from 31.0 mbsf contains arcuate bands of pyrite ~0.5 mm thick, which form a nearly complete ovoid structure about 6 mm long × 1.5 mm wide. The center of the ovoid is filled with chalcopyrite (Fig. F90). Immediately adjacent is a dismembered structure with arcuate fragments of pyrite defining a crude and incomplete ovoid shape, ~11 mm × 6 mm in diameter, filled with chalcopyrite and, in the center, anhydrite (Fig. F91), some of which is altered to gypsum. These structures are very similar to mineralized worm tubes in sulfide chimneys (cf. Ixer, 1990, fig. 24d), which act as conduits for fluid flow from the interior to the exterior of the chimneys. This texture has not been described from veins. If the interpretation is correct that this structure represents a fluid conduit in a chimney or a chimney fragment within a sulfide mound and given the presence of overlying dacites, it would suggest the sample is derived from a buried exhalative sulfide deposit. Alternatively, these relationships may simply represent subsurface sulfide textures. For the most part, the coarse granular fabric

F87. Quartz vein with chalcopyrite diseased sphalerite and chalcopyrite intergrown with pyrite, p. 157.

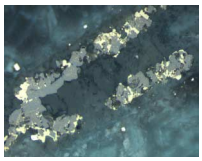

F88. Apparent pseudomorphous replacement of magnetite by pyrite and hematite, p. 158.

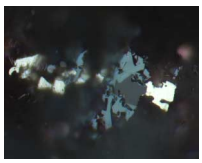

F89. Paragenetic sequence for Hole 1189A, p. 159.

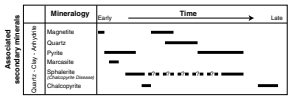

F90. Ovoid structure with a thin pyrite rim and chalcopyrite fill, p. 160.

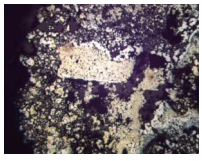

F91. Possibly dismembered ovoid structure filling the center of the field of view, p. 161.

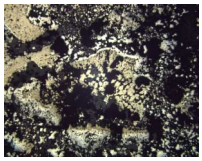

of the anhydrite gangue is unlike the frondescent or acicular texture of sulfate minerals that are rapidly deposited in chimneys. Furthermore, parts of the sample contain relatively closely packed angular fragments of pale, altered dacite glass containing disseminated pyrite. This is not characteristic of chimneys, except rarely at their basal contact with volcanic substrate. The anhydrite gangue resembles vein occurrences from which the sample differs chiefly in proportion and grain size of sulfide and anhydrite. It separates volcanic clasts breccia-style, as observed throughout much of Hole 1189B. Elongate bands of chalcopyrite are observed and overgrown by euhedral pyrite along the margins of the anhydrite veins.

Framboidal pyrite is present in Hole 1189B in Samples 193-1189B-15R-1 (Piece 11, 86–88 cm) and 16R-1 (Piece 2, 11–14 cm) (Fig. F92). The framboids are 0.01–0.05 mm in diameter with individual elements that are 0.001–0.002 mm. Given that the accepted origin of framboidal pyrite is within the water column, the framboidal forms observed within these veins possibly comprise or originated as the similar-looking Fe sulfospinel greigite, which is stable under hydrothermal conditions (Wilkin and Barnes, 1997).

F92. Framboids of pyrite in quartz, p. 162.

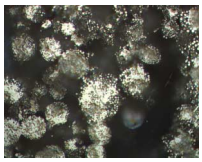

Copper Sulfides

Chalcopyrite is more enriched in Hole 1189B than in other holes drilled during Leg 193, achieving modes >10% in Sample 193-1189B-1R-1 (Piece 1) and even 20% in thin section (Fig. F48). Within this sample of semimassive sulfide is the arcuate pyrite-chalcopyrite aggregate described above. In contrast, there are other examples in the same section of arcuate pyrite aggregates whose convex surfaces are mantled by chalcopyrite. Elsewhere within this sample, chalcopyrite is present as anhedral 0.1-mm inclusions within pyrite.

After the initial core (Section 193-1189B-1R-1), chalcopyrite is present sporadically to near the bottom of the hole mostly in trace amounts; lining vesicles, on fracture surfaces, associated with covellite (possibly bornite) in three instances (e.g., Sample 193-1189B-16R-1 [Piece 11]); and rarely as disseminated grains within the altered volcanic groundmass (e.g., Sample 193-1189B-17R-1 [Piece 19]).

One sample (Sample 193-1189B-13R-1 [Piece 6]) contains what appears to be tennantite. The mineral has a tetragonal form, a bright gray luster, and is relatively soft (Mohs hardness = ~3). It is present within microveinlets associated with pyrite and sphalerite.

Covellite also is present as a trace mineral. In hand specimen, there is a suggestion that covellite may locally coat pyrite grains (e.g., Sample 193-1189B-3R-1 [Piece 5]), recognized as an iridescent indigo blue coating. This coating might also be bornite. Elsewhere, covellite is positively observed along fracture surfaces associated with chalcopyrite (e.g., Sample 193-1189B-16R-1 [Piece 11]) and associated with drusy pyrite within quartz-lined vesicles (e.g., Samples 193-1189B-16R-1 [Piece 18] and 17R-1 [Piece 17]).

Sphalerite

Sphalerite is found sporadically throughout the hole, mostly in trace amounts (Fig. F48). Honey-yellow sphalerite is observed in quartz amygdules (Fig. F93), within the massive sulfide sample (Sample 193-1189B-6R-1 [Piece 6]), disseminated with pyrite in the quartz matrix of volcanic breccia, and within an anhydrite-pyrite vein with trace

F93. Amygdule filled with quartz and sphalerite, p. 163.

amounts of tennantite. In Sample 193-1189B-14R-1 [Piece 15], colloform masses of sphalerite, ranging in color from brownish yellow (Fe poor) in the center to dark brown and black (Fe rich) on the outside, line the wall of an anhydrite-filled cavity. The sphalerite shows local intergrowth with chalcopyrite and chalcopyrite disease toward the margins of grains (Fig. F94). Also in this sample, pyrite encloses sphalerite free from chalcopyrite disease, whereas elsewhere in the section pyrite is included within coarse (1.4 mm) chalcopyrite-diseased sphalerite.

Iron Oxides

Magnetite is present predominantly in Type 3 pyrite-anhydrite-quartz veinlets but also as a sparse dissemination in altered volcanic rock and in dark halos of larger veins. Within the veins, magnetite is most commonly observed as fine inclusions within quartz (Sample 193-1089B-8R-1 [Piece 3, 7–9 cm]). Groundmass magnetite is associated with pyrite in a few samples (Fig. F95).

Hematite is present as bladed masses within quartz veins (Fig. F96) and as acicular masses within amygdules (Sample 193-1189B-15R-2 [Piece 10, 61–64 cm]). Hematite also partially replaces magnetite in the groundmass (Fig. F97).

Paragenetic Sequence

The parageneses of oxides and sulfides observed within Hole 1189B is similar to that already reported in Holes 1188A, 1188F, and 1189A. Magnetite is observed as Ti magnetite within the volcanic precursors to the alteration assemblage. Secondary magnetite is present within early quartz veins or as small grains locally enclosed within pyrite. Hematite, the other oxide present, rims magnetite (Sample 193-1189B-15R-2 [Piece 10, 61–64 cm]) and also occurs as acicular masses within quartz veins; it therefore most likely postdates the magnetite. However, establishing a paragenetic sequence for hematite relative to the sulfides is problematic within Hole 1189B because the mineral does not occur in close association or within any of the sulfides.

Chalcopyrite generally is present with quartz, although it can be observed as isolated grains within clay-altered groundmass of the volcanic rock. Chalcopyrite is also observed in some late crosscutting veins (Sample 193-1189B-8R-1 [Piece 10, 37–40 cm]). The mineral commonly is present as chalcopyrite disease within sphalerite and locally replaces sphalerite (Sample 193-1189B-13R-1 [Piece 10, 52–54 cm]).

Pyrite is both intergrown with and contains inclusions of chalcopyrite. Sphalerite is more evident within Hole 1189B than in any other core to date and provides convincing evidence for two generations of sphalerite deposition, before and after a period of pyrite formation.

Concluding Remarks for Site 1189

The paragenetic data for Holes 1189A and 1189B are combined in a schematic paragenetic sequence in Figure F98. The diagram suggests at least two similar episodes of sulfide precipitation, probably as a continuous process. In particular, the contrasting relationships between pyrite and sphalerite and pyrite and chalcopyrite are consistent with at least two sulfide mineralization events. Both events are evident in Hole 1189A. It is not known if the parageneses in Hole 1189B belong to the first or second event.

F94. Zoned sphalerite with chalcopyrite disease in its outer portion, p. 164.

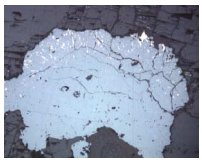

F95. Pyrite replacing magnetite, p. 165.

F96. Bladed hematite embedded in quartz together with pyrite, chalcopyrite, and magnetite, p. 166.

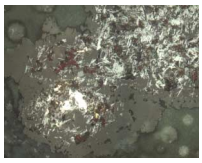

F97. Magnetite, hematite, and pyrite assemblage in groundmass, p. 167.

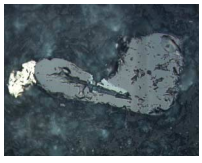

F98. Paragenetic diagram for Site 1189, p. 168.

Given the proximity and broadly similar depth interval over which these two holes were drilled, broad coherence in the sulfide setting and parageneses is to be expected. Within the two holes, pyrite is the dominant sulfide. It is disseminated within the groundmass of the volcanic rocks (Type 1), within quartz-anhydrite veins (Type 2), and finally, as linings and cores to vesicle fill (Type 2a). However, the accessory sulfides, sphalerite and chalcopyrite, are more abundant in Hole 1189B than in Hole 1189A. The relationships between the accessory sulfides and the pyrite provide further evidence for at least two generations of pyrite-quartz precipitation within the holes. Nevertheless, the overall sulfide content of this site is low. However, given the exceptionally low recovery rates in the upper 100 m of Hole 1189B, the meaning of this is uncertain.

STRUCTURAL GEOLOGY

Two holes (Holes 1189A and 1189B) were cored at Site 1189, situated ~30 m apart. Hole 1189A was cored from the seafloor, whereas Hole 1189B was cased and coring started at 31 mbsf. The structures identified in the two holes were primary volcanic layering, brecciation of volcanic rocks, orientation of veins, and age relationship between veins. The structures were described on the structural visual core description forms, and the data were entered in the structural log (see **"Site 1189 Visual Core Descriptions,"** p. 1 and **"Site 1189 Structural Logs,"** p. 148).

Hole 1189A

Orientation of Volcanic Layering

Primary volcanic layering (S_o in the structural logs) was represented in the cores by trails of elongated vesicles and by millimeter-scale laminations, between 0.5 and 2 mm thick, which were interpreted to be flow banding. The 26 measurements show that the dip of primary layering varies from horizontal to vertical and that there is no obvious relationship between dip variation and depth in the hole (Fig. **F99**). The wide range of dips could be caused by the hole intersecting several detached and rotated lava blocks and/or different parts of lobate lava flows with differing primary dips within or between flows. Because of the very low recovery of core in the hole, it is impossible to offer any definite conclusion as to the meaning of these variations in dip. However, the intersection of thick sequences of breccia with rotated clasts suggests that block rotation is likely to be an important factor.

F99. Dip of primary volcanic layering vs. depth, Hole 1189A, p. 169.

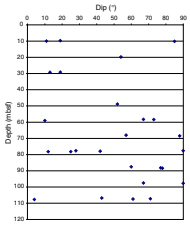

Breccias

Two different types of breccias were intersected in Hole 1189A. In lithologic Units 3 and 4 (i.e., interval 193-1189A-2R-1, 93–136 cm [10.63–11.06 mbsf]), 2- to 50-mm-long angular fragments of altered volcanic rocks are present in a matrix of coarse anhydrite, minor quartz, and scattered grains of pyrite (Fig. **F100**). The fragments vary in color from white to blue-green, presumably because of differences in clay mineral and chlorite content. These differences between the individual fragments show that they represent volcanic rocks that have gone through different degrees of alteration, but also that the alteration must

F100. Anhydrite-cemented breccia with fragments of pervasively altered volcanic rock, p. 170.

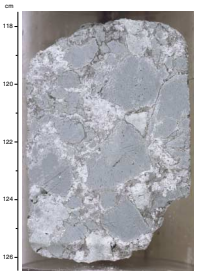

have preceded the brecciation. The contacts between the fragments and the matrix are sharp, which show that little or no alteration has taken place during fragmentation and later cementation by the anhydrite matrix. A similar breccia is present in Unit 6 (i.e., interval 193-1189A-3R-1, 56–63 cm [19.96–20.03 mbsf]). Here, the anhydrite cement and flow-banded green clay-chlorite altered volcanic fragments are crosscut by quartz veins with minor pyrite (Fig. F101). Microscopic examination confirms that there are no alteration halos at the contacts between the fragments and the matrix.

Alteration both preceded and accompanied brecciation in Unit 9, the interval from 38.8 mbsf (i.e., Section 193-1189A-5R-1, 0 cm) to 49.22 mbsf (i.e., Section 193-1189A-6R-1, 62 cm). During the first stage, the volcanic rocks were completely altered to an assemblage of mainly white phyllosilicates (illite and pyrophyllite) and silica. During the second stage, the altered volcanic rocks were brecciated and the fragments altered to green chlorite and smectite (Fig. F102). In contrast to the breccias encountered in Units 3, 4, and 6 (Sections 193-1189A-2R-1 and 3R-1; discussed in the previous paragraph), the contacts between the gray-green matrix and the fragments are diffuse. The degree of alteration of the fragments varies from incipient to complete. Relict flow lamination was recognized in several of the fragments, and in many cases the clasts could be fitted together. Incipient brecciation was noted in several pieces of core in Unit 9 (i.e., interval 193-1189A-6R-1, 31–42 cm [48.91–49.02 mbsf]), where a 2- to 3-cm silica-pyrite-anhydrite vein contains several 2- to 10-mm unoriented fragments of flow-laminated volcanic rock and thin offshoots from the main vein intrude into the wall rock.

Similar types of breccias were also found in many of the pieces in Units 9, 10, 16, and 17 (i.e., Sections 193-1189A-6R-1, 7R-1, and 9R-1), alternating with pieces containing veins and vein-network structures, some showing minor brecciation.

Vein Mineralogy and Paragenesis

The veins in Hole 1189A consist of varying proportions of quartz, anhydrite, and pyrite. Minor chalcopyrite is associated with pyrite in some veins in Units 5, 16, 17, and 19 (i.e., Sections 193-1189A-3R-1, 9R-1, and 10R-1). Most of the veins are dominated by quartz with or without anhydrite and minor pyrite (Fig. F103). This is especially the case for Units 8, 9, 10, 15, and 19, where the veins form networks of <0.5- to 2-mm-thick veins and veinlets (Fig. F104). In Unit 19, some veins are dominated by quartz and some by anhydrite (Fig. F103).

In the brecciated volcanic rocks, especially in Unit 9 (i.e., Sections 193-1189A-5R-1 and 6R-1, as described above), quartz-pyrite-anhydrite veins cut across and replace both earlier infill and veins of anhydrite between the altered volcanic fragments. In a few cases, thin anhydrite veins cut across earlier anhydrite ± pyrite veins with alteration halos. Also, in some of the thin sections, hairline veins and fractures filled with quartz cut across veins of predominantly anhydrite or quartz.

Alteration halos around the veins in the brecciated units are typically gray to green, apparently consisting of clay and/or chlorite. In most other cases, the alteration halos consist of quartz, in one unit as poikiloblasts overgrowing the groundmass of the altered volcanic rocks (Fig. F105A, F105B). Rare second generation anhydrite and quartz veins (only seen in thin sections) do not seem to have any halos associated with them.

F101. Fragments of flow-banded altered volcanic rock, p. 171.

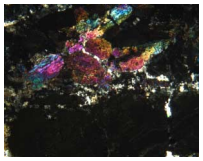

F102. Brecciation, alteration, and quartz-pyrite veining of completely altered volcanic rock, p. 172.

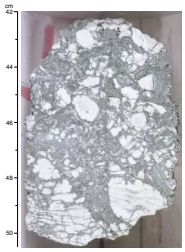

F103. Distribution of veins according to mineralogy vs. lithologic units, Hole 1189A, p. 173.

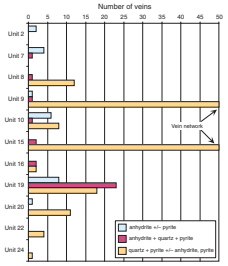

F104. Network of quartz-pyrite veins crosscutting silica-clay alteration, p. 174.

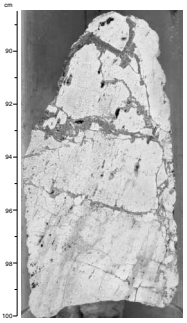

Microscopic examination shows that in many cases the veins exhibit a distinct zonation. Where anhydrite is present, it tends to occupy the center of the veins, whereas quartz forms the selvages (Fig. F105C, F105D). Pyrite and locally chalcopyrite are associated with the anhydrite. Pyrite in many cases rims the veins (Fig. F105A, F105C).

Vein Geometries

With respect to vein thickness, ~70% of the veins in Hole 1189A are <2 mm thick, whereas only 2% are thicker than 10 mm (Fig. F106A). Although the anhydrite-dominated veins are generally thinner than the quartz veins, the thickest veins consist of anhydrite with minor quartz and pyrite (the thickest is a vein >30 mm in width in Unit 7 [i.e., interval 193-1189A-3R-1, 89–94 cm]).

The dips of the veins range from horizontal to vertical. However, most of the veins have dips between 30° and 60° (Fig. F106B). There is no obvious systematic variation in the dips of the veins with depth in the hole (Fig. F106C). This is possibly because almost all the measurements were taken over the interval from 60 to 90 mbsf.

Hole 1189B

Orientation of Primary Volcanic Structures

Primary volcanic layering was identified in the cores of Hole 1189B by alternating millimeter-thick lamina, marked by differences in color from gray to green or white. This structure was interpreted to represent flow banding that had undergone different degrees of silica-clay alteration. Layering was also defined by trails of aligned, stretched, and flattened vesicles. Trails of plagioclase phenocrysts were also used to define the primary layering, although such indicators were rare. With three exceptions, the 15 measurements shown in Figure F107 are from lithologic Unit 19, between 128 and 139 mbsf, which is a highly silicified vesicular volcanic rock (see "Igneous Petrology," p. 8). The vesicles are variably stretched and flattened. The dips of the layering (S_o) and the plunges of stretched vesicles (L_o) range between 33° and 90° in this interval with most between 65° and 90° (Fig. F107). This localized steep layering and coeval stretching of vesicles over a thickness of >10 m could indicate that the hole intersected a major zone of upflow of lava, or even a dike.

Breccias and Vein Network Structures

Hole 1189B is characterized by brecciated rocks and vein network (stockwork) structures. Three intervals of breccias and veins were intersected, separated by highly altered, gray, siliceous volcanic rock crosscut by only a few veins. The breccia-vein network intervals are Unit 1 (i.e., Section 193-1189B-1R-1, 0 cm [31.00 mbsf]) to Unit 18 (i.e., Section 11R-1, 43 cm [128.03 mbsf]), Unit 20 (i.e., Section 13R-1, 20 cm [147.20 mbsf]) to Unit 26 (i.e., Section 16R-1, 74 cm [176.44 mbsf]), and Unit 32 (i.e., Section 17R-1, 104 cm [186.34 mbsf]) to Unit 36 (i.e., Section 18R-2, 115 cm [197.57 mbsf]), which is the bottom of the hole.

In the interval 31.00–128.03 mbsf, the brecciated rocks contain irregular fragments of highly altered volcanic rock, partly with flow banding or vesicles still preserved (Fig. F108). In some of the pieces, the breccias are polymict (i.e., contain fragments of different composition or tex-

F105. Vein textures, Hole 1189A, p. 175.

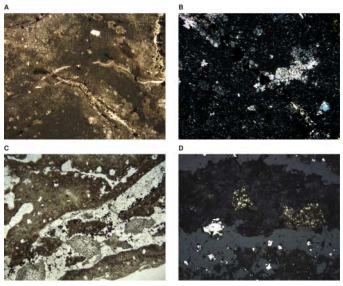

F106. Distribution of vein thicknesses, vein dip, and dip of veins vs. depth, Hole 1189A, p. 177.

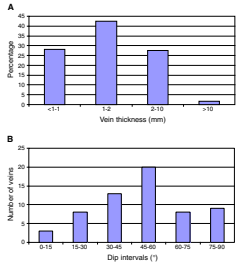

F107. Dip of primary volcanic layering and plunge of stretched vesicles vs. depth, Hole 1189B p. 179.

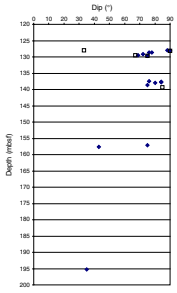

F108. Matrix-supported breccia, p. 180.

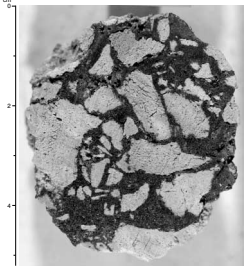

ture). In most cases the breccias are matrix supported. The matrix or cement between the fragments above 49.7 mbsf consists predominantly of anhydrite with rare gypsum, whereas quartz dominates between 49.7 and 128 mbsf. Microscopic examination showed that gypsum, where present, replaces anhydrite. Pyrite is present throughout as part of the matrix, locally with minor amounts of chalcopyrite. The pieces of rock between the intervals of brecciated rock consist predominantly of highly altered volcanic rocks, crosscut by a fine network of quartz-pyrite veins.

In the interval between 147.20 and 176.44 mbsf, the brecciated rocks predominantly contain fragments of flow-banded volcanic rocks (Fig. F109). In contrast to the interval described in the previous paragraph, the brecciated pieces in this interval are commonly clast-supported (cf. Figs. F108, F109). The matrix here is mainly quartz with variable amounts of anhydrite and pyrite. In places, late anhydrite veins cut across both the matrix and fragments (Fig. F109).

Brecciation in this interval is caused by both volcanic and hydrothermal processes. In rare cases (Fig. F23), ductile flow facies are seen to cut brecciated rocks. Such examples are clear evidence of autoclastic brecciation.

Another example of brecciation and network veining is shown in Figure F110. In this case, the veins and open-space fill consist of quartz, anhydrite, sphalerite, pyrite, and trace chalcopyrite. Quartz forms the rim of the veins, and euhedral sphalerite and pyrite have been crystallized farther into the veins and into what must have formed as open spaces, whereas coarse anhydrite crystallized as the last phase in the middle of the veins and in the open spaces. The sphalerite has a light brown, Zn-rich core, whereas the rim is darker and Fe rich. In this case the brecciation is clearly secondary, affecting a primarily coherent volcanic rock. The different fragments all fit together and form a jigsaw-fit breccia structure. Movements between the fragments are evident, as traced by prominent flow bands (some of which are labeled A–G on Fig. F110B).

Another example of secondary brecciation and network veining is shown in Figure F111. Here, the veins consist of quartz, magnetite, and pyrite. Magnetite is located principally in the vein selvages, whereas pyrite occupies the center of the thicker veins and open spaces. The fluids affected the rocks by forming clay-silica alteration halos around the veins. Secondary hairline anhydrite veinlets cut across the breccia and vein network.

In general, vein-network formation obviously was later than the primary volcaniclastic brecciation of the rock. This is shown in Figure F109, where a dense network of mainly silica (according to XRD measurements, it is probably cristobalite; see "Hydrothermal Alteration," p. 23) cuts across the fragments and the flow banding. In places, the fine and small veins are surrounded by halos of silica-clay alteration (Fig. F112).

The interval of brecciated rocks and vein networks from 186.34 mbsf to the bottom of the hole at 197.57 mbsf is very similar to the previous interval. However, veins and open-space fill in this interval contain fine-grained hematite together with quartz and anhydrite.

Vein Mineralogy and Paragenesis

The veins in Hole 1189B may contain quartz, anhydrite, pyrite, magnetite, and/or hematite with minor to trace sphalerite, chalcopyrite,

F109. Clast-supported breccia cut by dense silica vein network, p. 181.

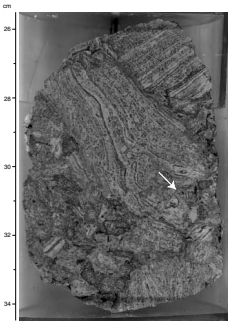

F110. Photomicrograph and sketch of vein network and jigsaw-fit breccia in altered, flow-banded volcanic rock, p. 182.

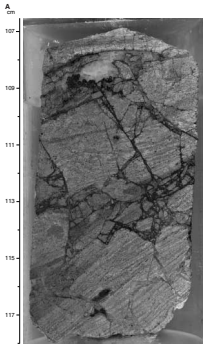

F111. Vein network and brecciated, silicified volcanic rock, p. 184.

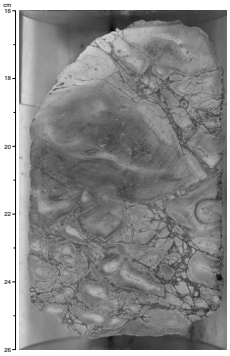

F112. Network of silica veins with alteration halos cutting flow-banded volcanic rock, p. 185.

and gypsum. More than 90% of the veins are dominated by quartz (Fig. F113). Veins dominated by anhydrite, partly replaced by gypsum, are found mainly in the networks in the upper part of the hole, especially in Units 1 to 3 (above 49.7 mbsf) and in veins intersecting the thick, rather monotonous, volcanic rock of Unit 19 (Fig. F114). Anhydrite also commonly forms late vein structures, crosscutting earlier quartz-dominated veins (see Figs. F109, F111, F115).

Hematite is present in the vein network and breccias in Unit 5 (interval 193-1189B-6R-1, 0–56 cm). Otherwise, hematite is found in the brecciated rocks and vein network in the lower part of the hole (186.34–197.57 mbsf), as described above. Magnetite is common in the network veins in Unit 26 (interval 193-1189B-16R-1, 7–88 cm) and in some of the veins in the upper part of Unit 32 (interval 193-1189B-17R-1, 104–145 cm), where it appears in selvages and halos around quartz veins with minor pyrite.

With respect to sulfides, pyrite is present as a minor component in most of the veins, whether they are single veins, or parts of a vein network. Sphalerite is a minor component in the vein networks in Unit 13 (i.e., Section 193-1189B-10R-1, Pieces 1 and 3) and is a trace component in the vein network in Units 32 through 34 (i.e., interval 193-1189B-18R-1, 0–142 cm). Chalcopyrite is a minor component in the breccias in the upper part of the hole in Units 1 through 3 (Sections 193-1189B-1R-1 and 2R-1) and is otherwise found in trace amounts, commonly associated with pyrite or sphalerite throughout the hole.

The veins in Hole 1189B can be divided into two generations. The second generation consists of late anhydrite veins, which cut across first-generation veins and vein networks consisting predominantly of quartz and pyrite ± iron oxides (Figs. F109, F111, F115).

Vein Geometries

Of the veins in Hole 1189B, 52% are 1 mm thick or less, ~40% are between 1 and 2 mm thick, and <1% are thicker than 10 mm (Fig. F116A). Most of the veins <1 mm thick belong to the fine vein network of quartz and pyrite in the brecciated intervals.

The dips of the veins range from horizontal to vertical. However, >50% of the veins have dips between 30° and 60° (Fig. F116B). In some cases, the veins tend to follow primary layering in the volcanic rocks (Fig. F115). There appears to be no systematic variation in dip of the veins with depth in the hole (Fig. F116C).

Summary

Holes 1189A and 1189B are ~30 m apart, and the vertical difference between their collars is ~6 m; therefore, the holes together provide an insight into the lateral variation of the Roman Ruins hydrothermal site.

There are several interesting similarities and differences between the two holes with respect to vein structures:

1. The volcanic rocks in Hole 1189B are much more brecciated than the rocks in Hole 1189A.
2. The vein intensity is higher and intervals of network veining are thicker in Hole 1189B.
3. The brecciated rocks in the two holes are very similar, consisting of variably altered volcanic fragments and crosscut by vein networks of quartz with pyrite and minor anhydrite. However, in

F113. Distribution of veins according to mineralogy, Hole 1189B, p. 186.

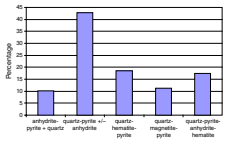

F114. Distribution of veins according to mineralogy vs., lithologic units, Hole 1189B, p. 187.

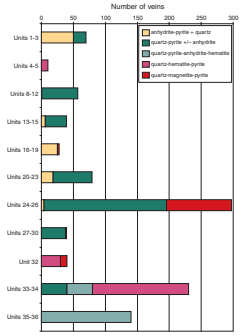

F115. Quartz-anhydrite vein network and later anhydrite vein crosscutting highly altered volcanic rock, p. 188.

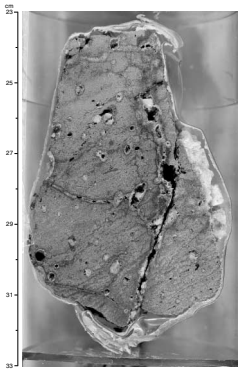

contrast to Hole 1189A, magnetite and hematite are present in the networks as minor components, and sphalerite and chalcopyrite are present as trace minerals in Hole 1189B.
4. In both holes, late coarse-grained anhydrite veins crosscut vein networks and brecciated rocks.
5. The distribution of dips of the veins in the two holes is very similar; in both, veins dipping between 30° and 60° are the most common.

F116. Distribution of vein thicknesses, veins in different intervals of dip, and dip of veins vs. depth, Hole 1189B, p. 189.

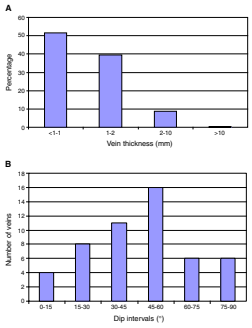

GEOCHEMISTRY

Twenty-two rock samples were taken for shipboard analysis from Holes 1189A and 1189B. The samples from Hole 1189A are highly altered, with the exception of the uppermost sample (193-1189A-1R-1, 0–4 cm), which is a fresh dacite. Most samples analyzed from Hole 1189B are less altered than Hole 1189A samples and represent a different sampling scheme, following a great deal of trial and error with inductively coupled plasma–atomic emission spectroscopy (ICP-AES) methodologies.

A subset of samples obtained from Hole 1189A contains 5–10 wt% total sulfur and was initially measured with the ICP-AES using the sulfur method (see **"Geochemistry,"** p. 15, in the "Explanatory Notes" chapter). However, the results were found to be mismatched to the standard reference materials for sulfides and these samples were therefore reanalyzed using the method developed for igneous rocks with a dacite-rhyodacite composition (see **"Geochemistry,"** p. 15, in the "Explanatory Notes" chapter). Despite the high degree of alteration, there was, in general, a much better match with the matrix of the igneous rock standards. In about half of the analyzed rocks from Hole 1189A, the dominant portion of the total measured sulfur is sulfate-sulfur (i.e., anhydrite, barite, and other minor sulfates) and in the other half, the dominant phase is reduced sulfur, predominately in pyrite form. In Hole 1189B, the first two samples have very high sulfur contents with appreciable water-soluble sulfate.

Results

The results of the ICP-AES, nitrogen, carbon, and sulfur (NCS), ion chromatography (IC), and gravimetric analyses of representative samples from Hole 1189A are given in Table **T7,** and those for Hole 1189B are given in Table **T8.** The samples are listed by assigned units, in order of increasing depth. Note that the ICP-AES analyses for all samples and standards were conducted on ignited powders as described in **"Geochemistry,"** p. 15, in the "Explanatory Notes" chapter. Two samples from Hole 1189B, although high in sulfide content, were also measured using the igneous method, and the data should, therefore, be used with caution. The reported ignited powder values are ordered with respect to major element oxides and expressed as weight percent. Values for loss on ignition (LOI) (in weight percent) of the unignited powders follow. The major element data precede the trace element concentrations (in parts per million [ppm]) for the ignited powders. The concentrations of the major elements in the ignited powders were recalculated using the LOI for the original rock composition, including volatiles, and the results are given in the lower half of Tables **T7** and **T8.** In addition, gravimetric determination of soluble sulfate-sulfur in the

T7. Major element oxides and selected trace elements, Hole 1189A, p. 243.

T8. Major element oxides and selected trace elements, Hole 1189B, p. 244.

unignited powder is reported at the bottom of the tables. In Tables T9 and T10, the data for NCS analysis of the unignited (pre-LOI) water and sulfur contents are presented.

As discussed in "Geochemistry," p. 65, in the "Site 1188" chapter, a representative composite of small fragments (Hole 1189A) was collected from a bag labeled "1189A bulk residue" stored in the core splitter room. This included some off-cuts from sawing, and it is not certain what interval of the hole the fragments represent. The composite is probably biased toward the lower 30–50 m. The sample was sent by helicopter to the Commonwealth Scientific and Industrial Research Organisation (CSIRO) Division of Exploration and Mining, Sydney, Australia, for ICP-AES and neutron activation analysis (NAA) primarily to check the gold content, and the results are presented in Tables T11 and T12.

T9. Total sulfur and water analyses, Hole 1189A, p. 245.

T10. Total sulfur and water analyses, Hole 1189B, p. 246.

T11. ICP-AES analyses of composite sample, Hole 1189A, p. 247.

T12. NAA analyses of composite sample, Hole 1189A, p. 248.

Hole 1189A

Owing to the internal inhomogeneity observed in the various units, the bias toward the samples with low sulfide contents, and the limited sample size (due to poor recovery), an interunit comparison should be made with caution. The variation of selected major oxide and trace element compositions with depth are plotted together with bulk mineralogy from XRD and the alteration log in Figure F117. The observed chemical variations are generally less pronounced than at Site 1188; they are consistent with the mineralogy and alteration style observed in thin section and XRD. However, in general, higher Na_2O concentrations correspond to the presence of plagioclase observed in thin section, whereas K_2O contents correlate with the proportion of illite and K-feldspar observed.

F117. Downhole variations in major element oxides and trace elements, Hole 1189A, p. 191.

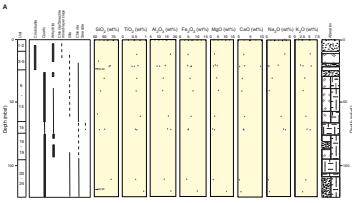

Igneous Geochemistry

Only one fresh volcanic rock sample was analyzed from Hole 1189A (Unit 1; Sample 193-1189A-1R-1, 0–4 cm). This sample may be classified as a dacite, based on both total alkali vs. silica and using the International Union of Geological Sciences Subcommission on the Systematics of Igneous Rocks (CIPW norm) classification.

Alteration Geochemistry

Three major alteration types have been identified in the cores from Hole 1189A: (1) GSC, (2) bleached (Bl), and (3) silicification (Sil). For more detailed descriptions of these alteration types, see "Hydrothermal Alteration," p. 23. Table T7 shows the alteration styles assigned to each sample. Based on chemical composition alone, the three alteration styles do not seem very distinct. In general, the variations observed in the GSC altered rocks correspond to changes in phyllosilicate mineralogy and amounts of silica. The samples from Section 193-1189A-3R-1 (6–10, 59–63, and 70–73 cm, all at ~20 mbsf in Fig. F117) show the variance between the three alteration styles. The GSC altered rock has high water and sulfur contents and shows a clear decrease in Al_2O_3 and Na_2O contents and an increase in CaO and Fe_2O_3 contents relative to the fresh dacite. In general, the changes in Fe_2O_3 and total sulfur can be attributed to the formation of pyrite, whereas the changes in Fe_2O_3 and MgO correspond to the formation of chlorite and clay minerals.

The NAA analyses conducted on the composite sample from Hole 1189A (Table T12) reveal that this sample contains 20 ppb Au, which is higher when compared with the composite samples from Site 1188, but is not anomalous in an economic geology sense.

Hole 1189B

Alteration Chemistry

The upper 100 m recovered from Hole 1189B is extensively altered, and recovery was very low; only two samples were analyzed from this interval. Six samples were analyzed from the lower sequence of Hole 1189B. The variations with depth of selected major oxide and trace element compositions are plotted together with bulk mineralogy in Figure F118. All samples above 147 mbsf are classified as GSC altered, whereas the last two samples represent the silicification rock alteration style. In general, SiO_2, CaO, and Na_2O contents increase below 100 m, which is in agreement with the increases in plagioclase and quartz contents. The increase in SiO_2 is relative, because the first sample (193-1189B-1R-1, 20–30 cm) is an unusually soft, clay-rich alteration product of vesicular dacite, dominated by illite, mixed-layer clays, and pyrite, and is particularly low in silica. The second sample (193-1189B-8R-1, 7–9 cm) is a K-feldspar–bearing, brecciated rock with a stockwork sulfide overprint. Therefore, these two samples are not mineralogically comparable with samples from the lower sequence. They have overall low silica, CaO, and Na_2O, high Al_2O_3 contents, and higher TiO_2, Fe_2O_3, and K_2O than the deeper samples. Below 128 mbsf, the water and sulfur contents decrease with depth, and S contents are particularly low, whereas Sr and the Zr/TiO_2 ratio (Zr in ppm, TiO_2 in wt%) are higher. This latter feature is consistent with the change from aphyric to sparsely porphyritic rock (dacite to rhyodacite parent) (see "Igneous Petrology," p. 8) at ~100 mbsf.

F118. Downhole variations in major element oxides and trace elements, Hole 1189B, p. 193.

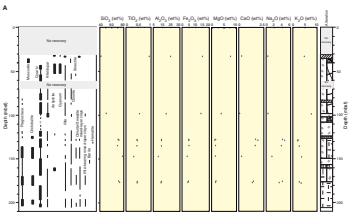

Water Chemistry

One water sample was collected by the water-sampling temperature probe (WSTP) in Hole 1189B at 130 mbsf. The in situ measured water temperature was 55°C. Immediately after recovering the sampling tube, the pH, alkalinity, and salinity were determined. The water chemistry was measured using IC and ICP-AES methods (see "Geochemistry," p. 15, in the "Explanatory Notes" chapter), and the results, as well as the pH, alkalinity, and salinity values, are reported in Table T13. The measured pH and alkalinity are slightly lower and chloride, calcium, strontium, and particularly sulfate are higher than standard seawater. The anomalously high value for manganese (236 µmol/L), which is similar to the first water sample from Hole 1188B (278 µmol/L), reflects leaching from altered host rocks, which tend to be conspicuously depleted in this element.

T13. Water chemistry data from borehole fluid, surface seawater, and IAPSO standard, Hole 1189B, p. 249.

In comparison with the water data from Site 1188, most ion concentrations are slightly elevated. The pH is lower by ~1, whereas sulfate and strontium values are ~15%–25% higher. In addition, in Hole 1189B, the concentration of lithium is almost five times higher, iron about four to ten times higher, and calcium about two times higher than concentrations in the three samples from Holes 1188B and 1188F, indicating a larger hydrothermal input and possibly also some dissolution of anhydrite (increased sulfate).

MICROBIOLOGY

Samples were collected prior to curation from Holes 1189A and 1189B for shipboard studies (direct bacterial count, adenosine triphosphate (ATP) analysis for biomass activities, micromorphological descriptions, and enrichment cultivation). Corresponding samples will be used for shore-based studies, including aerobic and anaerobic culturing, biochemical and molecular typing, microscopic determination of the role of microorganisms in mineralization and alteration, and search for potential bioactive molecules.

Total Bacterial Enumeration

Following the methods described in "Microbiology," p. 19, in the "Explanatory Notes" chapter, samples were stained with 4,6-diamindino-2-phenylindole (DAPI) and the direct bacterial counts are shown in Tables T14 and T15. The DAPI dye binds to DNA, hence these bacterial counts represent both the dead (provided that the DNA is intact) and the living microbial population. In Hole 1189A, bacteria were found in the three uppermost samples, and the amount of microbial mass decreases with increasing depth (Table T14). The uppermost core enumerated (Sample 193-1189A-2R-1, 35–38 cm; 9.70 mbsf) contains 1.3×10^7 cells/cm^3, the population decreases to 4.6×10^5 cells/cm^3 in the next sample (Sample 193-1189A-5R-1, 33–35 cm; 39.13 mbsf), and to 9.8×10^5 cells/cm^3 (Sample 193-1189A-6R-1, 18–21 cm; 48.6 mbsf). No bacteria were detected in samples from greater depths. The results of the bacterial enumeration from Hole 1189B are listed in Table T15. Bacteria were detected only in the uppermost core counted (Sample 193-1189B-1R, 0–4 cm; 31.0 mbsf) at a population of 3.1×10^6 cells/cm^3. No bacteria were detected in samples from greater depths. The detection limit of the direct count procedure is ~1×10^5 cells/cm^3. It is, therefore, possible that a more sparing microbial population exists below this detection limit. As noted previously (see "Microbiology," p. 71, in the "Site 1188" chapter), the major limitation with this direct count procedure is the difficulty in distinguishing bacterial cells from mineral particles that fluoresce.

The microbial mass profile observed at this site is similar to that in Site 1188, where bacterial mass was detected down to ~50 mbsf. These results demonstrate that microogranisms may exist in the subseafloor at sites of active venting of high-temperature hydrothermal fluid; therefore, they may play a role in mineralization and alteration processes.

T14. Total bacterial count and ATP measurements, Hole 1189A, p. 250.

T15. Total bacterial count of samples, Hole 1189B, p. 251.

Biomass Activities

ATP was measured using the luciferin-luciferase method to determine the biomass activities, and the results of the analysis of samples from Hole 1189A are shown in Table T14. ATP was detected only in the two uppermost samples (Samples 193-1189A-2R, 35–38 cm [9.7 mbsf with 18.2 pg/cm^3] and 193-1189A-5R, 33–35 cm [39.13 mbsf with 4.8 pg/cm^3]). All samples collected from depths >40 mbsf showed no evidence of biomass activity. ATP was not measured in samples from Hole 1189B because of an unavailability of the reagents required to do these analyses.

The bacterial count data suggest bacterial existence as deep as ~50 mbsf (Table T14). The absence of microbial activities below this depth

suggests an unsuitable environment for existence and/or bacterial mass with much reduced activity. However, note that the detection limit of this analytical procedure is 0.5 pg/cm^3 (1 × 10^4 cells/cm^3). Therefore, it remains possible that microorganisms are present at deeper levels but in sparse amounts.

Enrichment Cultures

Enrichment cultivation experiments were performed to improve the yield of microorganisms in the samples. These experiments were conducted at varying temperatures and oxygen partial pressures for a period of 1 week. Bacterial growth was determined by comparing culture medium inoculated with core samples with the uninoculated medium, where turbidity in the medium indicates growth. In cultures where it was difficult to make an assessment based on visual inspection, ATP analysis was used to verify growth.

The results of the enrichment cultivation experiments with samples from Hole 1189A are shown in Table T16. In the aerobic experiments, growth was observed at 4°C (Sample 193-1189A-2R-1, 35–38 cm, 9.70 mbsf) and 25°C (Samples 193-1189A-2R-1, 35–38 cm [9.70 mbsf]; 5R-1, 33–35 cm [39.13 mbsf]; and 6R-1,18–21 cm [48.6 mbsf]). No bacterial growth was observed in samples incubated at 60°C. In the anaerobic experiments, bacterial growth was observed at 25°C (Samples 193-1189A-2R-1, 35–38 cm [9.70 mbsf]; 5R-1, 33–35 cm [39.13 mbsf]; 6R-1, 18–21 cm [48.60 mbsf]; and 8R-1, 39–41 cm [68.39 mbsf]), 60°C (Samples 193-1189A-5R-1, 33–35 cm [39.13 mbsf]; 6R-1, 18–21 cm [48.60 mbsf]; and 8R-1, 39–41 cm [68.39 mbsf]) and 90°C (Samples 193-1189A-2R-1, 35–38 cm [9.70 mbsf]; 5R-1, 33–35 cm [39.13 mbsf]; and 8R-1, 39–41 cm [68.39 mbsf]). Enrichment cultivation experiments with samples from Hole 1189B were conducted only in anaerobic conditions and results are shown in Table T17. Microbial growth was observed only in samples at depths between 80 and 100 mbsf (Samples 193-1189B-6R-1, 7–19 cm [79.07 mbsf], and 8R-1, 0.0–4.0 cm [118.10 mbsf]) at both 60° and 90°C, and as deep as ~130 mbsf (Samples 193-1189B-10R-1, 20–24 cm [118.1 mbsf], and 11R-1, 66–76 cm [128.94 mbsf]) at 90°C. No growth was observed in the samples from the uppermost 70 mbsf (Samples 193-1189B-1R-1, 0–4 cm [31.0 mbsf] through 5R-1, 14–18 cm [69.8 mbsf]) or from depths >140 mbsf (Samples 193-1189B-12R-1, 130–133 cm [140.01 mbsf] through 16R-1, 25–28 cm [175.5 mbsf]). A negative control experiment (surface seawater used instead of core) reveals no microbial growth, suggesting that microbial growth is not caused by contamination from seawater.

T16. Enrichment cultivation results, Hole 1189A, p. 252.

T17. Enrichment cultivation results, Hole 1189B, p. 253.

The distribution of anaerobic high-temperature microbial populations differs among the two holes at Site 1189. In Hole 1189A, microbial mass was detected in the uppermost 70 mbsf. In contrast, microbial mass was established at depths between 80 and 130 mbsf in Hole 1189B. Furthermore, the bacterial growths in the anaerobic (and high temperature) cultures were detected in samples from greater depths (80–130 mbsf) in Hole 1189B compared to <35 mbsf in holes from Site 1188. These data suggest differences in nutrient supplies and temperature profiles between the two holes at Site 1189 and more so, between the Snowcap hydrothermal site (Site 1188) and Roman Ruins (Site 1189) hydrothermal sites. These observations probably reflect a large biological diversity that likely exists within this hydrothermal system.

Cultivation with Different Seawater Types

A cultivation experiment was conducted to study the effects of different types of seawater and core, at different growth conditions, on the microbial habitation. Seawater was used in the aerobic experiments, whereas sterilized seawater and artificial seawater were used in the anaerobic experiments. These seawater media were inoculated with ~5 g of core (Sample 193-1189A-5R-1, 33–35 cm; 39.13 mbsf) and incubated at 25° and 60°C in the dark for a period of 4 weeks (Table T18). Corresponding control experiments (without core) were also conducted. Sample 193-1189A-5R-1, 33–35 cm (39.13 mbsf), is a completely altered hydrothermal breccia with flow-laminated volcanic clasts and hosts an active bacterial population (Table T14). The descriptions of the cloudy materials at the bottom of the culture bottle, the estimations of the microbial growth, and the pH of the medium after 4 weeks of incubation are presented in Figure F119.

Microscopic observations reveal that the cloudy materials formed at the bottom of the culture bottles are composed of a suspension of clay minerals (most probably mixed-layer chlorite-smectite clay, smectite, and illite as identified by XRD in the core used). This suspension was present in cultures of natural seawater, artificial seawater, and to lesser extent in sterilized seawater. The fact that no such clay suspension was observed in the aerobic culture at 25°C suggests that formation of this suspension is temperature dependent. In contrast, under anaerobic conditions, formation of such a suspension appears to be dependent on the type of seawater.

In the aerobic cultures, bacterial mass exists within the suspension of clay minerals (Fig. F120A) and forms exopolymeric clusters (Fig. F120B, F120C). The bacterial population can be clearly distinguished from fluorescent minerals. Small numbers of similar bacterial populations were also found in the control culture. These observations imply that natural seawater microbes are able to exist in such clay mineral assemblages, under aerobic conditions at temperatures ≤60°C. In the anaerobic cultures, bacterial populations exist within the clay mineral suspensions in both the sterilized seawater and the artificial seawater at 25°C, and to a lesser extent at 60°C (Fig. F119). These bacteria are morphologically distinct from those observed in aerobic cultures. The clay mineral suspension and bacterial habitation within these suspensions are shown in Fig. F121. Bacteria were not detected in the control cultures. These observations mean that bacteria within the core materials are able to exist at temperatures ≤60°C within the clay mineral suspensions.

The microbial habitation is also dependent on pH, and because the core contains sulfides (e.g., pyrite) and sulfates (e.g., anhydrite), dissolutions of these minerals could alter the pH of the medium. Likewise, changes in pH can result from microbial activity (e.g., demineralization, production of organic acids). As shown in Table T18 and Figure F119, the pH of natural and sterilized seawater cultures decreased, whereas that of the synthetic seawater increased after the 4 weeks of incubation. In both cases, however, the changes in the pH were small (0.2–0.5 pH units). Likewise, changes in pH (of similar magnitudes) were also observed in the control cultures. These observations, therefore, suggest that mineral dissolution and/or bacterial activities do not significantly alter the pH of the media at temperatures ≤60°C.

The results of these experiments suggest that clay-sulfide-sulfate assemblages may be the primary habitats for microbial populations within the PACMANUS hydrothermal field and that seawater is the

T18. Cultivation experiments with different seawater types, p. 254.

F119. Observations of cultivation experiment, p. 195.

Culture Conditions	Culture Media Descriptions		Bacterial Observations		pH	
	25°C	60°C	25°C	60°C	25°C	60°C
A	–	■	+++	+	7.92	7.79
B	–	–*	+	+	8.05	8.00
C	▒	▒	++	+	6.21	6.48
D	–	–*	ND	ND	6.32	6.41
E	■	■	+++	+	6.52	6.60
F	–	–	ND	ND	6.43	6.68

■ cloudy ▒ slightly cloudy – clear * gypsum deposits
+++ high bacterial growth ++ moderate bacterial growth + low bacterial growth ND not detected

F120. Microphotographs and schematic images of epifluorescence observations of aerobic culture after 2 weeks of incubation, p. 196.

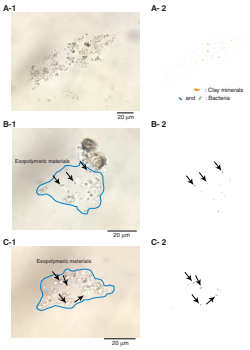

F121. Microphotographs and schematic images of epifluorescence observations of anaerobic cultures after 4 weeks of incubation, p. 197.

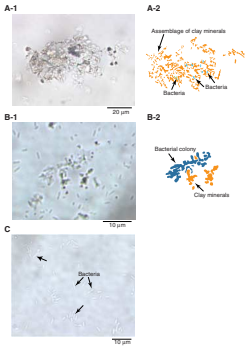

main source of nutrients and microorganisms, although nutrient concentrations may be affected by fluid-rock interaction.

Micromorphological Observations

Optical and epifluorescence microscopic techniques were used to characterize the interactions between microorganisms and minerals, particularly the micromorphology, size, chemical composition, and structure of minerals associated with the microorganisms. Such information is essential in establishing the biological habitat and the role of microbes in the mineralization and alteration processes in this hydrothermal system.

The three uppermost samples examined show definite microbial habitation. Sample 193-1189A-2R-1, 35–38 cm (9.70 mbsf) consists of brown translucent fragments (volcanic glass with abundant fine-grained inclusions of silica, clay, and magnetite) and translucent materials (broken plagioclase phenocrysts). Staining with DAPI reveals that bacteria are located exclusively on the brown translucent volcanic glass. Samples 193-1189A-5R-1, 33–35 cm (33.13 mbsf), and 193-1189A-6R-1, 18–21 cm (48.6 mbsf), are completely altered hydrothermal breccias with flow-laminated volcanic clasts. They contain transparent blocky crystals of anhydrite and flaky brown translucent clusters of altered volcanic glass, clay, and pyrite (Fig. F122A). Bacterial staining with DAPI indicates the presence of bacteria on the surface of the flaky clusters (Fig. F122B), whereas the anhydrite crystals did not show any bacterial habitation (Fig. F122C).

The direct bacterial counts for Hole 1189A show bacterial habitation as deep as ~50 mbsf (Sample 193-1189A-6R-1, 18–21 cm; 48.6 mbsf). However, as noted previously, bacterial mass may exist below the detection limit of this procedure. Staining with DAPI revealed mineralized bacteria in Samples 193-1189A-8R-1, 39–41 cm (68.39 mbsf), and 193-1189A-12R-1, 41–50 cm (106.91 mbsf) (in chains of three to six bacteria), and bacterial secretion-like material (exopolymeric clusters, ~300 µm in size) in Sample 193-1189A-12R-1, 41–40 cm (106.91 mbsf) (Fig. F123). In view of the difficulties in distinguishing bacteria and minerals alluded to previously, further shore-based high-resolution microscopic studies will be conducted to verify the bacterial habitation profiles of Holes 1189A and 1189B.

Sample 193-1189A-10R-1, 103–115 cm (88.33 mbsf), is a completely altered hydrothermal breccia that is similar to Samples 193-1189A-5R-1, 33–35 cm (39.13 mbsf), and 193-1189A-6R-1, 18–21 cm (48.60 mbsf). However, no bacteria were located in this sample perhaps implying depth and temperature restrictions to microbial habitation.

F122. Microphotographs of transparent rectangular crystals and flaky brown translucent clusters showing bacterial habitation, p. 198.

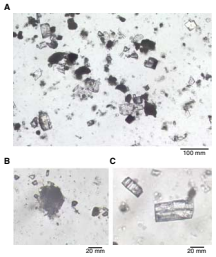

F123. Microphotographs showing possible bacterial habitation, p. 199.

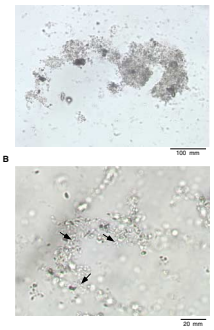

PHYSICAL PROPERTIES

Physical properties measurements taken on cores recovered from Site 1189 (Roman Ruins hydrothermal site) included magnetic susceptibility, natural gamma radiation, thermal conductivity, compressional wave velocity, and standard index properties. In most cases, measurements were made at least once per lithologic unit. In areas of large-scale heterogeneity and when recovery allowed, sampling density was increased. On the multisensor track (MST), the magnetic susceptibility meter (MSM) and the natural gamma radiation (NGR) device were used on Cores 193-1189A-2R through 12R and 193-1189B-11R through 18R.

Because the other cores were particularly fragmented, incomplete, or disturbed, they did not lend themselves to the continuous automated measurements of the MST. Where possible, compressional wave velocity measurements were made on discrete samples in one direction, which is perpendicular to the hole's vertical axis. Thermal conductivity was measured on almost every lithologic unit for both holes, except where recovery was too low or rock pieces were too small (<5 cm) for the measurement procedure. Index properties, also measured in every lithologic unit when recovery allowed, were measured on minicores, rock fragments, or both. Because of these recovery and size considerations, the lower sequence of Hole 1189 (>125 mbsf) received more attention than its upper sequence. Accompanying diagrams that integrate data from both holes at Site 1189 should be examined in the context of the caveats stated above regarding correlations between the holes (see "Hydrothermal Alteration," p. 23).

Magnetic Susceptibility

Figure F124 shows the downhole profile for magnetic susceptibility in Holes 1189A and 1189B from 0 to 200 mbsf. Magnetic susceptibility varies greatly over the length of recovered core, ranging from -0.2×10^{-5} to 3101.5×10^{-5} SI, with an average of 486×10^{-5} SI. In Hole 1189A, magnetic susceptibility has high values at the top of the core, from ~9 to 20 mbsf, and moderately elevated values from 58 to 88 mbsf. Magnetic lows are found from ~29 to 49 mbsf, at 78, and from 96 to 107 mbsf. With the exception of the peak found in Core 193-1189A-2R, the magnetic susceptibility coincides with magnetite occurrences in the core. Although thin sections from Core 193-1189A-2R do not show significant amounts of magnetite, it is likely that fine-grained magnetically susceptible material exists in the groundmass.

In the lower sequence of Hole 1189B, magnetic susceptibility values are generally high throughout, with intervals of low values from 148 to 165 and from 180 to 200 mbsf. As in Core 193-1189A-2R, only trace amounts of magnetite were found in thin section, although very fine grained magnetically susceptible material may again be present. However, the high magnetic susceptibility close to seafloor at the site likely corresponds to preservation of igneous magnetite, which indicates low amounts of alteration, whereas the high values at deeper levels of the site are likely caused by magnetic materials in veins associated with more intense alteration (see "Structural Geology," p. 41).

F124. Magnetic susceptibility, p. 200.

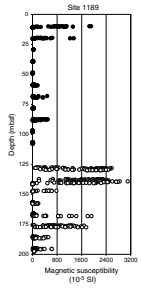

Natural Gamma Radiation

The NGR records are summarized in plots of total counts per second (cps) vs. curated depth (see Fig. F125). The NGR values from Site 1189 cover a much wider range than those at Site 1188 and range from 0 to 64.9 cps, with an average of 20 cps. As with Site 1188, much of the variation found within each hole may be caused by errors in the measurement process (see "Physical Properties," p. 74, in the "Site 1188" chapter).

Even with the inaccurate data, there are definite peaks in the NGR measurements in Cores 193-1189A-10R (87–88 mbsf) and 193-1189B-17R (185–195 mbsf). Other high values are found in Cores 193-1189A-2R (9–11 mbsf), 6R through 8R (48–69 mbsf), and 193-1189B-16R (156–168 mbsf). These variations in NGR values do not coincide directly with lithologic changes or alteration patterns. However, the high values at

F125. Natural gamma radiation, p. 201.

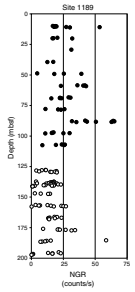

this site as compared to Site 1188 can be attributed to the high percentage of K_2O (see "Geochemistry," p. 46) and the presence of potassium feldspar in the core.

Compressional Wave Velocity

Compressional wave velocities and sample descriptions are given in Table T19 and are plotted in Figure F126. Values range from ~3.4 to 5.0 km/s and average 4.4 km/s. Velocity values generally increase with depth. There is also an apparent trend of decreasing velocity as the percentage of vesicles increases. Although there are some deviations from these trends, lithologic variations, amount of alteration, and structural features may account for some of the variance in the velocity values.

Thermal Conductivity

Thermal conductivity values from Holes 1189A and 1189B range from 0.99 to 5.13 W/(m·K), as shown in Figure F127. Most of the values from Hole 1189A are between 1.7 and 2.5 W/(m·K), with an average of 2.12 W/(m·K), very similar to those found at Site 1188. The low values in shallow cores correspond to unaltered dacite. The highest value of 5.13 W/(m·K), found at 107 mbsf, comes from a core interval with the highest amount of pyrite (50% combined pyrite and chalcopyrite).

As at Site 1188, thermal conductivity values in Hole 1189A are generally higher in brecciated rocks and lower in fresh and altered dacites. Every brecciated rock, with the exception of one, has a thermal conductivity value >2.1 W/(m·K). The one low-value brecciated rock consists mostly of altered dacite with very few, thin veins running through it. Most of the unbrecciated rocks have thermal conductivity values <1.9 W/(m·K); samples in this group that do not have a low thermal conductivity generally have abundant pyrite in vesicles, which could account for the increased values.

Thermal conductivity values from the lower sequence of Hole 1189B are relatively constant. There is a slight trend for brecciated samples to have thermal conductivity values higher than those of dacites, although this is not as defined as in Hole 1189A. Of the nine unbrecciated samples, two that have values >2.0 W/(m·K) contain pyrite veins. Only three out of eight breccia and pseudobreccia samples have values >2.0 W/(m·K). The majority of the low-valued breccias have a high clay content (up to 85%), which may contribute to the lower thermal conductivity values.

Index Properties

The data for water content, bulk density, dry density, grain density, porosity, and void ratio are displayed in Table T20. Figures F128 and F129 show grain density and porosity values, respectively, for both holes as a combined depth profile. Grain densities of powder samples prepared for ICP-AES analyses are given in Table T21. In cases where index properties were measured on both rock fragments and minicores, values were consistent for both types of sample. Similarly, where grain density was measured on both ICP-AES powders and whole samples, values were consistent as well. Grain density values are relatively constant throughout the cored interval, but range overall from 2.37 to 3.75 g/cm³, with an average of 2.77 g/cm³. The unaltered rocks from the very top of Hole 1189 have an average value close to 2.5 g/cm³. Below 0.2

T19. Compressional wave velocity, p. 255.

F126. Compressional wave velocity, p. 202.

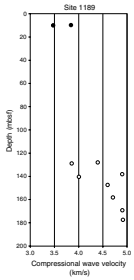

F127. Thermal conductivity, p. 203.

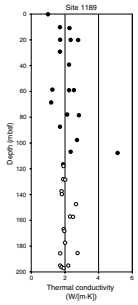

T20. Index properties, p. 256.

F128. Grain density, p. 204.

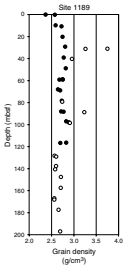

F129. Porosity, p. 205.

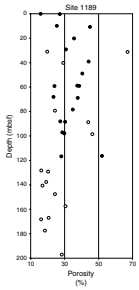

mbsf, these rocks become altered and grain density values increase. The higher densities of some alteration products, such as pyrite, anhydrite, and magnetite, most likely account for the increased grain density in the altered rocks. For example, semimassive sulfide Sample 193-1189B-1R-1, 0–2 cm, which has the highest grain density, contains 35% pyrite and 20% chalcopyrite.

Porosity values span a wide range, from 15.8% to 67.1%, with an average of 30.2%. The combined data set has a trend of decreasing porosity with depth, as seen at Site 1188, although in this case the trend arises from lower porosity of the lower sequence (>120 mbsf) in Hole 1189B. High porosity values, as in Sample 193-1189B-1R-1, 20–30 cm, are usually coincident with vesicular rocks that have high clay content. As at Site 1188, such high porosity is generally not observed in thin section.

T21. Bulk densities of ICP-AES powders, p. 257.

ROCK MAGNETISM

Core recovery at Site 1189 (Roman Ruins hydrothermal site) was low overall, although it improved in the lower sequence of Hole 1189B (>120 mbsf), yet with numerous gaps between pieces. Samples from <120 mbsf in Hole 1189B were too small for magnetic measurements. Standard measurements were made on both archive-half cores and discrete minicores from Hole 1189A down to 106 mbsf and from Hole 1189B from 117 mbsf to the end of the hole. The data from both holes have been combined for the purposes of profile plots in this chapter. As at Site 1188, we had time to conduct additional rock magnetic analyses to determine the nature of magnetic carriers. The results of our analyses show that Site 1189 as represented in the combined profile is similar to the upper half of Site 1188 in many respects, although the susceptibility and remanence values tend to be lower overall at Site 1189. For instance, both sites are characterized by a relatively high remanence at the top (above 25–35 mbsf) and a large interval of lower remanence and remanent intensity values below. As at Site 1188, there is also a region of relatively high susceptibility below 130 mbsf. One important difference between the two sites is that at Site 1188 the susceptibility increases with depth between 135 and 211 mbsf, whereas the remanent intensity decreases. However, at Site 1189, the opposite is true. We see a decrease in susceptibility and an increase in remanent intensity toward the bottom of the lower sequence in Hole 1189B.

Archive Half-Core Measurements

Susceptibility

The susceptibility of whole cores was first measured using the magnetic susceptibility meter mounted on the MST. The results of these measurements are described in "Physical Properties," p. 52. Because of significant gaps in the cores, susceptibility readings were taken from the archive-half cores using point measurements instead of making a continuous measurement along the entire length of the archive half. In this way, we avoided taking measurements in core gaps and undesirable pieces of core sections. The susceptibility probe on the archive multisensor track has a depth range of 2 cm. A total of 197 susceptibility measurements were performed on pieces that were longer and thicker than 2 cm. The downhole profile of these measurements is shown in

Figure F130. All susceptibility values in this report are given in SI units. The susceptibility profile shows several peaks. The top 25 m in Hole 1189A exhibits high susceptibility values. Although there are a few very low values, in general, the susceptibility ranges from 0.01 to 0.028 SI, which is similar to the top 35 m of Hole 1188A but with a greater degree of scatter (see Fig. F124, p. 234, in the "Site 1188" chapter). Below 25 mbsf, the susceptibility is very low, except between 57 and 90 mbsf where there is a moderate increase to ~0.01 SI. The susceptibility then increases from ~120 mbsf in the lower sequence of Hole 1189B and reaches its maximum value (0.031 SI) between 130 and 140 mbsf. Below 170 mbsf, there is another region of high susceptibility (0.021 SI), which peaks at ~175 mbsf. The presence of relatively high susceptibility below 130 mbsf is similar to susceptibility data from Site 1188 (see Fig. F124, p. 234, in the "Site 1188" chapter). There is also an apparent decrease in the susceptibility values in the lower 75 m at Site 1189, whereas no such pattern was recognized in the data from Site 1188. However, the susceptibility values at Site 1189 are lower (maximum values at Site 1189 are a third of the maximum values at Site 1188).

Remanent Intensity

Archive-half cores that had sufficiently long (>10 cm) unbroken pieces were passed through the cryogenic magnetometer for remanent intensity measurements. These cores were then demagnetized progressively in an alternating field (AF) with peak values of 10, 15, 20, and 30 mT. The remanence was measured after each demagnetization step. Measurements on the cryogenic magnetometer were conducted at 2-cm intervals. Because of the gaps in the sample sequences and irregularities in the volume of the core, the remanent intensity values were not downloaded to the Janus database. We show the downhole profile of these uncorrected natural remanent magnetization (NRM) intensity values only to examine the general trend (Fig. F131). The general NRM intensity trend of the archive-half cores is quite similar to that of the susceptibility. The top of the hole shows a peak intensity of 2.85 A/m very near the seafloor. This is followed by a zone of relatively low remanent intensity (<0.5 A/m) between 25 and 120 mbsf. Below 120 mbsf, the remanent intensity shows a significant increase and a maximum intensity of 3.55 A/m is seen at 169 mbsf. We do not observe the apparent decrease in susceptibility values below 130 mbsf reflected in remanent intensity. These data show a gradual increase from 20 to 180 mbsf, with a sharp decrease in intensity over the lowermost 20 m of the section. Based on these observations, it appears that, as at Site 1188, the most significant source of surface magnetic anomalies at Site 1189 would not be at the seafloor, but at a depth >120 mbsf.

Discrete Measurements

We analyzed 14 discrete minicore samples from Hole 1189A and the lower sequence (>120 mbsf) of Hole 1189B. Table T22 summarizes the location, dimensions, and brief descriptions of these minicores. The anisotropy of magnetic susceptibility of minicore samples was measured at 15 different positions. The results are provided in Table T23. Magnetic susceptibility varies by several orders of magnitude. Figure F132 shows a plot of average susceptibility (k) vs. depth. Overall, the susceptibility of minicores is consistent with the downhole profile of the archive-half cores (Fig. F130). The susceptibility values of the mini-

F130. Volume susceptibility of archive-half core samples, p. 206.

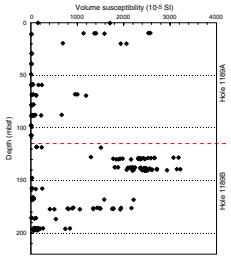

F131. Remanent intensity of archive-half core samples, p. 207.

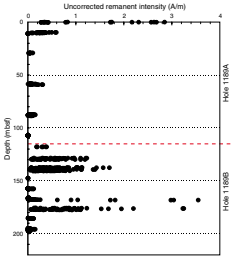

T22. Magnetic properties of minicores, p. 258.

T23. Anisotropy of magnetic susceptibility, p. 259.

F132. Magnetic susceptibility of minicore samples, p. 208.

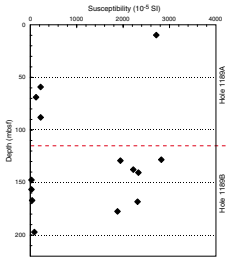

cores tend to be considerably lower at Site 1189 than at Site 1188, as is found in the values of the archive-half cores at Site 1189. Susceptibility values >0.01 are too high to be explained without the presence of a ferromagnetic mineral, because most paramagnetic minerals have lower magnetic susceptibilities (Collinson, 1983). As at Site 1188, there appears to be only a minor amount of anisotropy among the minicore samples from Site 1189. The maximum anisotropy (1.0877) was determined for Sample 193-1189B-11R-1, 64 cm, which is the minicore sample with the highest average susceptibility (0.028). Figure F133 is a Flinn-type diagram showing the lineation and foliation of the susceptibility ellipsoid. Sample 193-1189B-12R-1, 35 cm, which has a high lineation (0.081), also has a relatively high average susceptibility (0.022).

Figure F134 shows the NRM intensity measurements taken from the minicore samples at Site 1189. The only fresh dacite minicore from the upper 25 m of the profile is Sample 193-1189A-2R-1, 10 cm, which exhibits a remanent intensity of 1.55 A/m. This value is 45% lower than that of fresh dacite at Site 1188. There is a significant increase in the NRM intensity between 120 and 190 mbsf. This region of high intensity is separated by a zone of low intensity at 160 mbsf. The presence of a high NRM intensity region below 130 mbsf is similar to Site 1188. However, the intensity values are much lower than those of Site 1188. For example, Samples 193-1188A-17R-1, 109 cm (146.2 mbsf), and 17R-2, 30 cm (146.9 mbsf), have NRM intensities of 11.6 and 4.7 A/m, respectively, which are three to four times higher than the highest intensity samples measured from Site 1189. In addition, the peak intensity values at Site 1189 occur at greater depths (>160 mbsf) as compared to >140 at Site 1188.

Figure F135 shows a plot of inclination. In general, the inclination values of minicore samples are consistent with the present-day International Geomagnetic Reference Field Earth model, which predicts an inclination of –7.7° at Site 1189. However, there are several exceptions. Sample 193-1189A-10R-1, 76 cm, exhibits a high positive inclination of 87°. This sample piece is quite long (~25 cm) and it is highly unlikely that it was rotated during recovery or curation. Furthermore, a 180° rotation of the sample piece still would not explain its steep angle. Examination of this sample shows that it consists of brecciated pieces, and therefore, based on the observed inclination, it appears that this particular sample and possibly the whole unit has suffered some degree of deformation or rotation. Another notable exception is Sample 193-1189B-18R-2, 66 cm, from the very bottom of Hole 1189B. This sample shows a positive inclination of 27°. An examination of its demagnetization curve shows an irregular behavior during AF demagnetization (Fig. F136), which suggests that this sample is an amalgamation of materials that have different magnetic orientations. Sample 193-1189B-11R-2, 88 cm, is another exception. It has a steep negative inclination of –40°. This is again a very long piece (>22 cm), and it is unlikely that it was misoriented during curation.

IRM Measurement

Because of low recovery at Site 1189, we had time to conduct a few additional experiments that are not part of the standard ODP shipboard analyses. Monitoring the acquisition of isothermal remanent magnetization (IRM) is often used to distinguish between high-coercivity minerals such as hematite and low-coercivity minerals such as magnetite and titanomagnetite. Figures F137 and F138 show plots of IRM inten-

F133. Anisotropy of magnetic susceptibility, Holes 1189A and 1189B, p. 209.

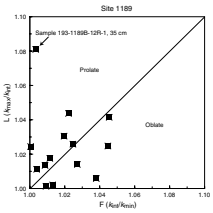

F134. Natural remanent magnetization intensity of minicore samples, p. 210.

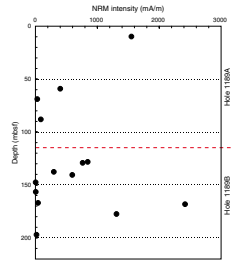

F135. Stable inclination of minicore samples, p. 211.

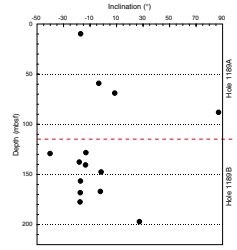

F136. Zijderveld plot and intensity-decay curve of sample with irregular demagnetization behavior, p. 212.

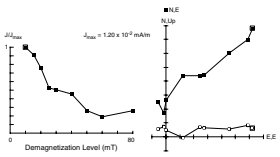

F137. Intensity of isothermal remanent magnetization, Hole 1189A, p. 213.

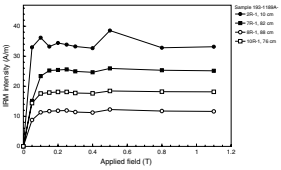

sity vs. applied impulse field for Holes 1189A and Hole 1189B, respectively. The field was applied at increasing steps of 50, 100, 150, 200, 250, 300, 400, 500, 800, and 1100 mT. As in Hole 1188A, the magnitude of saturation isothermal remanent magnetization (SIRM) correlates with that of the NRM.

In the case of Hole 1189A, all samples exhibit a steep rise in IRM acquisition within the first 200 mT (Fig. F137), which suggests that the dominant magnetic carriers are low-coercivity minerals. Sample 193-1189A-2R-1, 10 cm, shows a rather large fluctuation in IRM intensity. The high variability is caused by the shipboard magnetometer's inability to accurately measure intensity at high magnetization values.

The IRM curves from Hole 1189B are much more complex (Fig. F138). Samples from Sections 193-1189B-11R-1 through 12R-1, which have relatively high susceptibility and remanent intensity, all show very low coercivity. This complexity clearly contrasts with samples taken from cores in the upper part (Sections 193-1189A-2R-1 through 10R-1) of Hole 1189A. Core descriptions report the presence of magnetite in trace amounts in Cores 193-1189B-11R and 12R, consistent with the low-coercivity behavior. Sample 193-1189B-13R-1, 55 cm (148 mbsf), which has a much lower SIRM shows some stability in the IRM intensity values. It also shows a slightly higher coercivity (150–200 mT) than the samples above it. Core descriptions note a distinct lithology change between Cores 193-1189B-12R and 13R, the lower case being much more anhydrite rich and barren of Fe-Ti oxides. Samples 193-1189B-14R-1, 101 cm, and 15R-1, 87 cm, also have very low SIRM intensity and no magnetite reported in core descriptions. The alteration log for Sections 193-1189B-15R-2 and 16R-2 report the presence of trace amounts of magnetite, reflected in the low coercivity of the samples. Sample 192-1189B-18R-2, 66 cm, has a low SIRM value and similar characteristics as Samples 193-1189B-14R-1, 101 cm, and 15R-1, 87 cm; however, the description of the interval encompassing this sample reports the presence of magnetite. The discrete minicore sample likely intercepted a thin interval devoid of magnetite within the broader magnetite-bearing interval.

F138. Intensity of isothermal remanent magnetization, Hole 1189B, p. 214.

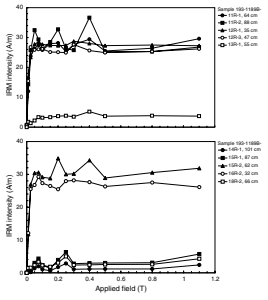

Thermal Demagnetization

Only two minicore samples from Hole 1189A were treated with thermal demagnetization and monitored for their magnetization intensity with increasing temperature. The two samples (Samples 193-1189A-7R-1, 82 cm, and 10R-1, 76 cm) that were already saturated from the previous IRM experiment were progressively heated up to 700°C, with smaller temperature intervals above 500°C. Figure F139 shows the variation in the intensity as a function of temperature. Sample 193-1189A-7R-1, 82 cm, shows a gradual decay in intensity between 100° and 500°C. This decay is followed by a sharper drop between 540° and 620°C. On the basis of the demagnetization curve, it appears that the dominant magnetic carrier is magnetite with a small contribution from titanomagnetite. In the case of Sample 193-1189A-10R-1, 76 cm, most of the magnetization intensity is lost gradually between 100° and 400°C. From 400° to 600°C, there is another gradual decay where the remaining intensity is lost. Our interpretation based on this demagnetization trend is that again magnetite and titanomagnetite are the two most probable magnetic carriers; however, the latter appears to be more dominant. Furthermore, the smooth decay in intensity of Sample 193-1189A-10R-1, 76 cm, suggests that the titanomagnetite may have been

F139. Thermal demagnetization of isothermal remanent magnetization, p. 215.

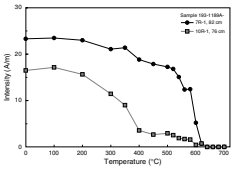

altered, in which case it may have been replaced by titanohematite. It is also possible that the complexity in the demagnetization curve is caused by impurities such as Mg, Al, Cu, V, and Si within the titanomagnetite (Thompson and Oldfield, 1986).

Discussion and Summary

Site 1189 has similar features as Site 1188. The uppermost sections of profiles at both sites are characterized by a zone of high susceptibility and high remanent intensity. The magnetic carriers in this zone consist primarily of magnetite and titanomagnetite. A second zone of high susceptibility and high remanent intensity occurs deeper in the section (below 130 mbsf). The low recovery at both sites makes it difficult to make a thorough comparison between the two zones. However, based on our analyses of the recovered cores, it appears that the deeper zone (below 130 mbsf) may contribute a significant component to the magnetic anomalies measured at sea level.

There are several notable differences between Sites 1188 and 1189. For instance, the susceptibility and remanent intensity are generally lower at Site 1189. Also, the peak magnetization intensity is deeper at Site 1189 than at Site 1188.

By examining the magnetic orientation of the minicore samples we were able to identify some sample pieces that may be have been deformed or rotated. In general, except for those pieces, the inclination value at Site 1189 is consistent with that predicted by the present-day Earth field but has a steeper angle.

DOWNHOLE MEASUREMENTS

Hole 1189B

Operations

On 25 December 2000, wireline logging operations in Hole 1189B began with the deployment of the high-temperature/pressure telemetry gamma-ray cartridge (HTGC) with real-time cable head temperature capabilities (MTEM). The water depth was estimated from pipe measurements at ~1693 mbrf, and the bottom of the hole was estimated at 206 mbsf. A casing string had been set to a depth of ~32 mbsf, so the drill pipe was placed at ~28 mbsf (see **"Return to Site 1189,"** p. 12, in "Operations Summary" in the "Leg 193 Summary" chapter). A wiper trip to the bottom of the hole was done ~8 hr before logging operations began, and several bridges were found in the bottommost 40 m of the hole. After the wiper trip, the bit was released at seafloor using the mechanical bit release (see **"Return to Site 1189,"** p. 12, in the "Operations Summary" in the "Leg 193 Summary" chapter), and the hole was reentered to begin logging operations.

The MTEM-HTGC tool string was deployed, and the wireline heave compensator was engaged by circumventing the ground fault interrupt switch as described in **"Downhole Measurements,"** p. 86, in the "Site 1188" chapter. This tool string was deployed first because of concerns with potentially high-temperature conditions as active venting was clearly observed while surveying the area. The tool reached a logging total depth (TD) of 198 mbsf, and on the way up, the tensiometer on the winch unit registered several thousand pounds of overpull at ~189

mbsf. The MTEM sensor recorded a high temperature of 47.8°C, therefore a WSTP deployment using the sand line was scheduled to a depth of 132 mbsf.

The second wireline deployment included the MTEM–hostile-environment natural gamma-ray sonde (HNGS)–accelerator porosity sonde-hostile-environment lithodensity sonde (HLDS)–dual induction resistivity (DIT)–tool string combination. A borehole restriction found at ~158 mbsf allowed the tool string to only reach 48 m from the bottom of the hole. The third tool string consisted of the MTEM–natural gamma-ray tool (NGT)–dipole sonic imager–FMS combination, and this run also achieved a logging TD of 158 mbsf. During the last two logging runs, heave measurements were recorded with the guideline tensiometer encoder (GTE) that was installed on the wireline heave compensator (WHC) for LWD operations. These records show <1-ft average heave for most of the second deployment and for the entire third logging run (Fig. **F140**).

Borehole Conditions and Data Quality

The average dimensions of Hole 1189B are good for the acquisition of high-resolution logging data as the hole diameter decreases from 14.7 in at the top to 10 in toward the bottom. The average hole diameter measurements obtained with the two-arm FMS calipers are 12.0 and 12.5 in. The difference between measurements is most likely caused by a slightly elliptical borehole between 40 and 80 mbsf and also between 90 and 100 mbsf (Fig. **F141**). The only significant borehole enlargement (apart from cavitation below the end of casing; 36–41 mbsf) was present at 133 mbsf, and it affects all measurements (Fig. **F141**).

Electrical Resistivity Measurements

Similar to the results from Holes 1188B and 1188F, electrical resistivity measurements are low. The deep resistivity values range between 0.1 and 2.8 Ωm, and the medium resistivities are between 0.06 and 6.4 Ωm. The shallow resistivity curve shows isolated peaks with extremely high measurements up to 101 Ωm. Although these peaks tend to correlate with the other resistivity measurements, they may be erroneous. A different induction tool was used in Hole 1189B than the one deployed in Hole 1188F that showed similar results with the medium resistivity curve. Overall, electrical resistivity measurements show cyclic patterns with increasing resistivity with depth between 67 and 122 mbsf (Fig. **F141**).

Natural Radioactivity Measurements

Gamma-ray measurements in Hole 1189B were obtained with HTGC, HNGS, and NGT. The gamma-ray curves show good correlation, only the values measured with the HNGS are slightly higher than those measured with the NGT. The major difference between these tools is that the HNGS uses bismuth germanate scintillation crystals that provide significantly better spectral response because of their enhanced ability to stop gamma rays and convert their energy to full amplitude signals. In addition, the HNGS curves are corrected for hole size during recording. These differences may explain the discrepancy in the magnitude of the signals recorded by the different tools. In Figure **F141**, only the measurements from the HNGS are displayed for simplicity.

F140. Heave records for the second and third wireline logging runs, Hole 1189B, p. 216.

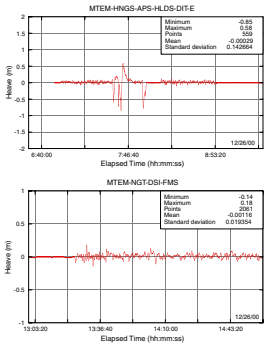

F141. Downhole wireline logs, Hole 1189B, p. 217.

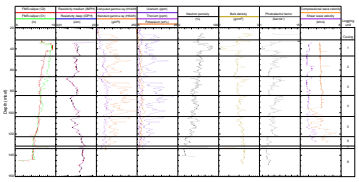

Total gamma-ray counts in the open hole vary between 37 and 249 gAPI. Uranium measurements range from 2.5 to 22.5 ppm, thorium from 0.3 to 4.6 ppm, and potassium from 0.6 to 5.5 wt%. Correlation between the total gamma-ray readings and the uranium content is much stronger than between the total gamma-ray and potassium content. Thus, uranium makes a large contribution to the total gamma-ray spectrum of Hole 1189B.

Neutron Porosity and Density Measurements

Neutron porosities vary from 12% to ~100% with an average value of 50.7%. The largest values are observed below the casing where the tool stand off is the greatest (Fig. F141). The neutron porosity log shows a steady downward decrease that may be related to a decrease in hole diameter (Fig. F141). A sharp increase in neutron porosity over a few meters is also present at 133 mbsf, where an enlargement of the borehole was observed in the caliper readings.

Density values range from 1.1 to 2.6 g/cm^3 with a mean value of 2.0 g/cm^3. The density values show a slight increase with depth, which might be caused by a decrease in hole diameter. The density log also shows a sharp decrease at the borehole enlargement at 133 mbsf. The photoelectric factor log shows variations between 1.8 and 10.5 barn/e$^-$. The photoelectric factor also shows cyclic trends between 67 and 104 mbsf that are opposite to those observed in the electrical resistivity measurements (Fig. F141).

Sonic Velocity Measurements

The compressional and shear wave velocity curves were derived using a slowness time coherence technique on the recorded waveforms. This process was performed on board with the Schlumberger Multitask Acquisition and Imaging System (MAXIS) in near-real time during the logging operation. The data from this hole have several invalid intervals and should, therefore, be used as a qualitative data set. For simplicity and clarity of presentation, the invalid intervals were excluded from plots presented in this chapter (Fig. F141).

Compressional wave velocity values range from 1.9 to 5.6 km/s, and shear wave velocity values show variations from 1.7 to 3.5 km/s. Overall, compressional wave velocities show a steady increase from below the casing to an approximate depth of 95.4 mbsf (Fig. F141). Below this depth, there is an abrupt decrease in compressional wave velocities followed by a general increasing trend with depth. The abrupt decrease in velocity correlates only with high values in uranium and may be representative of either tool malfunction or inadequate processing because of a low energy transmission interval. The shear wave profile shows a subtler increasing trend with depth, with several high velocity values generally correlating with highs in density and photoelectric factor and low values of porosity.

Temperature Measurements

Temperature measurements were obtained in Hole 1189B with the MTEM sensor during every wireline run (Fig. F142). As in Hole 1188F, all the temperature curves show similar patterns inside the drill pipe and at the transition between casing and the open hole. The first run shows signs of drilling disturbances as the temperature profile varies

F142. Temperature records obtained with the wireline cable sensor during all the logging runs, Hole 1189B, p. 218.

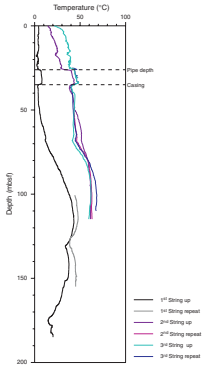

significantly with depth. A low temperature recorded at 60 mbsf (<10°C) is followed by a steady temperature increase down to 115 mbsf (~43°C) and alternating decreasing and increasing trends until the bottom of the hole. The temperature measurements from the later logging runs show significantly higher temperature patterns. The maximum temperature recorded in Hole 1189B is 68°C, measured during the second pass of the last tool deployment at an approximate depth of 107 mbsf. The time elapsed between the first and the last temperature measurement was ~15 hr.

A WSTP temperature measurement was obtained at a depth of 132 mbsf. The record shows that the tool descended to the selected depth for a 15-min station; however, the valve opened prematurely (Fig. F143). A water sample was still collected as the check valve and coils contained warm fluids (see "Geochemistry," p. 46). The short temperature record at this depth shows nearly isothermal temperatures with an average value of 54.5°C.

Formation Evaluation

Eight logging units were identified in Hole 1189B (Fig. F143). Logging Unit 1 is a transitional unit at the top of the logged interval, whereas cyclic trends in the electrical resistivity and/or photoelectric factor curves define logging Units 2 through 4. Several small intervals in these units show high density and photoelectric factor values that correlate with low electrical resistivities. These responses may be indicative of higher concentrations of sulfides. Logging Unit 5 shows a downward increasing trend in electrical resistivity that may indicate a change in alteration. Logging Units 6 and 8 are characterized by uniform log responses in the electrical resistivity, neutron porosity, density, and photoelectric factor logs. Logging Unit 7 corresponds to the small interval with an enlarged section of the borehole causing the electrical resistivities, gamma ray, density, and photoelectric factor log responses to decrease and the neutron porosity to increase. This logging unit represents a highly fractured interval or a fault zone. Apart from logging Unit 7, the logging units do not show any apparent correlation with the natural radioactivity logs.

FMS Images

FMS images show significant changes with depth in the styles of alteration and fracture density. Below casing, the images show that the upper part of the borehole (Fig. F144) contains a higher concentration of disseminated conductive minerals than the lower sections. These conductive minerals seem to correlate to the higher concentrations of sulfides found in the recovered cores. Changes in alteration, such as the transition between logging Units 2 and 3, are also prominent features in the FMS images (Fig. F145). The changes in resistivity of logging Unit 6 are characterized by distinctive conductive layers that are interbedded with more resistive and foliated units (Fig. F146).

The bottom of the logged interval shows completely different features as the images show a more resistive and fractured unit that tends to correspond to the less altered cores of Hole 1189B. A series of steep fractures comprising a 3-m-thick interval correlate with logging Unit 7 (Fig. F147). This zone may correspond to a faulted interval. Below this zone, the images are characterized by a series of subhorizontal and subvertical fractures (Fig. F148).

F143. WSTP temperature record of a deployment to 132 mbsf, Hole 1189B, p. 219.

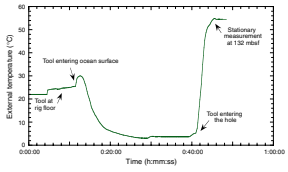

F144. FMS images of the topmost logged section of Hole 1189B showing the presence of conductive minerals, p. 220.

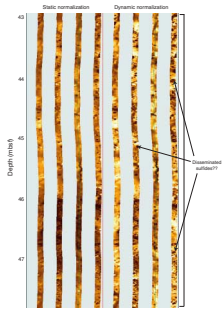

F145. A change in alteration as seen in the FMS images, Hole 1189B, p. 221.

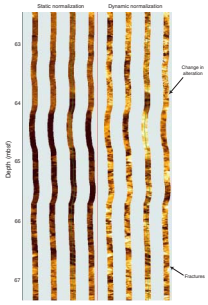

F146. Alternating conductive and resistive thin and shallowly dipping units, Hole 1189B, p. 222.

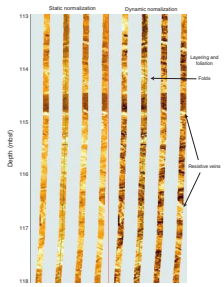

Hole 1189C

Operations

LWD/RAB operations in Hole 1189C began on 28 December 2000, and were terminated on 29 December 2000, after reaching a depth of 166 mbsf. The water depth was estimated at 1700 mbrf and drilling operations were done with a 9.875-in bit. The RAB BHA was changed from the previous configuration to contain one monel (nonmagnetic) sub above the tool and two below. This was done to isolate the tool from potential changes in magnetization of the BHA because of the presence of magnetic minerals in the formation. A sampling rate of 10 s was used for the LWD operations.

After drilling Hole 1189C, additional logging operations were planned to establish a direct comparison between LWD and wireline measurements and for facilitating the interpretation of the subsurface stratigraphy. The ultra-high-temperature multisensor memory tool (UHT-MSM) temperature probe was deployed first because the MTEM sensor that was previously used in other holes was not working after the last deployment in Hole 1188F. The UHT-MSM deployment found a hole obstruction at 71 mbsf and recorded a maximum temperature of 45°C, hence, wireline deployments of the HNGS-HLDS-DIT-E and NGT-FMS tool string combinations followed. The bottom of the drill pipe was placed at 10 mbsf, and both tool strings logged an interval ranging from 10 to 67 mbsf.

Borehole Conditions and Data Quality

During the two logging runs, heave measurements were recorded with the GTE that was installed on the WHC for LWD operations. These records show a high of ~1 m heave during the first deployment and a high of ~1.5 m motion for the second run (Fig. **F149**). The upper 70 m of Hole 1189C is irregular, and measurements from the FMS calipers show an average diameter of 13.5 in (Fig. **F150**). Below 50 mbsf, there are several small isolated zones where the FMS calipers were close to being fully extended. Borehole sections between 44 and 49 mbsf, as well as between 22 and 29 mbsf, are also close to reaching the maximum aperture of FMS calipers. A section between 17.5 and 21 mbsf shows a divergence in caliper readings because an obstruction that was encountered in every logging run.

Electrical Resistivity Measurements

Electrical resistivity measurements made in Hole 1189C show the same range of low values that were observed in other holes drilled in the Manus basin (Fig. **F150**). The deep resistivity values obtained with the DIT-E range from 0.8 to 2.6 Ωm. Medium and shallow resistivity measurements range from 0.7 to 3.2 Ωm and from 0.6 to 6.0 Ωm, respectively. RAB measurements show similar responses over most of the overlapped section with a few localized zones that show slightly higher maximum values (Fig. **F150**). Below 80 mbsf, the RAB measurements show a few peaks that correlate with lows in the gamma-ray curves. The LWD maximum resistivity values are 15.1 Ωm for the ring measurement (R_{RING}) and 14.3 Ωm for the medium button measurement (R_{BM}).

F147. Steep fractures in a potentially faulted zone, Hole 1189B, p. 223.

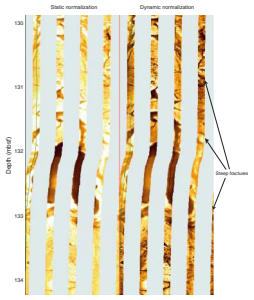

F148. FMS images showing the bottom of the logged interval, Hole 1189B, p. 224.

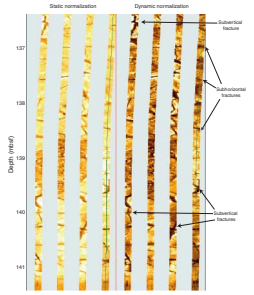

F149. Heave records for the two wireline runs made at Hole 1189C, p. 225.

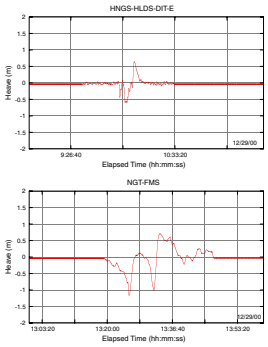

F150. Wireline and LWD logs for Hole 1189C, p. 226.

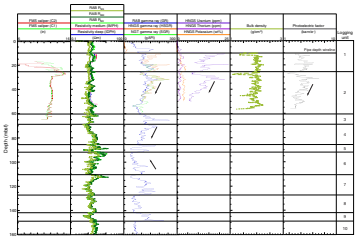

Natural Radioactivity Measurements

Total gamma-ray counts obtained with the HNGS over the 10- to 50-mbsf interval range between 90 and 258 gAPI with an average value of 148 gAPI (Fig. F150). The values obtained with the NGT over the 12- to 59-mbsf interval range from 18 to 253 gAPI with a mean value of 116 gAPI. Potassium values range from 0.6 to 4.3 wt% with an average of 2.7 wt%, whereas thorium and uranium values range from 0.2 to 3.6 ppm (average = ~1.4 ppm) and from 5.8 to 24.3 ppm (average = ~12.0 ppm), respectively. As in previous holes, there is a good correlation between the total gamma-ray and the uranium logs suggesting that, at least between 20 and 55 mbsf, uranium makes the largest contribution to the total gamma-ray spectrum.

Total gamma-ray values recorded with the RAB between the seafloor and 161 mbsf range from 13.2 to 257 gAPI (Fig. F150). The average value is 96.7 gAPI. Good agreement exists between the total gamma-ray measurements from wireline and LWD measurements in the overlapping interval. Total gamma-ray values show downward decreasing trends between 28 and 55 mbsf and between 64 and 80 mbsf and an upward decreasing trend between 86 and 105 mbsf.

Density Measurements

Density values measured during wireline operation between 10 and 56 mbsf are low. Values vary between 1.1 and 2.2 g/cm^3 with an average value of 1.9 g/cm^3 (Fig. F150). Measurements of the photoelectric factor range from 1.8 to 7.6 barn/e$^-$ with a mean value of 4.0 barn/e$^-$ (Fig. F150). The photoelectric factor log shows a downward decreasing trend between 28 and 50 mbsf similar to the one observed in the gamma-ray log.

Temperature Measurements

The UHT-MSM temperature probe was deployed prior to the wireline operations to determine the temperature conditions of Hole 1188C. The probe measured a maximum temperature of 46°C at the bottom of the hole (Fig. F151). A steep thermal gradient of 1°–2°C/m was estimated from the up and down logs from seafloor to ~13 mbsf. A gentler thermal gradient of 0.3°C/m was estimated from 13 to 55 mbsf.

F151. Temperature and pressure records for the temperature log obtained with the UHT-MSM probe in Hole 1189C, p. 227.

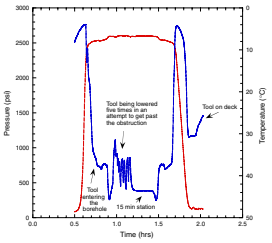

Formation Evaluation

The wireline logging data and logs from the RAB tool were used to identify 10 logging units (Fig. F150). Although logging Units 1 and 2 can be partly characterized using the full suite of logs obtained in Hole 1189C, the distinction of logging Units 3 through 10 is solely based on the resistivity and gamma-ray measurements from the RAB tool.

Logging Unit 1 represents the transition from the seafloor to a depth of 20 mbsf. This unit shows a rapid increase in gamma-ray values followed by several prominent highs and lows (Fig. F150). Logging Unit 2 is characterized by a decreasing trend with depth in the gamma-ray and photoelectric effect curves. Near the top of this unit, there is a gamma-ray high that corresponds to higher concentrations in uranium (Fig. F150) similar to those observed in previous holes. Logging Units 3 and 5 are represented by high gamma-ray values. The gamma-ray values measured in logging Unit 3 are the highest values recorded in the upper

166 m of Hole 1189C, but only slightly higher than those observed near the top of logging Unit 2 (Fig. F150).

Logging Units 4 and 6 represent opposite trends in the gamma-ray and resistivity curves. Logging Unit 4 shows a decreasing trend with depth in gamma-ray values that correlates with an opposite trend in the electrical resistivity profiles. Logging Unit 6 shows similar correlation between the two curves, but with downward increasing gamma-ray counts and higher resistivity values at shallower depths (Fig. F150). Logging Units 7 through 10 represent a sequence of alternating layers with high and low gamma-ray values.

RAB and FMS Images

Borehole images show that most of Hole 1189C is characterized by subhorizontal and subvertical fracturing as well as alternating numerous resistive and conductive features. RAB images from 46 to ~60 mbsf show a series of conductive subhorizontal features that seem to represent fractures (Fig. F152). This section also displays a significant vertical to subvertical resistive feature from 46 to 51 mbsf and a dipping resistive unit resembling a vein at 51 mbsf. Below this depth, a series of patchy resistive features are also prominent. A RAB section from 76 to ~90 mbsf also shows similar features resembling subhorizontal fractures and nearly vertical resistive features (Fig. F153). A comparison between RAB and FMS images shows good agreement with some of the larger features (Fig. F154). Although the FMS displays higher resolution and definition of structural features, fractures are clearly identified in both sets of images. However, the resistive units are not as clear in the FMS logs, perhaps because of the lower coverage of the borehole provided by the wireline tool.

F152. RAB static and dynamic images of Hole 1189C showing subhorizontal fractures and various resistive features, p. 228.

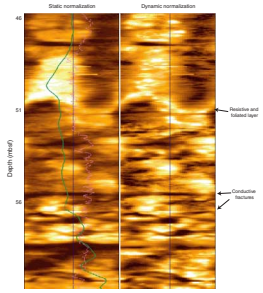

F153. RAB images showing a deeper section with more resistive features and conductive fractures, Hole 1189C, p. 229.

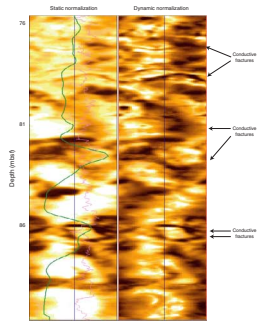

F154. Comparison between RAB and FMS images in Hole 1189C, p. 230.

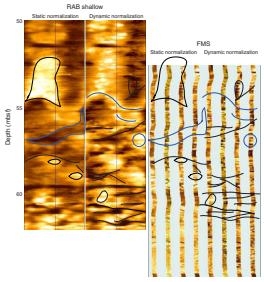

REFERENCES

Bischoff, J.L., and Seyfried, W.E., 1978. Hydrothermal chemistry of seawater from 25°C to 350°C. *Am. J. Sci.,* 278:838–860.

Bortnikov, N.S., Genkin, A.D., Dobrovolskaya, M.G., Muravitskaya, G.N., and Filimonova, A.A., 1991. The nature of chalcopyrite inclusions in sphalerite: exsolution, coprecipitation or "disease"? *Econ. Geol.,* 86:1070–1082.

Collinson, D.W., 1983. *Methods in Rock Magnetism and Palaeomagnetism: Techniques and Instrumentation:* London (Chapman and Hall).

Corbett, G.J., and Leach T.M., 1998. *Southwest Pacific Rim Gold-Copper Systems: Structure, Alteration, and Mineralization*. Spec. Publ.—Soc. Econ. Geol., 6.

Deer, W.A., Howie, R.A., and Zussman, J., 1992. *An Introduction to the Rock-Forming Minerals* (2nd ed.): New York (John Wiley & Sons).

Douville, E., Bienvenu, P., Charlou, J.L., Donval, J.P., Fouquet, Y., Appriou, P., and Gamo, T., 1999. Yttrium and rare earth elements in fluids from various deep-sea hydrothermal systems. *Geochim. Cosmochim. Acta,* 63:627–643.

Ixer, A., 1990. *Atlas of Opaque and Ore Minerals in Their Associations:* New York (Van Nostrand Reinhold).

MacDonald, G.J.F., 1953. Anhydrite-gypsum equilibrium relationships. *Am. J. Sci.,* 251:884–898.

McPhie, J., Doyle, M., and Allen, R., 1993. *Volcanic Textures: A Guide to the Interpretation of Textures in Volcanic Rocks:* Hobart (Tasmanian Govt. Printing Office).

Nagase, T., and Kojima, S., 1997. An SEM examination of the chalcopyrite disease texture and its genetic implications. *Mineral. Mag.,* 61:89–97.

Thompson, R., and Oldfield, F., 1986. *Environmental Magnetism:* London (Allen and Unwin).

Wilkin, R.T., and Barnes, H.L., 1997. Formation processes of framboidal pyrite. *Geochim. Cosmochim. Acta,* 61:323–339.

Williams, H., Turner, F.J., and Gilbert, C.M., 1982. *Petrography: An Introduction to the Study of Rocks in Thin Sections* (2nd ed.): New York (Freeman).

Figure F1. Hole locations for Sites 1189 and 1190. Shaded area around Site 1189 (Roman Ruins) = the approximate area of outcrop of chimney structures mapped by submersible and camera tow.

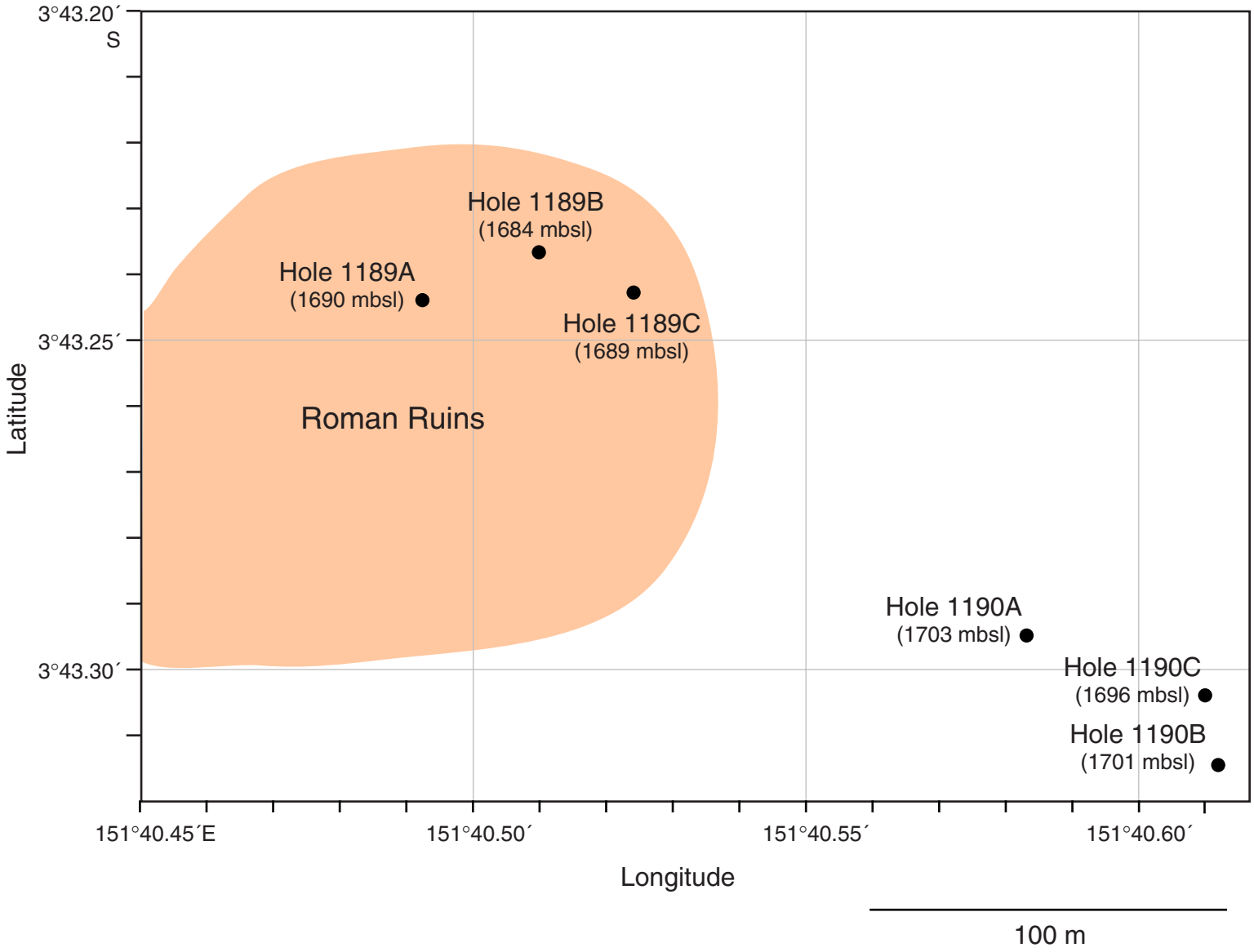

Figure F2. Graphic summary log for Hole 1189A showing the lithologic characteristics of the various units including alteration. See Figure F6, p. 45, in the "Explanatory Notes" chapter for the lithologic key.

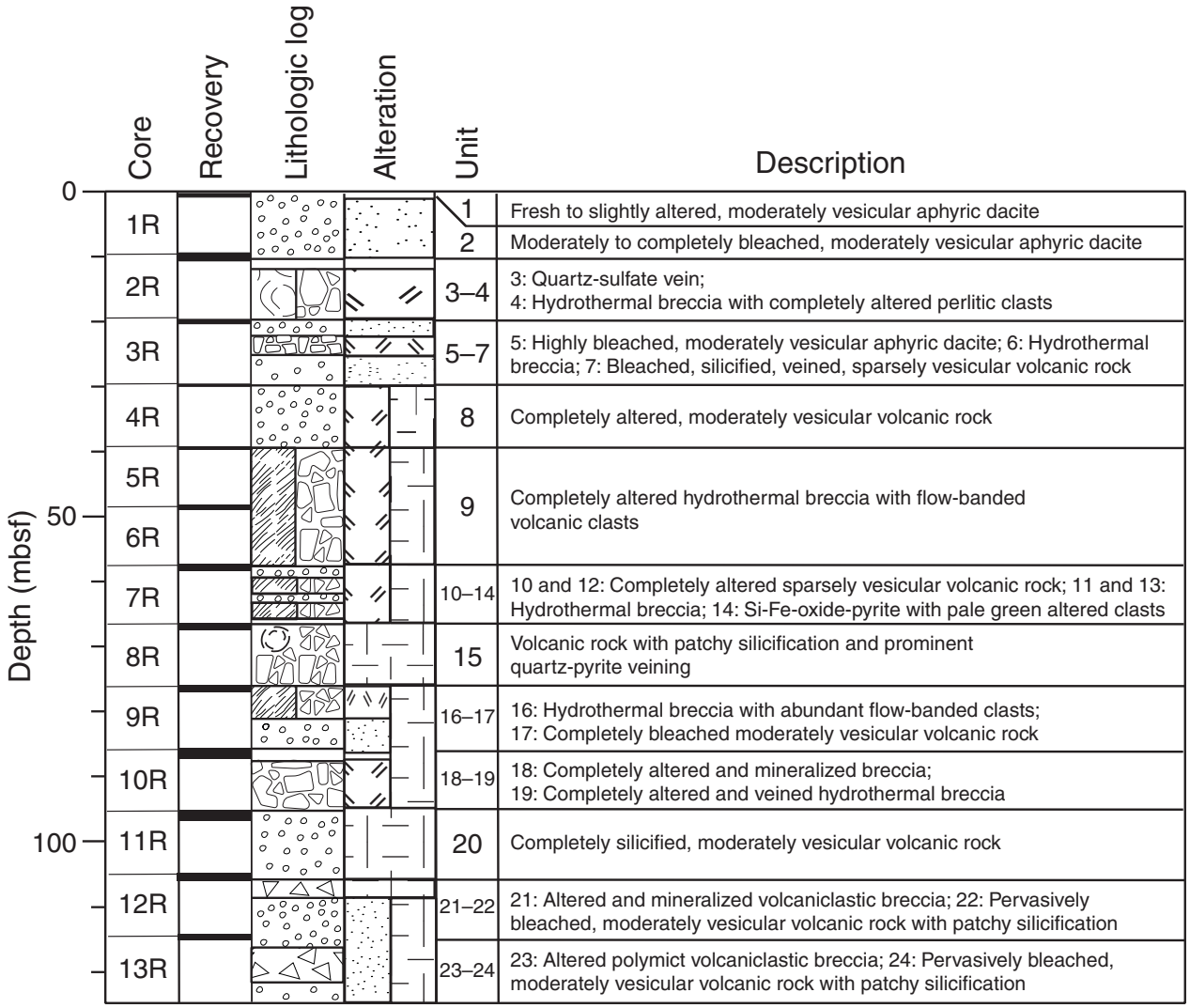

Figure F3. Hand specimen of hydrothermal breccia with completely altered volcanic fragments in an anhydrite-silica-pyrite stockwork matrix. Note the different colors and the sharp boundaries of the fragments (cf. Fig. F102, p. 172) (Unit 4; Sample 193-1189A-2R-1 [Piece 16, 118–126 cm]).

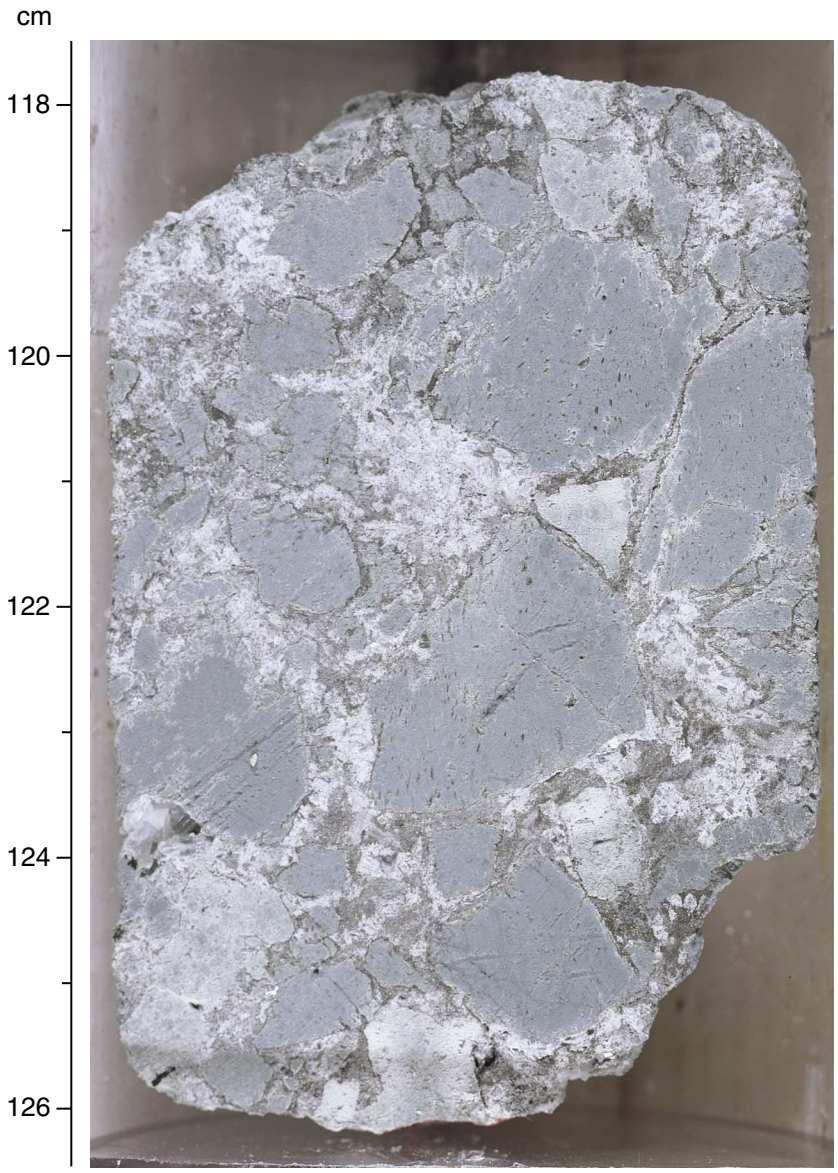

Figure F4. Some volcanic fragments in Unit 4 show perlitic groundmass texture. In thin section, arcuate, intersecting perlitic cracks are well-preserved. Perlitic groundmass domains are separated by linear to irregular fractures and arranged in a jigsaw-fit pattern (Sample 193-1189A-2R-1 [Piece 15, 113–115 cm]; width of view = 2.75 mm. Photomicrograph ID# 1189A_13; **thin section 33**).

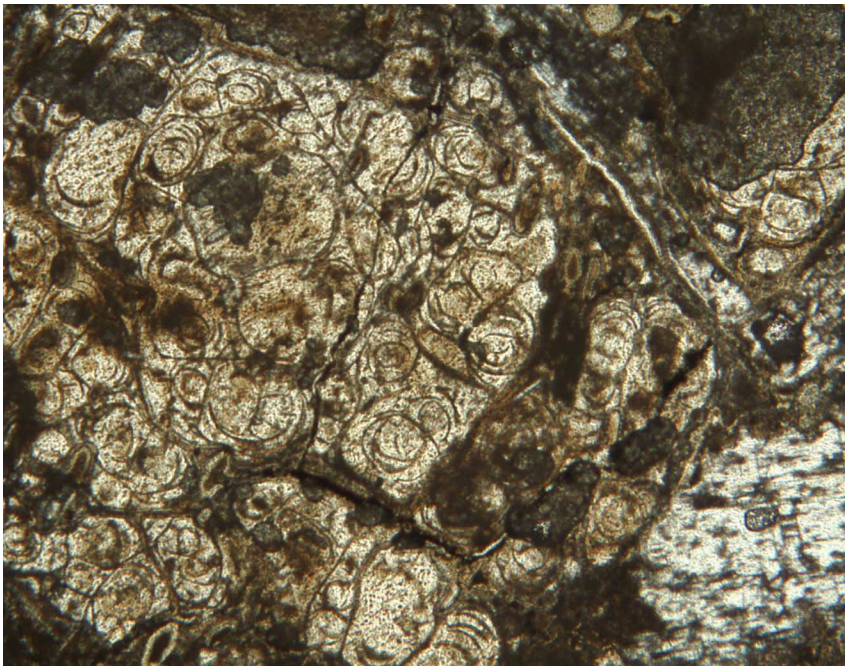

Figure F5. The groundmass of Unit 5 is rich in plagioclase microlites showing a pilotaxitic texture. Vesicles are abundant and typically partially filled with silica, zeolite, and/or anhydrite. Here, a radiating crystal aggregate of zeolite is attached to the inner surface of a vesicle and covered by a thin lining of opaline silica (Sample 193-1189A-3R-1 [Piece 2, 6–10 cm]; width of view = 1.38 mm. Photomicrograph ID# 1189A_12; **thin section 32**).

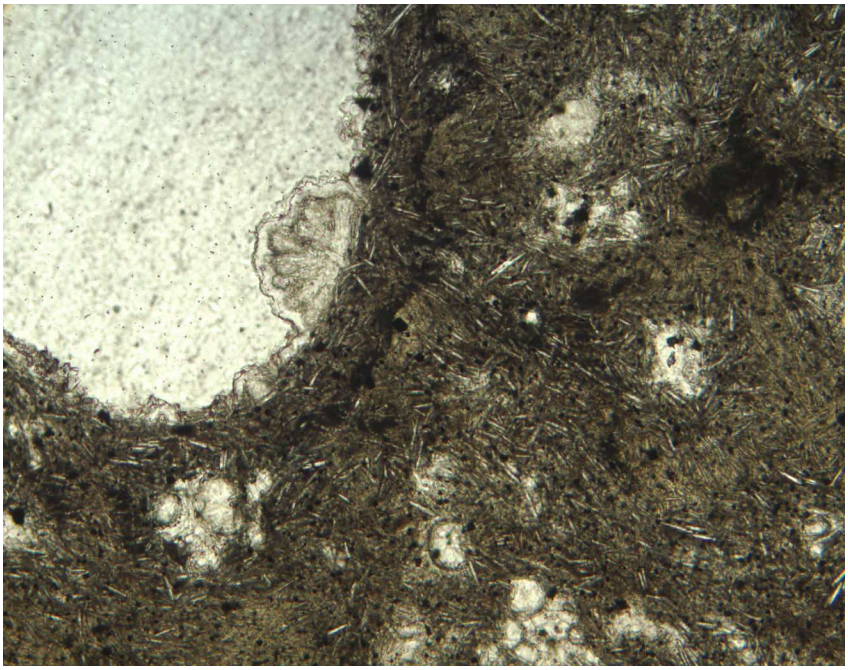

Figure F6. Flow banding is preserved in white to light gray silica-clay–rich fragments in Unit 9 (hydrothermal breccia) (Sample 193-1189A-5R-1 [Piece 7, 42–51 cm]). **A.** Close-up photograph of hand specimen. **B.** Line drawing of hand specimen.

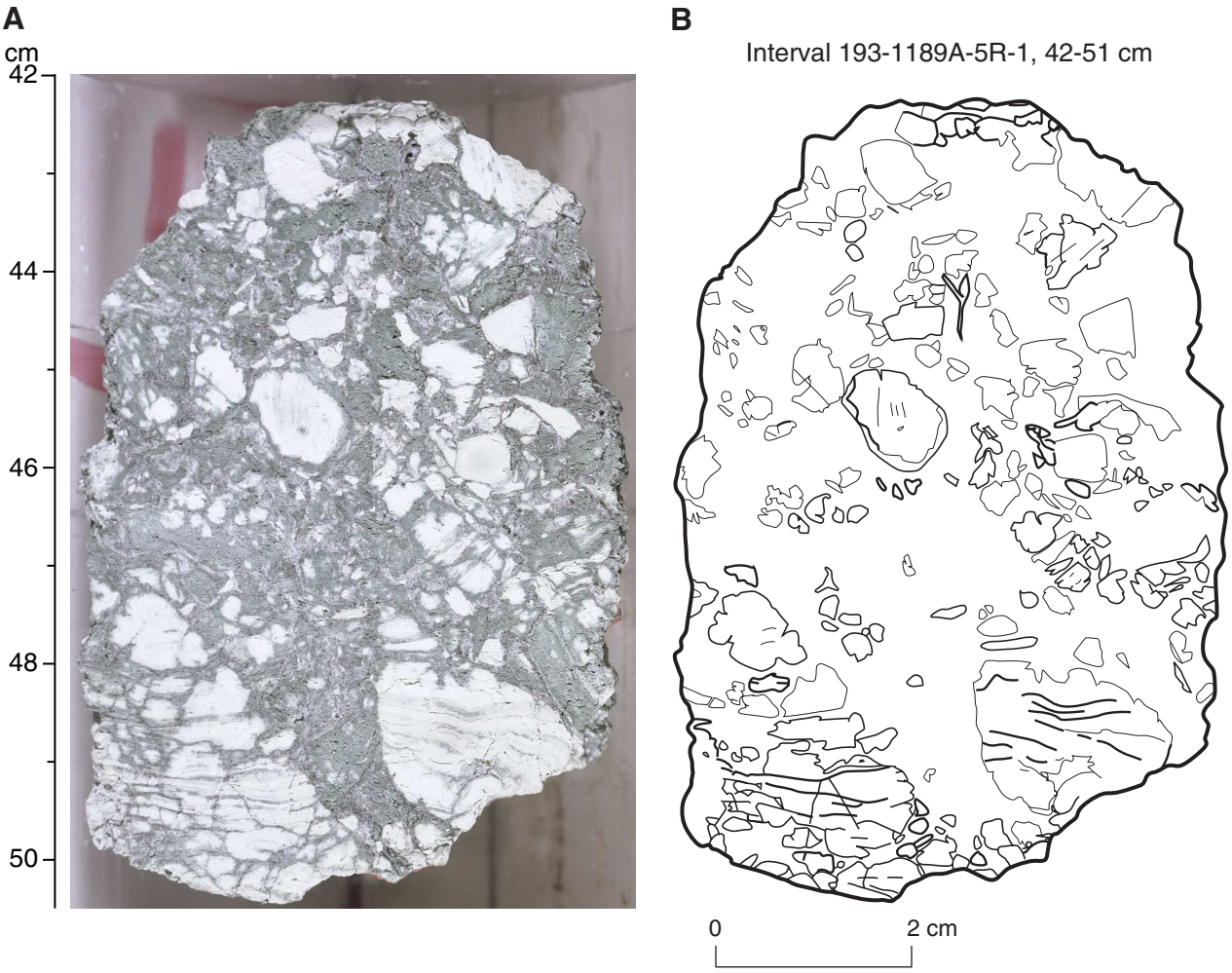

Figure F7. Hand specimen of Unit 15, a plagioclase-rich, poikiloblastically silicified volcanic rock showing a fine network of quartz-pyrite veining and associated jigsaw-fit breccia textures (Sample 193-1189A-8R-1 [Piece 14, 85–93 cm]).

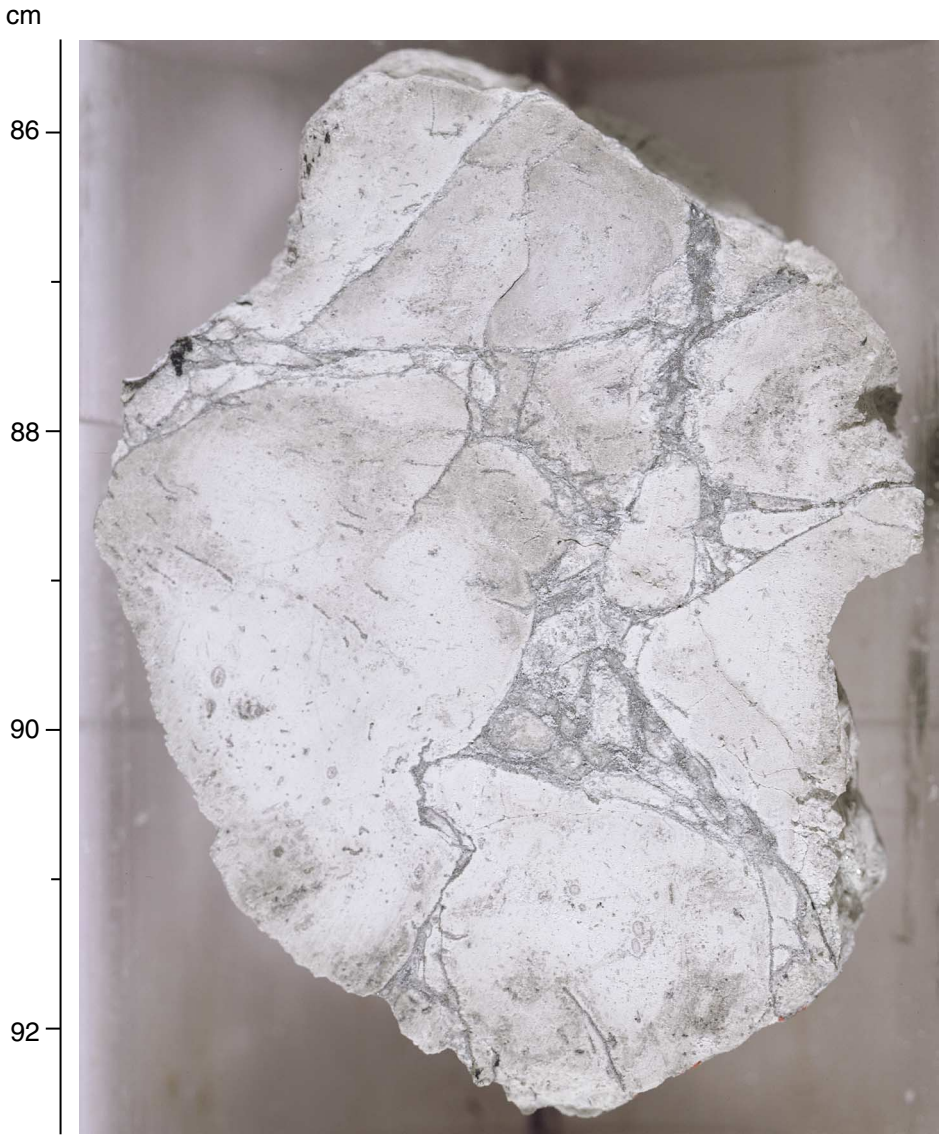

Figure F8. Flow-banded volcanic fragments in hydrothermal breccia (Unit 16; Sample 193-1189A-9R-1 [Piece 4, 17–27 cm]). The variable orientations of the internal laminar texture of adjacent fragments indicates that the fragments have been moved relative to each other (see arrow). **A.** Close-up photograph of hand specimen. **B.** Line drawing of hand specimen.

Figure F9. Flow-banded volcanic fragments in hydrothermal breccia (Unit 16; Sample 193-1189A-9R-1 [Piece 12, 77–85 cm]). Adjacent fragments have internal laminar textures showing variable orientations (see arrows). This indicates that the fragments have been rotated relative to each other. **A.** Close-up photograph of hand specimen. **B.** Line drawing of hand specimen.

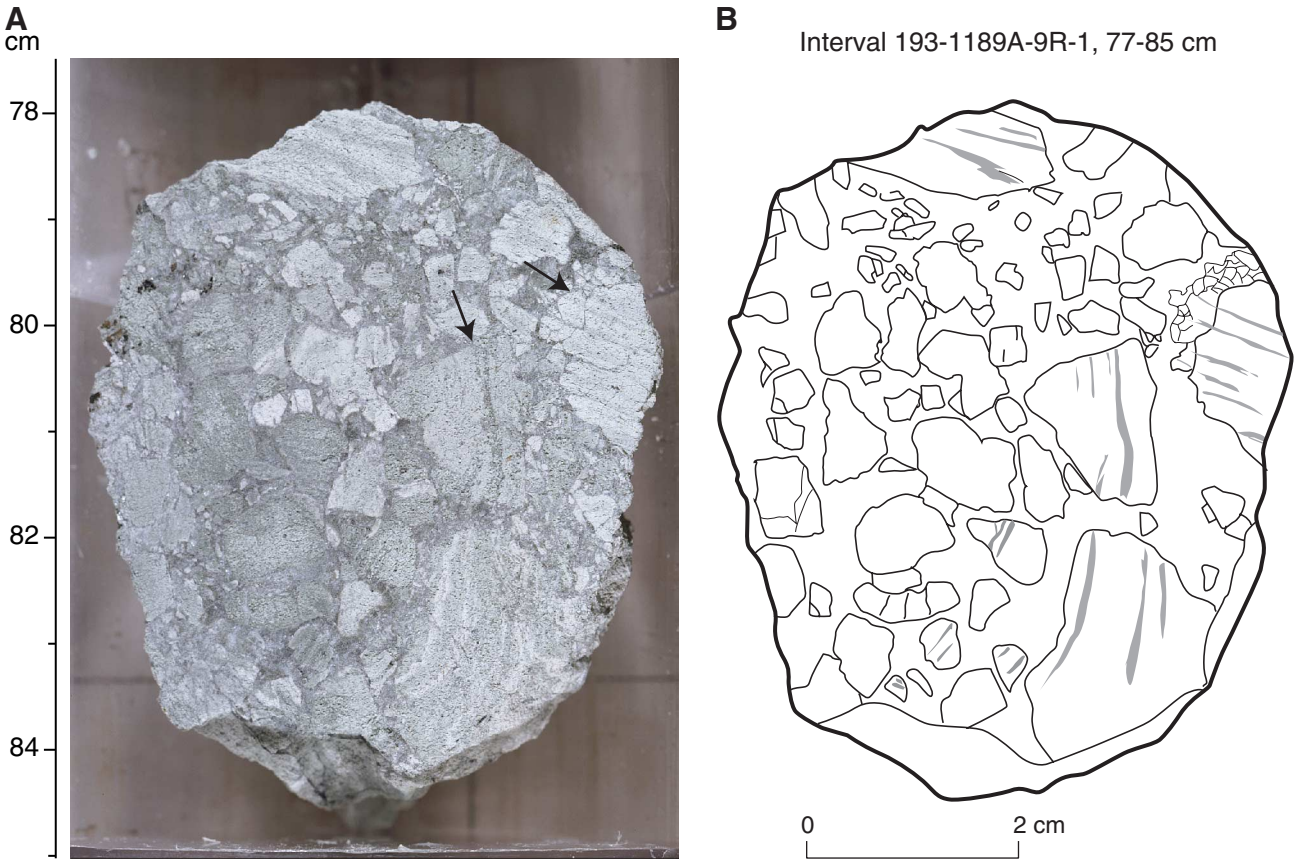

Figure F10. Jigsaw-fit texture in hydrothermal breccia with pervasive silica-clay alteration overprinted by silicification (Unit 19). Silicification is particularly prominent in the halos along the quartz-anhydrite-pyrite veins (Sample 193-1189A-10R-1 [Piece 9, 66–88 cm]). **A.** Close-up photograph of hand specimen. **B.** Line drawing of hand specimen. The shading highlights kernels of rock that have been least affected by silicification introduced along the quartz-anhydrite-pyrite vein set. (**Figure shown on next page.**)

Figure F10 (continued). (Caption shown on previous page.)

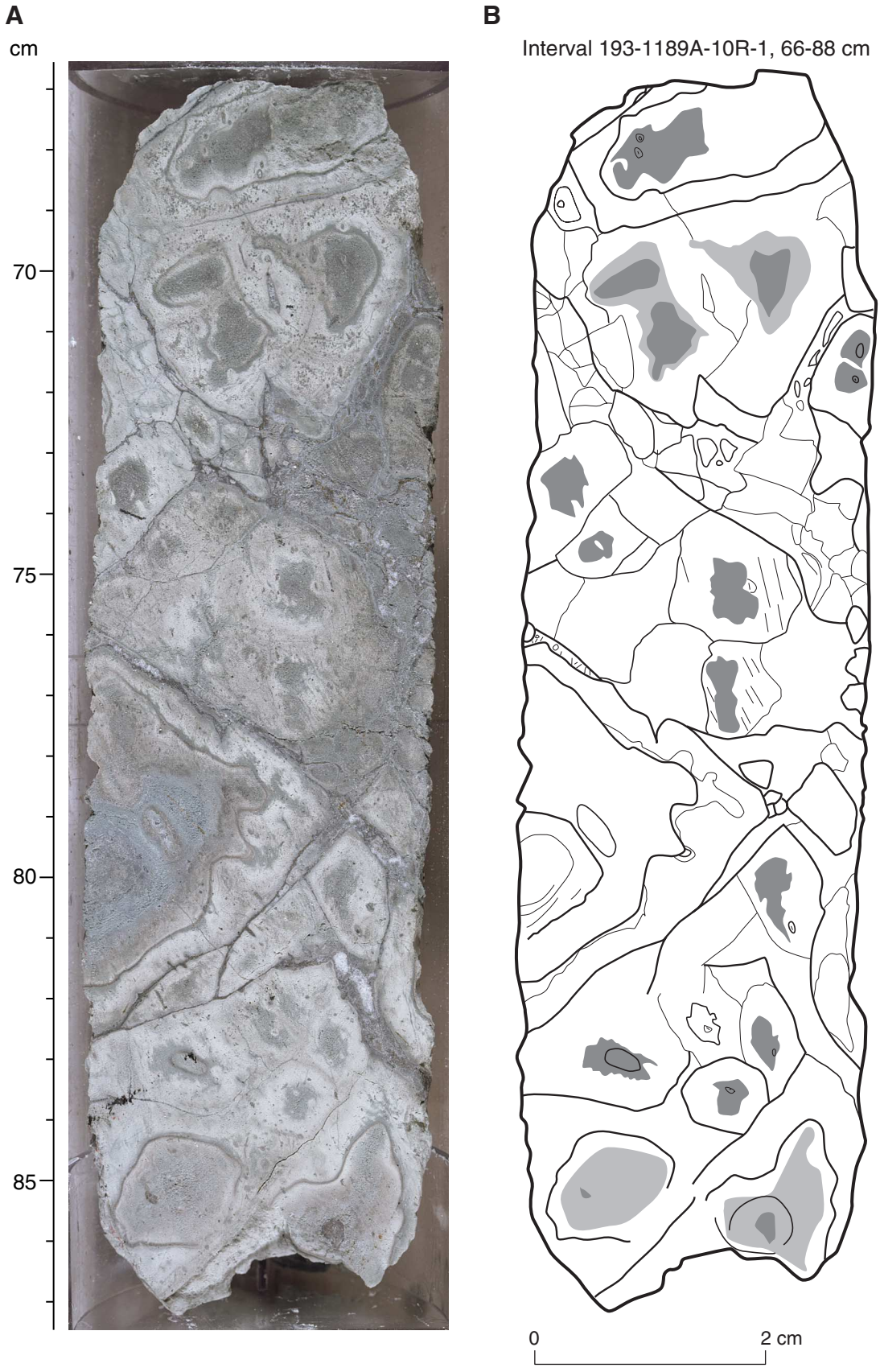

Figure F11. Unit 21 consists of a single piece of semimassive sulfide with abundant, angular, blocky to wispy volcanic clasts (Sample 193-1189A-12R-1 [Piece 16, 120–128 cm]). **A.** Close-up photograph of hand specimen. (Continued on next page.)

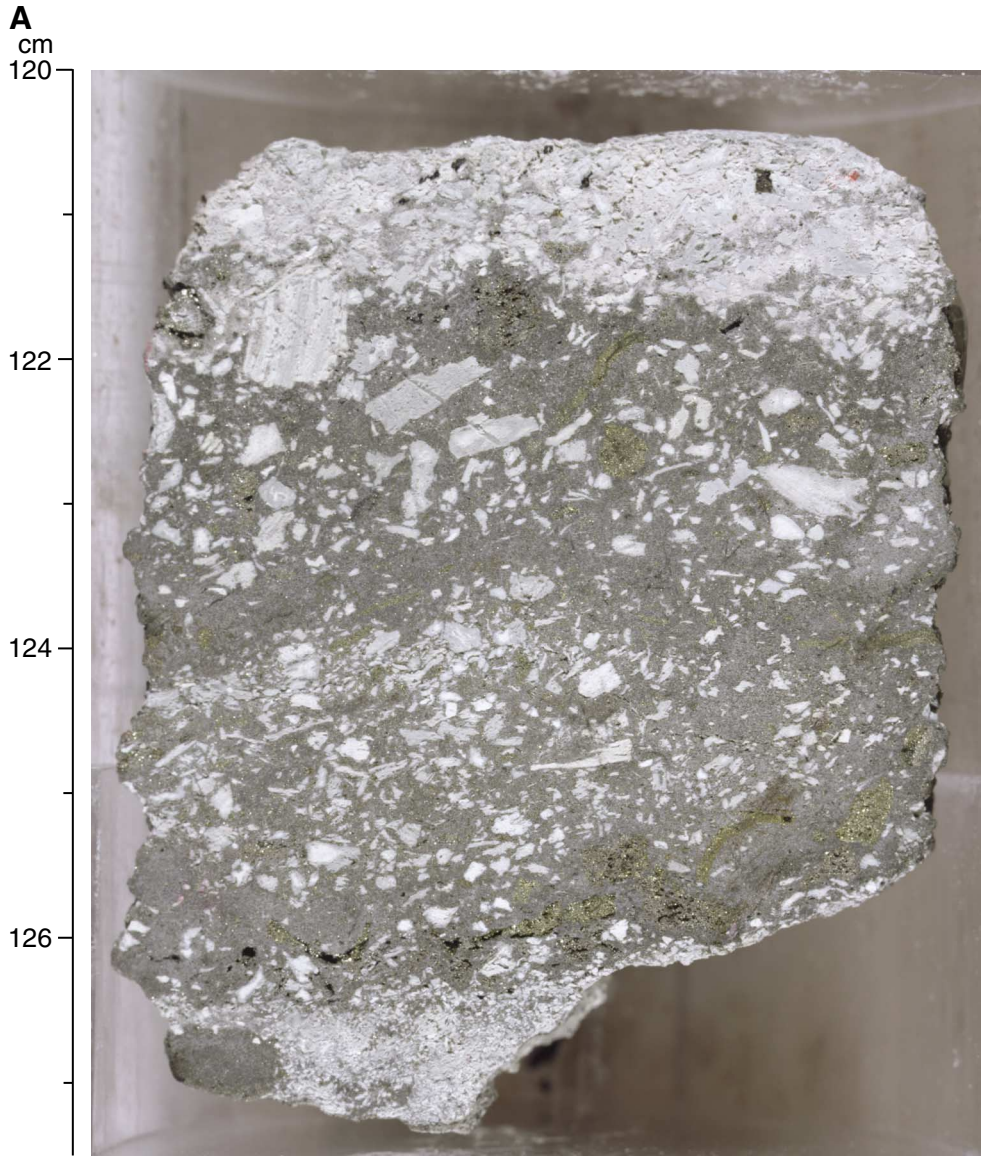

Figure F11 (continued). B. Line drawing of hand specimen. Highlighted areas denote possible clasts of chalcopyrite-bearing sulfide.

Figure F12. Volcanic clasts with fibrous, laminar internal texture are abundant in thin section of the sulfide-rich Unit 21. These delicate internal textures (arrow) are interpreted as the remnants of tube pumice vesicles (Sample 193-1189A-12R-1 [Piece 16, 122–126 cm]; width of view = 1.38 mm. Photomicrograph ID# 1189A_76; **thin section 42**).

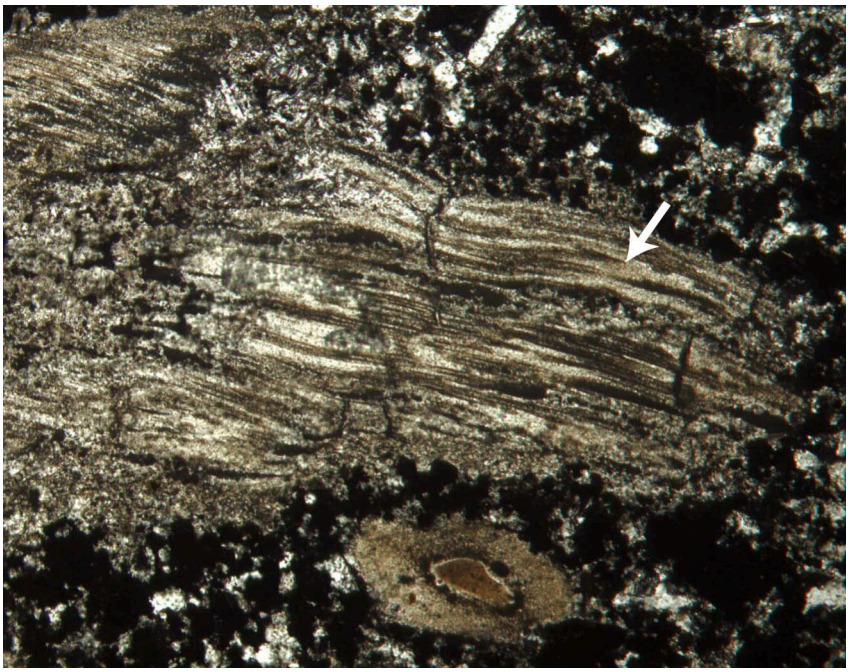

Figure F13. Angular, blocky to platy, vesicular and nonvesicular volcanic clasts are densely packed, forming a clast-supported fabric in sulfide-poor domains of Unit 21. This indicates that the unit is a volcaniclastic breccia. Arrow = the variable orientation of the clasts. (Sample 193-1189A-12R-1 [Piece 16, 122–126 cm]; width of view = 5.5 mm. Photomicrograph ID# 1189A_77; **thin section 42**).

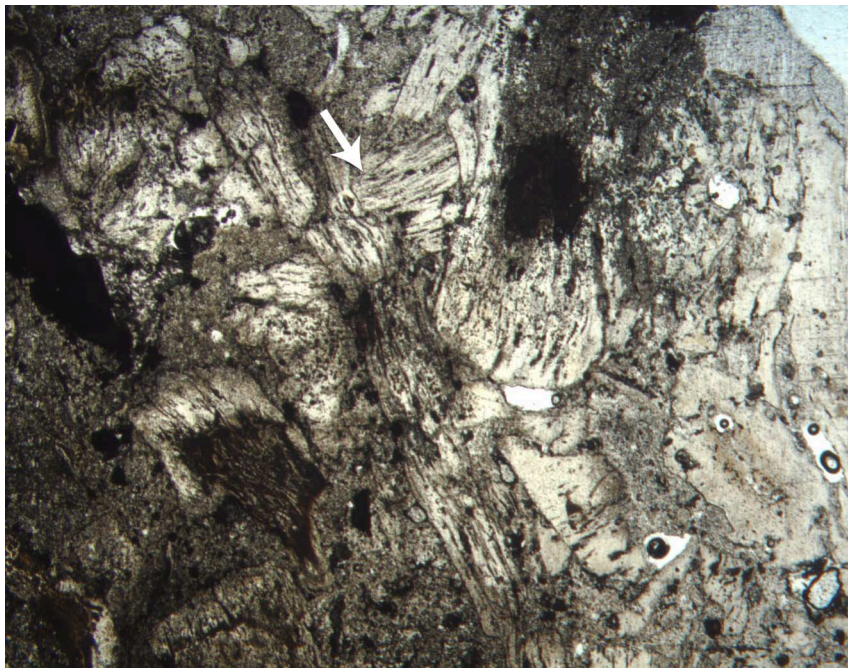

Figure F14. Remnant flow banding in volcanic fragments of hydrothermal breccia units is defined by alternating linear to wavy light gray and gray green domains in hand specimen (cf. Figs. F6, p. 72, F8, p. 74, F9, p. 75). In thin section, these bands correspond to light brown and brown to black groundmass domains (Sample 193-1189A-3R-1 [Piece 10, 59–63 cm]). **A.** A flow-banded volcanic fragment has been fractured by quartz-anhydrite veins. Microcrystalline flow bands are light brown and brown to black and gently folded (Field of view = 5.5 mm × 4.3 mm. Photomicrograph ID# 1189A_81). **B.** Enlarged view of area shown in (A) with a white box. Under high magnification, and using the condenser, very fine grained minerals with low birefringence (silica polymorphs, sulfate, and/or zeolite?) can be recognized in the light bands. Dark bands contain abundant, black cryptocrystalline material. The contacts between light and dark bands are weakly defined and irregular (Field of view = 0.54 mm × 0.69 mm. Photomicrograph ID# 1189A_82).

A

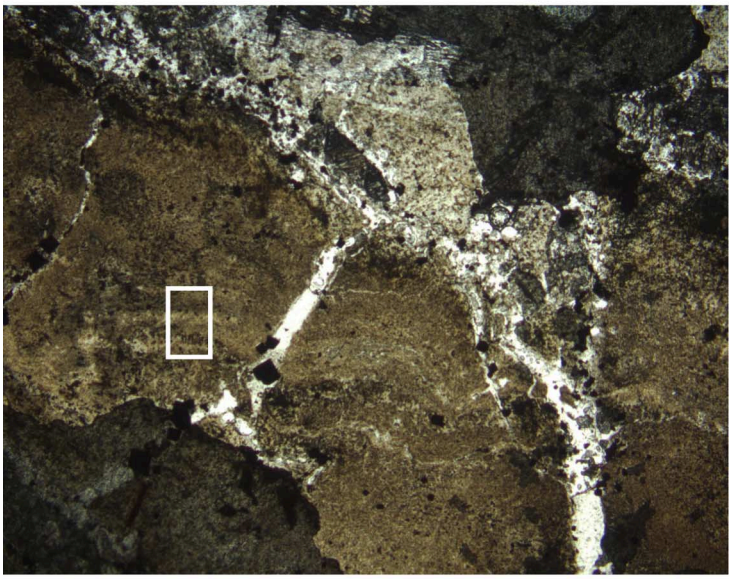

B

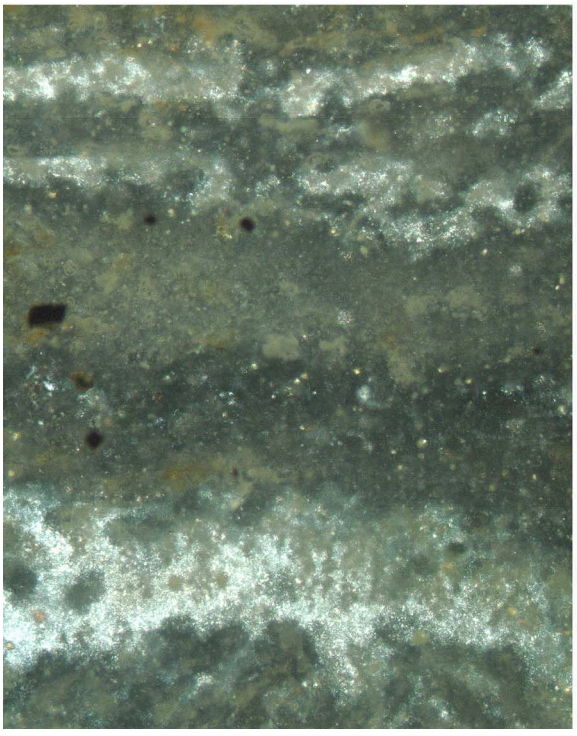

Figure F15. Photomicrograph from the core of a black patch in Unit 15. Former medium-grained acicular crystals are replaced by trails of clear anhedral grains (feldspar and/or quartz) with lines of fine opaque grains (magnetite, hematite, and pyrite) marking the original cores of the crystals. The groundmass is mostly chlorite (Sample 193-1189A-8R-1 [Piece 17, 103–105 cm]; width of view = 2.75 mm. Photomicrograph ID# 1189A_99; **thin section 54**).

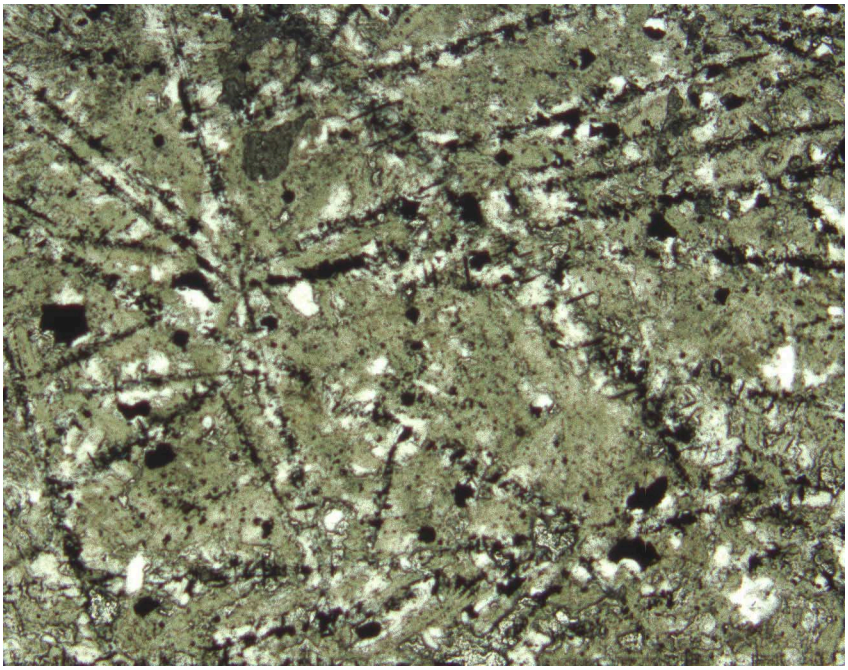

Figure F16. Photomicrograph from near the edge of a black patch in Unit 15. A small amount of host rock is visible along the left edge. The clear grains in the middle outline a 2-mm-long area, possibly originally a plagioclase phenocryst, that consists of optically oriented clear material (secondary feldspar or quartz?) (Sample 193-1189A-8R-1 [Piece 17, 103–105 cm]; width of view = 2.75 mm). **A.** Plane-parallel illumination (Photomicrograph ID# 1189A_100; **thin section 54**). **B.** Cross-polarized illumination (Photomicrograph ID# 1189A_101; **thin section 54**).

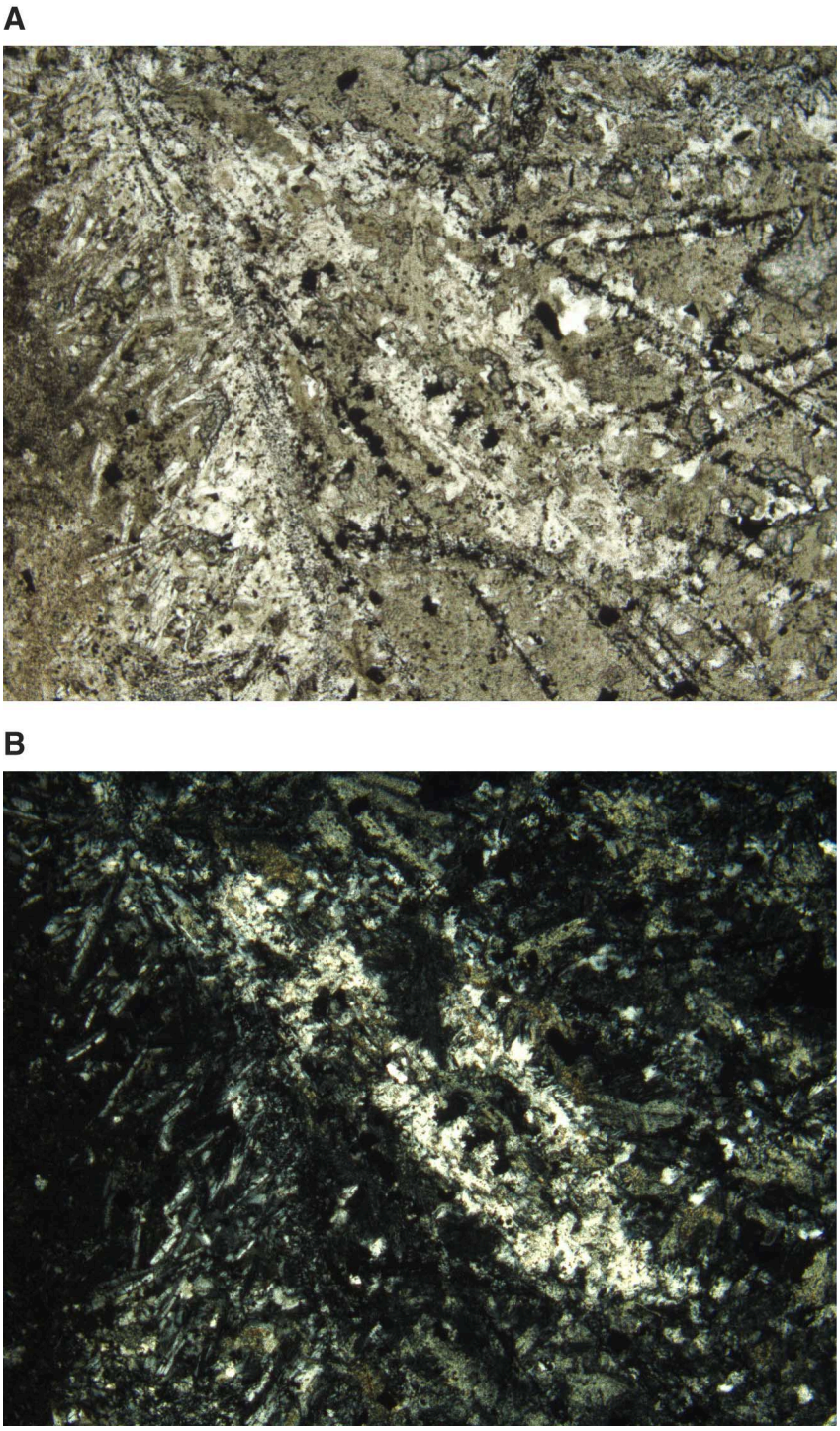

Figure F17. Photomicrograph from the edge of a black patch in Unit 15. Note that the scale differs from Figures F15, p. 83, and F16, p. 84. The image shows the millimeter-wide finer grained rim zone of the patch with relict bladed crystals (now clear grains with lineations of opaque grains) and interstitial variolitic skeletal plagioclases. The host rock (top) contains microlites oriented parallel to the contact (Sample 193-1189A-8R-1 [Piece 17, 103–105 cm]; width of view = 1.38 mm. Photomicrograph ID# 1189A_98; **thin section 54**).

Figure F18. Graphic summary log for Hole 1189B showing the lithologic characteristics of the various units including alteration. See Figure F6, p. 45, in the "Explanatory Notes" chapter for the lithologic key. NR = no recovery.

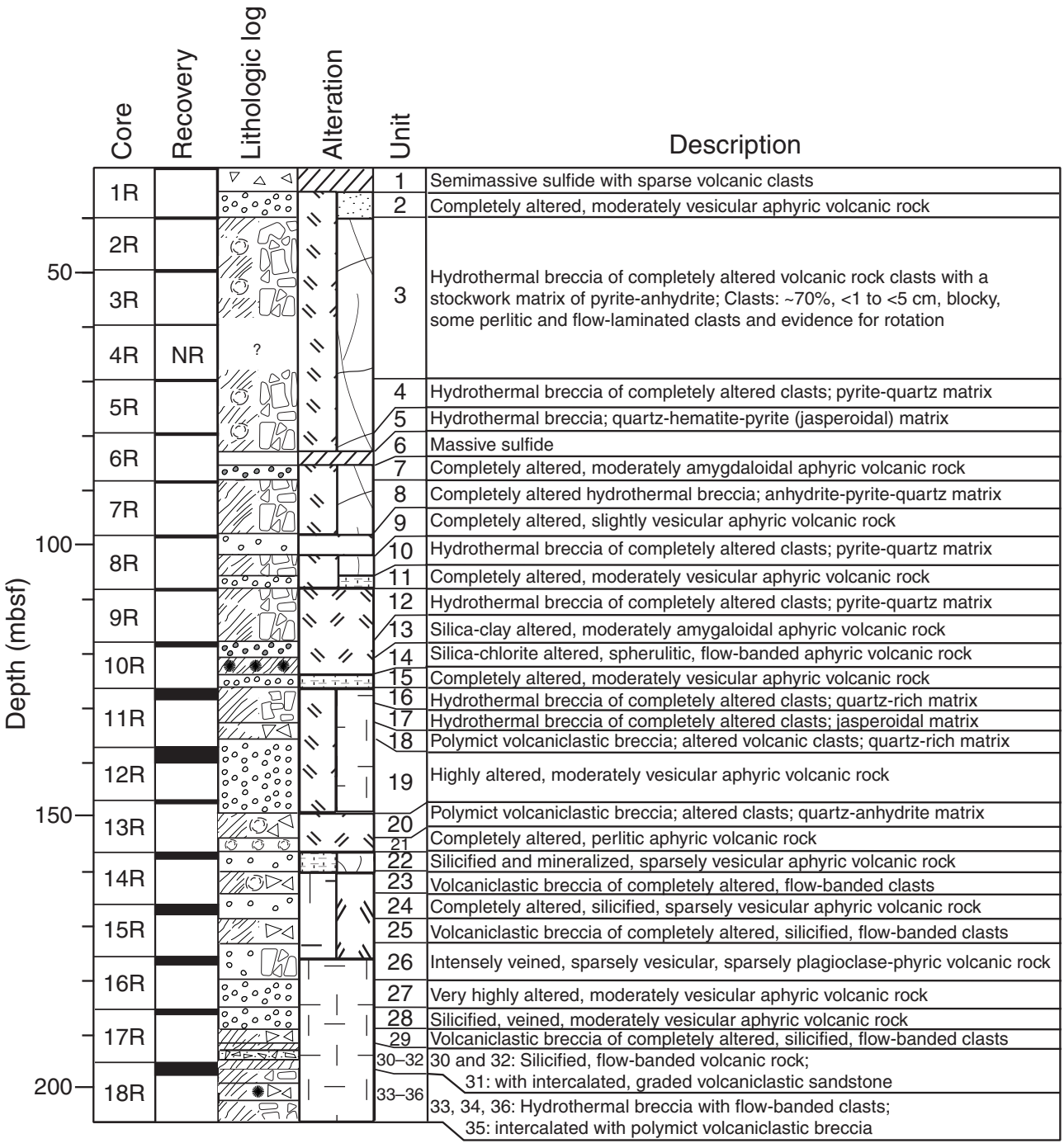

Figure F19. Hand specimen (Unit 8) of matrix-supported breccia comprising soft, clay-rich clasts with 2% disseminated pyrite hosted in an anhydrite-quartz-pyrite cement. Anhydrite is present as vug fill (cf. Fig. F109, p. 181) (Sample 193-1189B-7R-1 [Piece 1, 0–5 cm] at 88.70 mbsf).

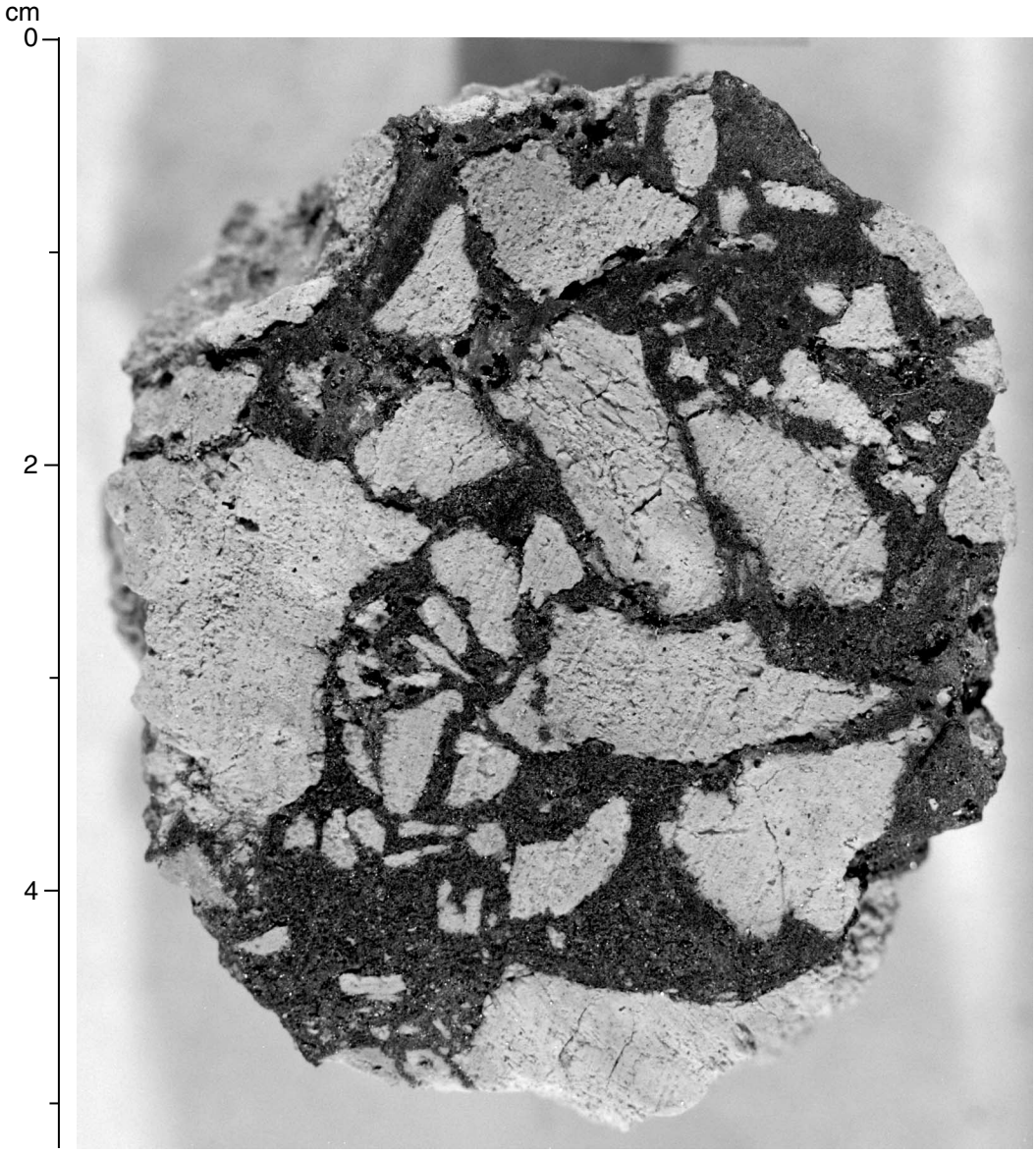

Figure F20. Close-up photograph of a green silicified moderately amygdaloidal, aphyric volcanic rock from Unit 13 with vesicles as large as 5 mm in size, mostly filled with quartz, although some are lined by anhydrite-pyrite. Several hairline quartz-anhydrite-pyrite veins with 1- to 2-mm dark gray siliceous halos are also visible. The coarser vein is filled with anhydrite and minor pyrite (interval 193-1189B-10R-1, 2–14 cm).

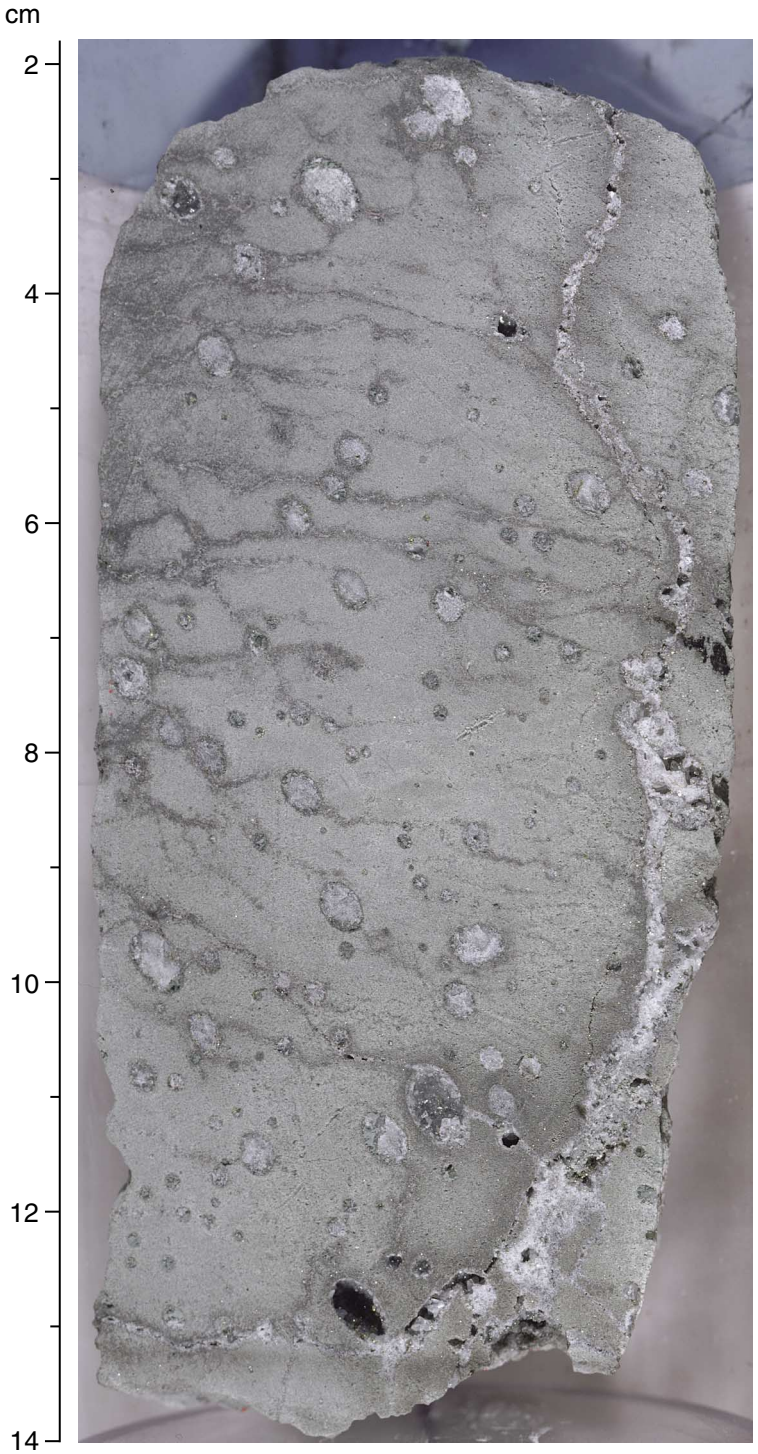

Figure F21. Flow banding on a millimeter scale is defined by alternating white bands consisting of coalesced microspherulites and dark bands with isolated microspherulites (Unit 20; Sample 193-1189B-10R-1, 56 to 61 cm).

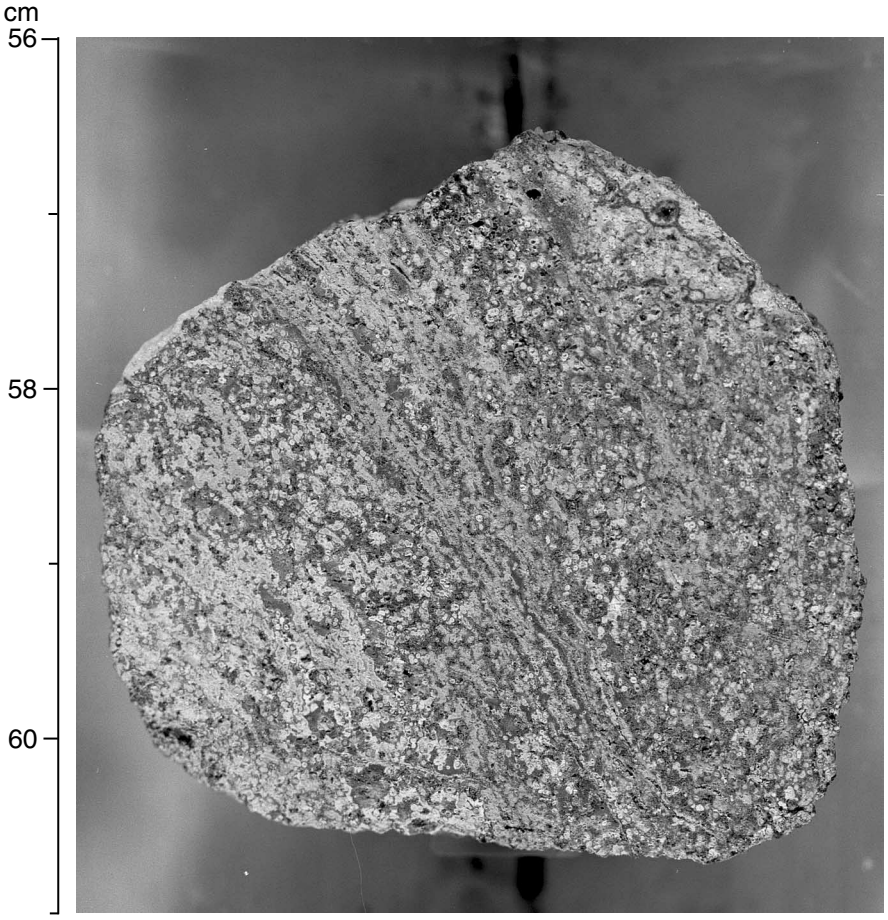

Figure F22. Unit 23 is a poorly sorted volcaniclastic breccia with green clay-rich, flow-banded volcanic clasts showing evidence for in situ fragmentation and rotation of clasts. The matrix is quartz, anhydrite, and minor pyrite. The fragments have been silicified along their rims. Veins from the matrix can be seen crosscutting the flow banding in the large fragment in the upper left of the piece (Sample 193-1189B-14R-1 [Piece 13, 86–95 cm] at 157.36 mbsf).

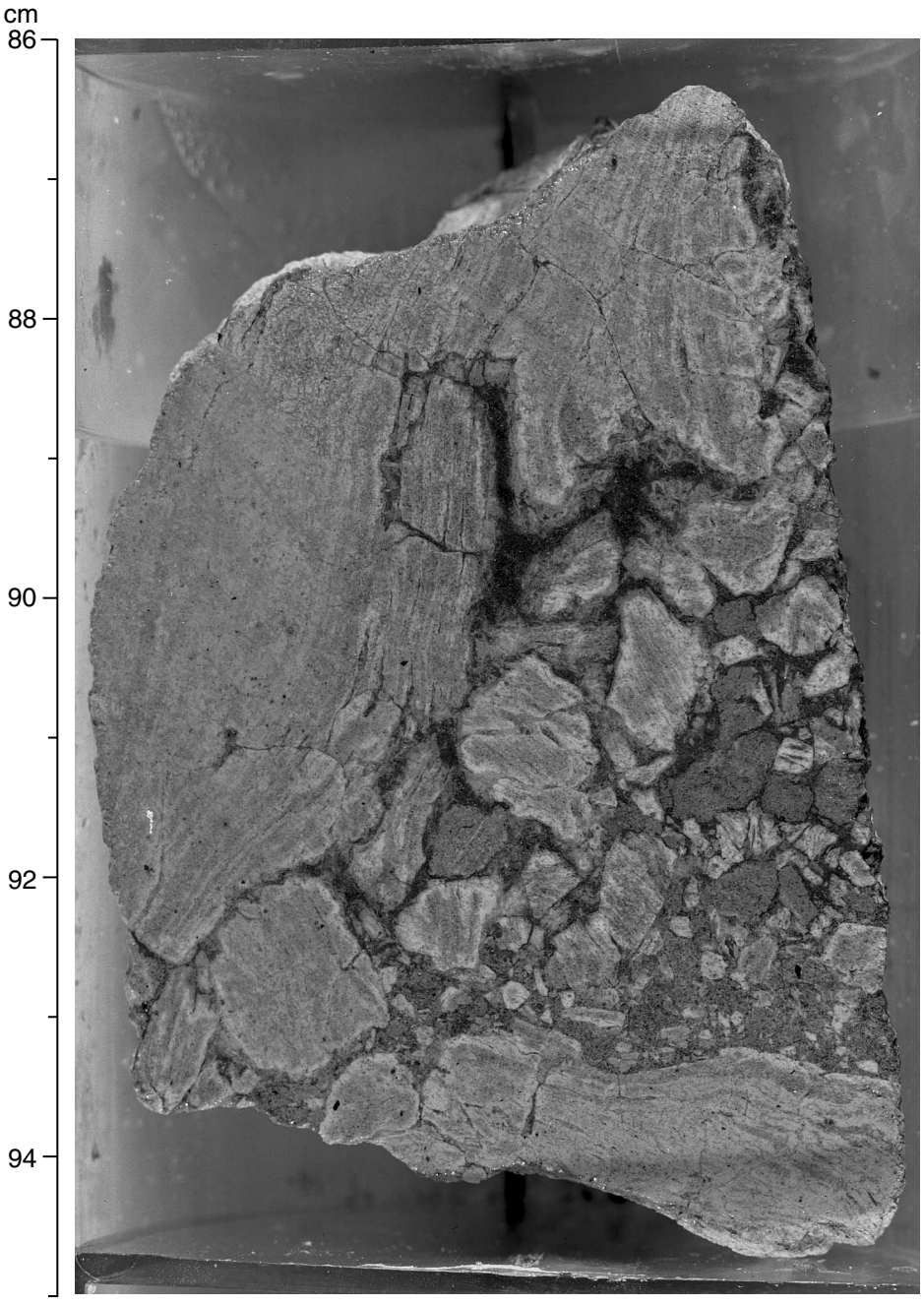

Figure F23. This piece of Unit 23 consists of a clastic domain that has been intruded by an apophysis of flow-banded lava. The coherent domain and the fragments in the clastic domain have the same composition, and we interpret this texture as a synvolcanic intrusion of molten lava into its own autoclastic breccia, and hence as a paleoseafloor horizon (Sample 193-1189B-14R-1, 65–75 cm).

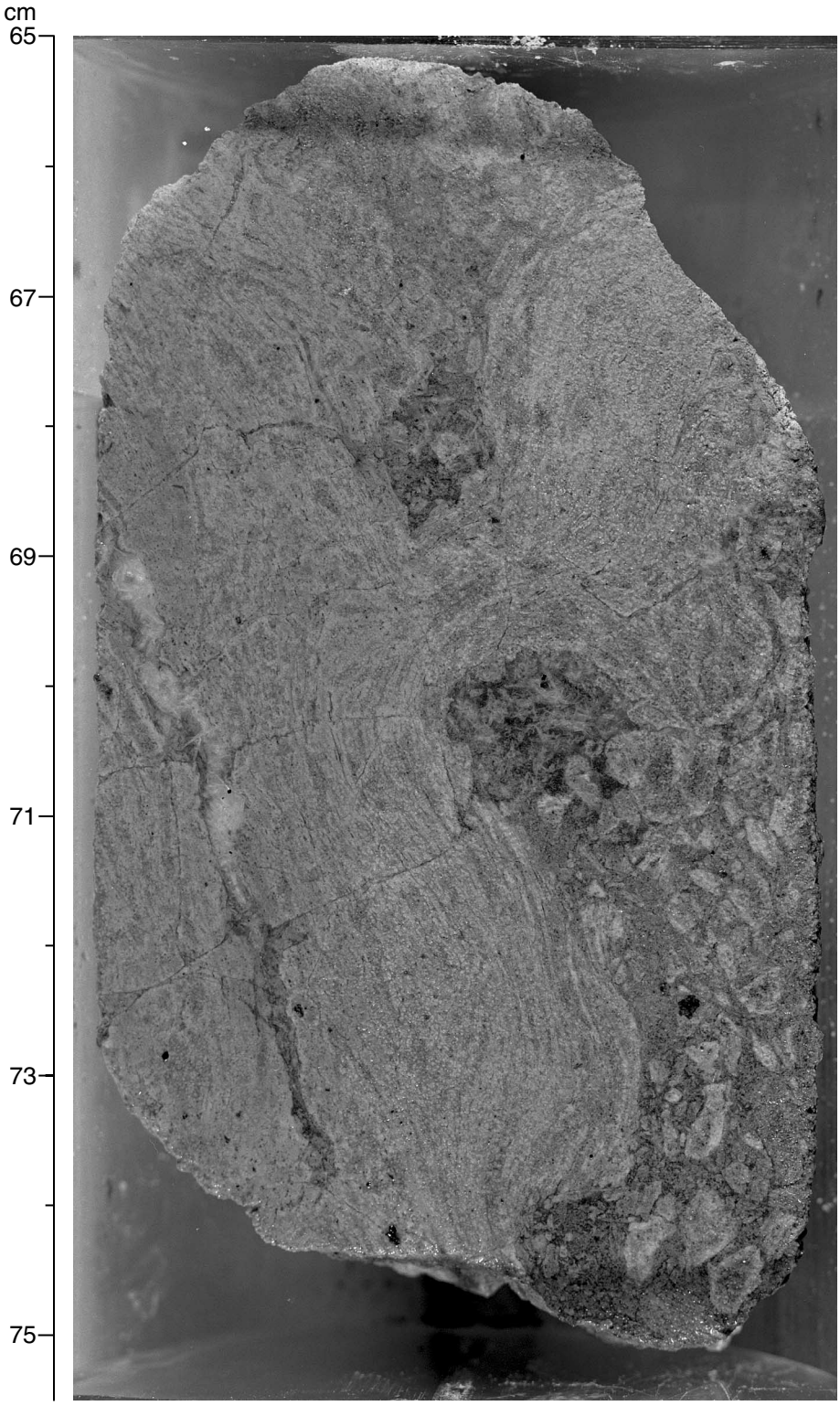

Figure F24. The poorly sorted, clast-supported volcaniclastic breccia of Unit 25 consists of flow-banded clasts with internal laminar textures at random orientation indicating clast movement. The brecciated rock is crosscut by a feeble but dense silica vein network. Arrow = late anhydrite vein, crosscutting the vein network in the fragments, running downward from right to left (Sample 193-1189B-15R-1 [Piece 4, 26–34 cm] at 166.35 mbsf).

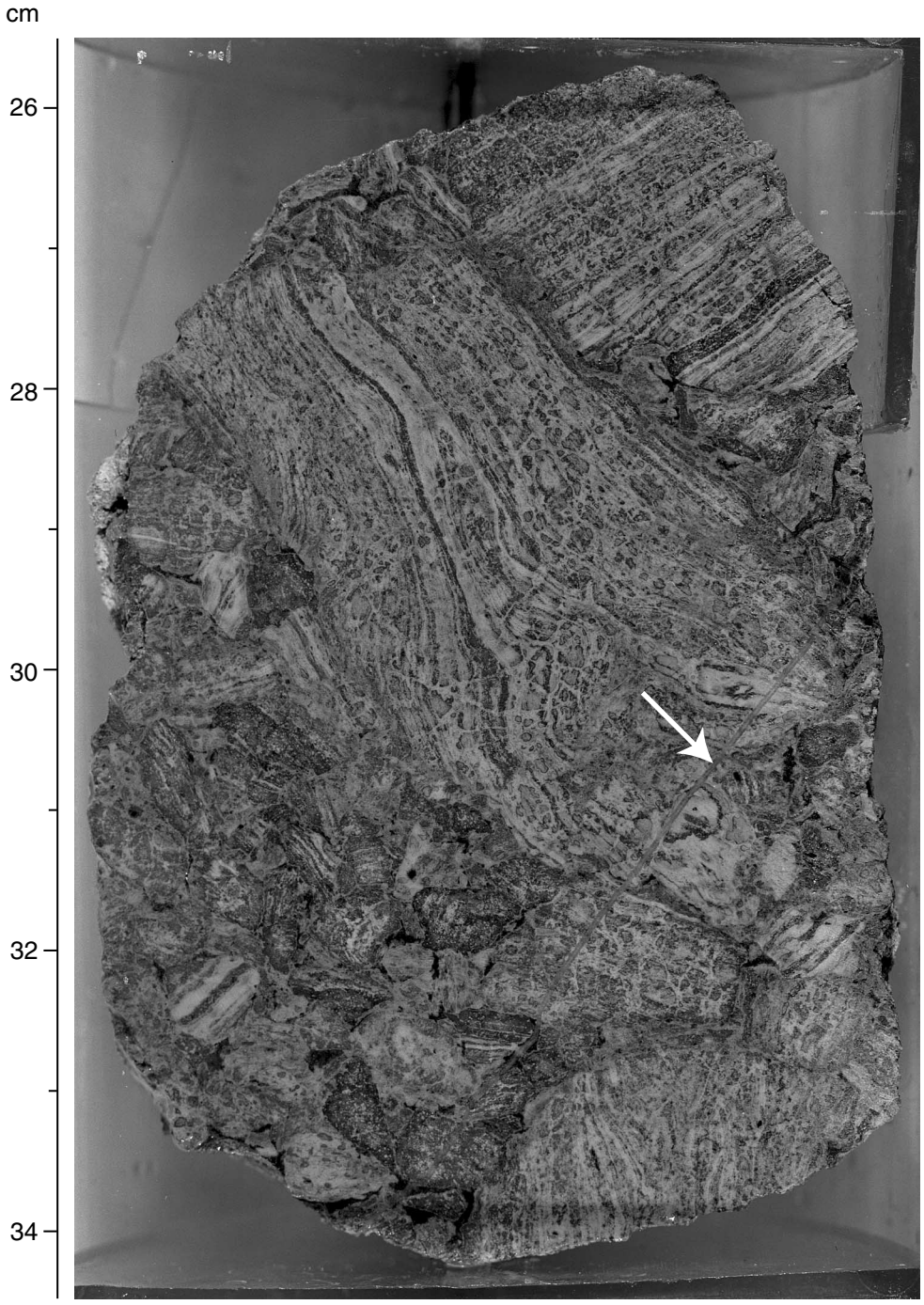

Figure F25. Photograph of coherent flow-banded core piece, with a pseudobreccia appearance created by silica-clay alteration halos around a feeble network of silica veins (interval 193-1189B-15R-1, 130–135 cm)

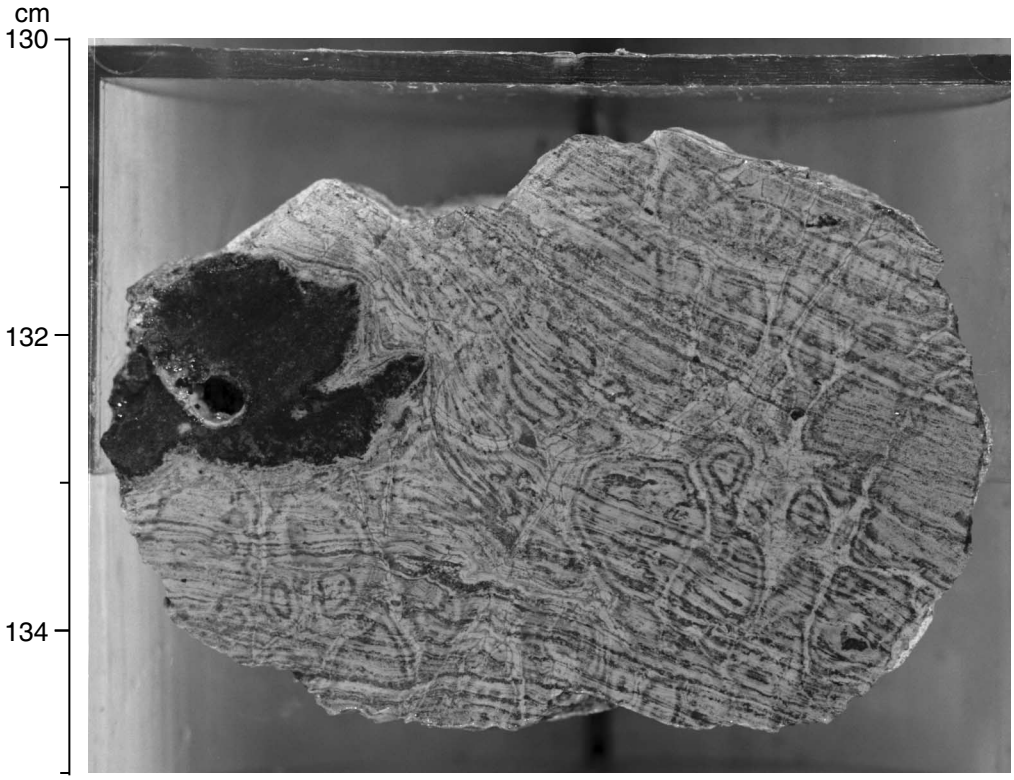

Figure F26. Intensely veined, weakly vesicular and sparsely plagioclase phyric volcanic rock, which is cut by a fine network of quartz-pyrite-magnetite veins with magnetite bearing alteration halos (Unit 26). Brecciation associated with the veining locally imparted a jigsaw-fit pattern on the otherwise coherent rock. In the upper right part of the piece, at 19 cm, a thin anhydrite vein (white) can be seen crosscutting the quartz-magnetite-pyrite vein network (Sample 193-1189B-16R-1 [Piece 3, 16–26 cm] at 175.85 mbsf).

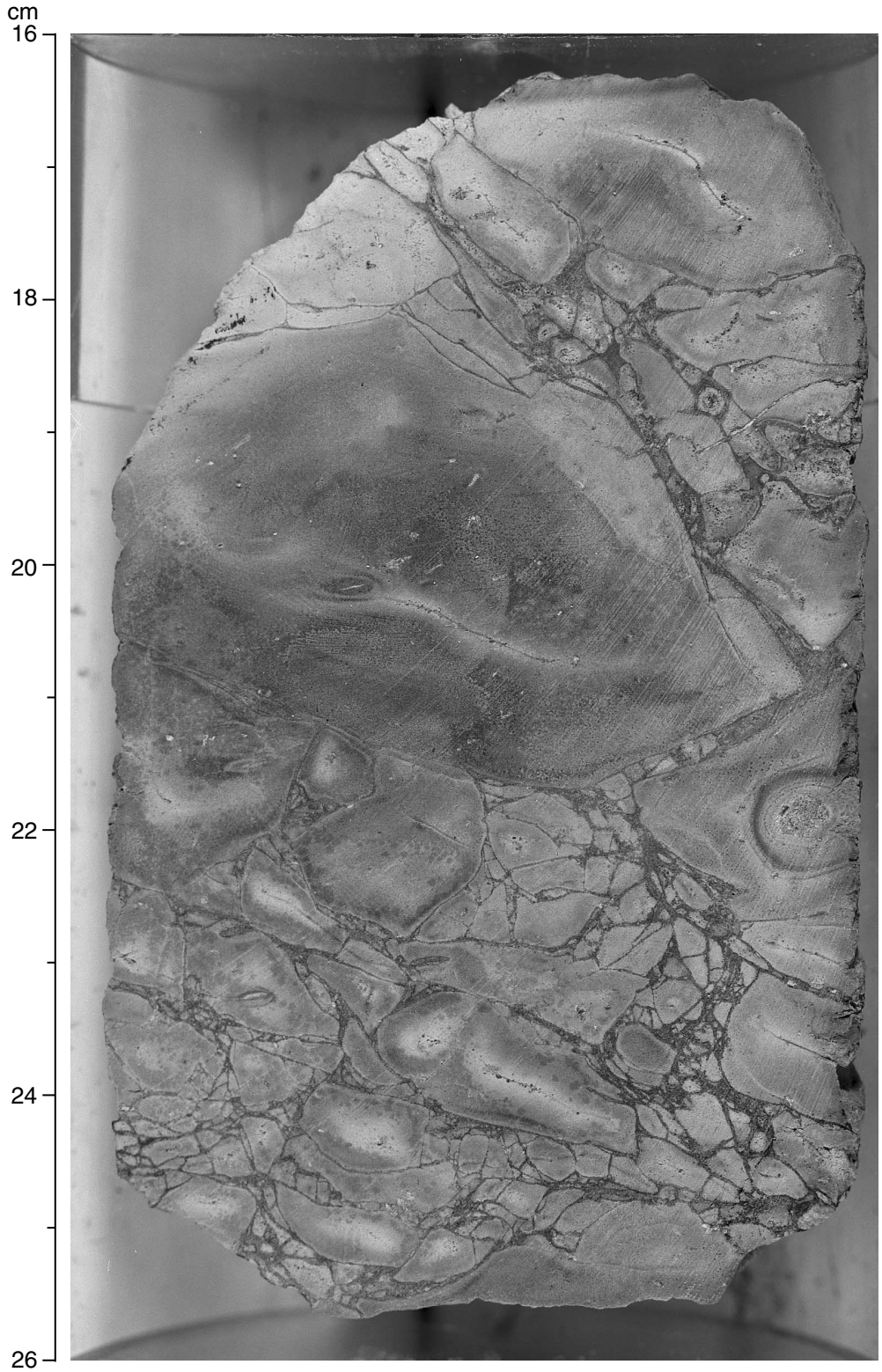

Figure F27. Photograph of moderately vesicular aphyric volcanic rock. The groundmass shows a spotty hieroglyphic texture caused by incomplete hydrothermal alteration with white, angular shard-shaped domains representing remnants of less altered groundmass (interval 193-1189B-16R-1, 114–121 cm).

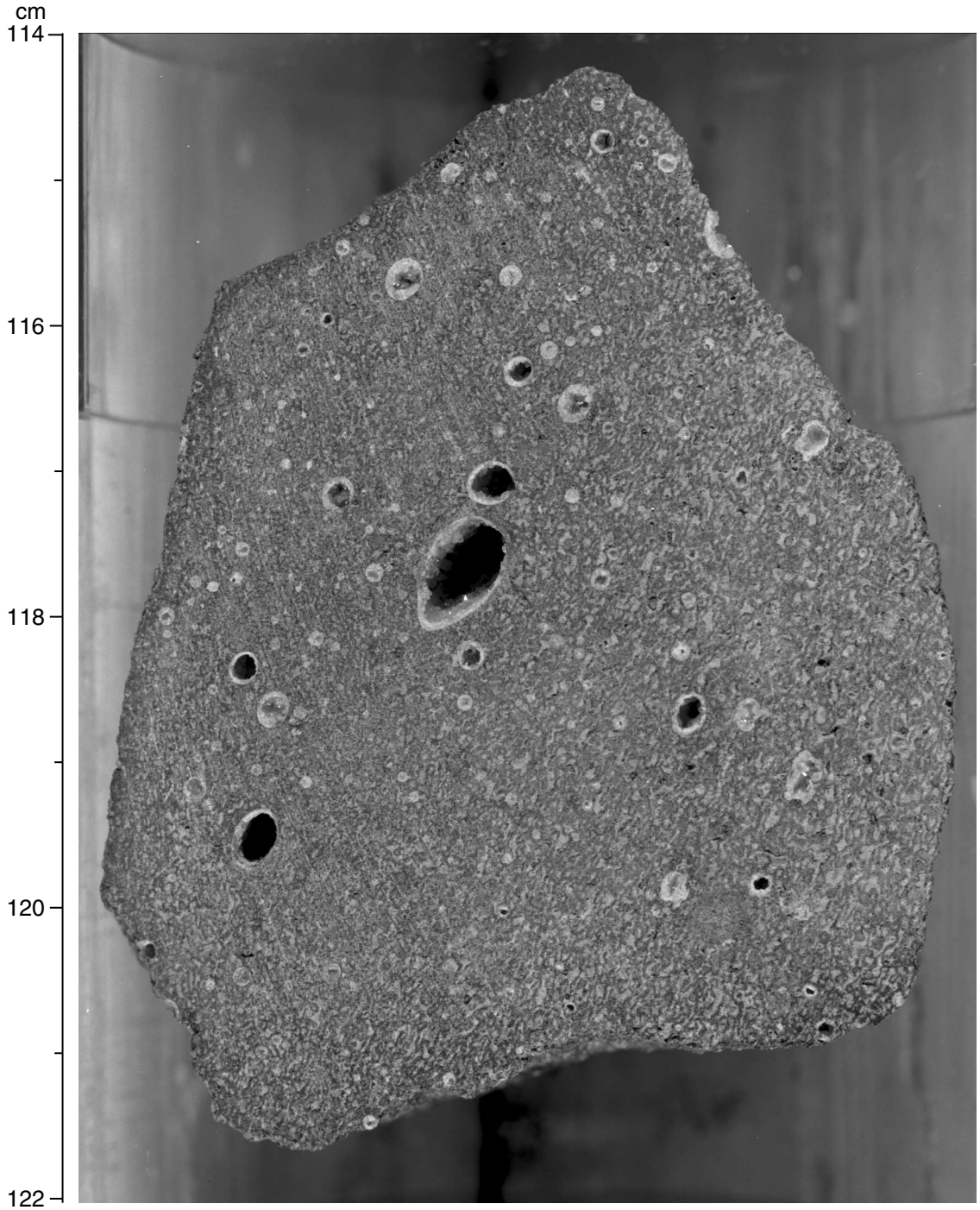

Figure F28. Unit 35 is a polymict volcaniclastic breccia with flow-banded clasts, dark green porous clasts, perlitic clasts, and textureless bleached clasts cemented in a quartz-hematite-sulfide matrix. Folded flow banding in one clast is truncated at the hinge of the fold, clearly indicating that the clast was abraded during transport. Fine sulfide veins in the clasts are terminated at the boundary of fragments, indicating that the formation of these veins predates erosion and deposition of the clasts (Sample 193-1189B-18R-2, 49–58 cm).

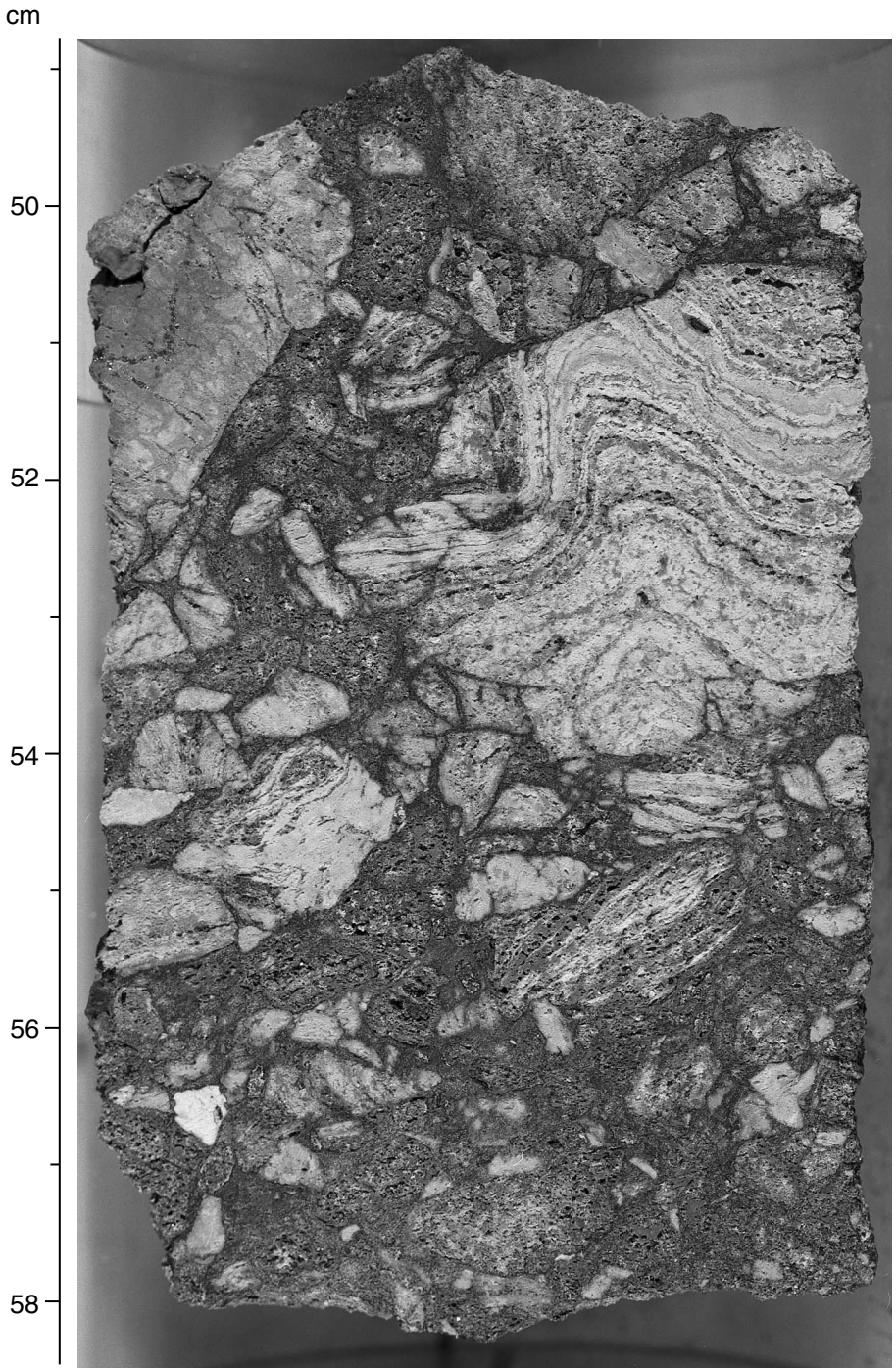

Figure F29. Plagioclase phenocrysts from the lower sequence of Hole 1189B are typically fresh and rounded. This group of fresh crystals are typical, with only slight clay alteration along the cracks. Fresh plagioclase microlites lie within altered groundmass. The granular texture in this photomicrograph is caused solely by a rough polish of the underlying glass side, not alteration (Sample 193-1189B-16R-1 [Piece 2, 36–39 cm]; width of view = 2.75 mm). **A.** Photomicrograph in plane-polarized light (Photomicrograph ID# 1189B_70; **thin section 136**). **B.** Photomicrograph in cross-polarized light (Photomicrograph ID# 1189B_71; **thin section 136**).

A

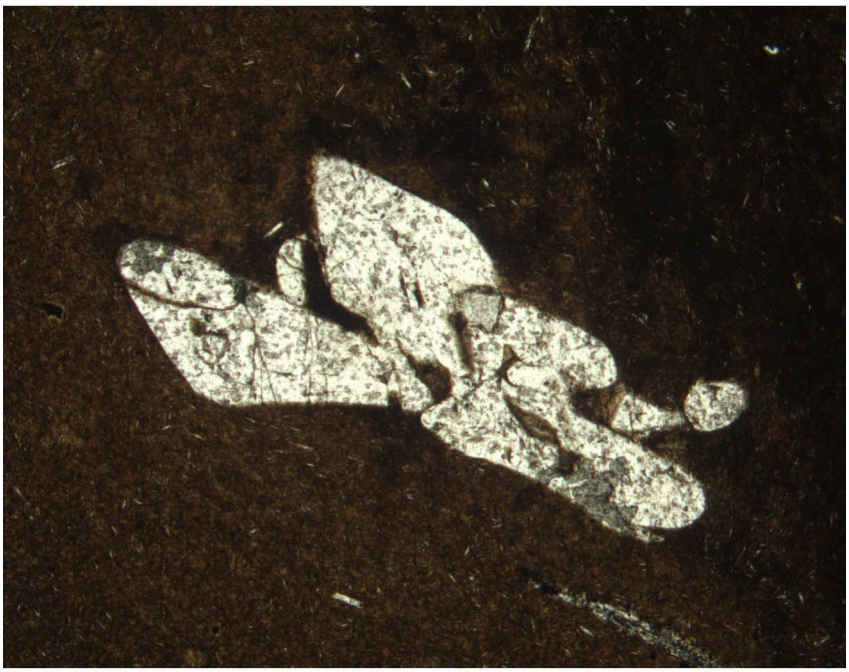

B

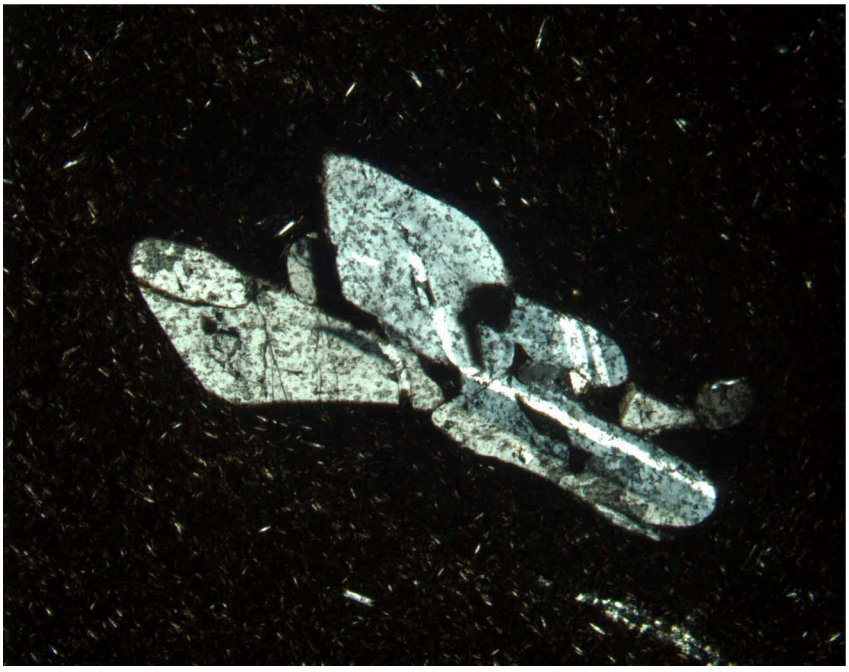

Figure F30. Photomicrograph of plagioclase and clinopyroxene phenocrysts from Unit 25. The plagioclase crystals are fresh, whereas the pyroxenes are completely altered to clay and quartz (Sample 193-1189B-15R-1 [Piece 10, 131–134 cm] in cross-polarized light; width of view = 1.38 mm. Photomicrograph ID# 1189B_47; **thin section 133**).

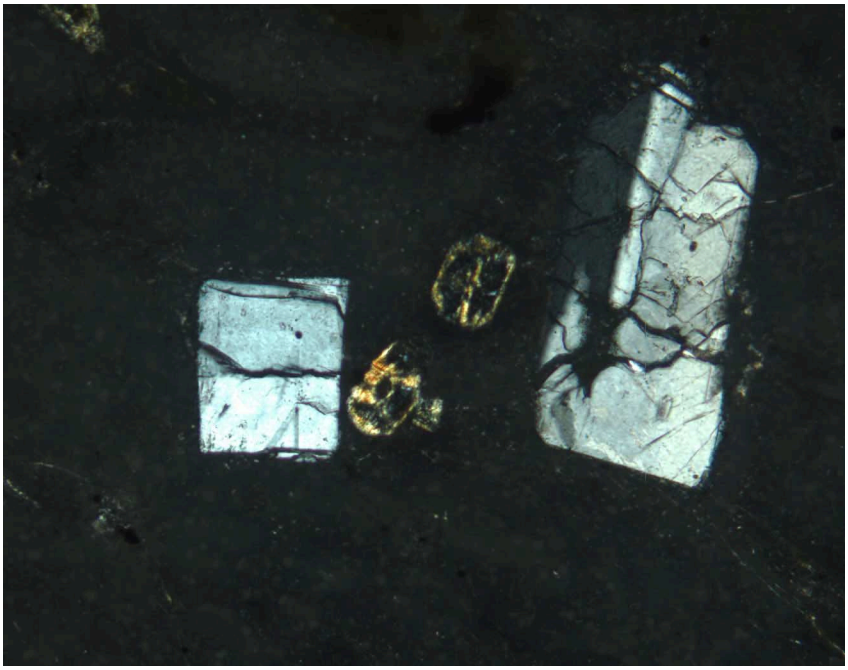

Figure F31. Quartz ± pyrite amygdules within a completely altered volcanic rock, Unit 11. Epoxy cement filling the center of partially filled vesicles shows apparent high relief arising from grinding marks on the underlying glass slide (Sample 193-1189B-8R-1 [Piece 10, 37–40 cm]; width of view = 2.75 mm). **A.** Photomicrograph in plane-polarized light (Photomicrograph ID# 1189B_28; **thin section 118**). **B.** Photomicrograph in cross-polarized light (Photomicrograph ID# 1189B_29; **thin section 118**).

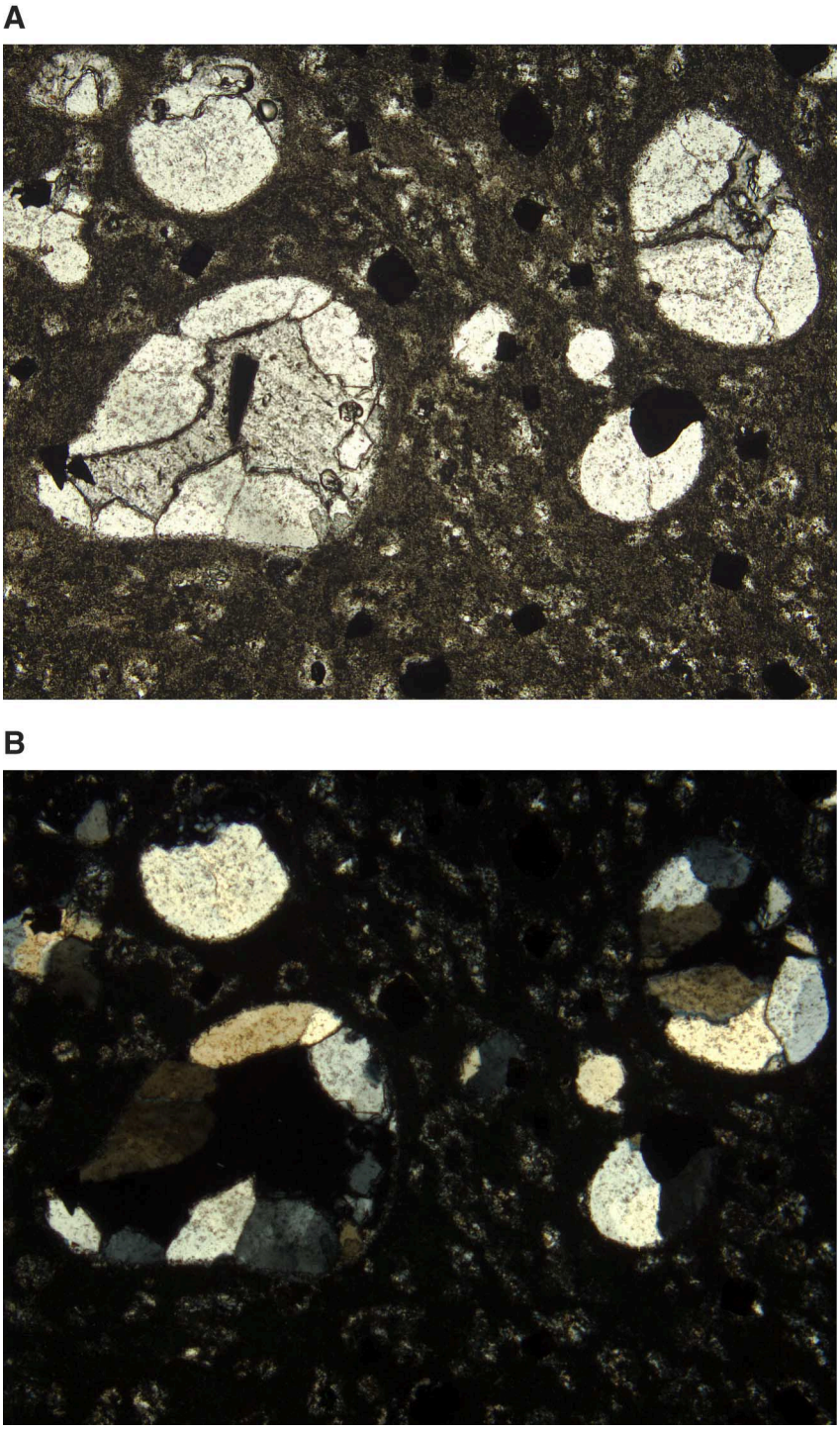

Figure F32. Quartz-sphalerite amygdule within highly altered volcanic rock from Unit 26 (Sample 193-1189B-16R-1 [Piece 2, 36–39 cm] in plane-polarized light; width of view = 1.38 mm. Photomicrograph ID# 1189B_51; **thin section 136**).

Figure F33. Remnant perlite texture in the altered groundmass of a completely altered, aphyric massive rock (Unit 21), where the arcuate cracks have been preserved despite replacement of the glassy volcanic groundmass by quartz, chlorite, and clay minerals (Sample 193-1189B-13R-1 [Piece 10, 52–54 cm]; width of view = 2.75 mm. Photomicrograph ID# 1189B_58; **thin section 129**).

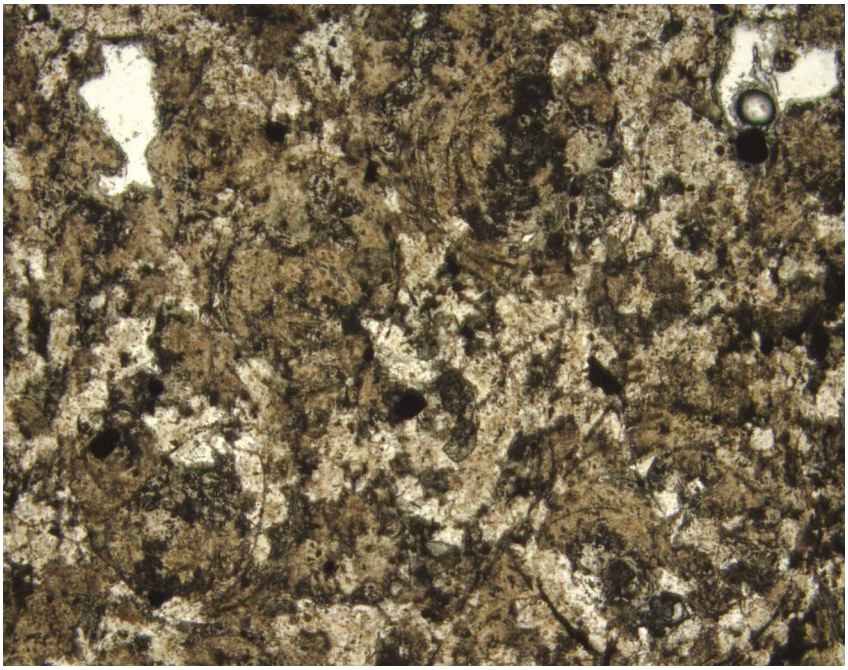

Figure F34. Perlitic cracking preserved in altered volcanic rock. The previously glassy rock now consists dominantly of microcrystalline quartz, and the fine, arcuate domains defining the perlitic cracks are occupied by chlorite and black, cryptocrystalline material (Sample 193-1189B-13R-1 [Piece 6, 34–36 cm]; width of view = 1.38 mm). **A.** Photomicrograph in plane-polarized light (Photomicrograph ID#1189B_63; **thin section 128**). **B.** Photomicrograph in cross-polarized light (Photomicrograph ID# 1189B_64; **thin section 128**).

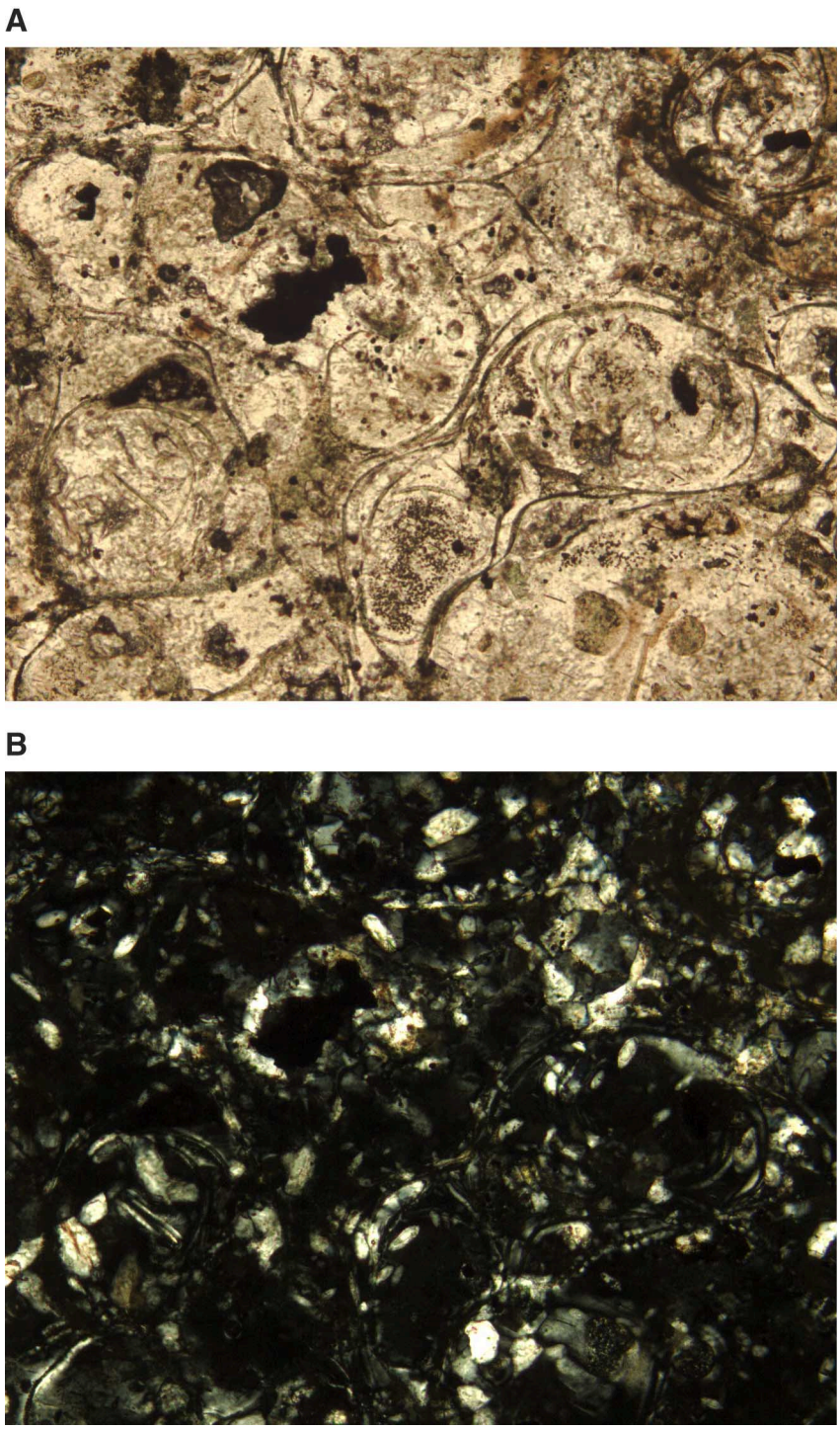

Figure F35. Former tube pumice clast with perlitic fabric and very fine, stretched, and aligned chlorite amygdules (Unit 20; Sample 193-1189B-13R-1 [Piece 6, 34–36 cm]; width of view = 5.5 mm. Photomicrograph ID# 1189B_35; **thin section 128**).

Figure F36. Perlitic texture preserved in the central part of a clay-altered volcanic clast (with a plagioclase phenocryst), which is hosted in a jasperoidal quartz stockwork matrix (Unit 5; Sample 193-1189B-6R-1 [Piece 2, 13–15 cm]; width of view = 5.5 mm. Photomicrograph ID# 1189B_26; **thin section 116**).

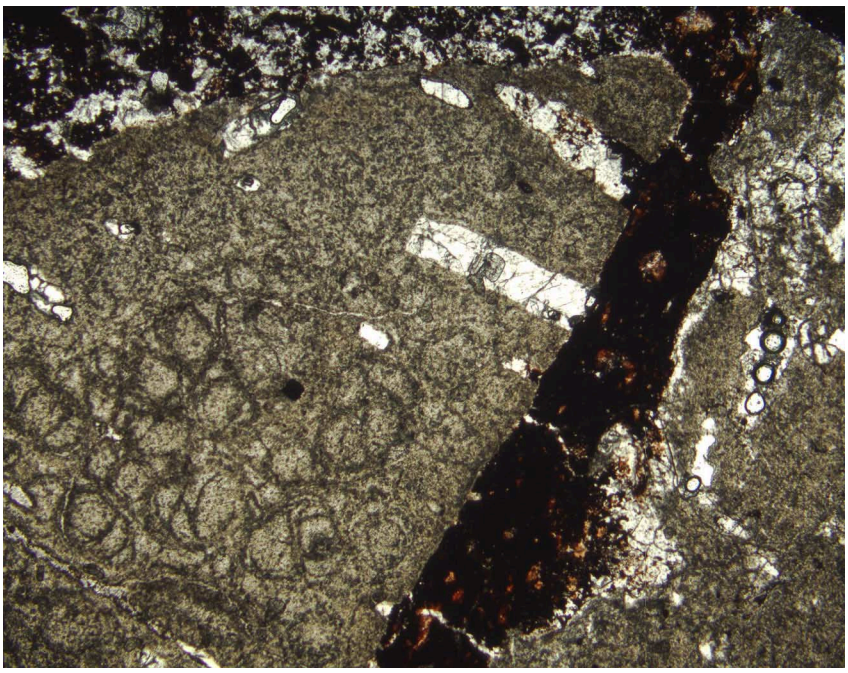

Figure F37. Altered perlitic clasts hosted in an anhydrite and gypsum-rich stockwork matrix. These clasts are locally consumed and replaced along their margins by stockwork veins (Unit 3; Sample 193-1189B-2R-1 [Piece 2, 11–14 cm]; width of view = 5.5 mm. Photomicrograph ID# 1189B_23; **thin section 115**).

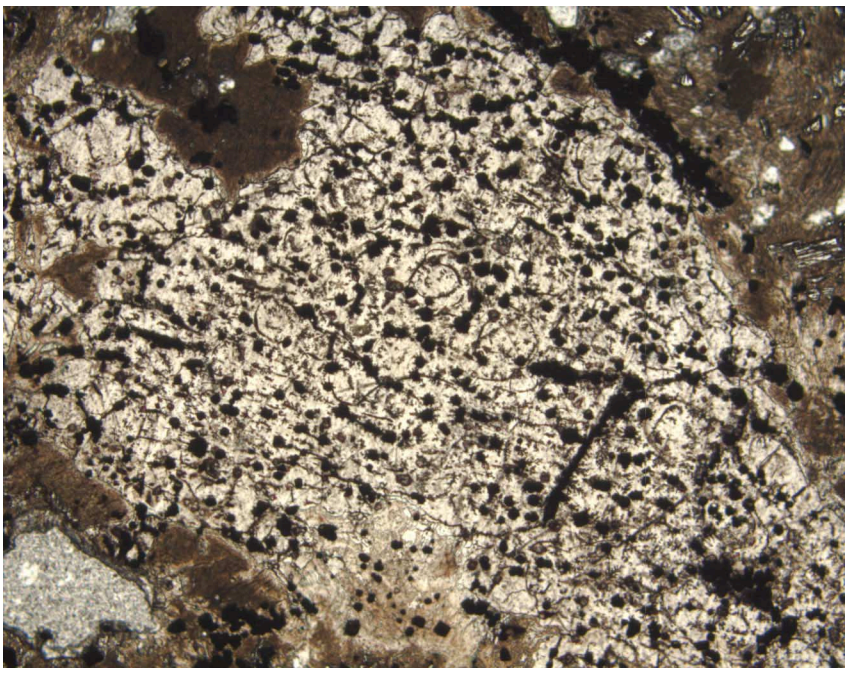

Figure F38. Flow banding in several units is commonly defined by aligned, coalesced spherulites forming "necklace-like" domains with bulbous margins. The spherulites are altered and consist of very fine grained, light gray to brown clay and quartz, which commonly occupies the central part (Unit 14; Sample 193-1189B-10R-1, 57–60 cm; width of view = 2.75 mm. Photomicrograph ID# 1189B_30; **thin section 121**).

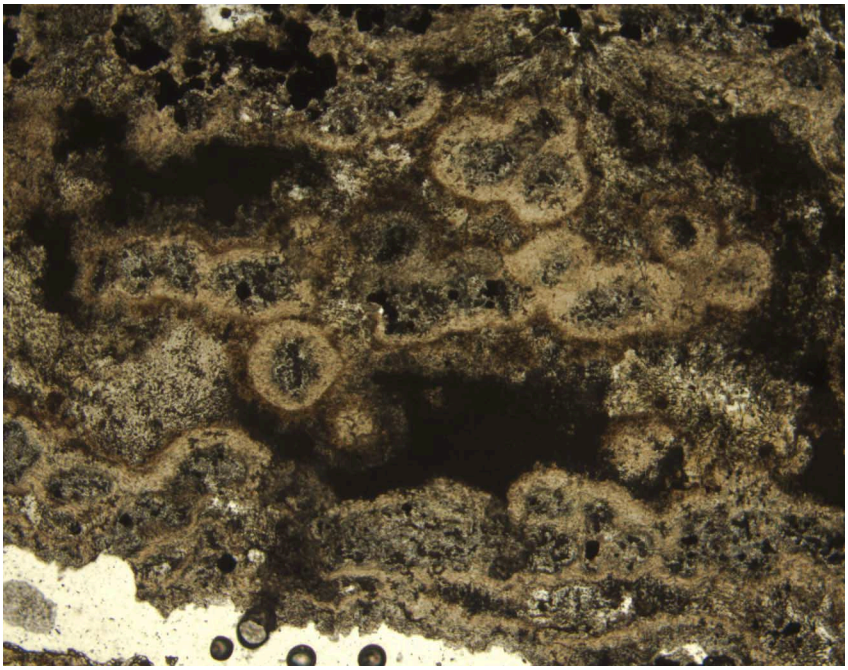

Figure F39. Alternating light gray bands of aligned and coalesced spherulites and brown to dark gray bands with only isolated spherulites can be observed in thin sections of flow banded clasts in Unit 25. The banding was generated during high-temperature devitrification, and the dark bands are inferred to represent former volcanic glass between the devitrified, spherulitic bands (Sample 193-1189B-15R-1 [Piece 15, 131–134 cm] in plane-polarized light; width of view = 5.5 mm. Photomicrograph ID# 1189B_42; **thin section 133**).

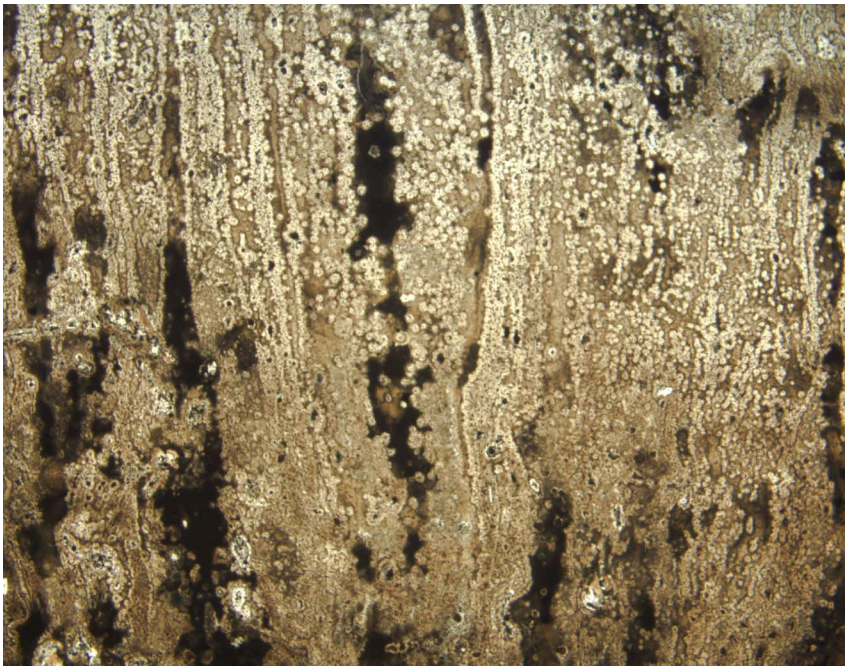

Figure F40. Some flow-banded clasts in Unit 20 show fine, wispy domains consisting of black, very fine grained material. Possibly, these bands consist of Fe oxides that filled stretched microvesicles during an early stage of alteration (Sample 193-1189B-13R-1 [Piece 4, 22–24 cm] in plane-polarized light; width of view = 1.38 mm. Photomicrograph ID# 1189B_32; **thin section 127**).

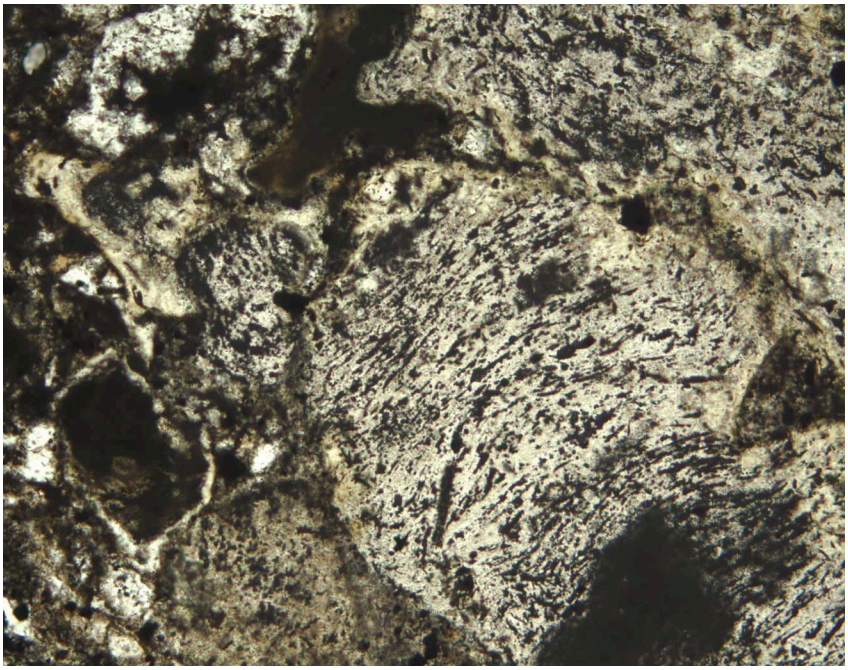

Figure F41. Unit 35 is a polymict volcaniclastic breccia and contains some clasts with well-preserved, densely packed spherulites impinging on each other. These radiating aggregates of quartz and feldspar crystals are, however, locally replaced by micropoikilitic quartz (Sample 193-1189B-18R-2, 65–67 cm, in cross-polarized light; width of view = 1.38 mm. Photomicrograph ID# 1189B_43; **thin section 140**).

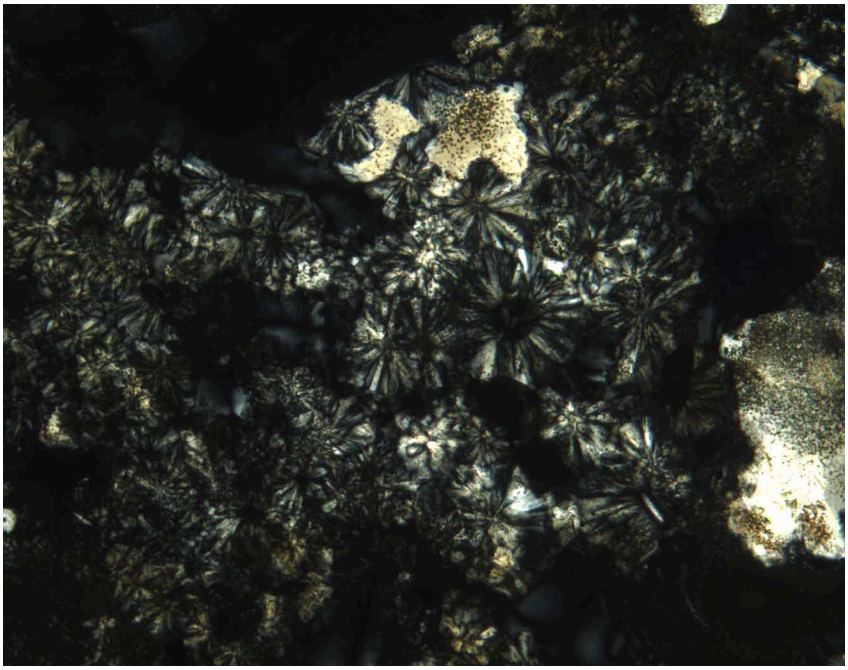

Figure F42. Photomicrograph of the edge of a xenolith with intergranular texture. Skeletal plagioclase, suggesting a quench texture, is surrounded by intergranular green, highly birefringent material (pyroxene, amphibole, or secondary clay). Fine-grained host volcanic rock is at the upper left (Sample 193-1189B-11R-2 [Piece 8, 89–91 cm] in plane-polarized light; width of view = 2.75 mm. Photomicrograph ID# 1189B_21; **thin section 123**).

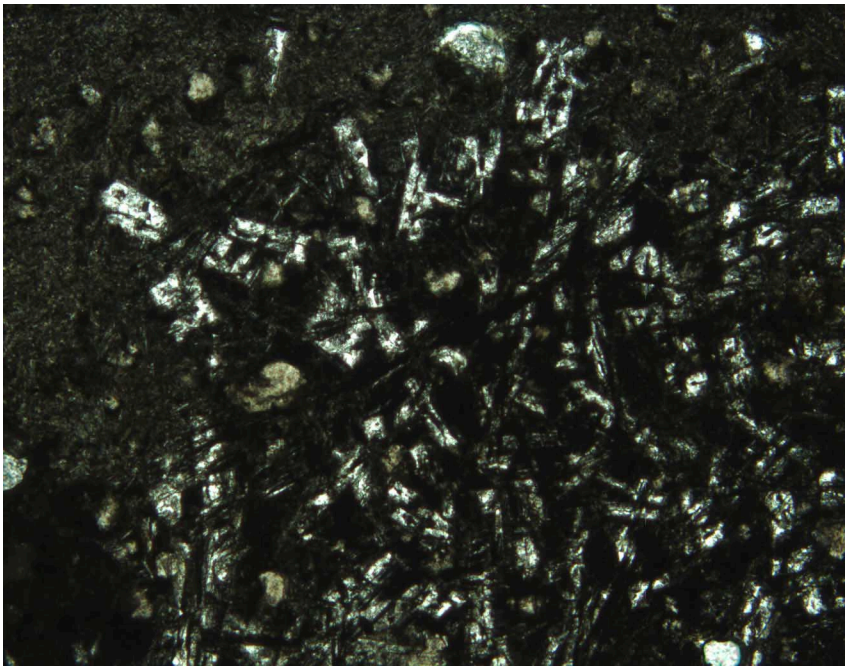

Figure F43. Variolitic plagioclase concentrated at the margin of a xenolith. The acicular plumose crystals extend slightly but distinctly into the host volcanic matrix (Sample 193-1189B-15R-2 [Piece 10, 61–64 cm] in plane-polarized light; width of view = 1.38 mm. Photomicrograph ID# 1189B_40; **thin section 134**).

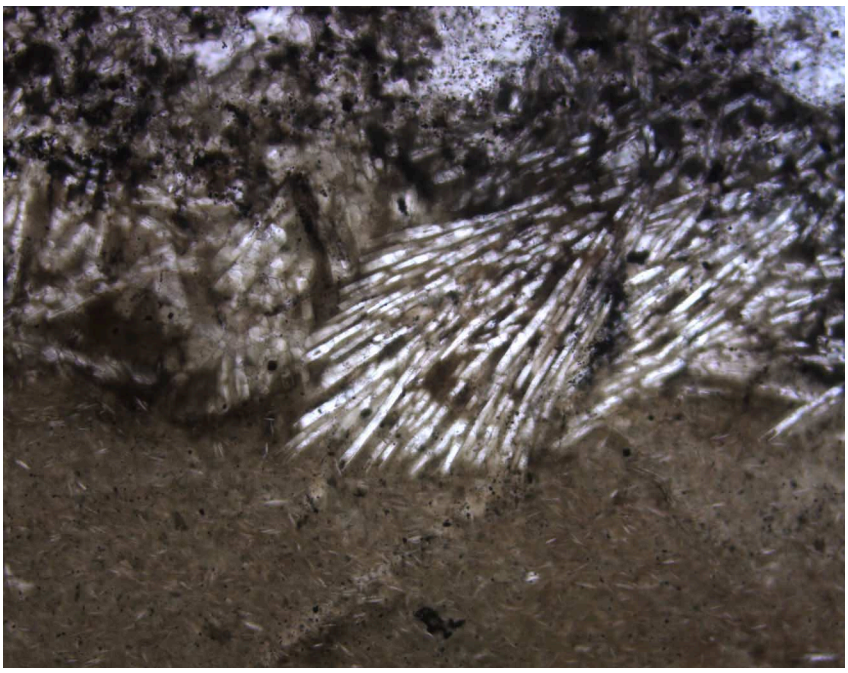

Figure F44. The graded volcaniclastic sandstone (Unit 31) contains a variety of submillimeter angular fragments including glassy (G), porphyritic (P), and perlitic (arrow) clasts (Sample 193-1189B-17R-2 [Piece 19, 98–100 cm] in plane-polarized light; width of view = 5.5 mm. Photomicrograph ID# 1189B_67; **thin section 139**).

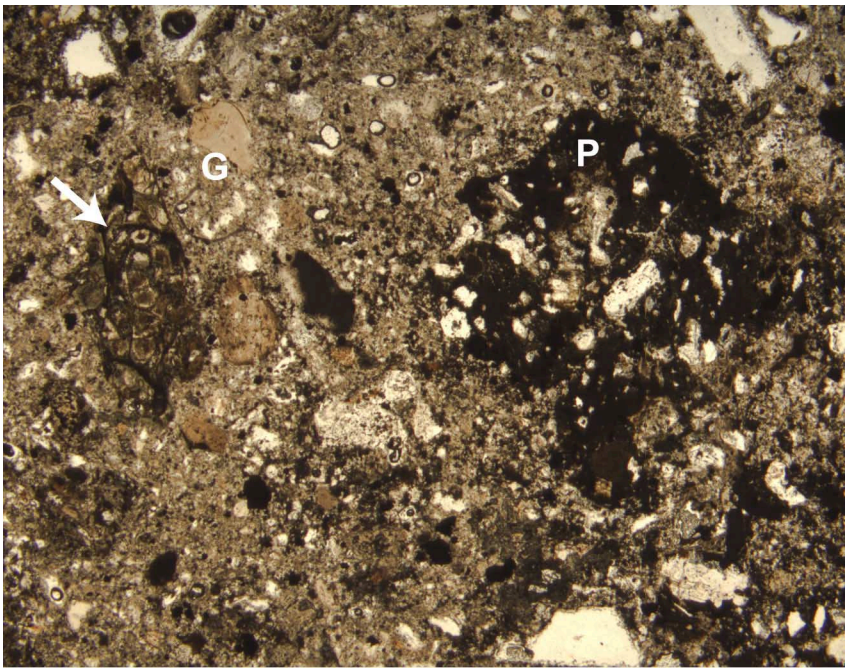

Figure F45. Hydrothermal brecciation has generated a clastic zone within an exceptionally large vein in coherent volcanic rock (Unit 26). The clasts are more intensely altered than the surrounding volcanic groundmass, and some have been moved relative to each other (Sample 193-1189B-16R-1, 7–15 cm).

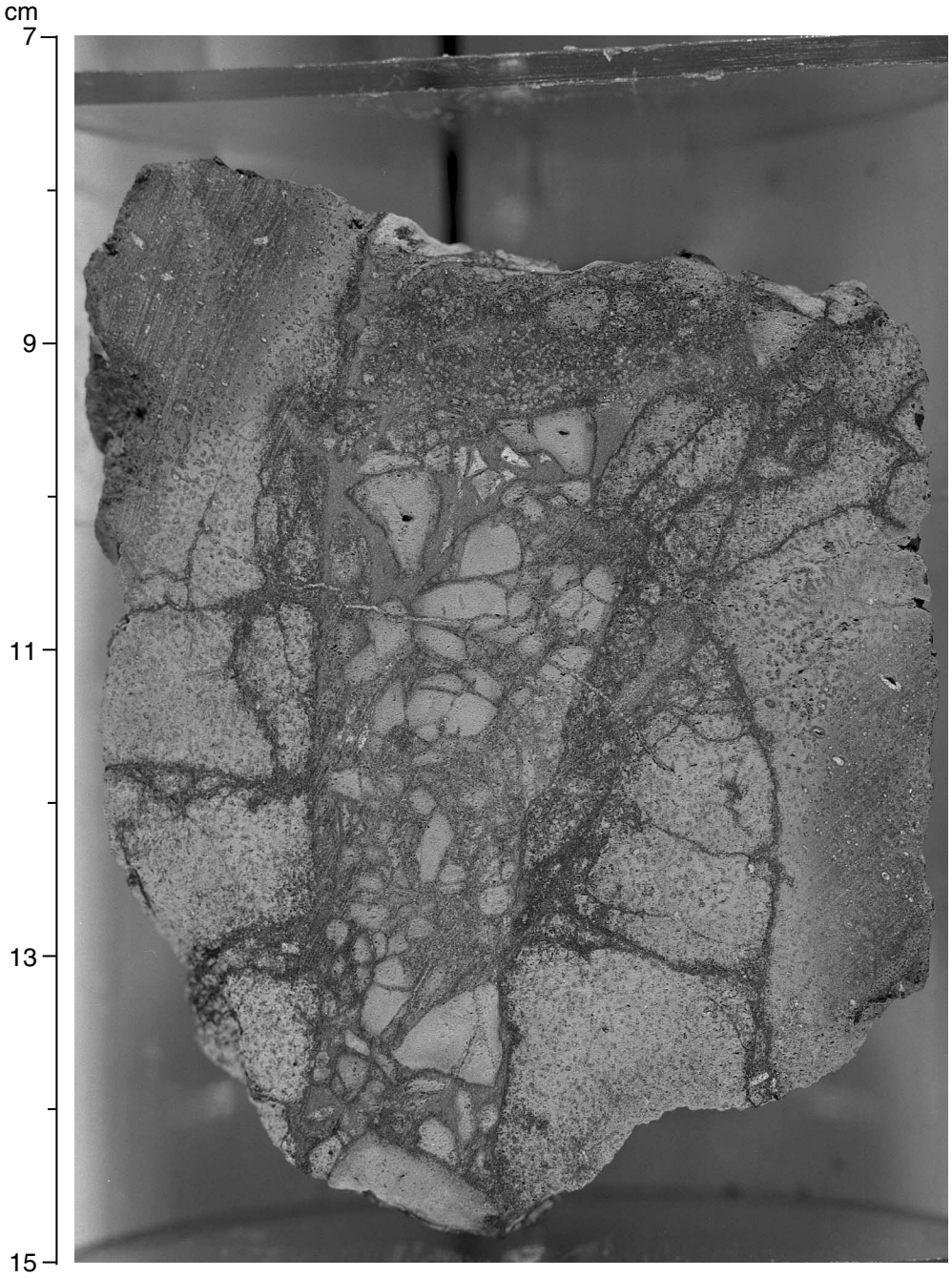

Figure F46. Summary of lithostratigraphic units, alteration type, and distribution of major (thick lines) and minor to trace (thin lines) alteration phases in Hole 1189A. Intervals where remnant igneous plagioclase was detected by X-ray diffraction (XRD) analysis are also indicated on the right side. Pyrite is present in all samples analyzed and is not included in the plot. Note the variation in silica species with depth. Clay phases are indicated where detected in XRD analyses; no indication of their abundance relative to one another or to other phases is implied. It is anticipated that detailed postcruise investigation will extend the distribution ranges for some of these minerals. The terms major, minor, and trace as used here apply to XRD analyses and do not imply quantitative abundances (see **"Hydrothermal Alteration,"** p. 8, in the "Explanatory Notes" chapter). As the data are still under evaluation, mineral distribution indicated by the portable infrared mineral analyzer (PIMA) is not included in the plot.

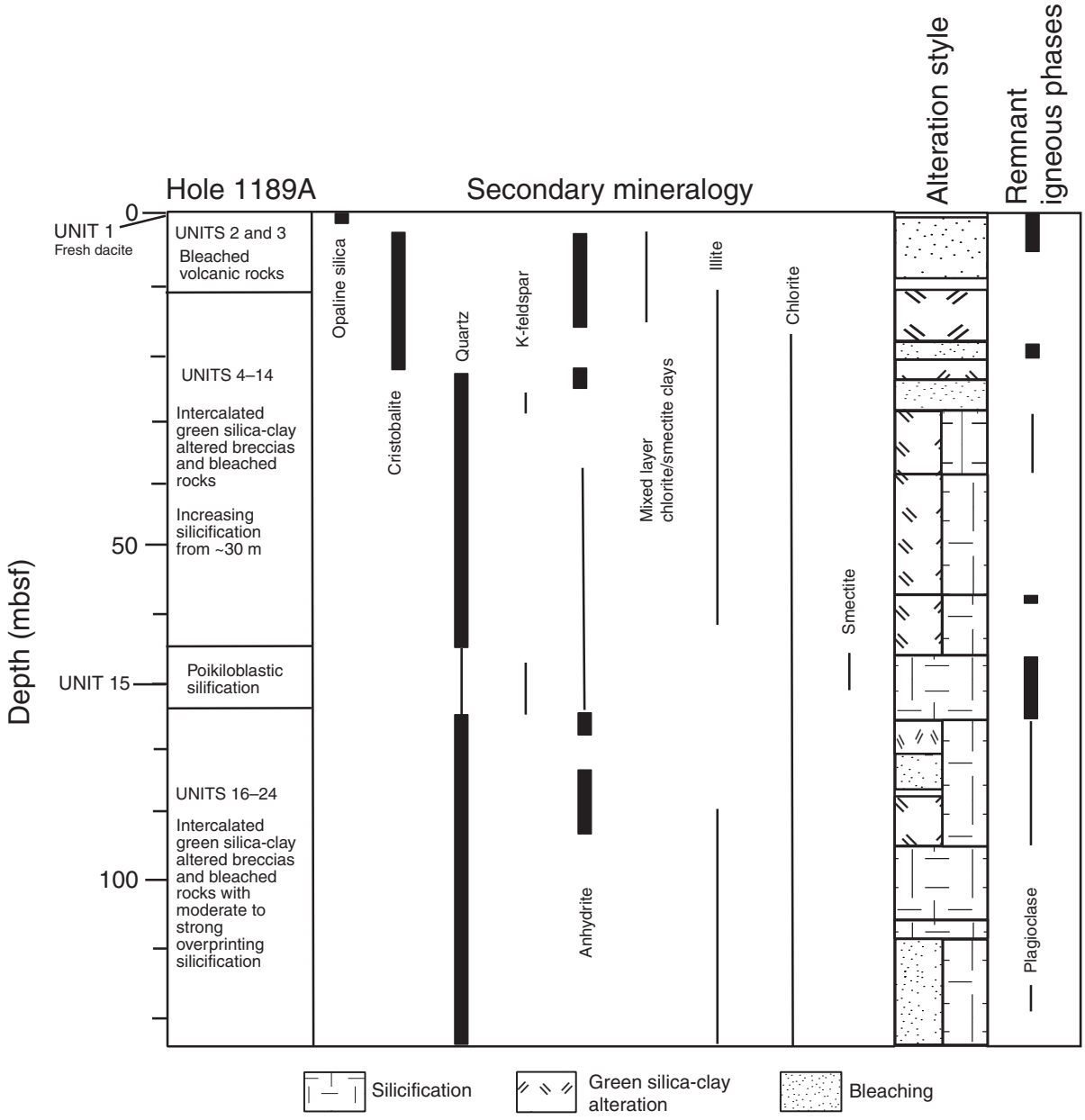

Figure F47. Summary of lithostratigraphic units, alteration type, and distribution of major (thick lines) and minor to trace (thin lines) alteration phases in Hole 1189B. Intervals where remnant igneous plagioclase was detected by X-ray diffraction (XRD) analysis are also indicated on the right side. Pyrite is present in all samples analyzed and is not included in the plot. Shaded intervals = cores where there was no recovery. Clay phases are indicated where detected in XRD analyses; no indication of their abundance relative to one another or to other phases is implied. It is anticipated that detailed postcruise investigation will extend the distribution ranges for some of these minerals. The terms major, minor, and trace as used here apply to XRD analyses and do not imply quantitative abundances (see **"Hydrothermal Alteration,"** p. 8, in the "Explanatory Notes" chapter). As the data are still under evaluation, mineral distribution indicated by the portable infrared mineral analyzer (PIMA) is not included in the plot. (**Figure shown on next page.**)

Figure F47 (continued). (Caption shown on previous page.)

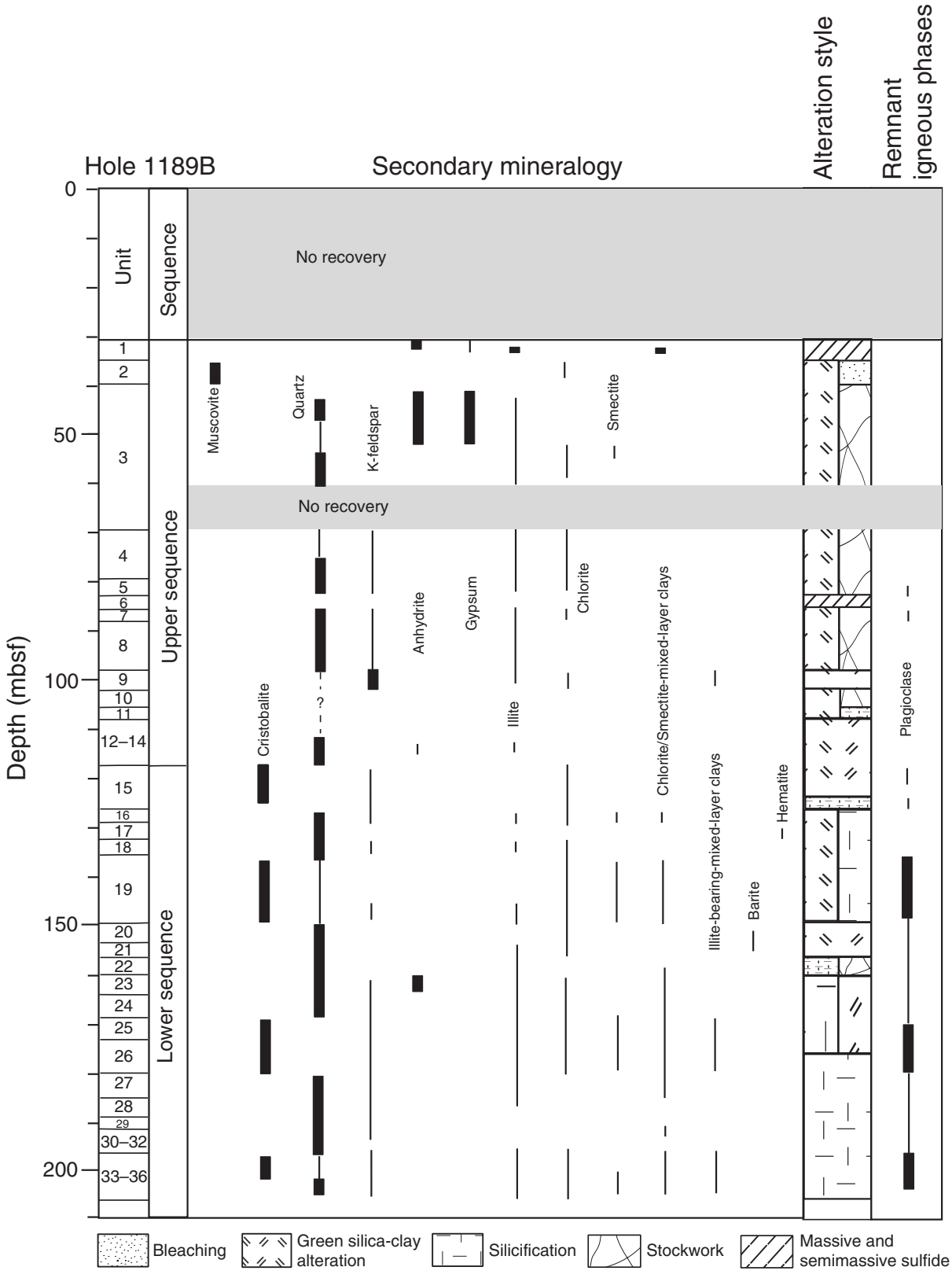

Figure F48. Variation in abundance of minerals with depth at Site 1189, as estimated in thin section for Hole 1189A (solid circles, continuous line) and Hole 1189B (open circles, dashed line). Note the antithetical relationship between quartz and cristobalite + plagioclase.

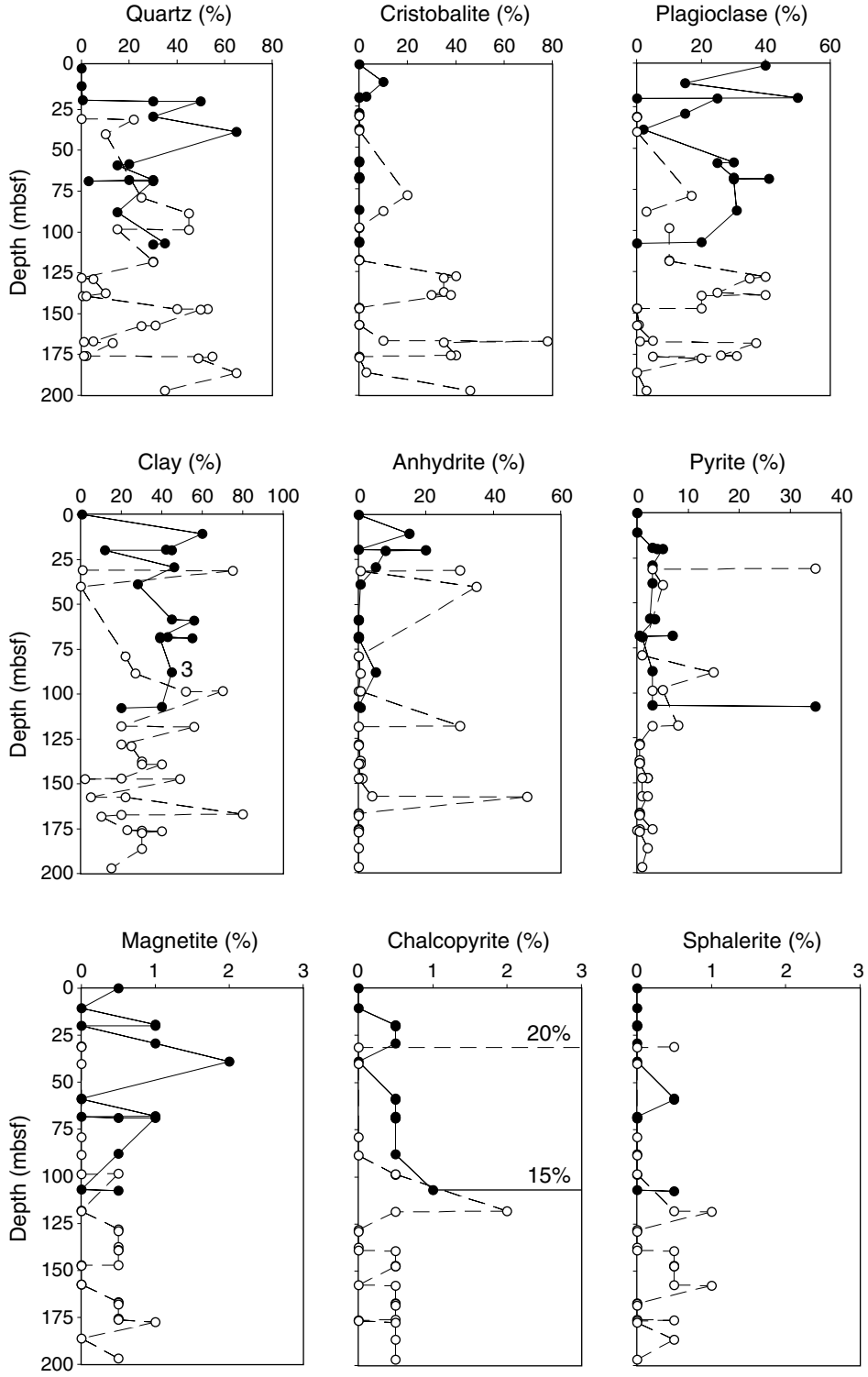

Figure F49. Brecciated, GSC altered rock (Unit 16) with flow-banded, rotated volcanic clasts hosted in a silica-pyrite vein network (interval 193-1189A-9R-1, 17–27 cm).

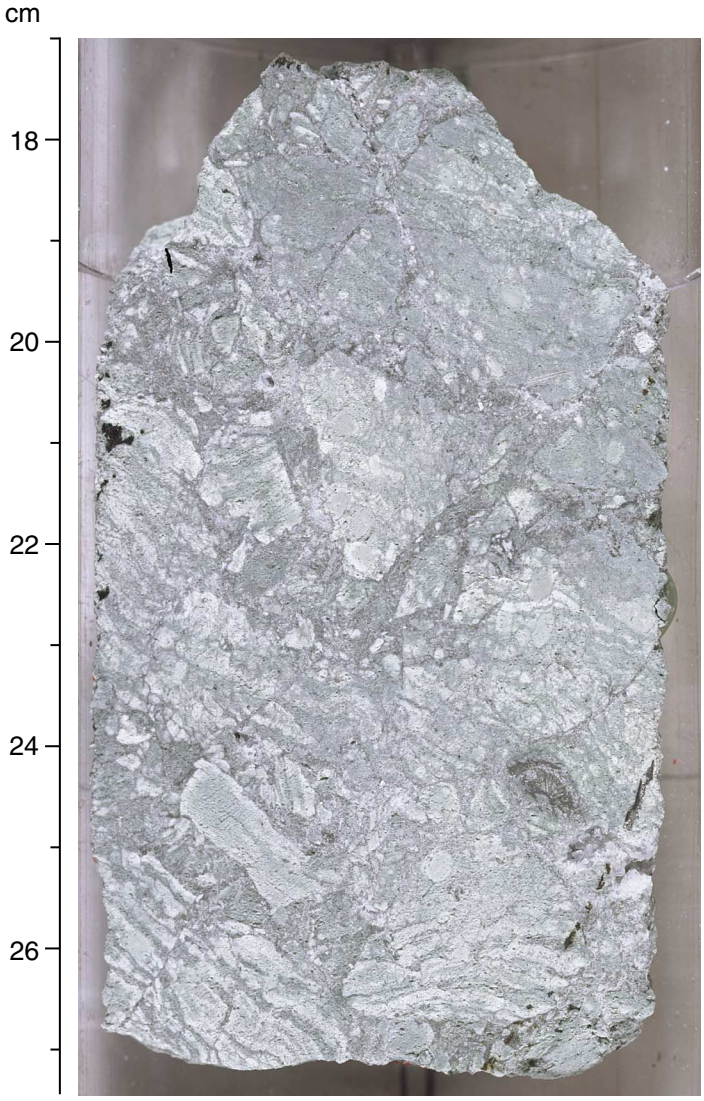

Figure F50. Photomicrograph of a GSC altered volcanic rock with preserved flow-banded texture and late crosscutting quartz veins (interval 193-1189A-5R-1, 14–16 cm, Unit 9, in plane-polarized light; width of view = 5.5 mm. Photomicrograph ID# 1189A_14; **thin section 34**).

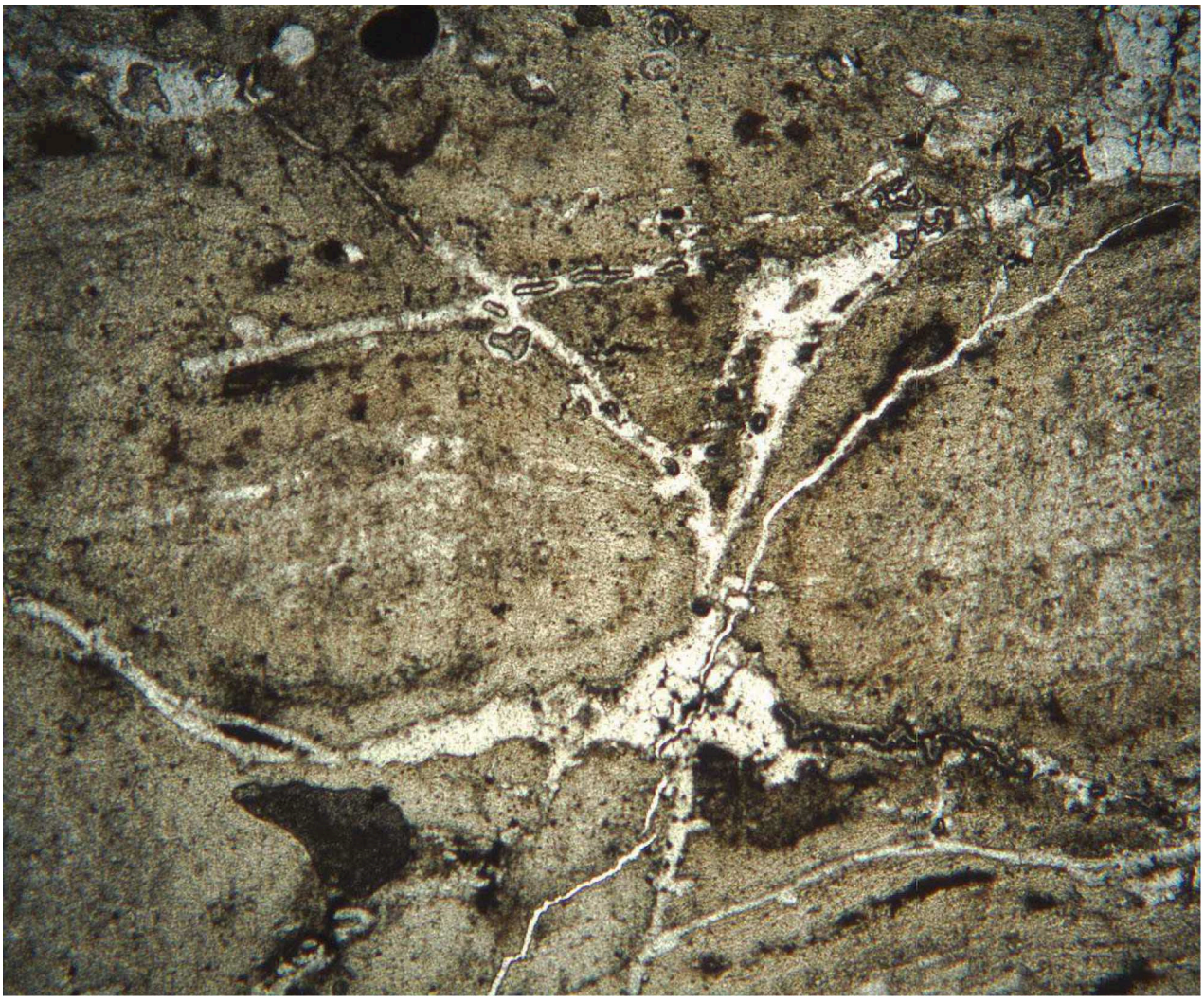

Figure F51. Photomicrograph of anhydrite-quartz-(pyrite) veining between GSC altered volcanic fragments (interval 193-1189A-3R-1, 59–63 cm, Unit 6, in cross-polarized light; width of view = 5.5 mm. Photomicrograph ID# 1189A_22; **thin section 31**).

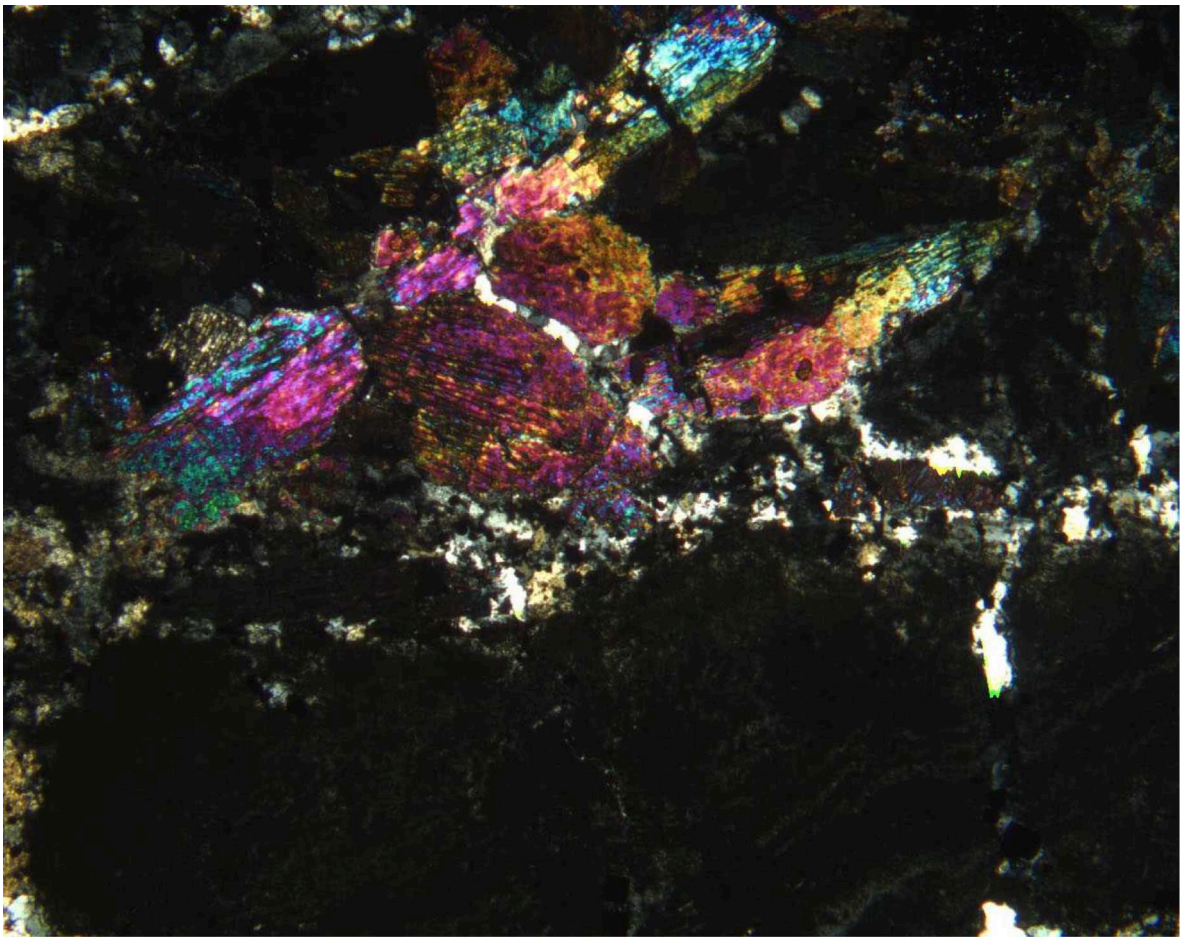

Figure F52. Photomicrograph showing remnant weakly aligned microlitic plagioclase in the groundmass of a bleached, sparsely vesicular volcanic rock. Clearly, alteration in this sample has not been strongly feldspar destructive (interval 193-1189A-3R-1, 6–10 cm, Unit 5, in plane-polarized light; width of view = 0.7 mm. Photomicrograph ID# 1189A_6; **thin section 32**).

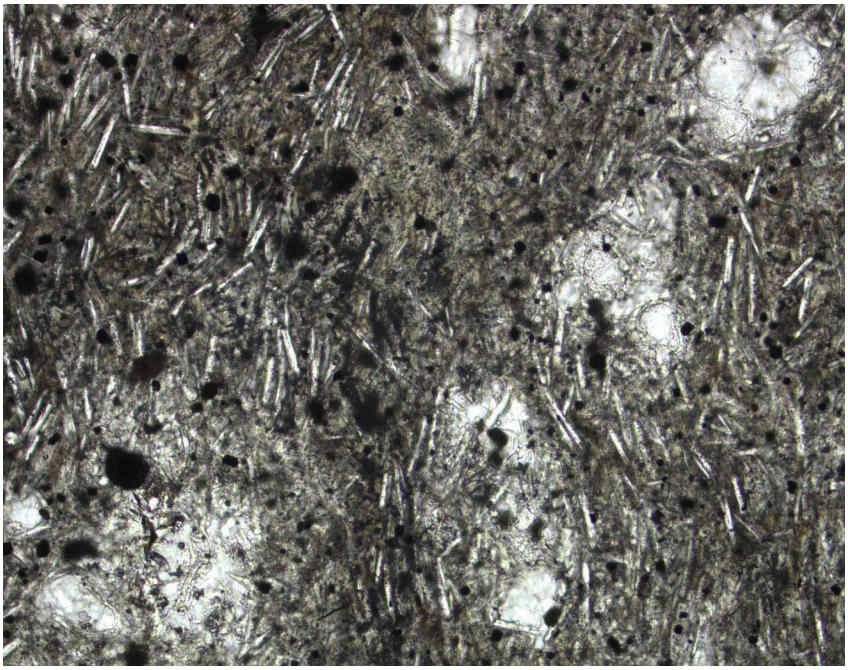

Figure F53. Coarse-grained, bladed anhydrite filling the center of a quartz-pyrite vein in a bleached volcanic rock. Silica-pyrite ± anhydrite veins with bleached alteration halos are abundant in bleached volcanic rocks and are interpreted to be intimately related to the alteration. Anhydrite, where present, is invariably the last phase to precipitate in these veins (interval 193-1189A-3R-1, 70–73 cm, Unit 9, in cross-polarized light; width of view = 2.75 mm. Photomicrograph ID# 1189A_20; **thin section 30**).

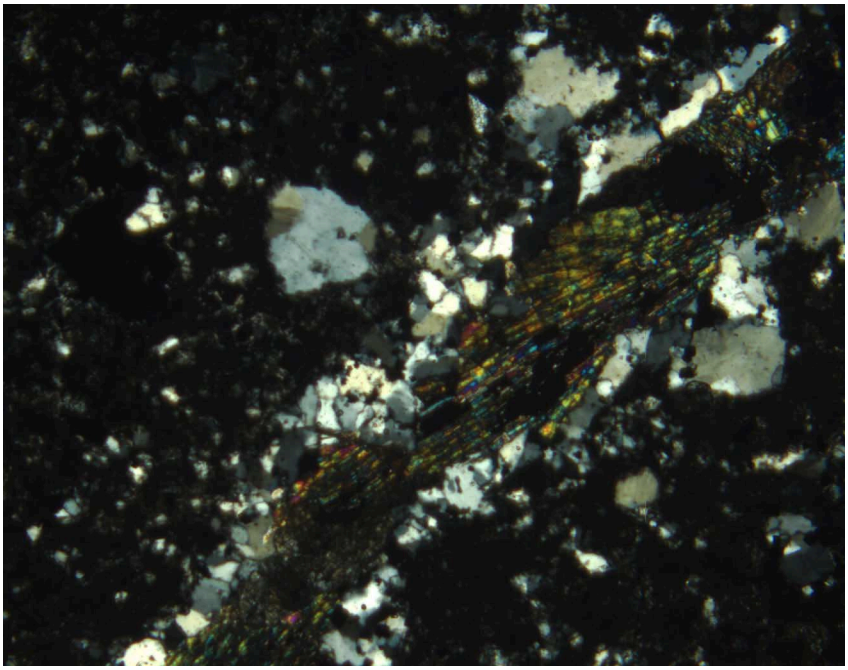

Figure F54. Photomicrograph of a pervasively silicified volcanic rock, showing quartz amygdules, granules, and microcrystalline silica-clay alteration of the formerly glassy portion of the microlitic groundmass. Remnant plagioclase microlites are visible (interval 193-1189A-12R-1, 67–69 cm, Unit 20, in cross-polarized light; width of view = 1.4 mm. Photomicrograph ID# 1189A_85; **thin section 41**).

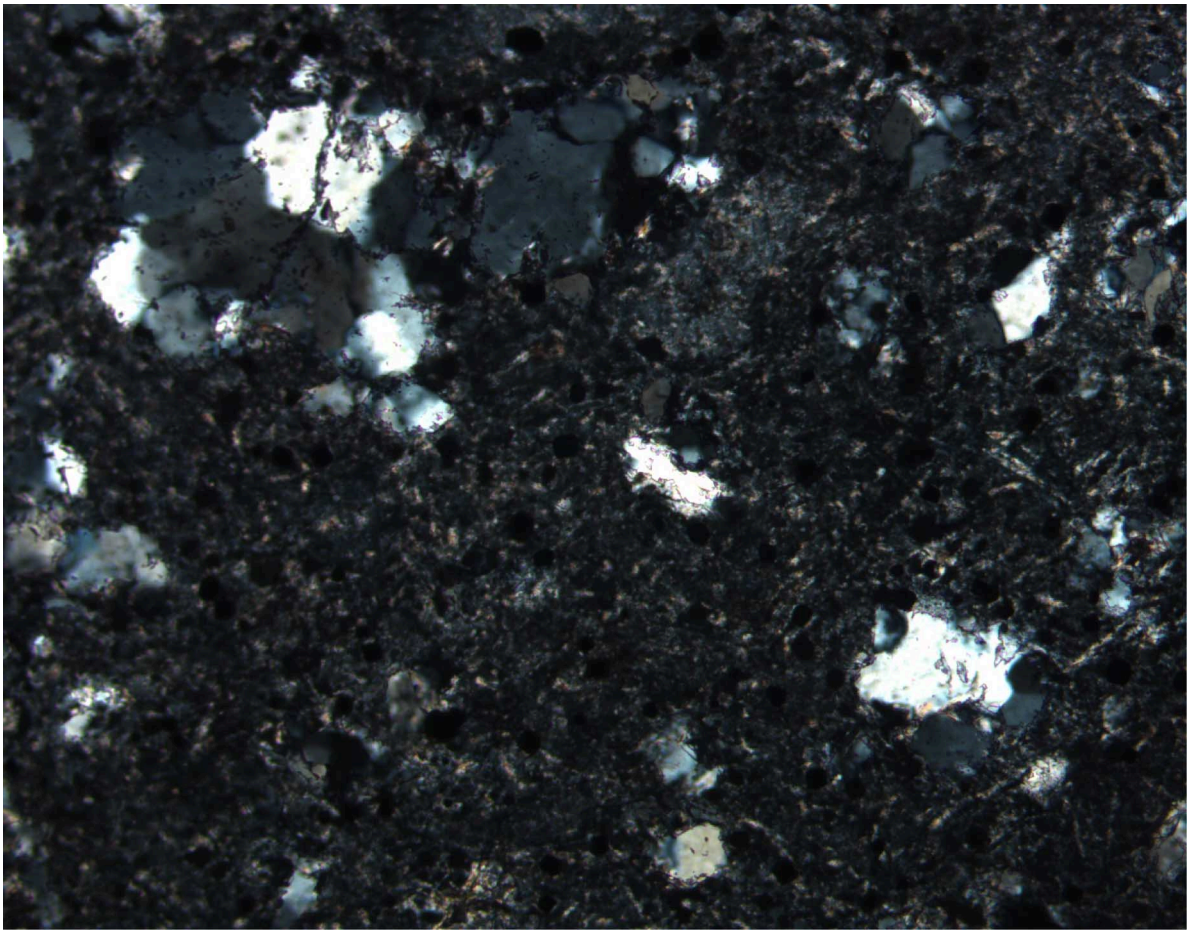

Figure F55. Hand specimen of Unit 15, a plagioclase-rich, poikiloblastically silicified volcanic rock showing a fine network of quartz-pyrite veining and associated jigsaw-fit breccia textures (Sample 193-1189A-8R-1 [Piece 14, 85–93 cm]).

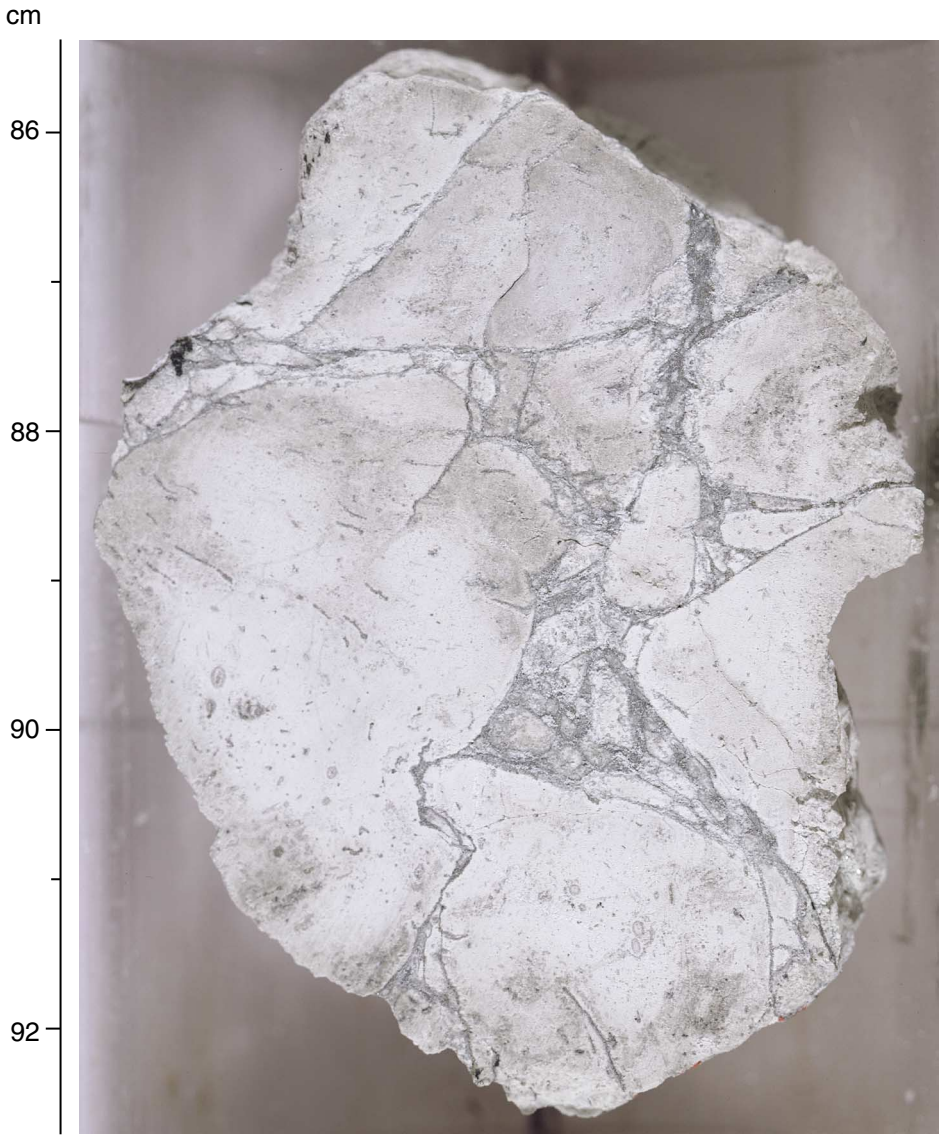

Figure F56. Photomicrographs of poikiloblastic silicification in Unit 15. All images are taken from interval 193-1189A-8R-1, 42–44 cm. **A.** Poikiloblastic quartz overgrowth on a possible quartz phenocryst. The overgrowth is optically continuous with the crystal (in cross-polarized light; width of view = 1.4 mm [Photomicrograph ID# 1189A_49; **thin section 38**]). **B.** Poikiloblastic quartz overgrowth on a quartz-pyrite amygdule (in cross-polarized light; width of view = 0.7 mm [Photomicrograph ID# 1189A_50; **thin section 38**]). **C.** Narrow quartz-pyrite vein with a patchily developed poikiloblastic quartz alteration halo. The poikiloblastic quartz is optically continuous with quartz grains in adjacent segments of the vein (in cross-polarized light; width of view = 1.4 mm [Photomicrograph ID# 1189A_52; **thin section 38**]). **D.** Hairline quartz vein with relatively coarse euhedral pyrite (bluish cream color). Poikiloblastic quartz alteration is developed in the groundmass of the rock in this field of view (in simultaneous plane-polarized transmitted and reflected light; width of view = 1.4 mm [Photomicrograph ID# 1189A_54; **thin section 38**]). (**Figure shown on next page.**)

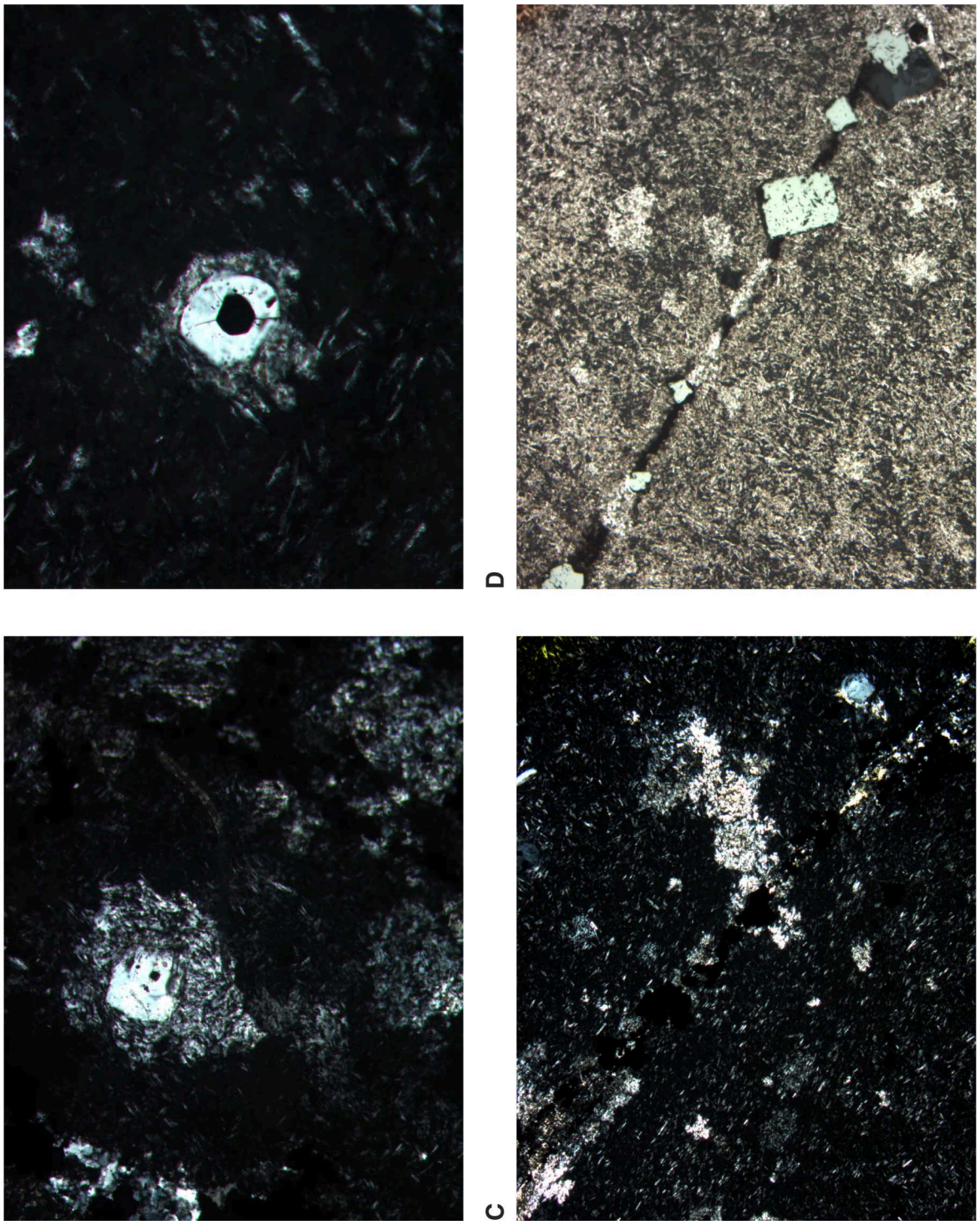

Figure F56 (continued). (Caption shown on previous page.)

Figure F57. Quartz amygdules in a spotted quartz-clay altered groundmass with disseminated pyrite (opaque minerals) from Unit 11, a vesicular sample from the upper sequence of Hole 1189B (interval 193-1189B-8R-1, 37–40 cm, in plane-polarized light; width of view = 2.75 mm [Photomicrograph ID# 1189B_28; **thin section 118**]). Apparent high relief derives from grinding marks on underlying glass slide.

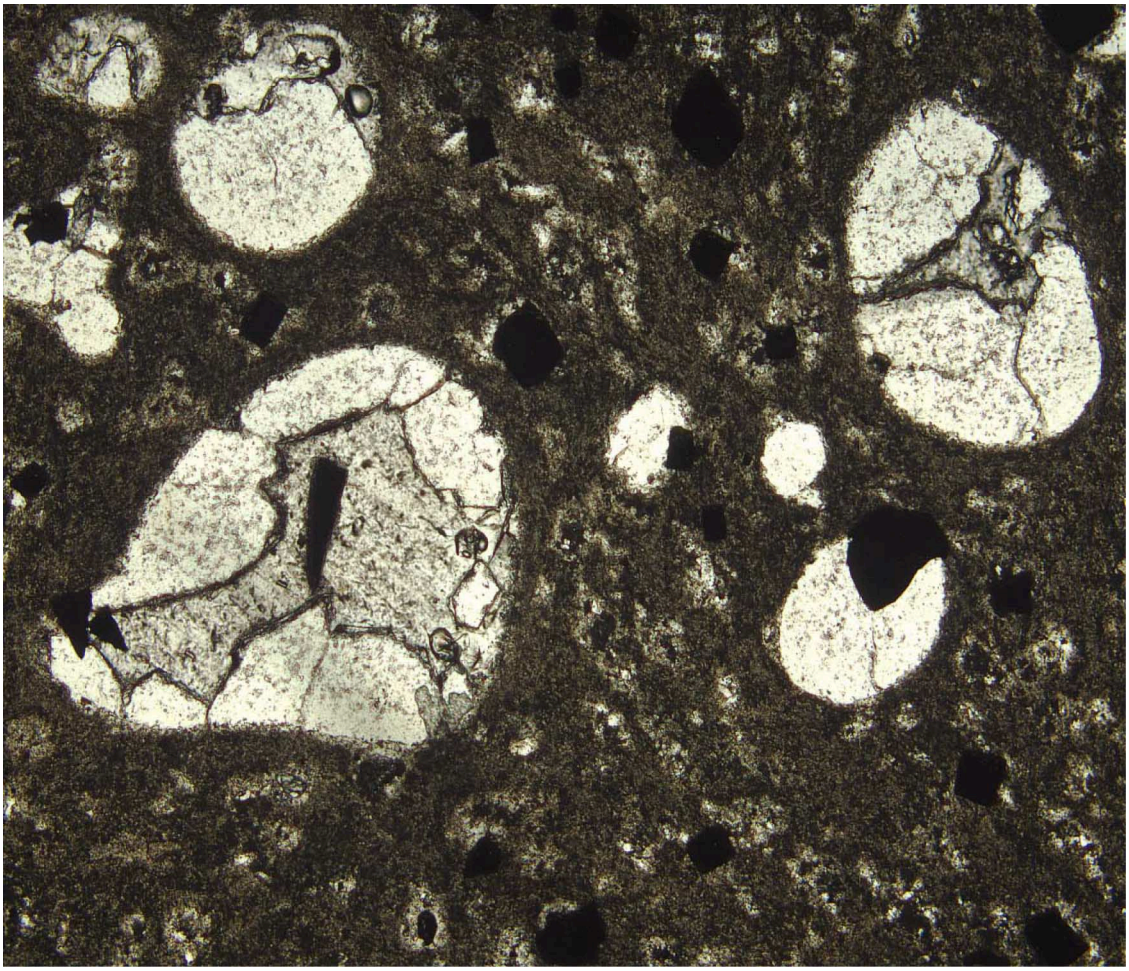

Figure F58. Close-up photograph of a green silicified moderately amygdaloidal, aphyric volcanic rock from Unit 13 with vesicles as large as 5 mm in size, mostly filled with quartz, although some are lined by anhydrite-pyrite. Several hairline quartz-anhydrite-pyrite veins with 1- to 2-mm dark gray siliceous halos are also visible. The coarser vein is filled with anhydrite and minor pyrite (interval 193-1189B-10R-1, 2–14 cm).

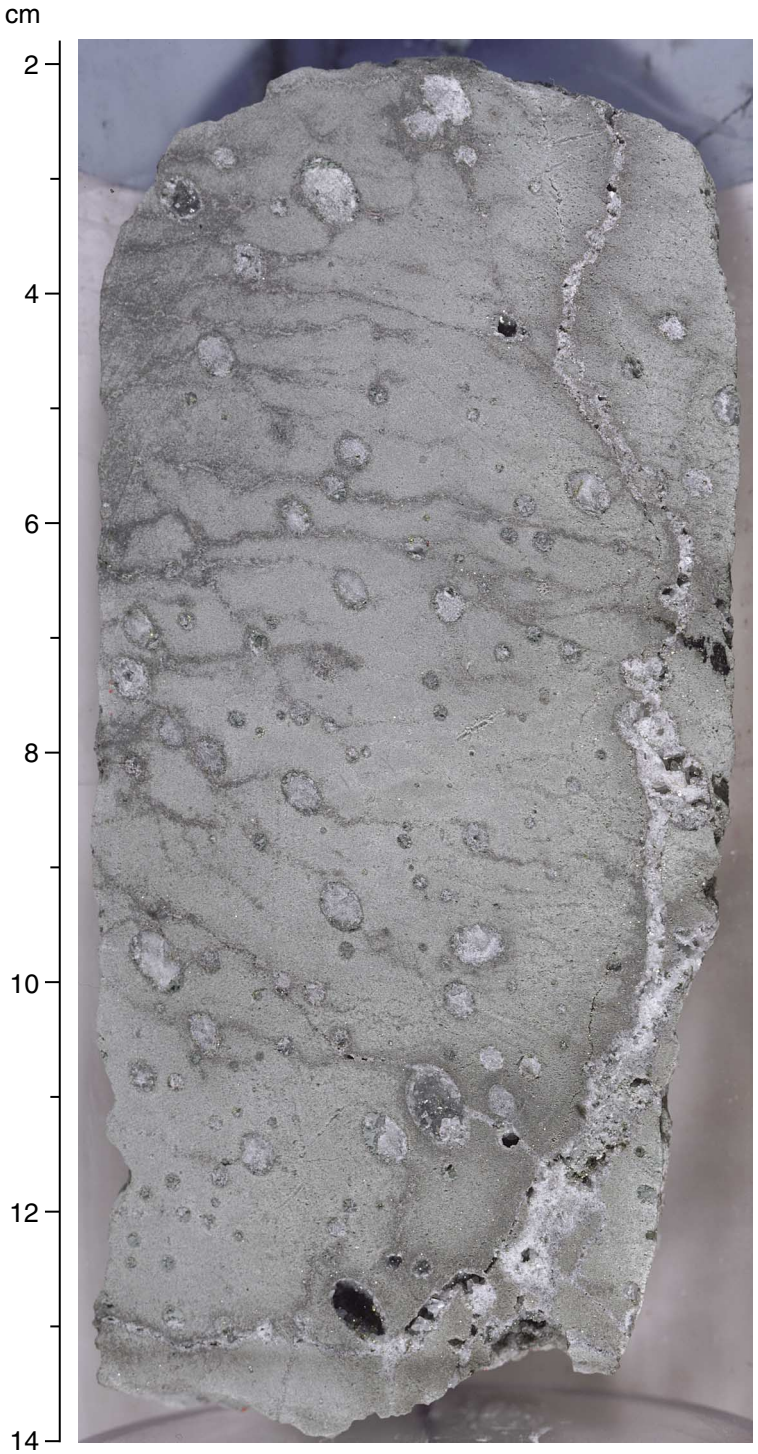

Figure F59. Relationship between volcanic fragments, anhydrite, and gypsum in Unit 3. Both images are from interval 193-1189B-2R-1, 11–14 cm. **A.** Anhydrite surrounded by and replaced along cleavage planes by fibrous gypsum. The opaque minerals are pyrite (in cross-polarized reflected light; width of view = 1.4 mm [Photomicrograph ID# 1189B_4; **thin section 115**]). **B.** Gypsum partly replacing anhydrite, which has partially replaced altered volcanic clasts (in plane-polarized light; width of view = 1.4 mm [Photomicrograph ID# 1189B_25; **thin section 115**]).

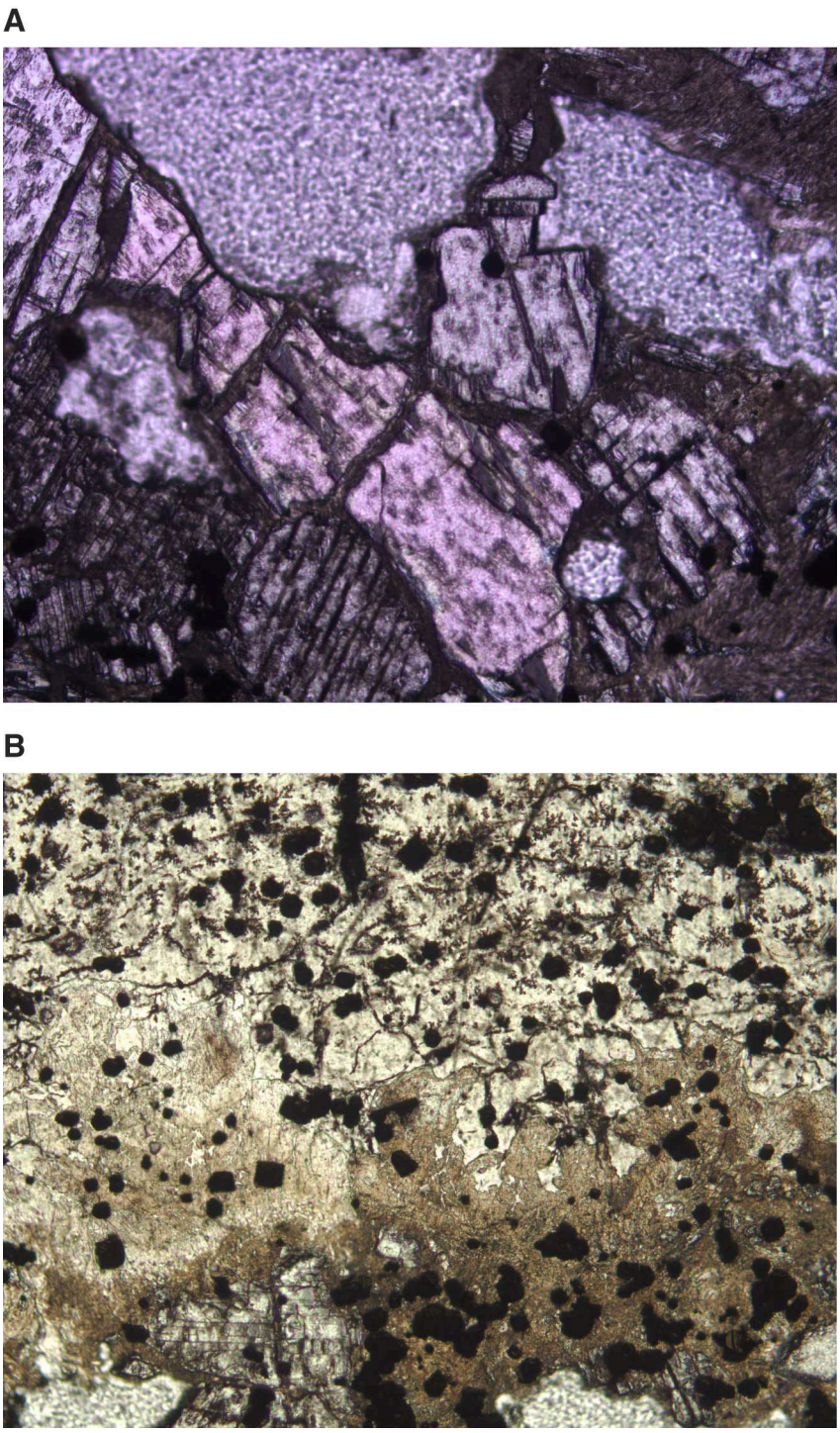

Figure F60. Jasperoidal silica breccia cement from Unit 5. Both images are from interval 193-1189B-6R-1, 13–15 cm. **A.** Jasperoidal quartz showing strong red internal reflections (in cross-polarized reflected light; width of view = 1.4 mm [Photomicrograph ID# 1189B_13; **thin section 116**]). **B.** Hematite completely enclosed in crystalline quartz. The opaque phase is pyrite (in cross-polarized reflected light; width of view = 1.4 mm [Photomicrograph ID# 1189B_14; **thin section 116**]).

A

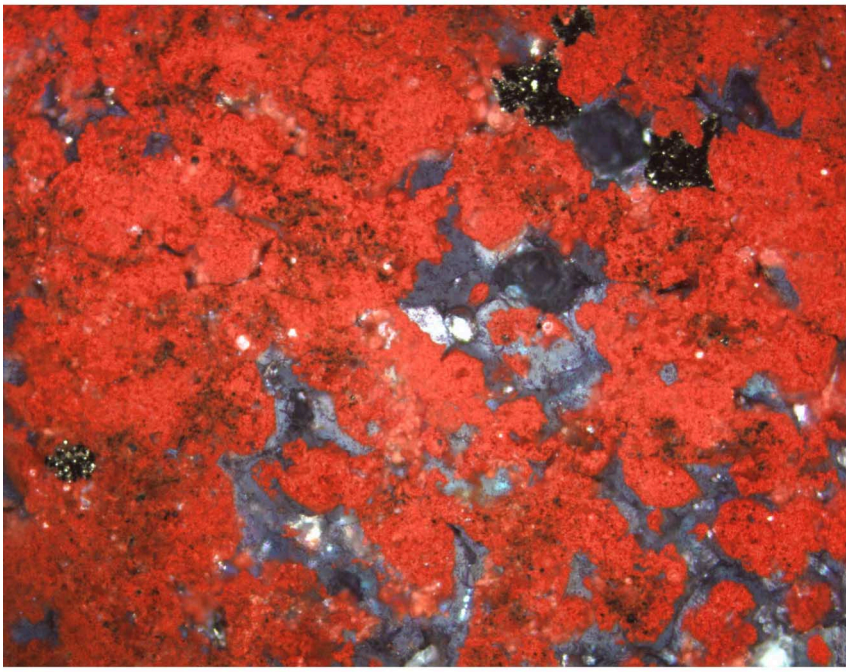

B

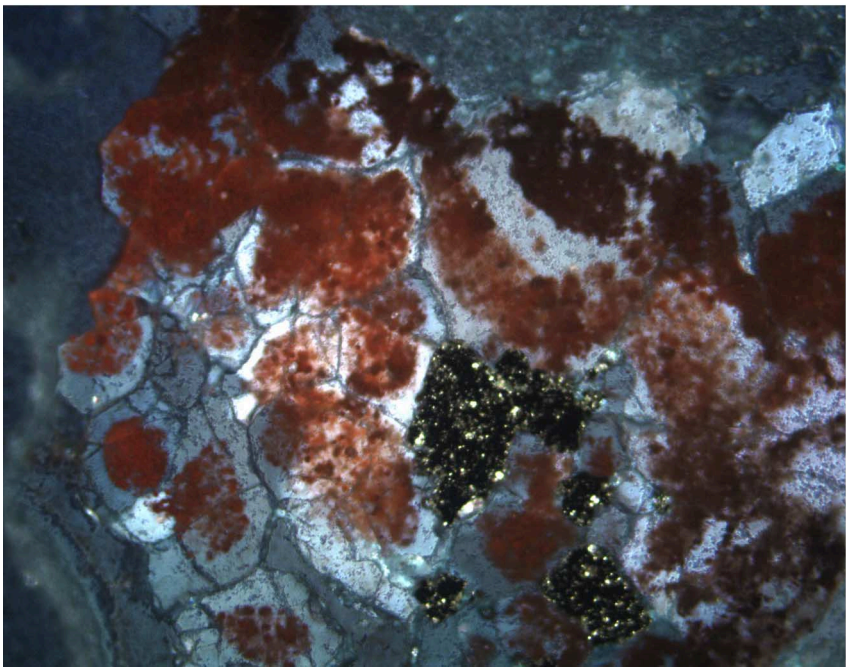

Figure F61. Hand specimen (Unit 8) of matrix-supported breccia comprising soft, clay-rich clasts with 2% disseminated pyrite hosted in an anhydrite-quartz-pyrite cement. Anhydrite is present as vug fill (cf. Fig. F109, p. 181) (Sample 193-1189B-7R-1 [Piece 1, 0–5 cm] at 88.70 mbsf).

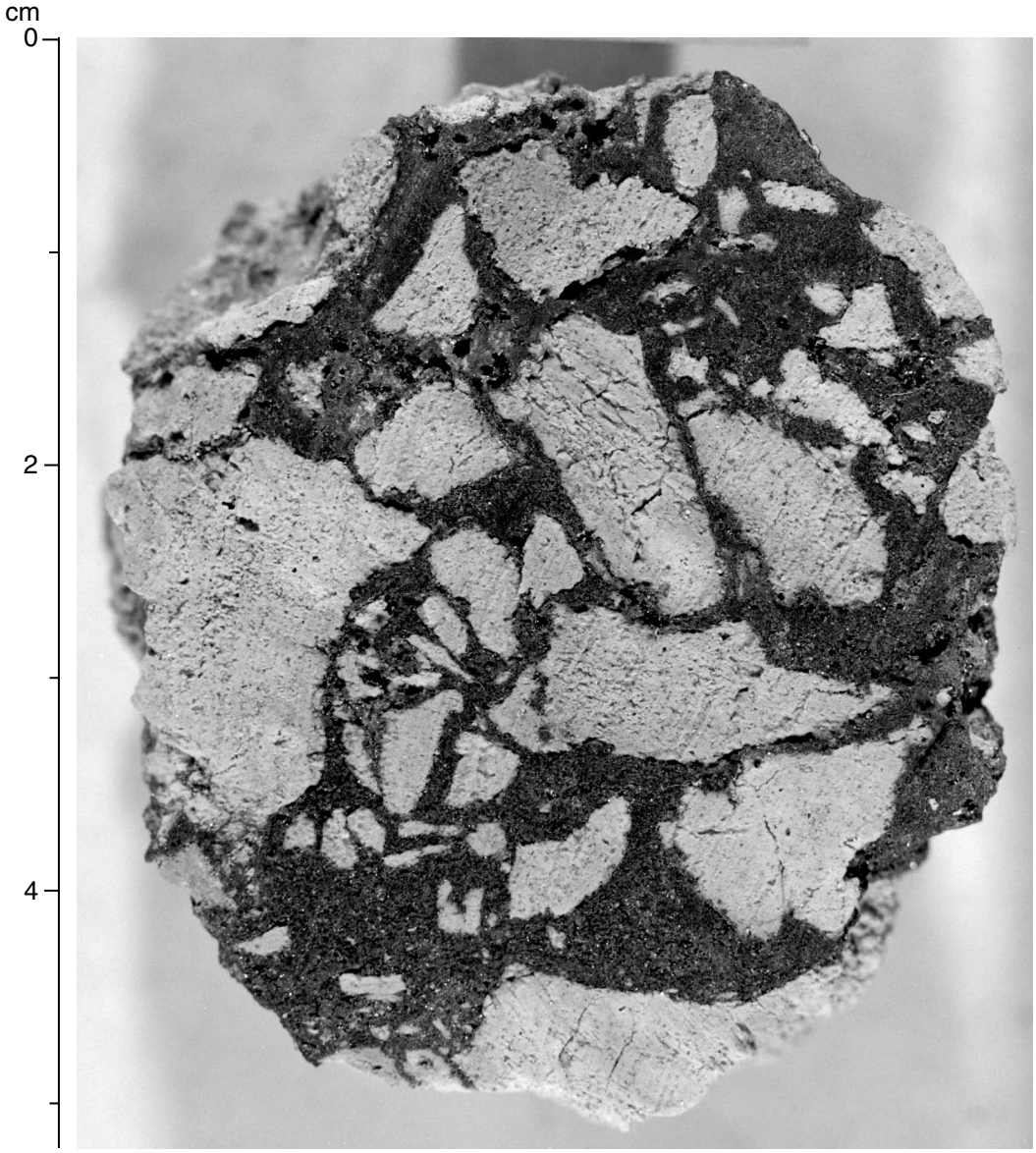

Figure F62. Photograph of moderately vesicular aphyric volcanic rock. The groundmass shows a spotty hieroglyphic texture caused by incomplete hydrothermal alteration with white, angular shard-shaped domains representing remnants of less altered groundmass (interval 193-1189B-16R-1, 114–121 cm).

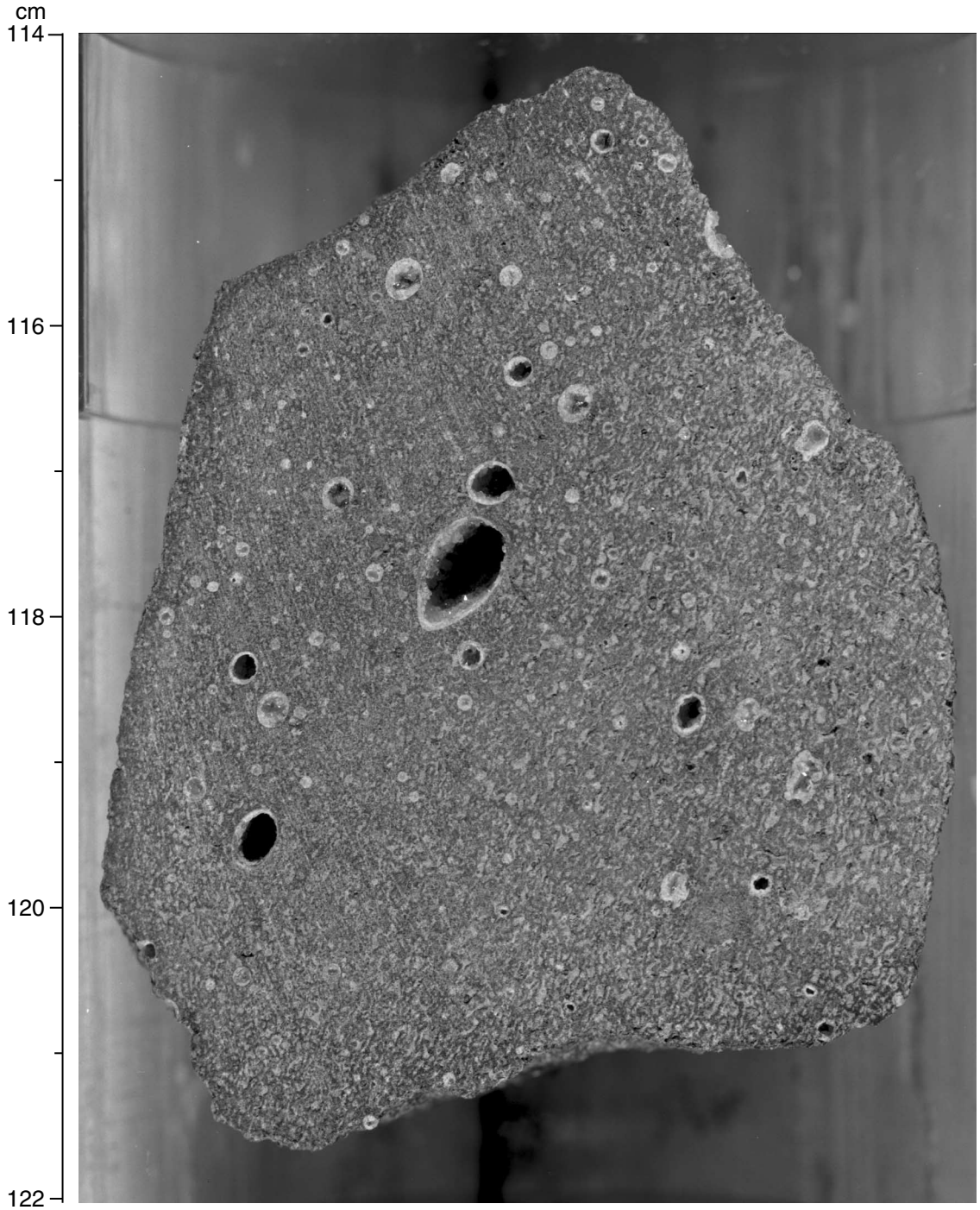

Figure F63. Intensely veined, weakly vesicular and sparsely plagioclase phyric volcanic rock, which is cut by a fine network of quartz-pyrite-magnetite veins with magnetite bearing alteration halos (Unit 26). Brecciation associated with the veining locally imparted a jigsaw-fit pattern on the otherwise coherent rock. In the upper right part of the piece, at 19 cm, a thin anhydrite vein (white) can be seen crosscutting the quartz-magnetite-pyrite vein network (Section 193-1189B-16R-1 [Piece 3, 16–26 cm] at 175.85 mbsf).

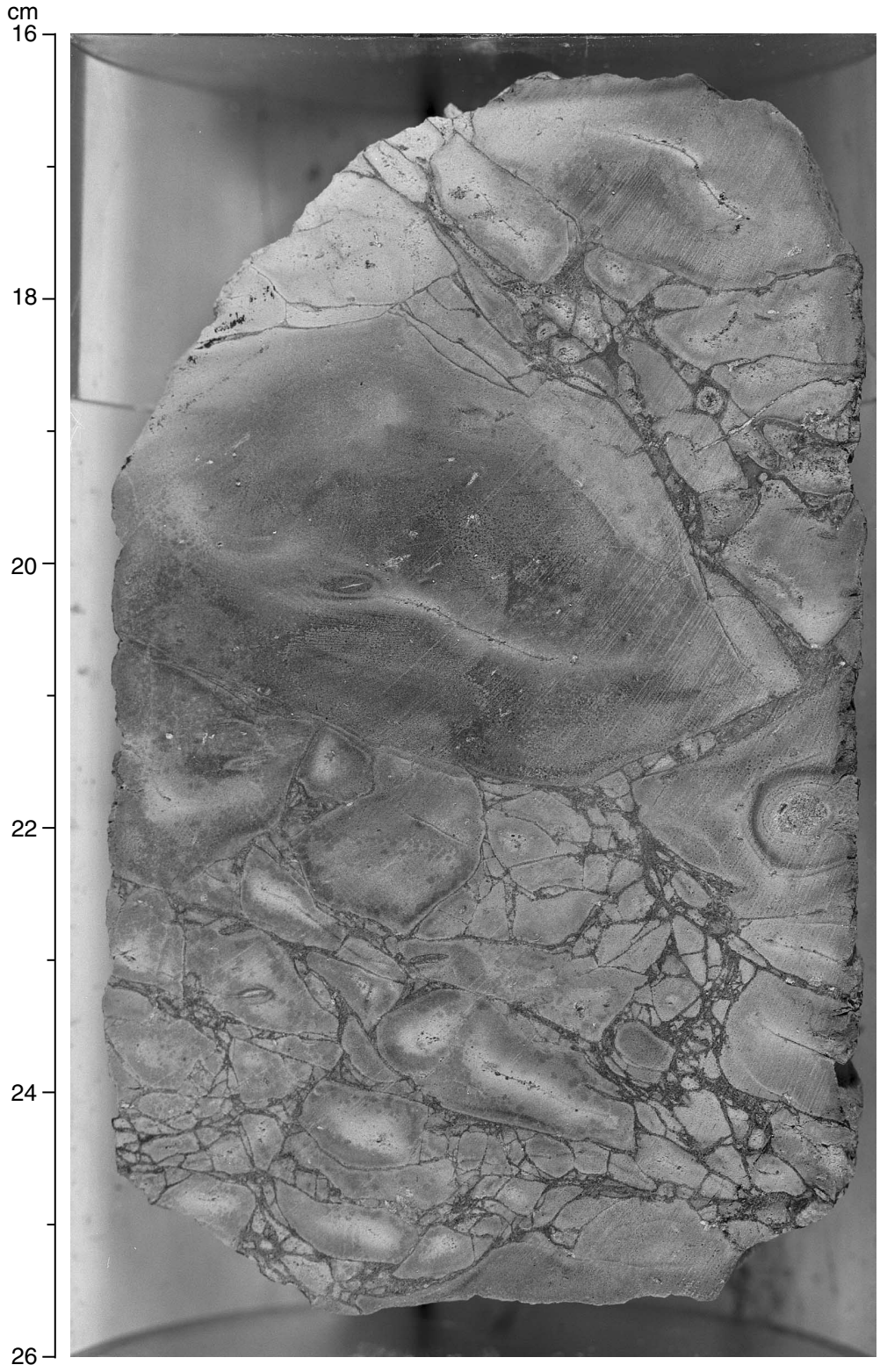

Figure F64. Breccia, comprising flow-banded, green silica-clay–altered, soft, white to light greenish-gray volcanic clasts, which are hosted in a quartz-rich cement. Note the pale, incipiently silicified margins of the clasts. Coarse anhydrite crystals are present as late vug fill in the clasts and matrix (Unit 23; interval 193-1189B-14R-1, 76–85 cm).

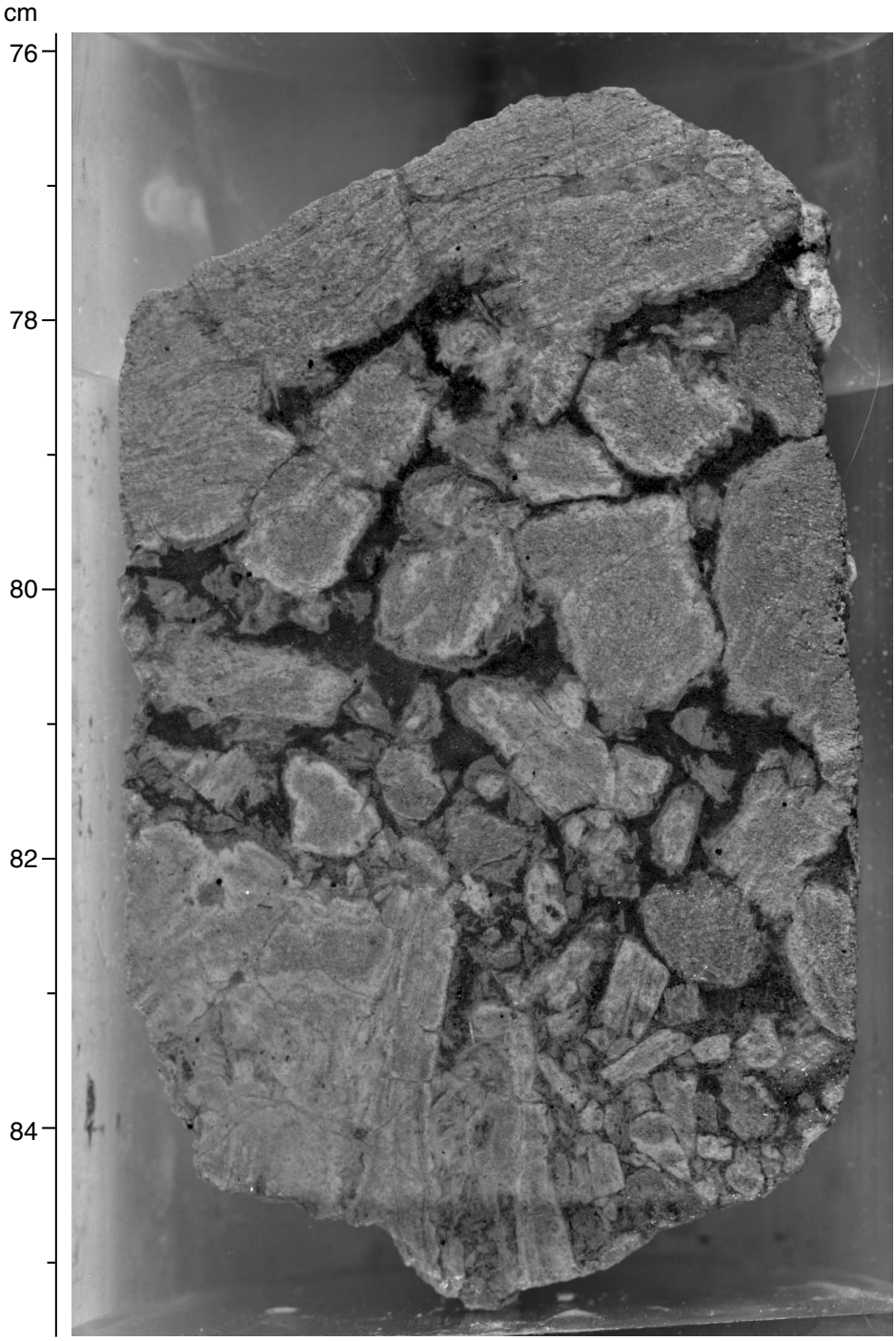

Figure F65. Partly coherent, flow-banded jigsaw-fit breccia, dissected by a network of quartz-sphalerite-pyrite veins with late anhydrite fill in vein centers. Vugs (10 mm in diameter) are rimmed by quartz-sphalerite-pyrite and have anhydrite cores (Unit 23; interval 193-1189B-14R-1, 107–118 cm).

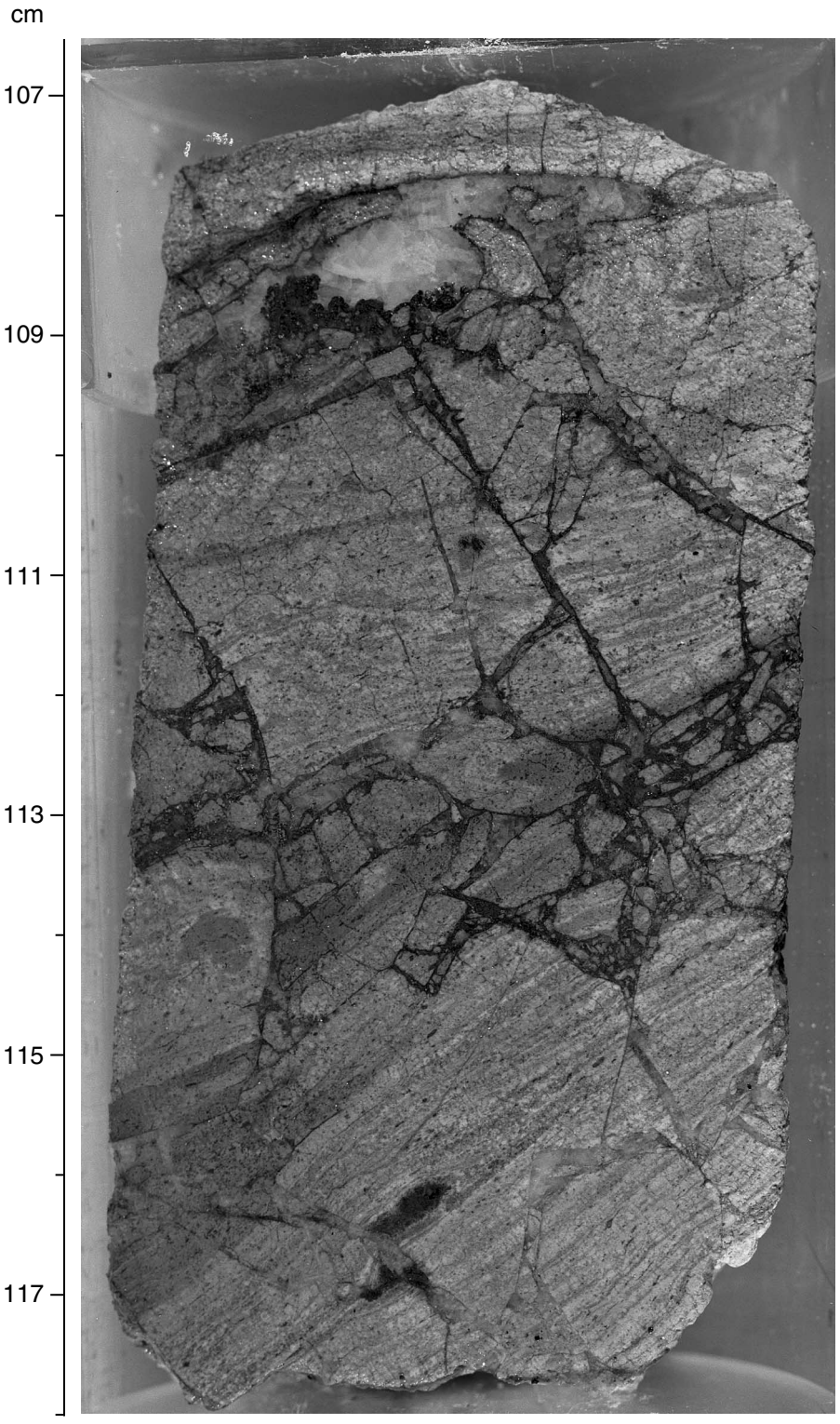

Figure F66. Rotated flow-banded fragments set in a dark gray, soft, vuggy matrix, and with spherulitic domains (Unit 25; interval 193-1189B-15R-1, 119–130 cm).

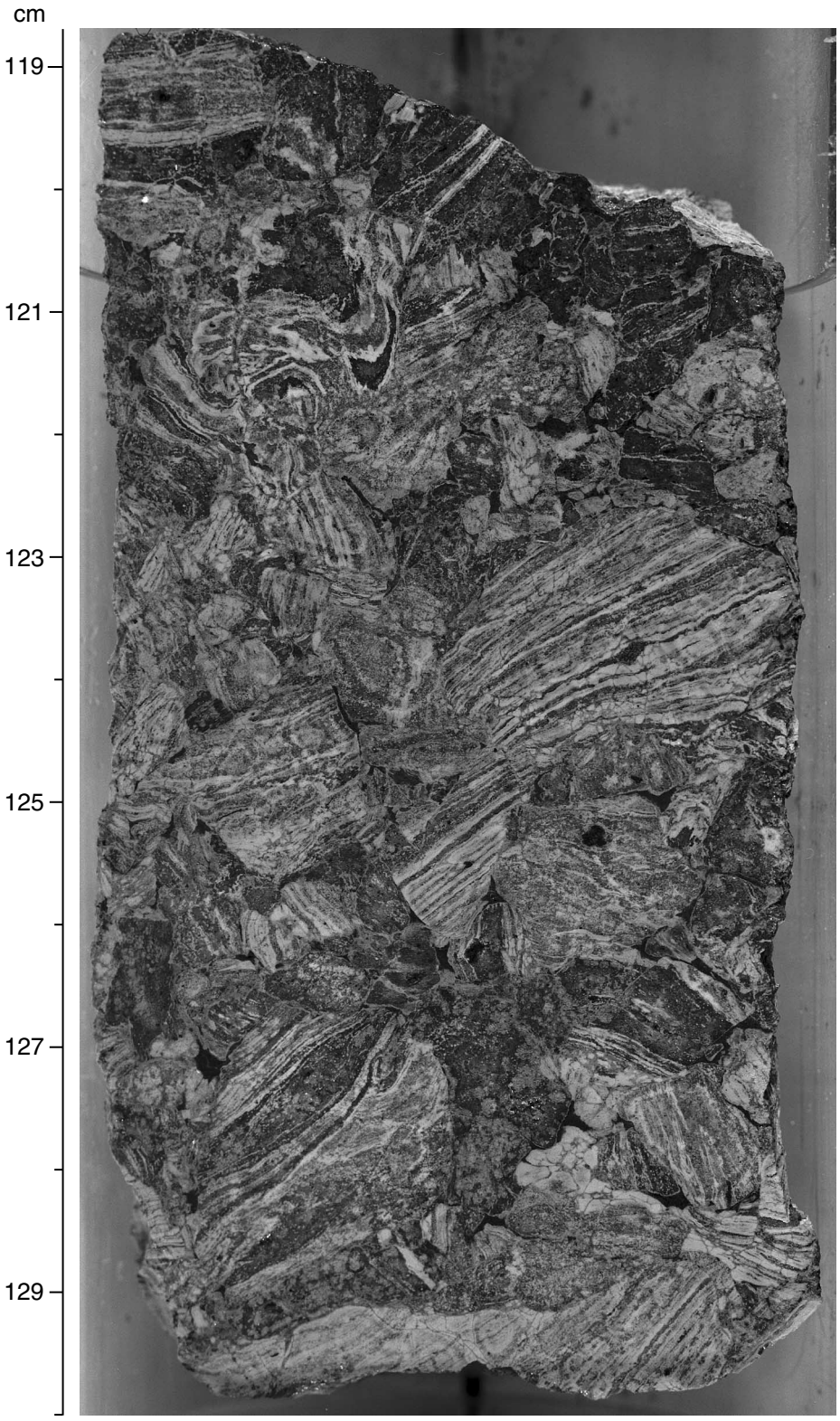

Figure F67. Photograph of coherent flow-banded core piece, with a pseudobreccia appearance created by silica-clay alteration halos around a feeble network of silica veins (interval 193-1189B-15R-1, 130–135 cm).

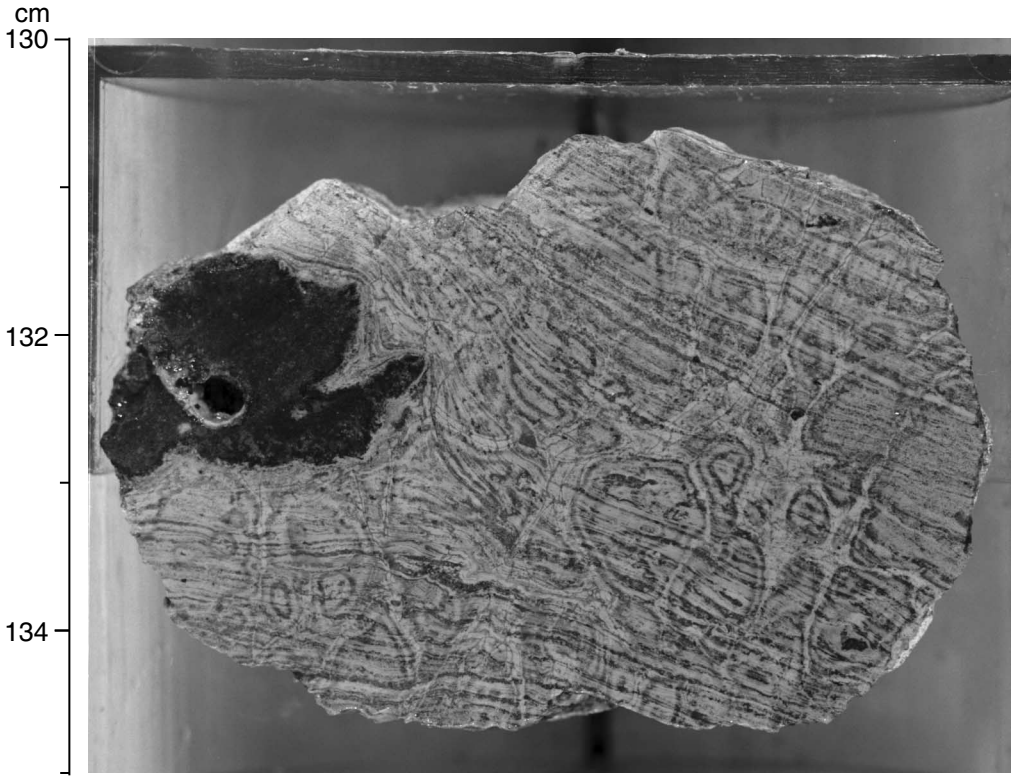

Figure F68. Unit 35 is a polymict volcaniclastic breccia with flow-banded clasts, dark green porous clasts, perlitic clasts, and textureless bleached clasts cemented in a quartz-hematite-sulfide matrix. Folded flow banding in one clast is truncated at the hinge of the fold, clearly indicating that the clast was abraded during transport. Fine sulfide veins in the clasts are terminated at the boundary of fragments, indicating that the formation of these veins predates erosion and deposition of the clasts (interval 193-1189B-18R-2, 49–58 cm).

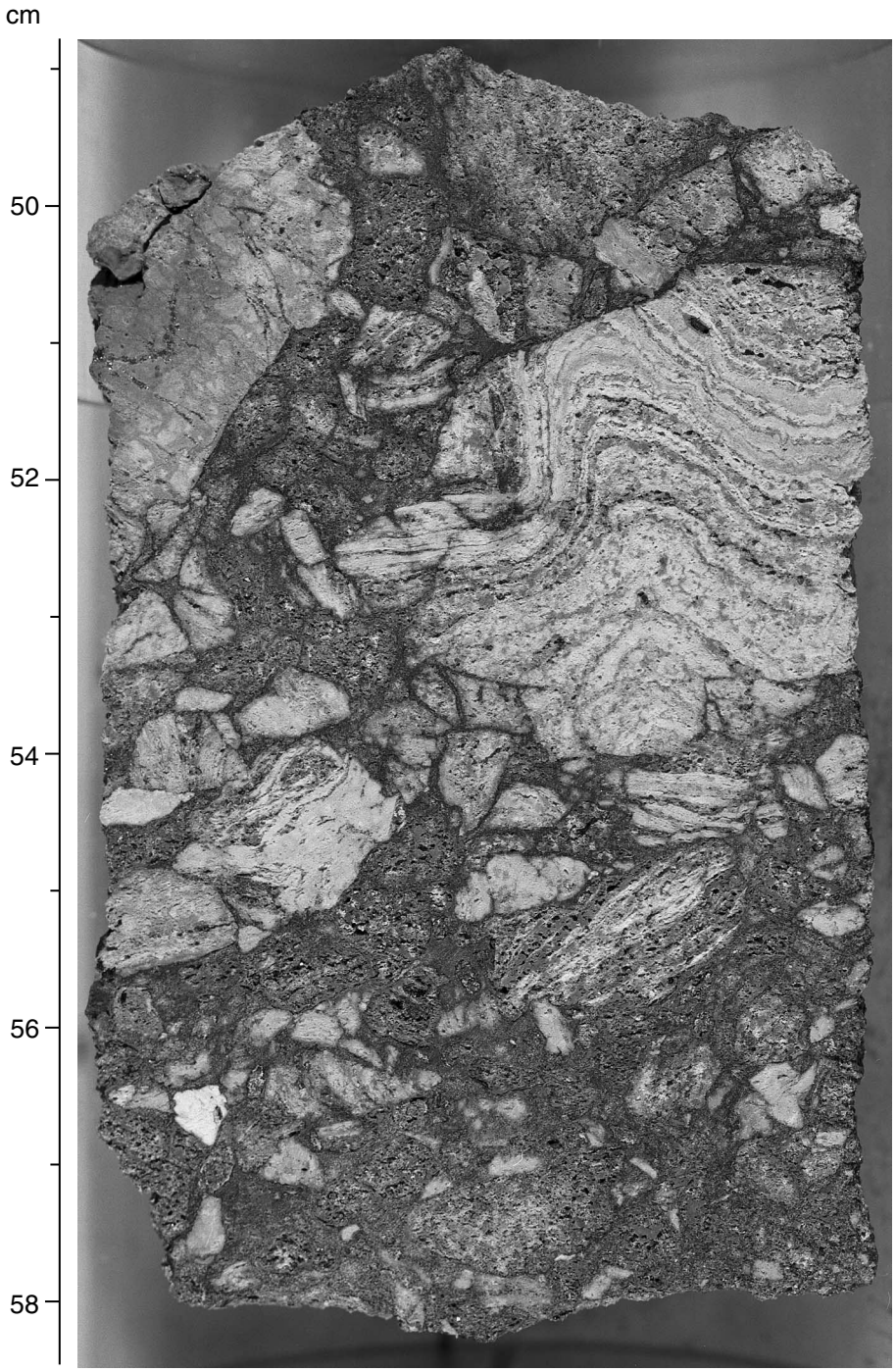

Figure F69. Chalcopyrite-sphalerite bearing clast in volcaniclastic sandstone. Both images are from Unit 31, interval 193-1189B-17R-1, 98–100 cm. **A.** Overview showing the relationship of the clast to the surrounding sedimentary matrix (in cross-polarized light; width of view = 1.4 mm [Photomicrograph ID# 1189B_61; thin section 139]). **B.** Increased magnification reflected light view of opaque phases (chalcopyrite and sphalerite) from the previous image (width of view = 0.7 mm [Photomicrograph ID# 1189B_62; thin section 139]).

A

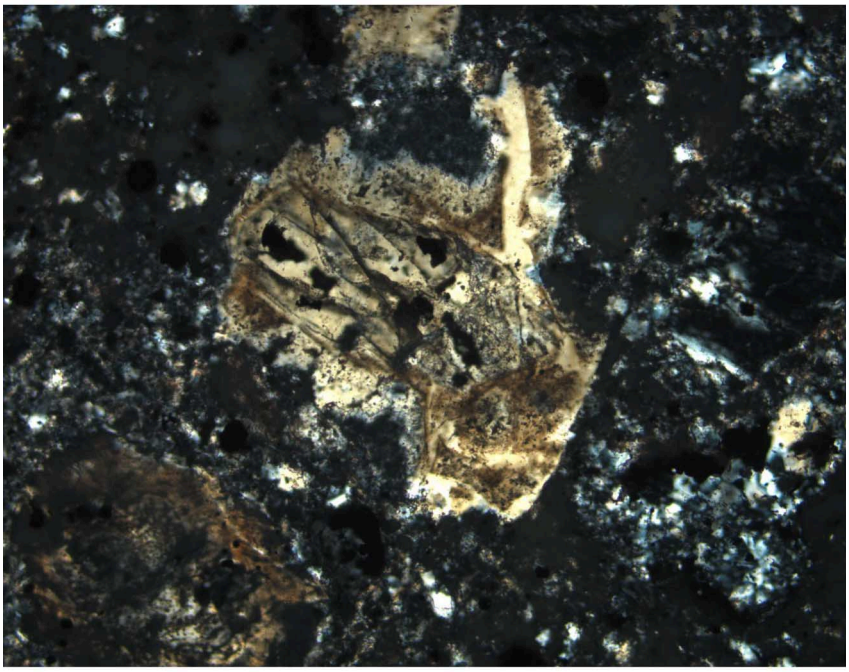

B

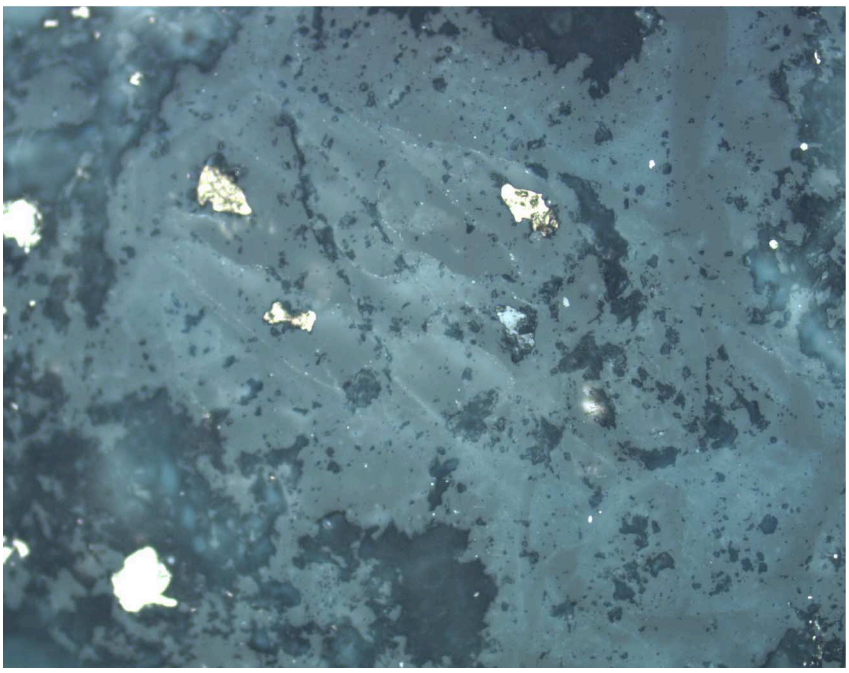

Figure F70. Barite (low birefringence) replacing and overgrowing anhydrite in a quartz-breccia matrix (interval 193-1189B-13R-1, 34–36 cm, Unit 20, in cross-polarized light; width of view = 1.4 mm [Photomicrograph ID# 1189B_54; **thin section 128**]).

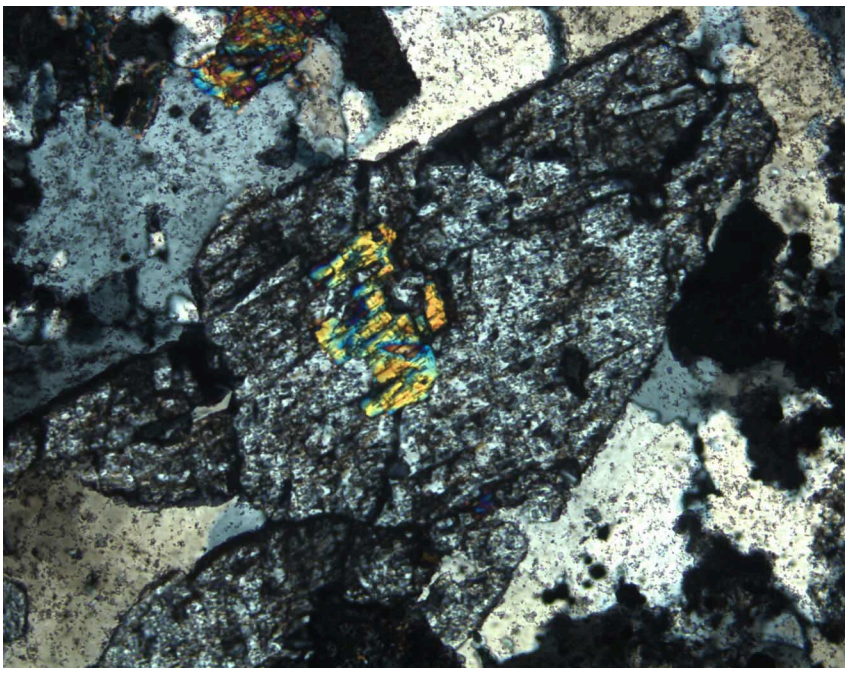

Figure F71. Type 2 anhydrite-quartz-pyrite vein in altered breccia (Sample 193-1189A-10R-1 [Piece 10A]; width of view = 25 mm).

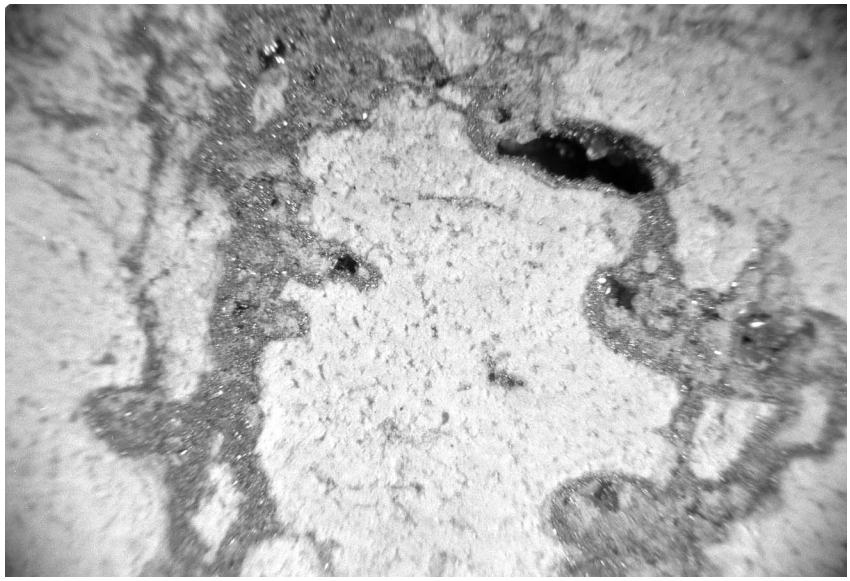

Figure F72. Narrow anastomosing quartz veins (medium gray) in altered rock. Pyrite (white) occurs both within the veins and the wallrock (Sample 193-1189A-3R-1 [Piece 10, 59–63 cm] in reflected light; width of view = 2.75 mm. Photomicrograph ID# 1189A_27; **thin section 31**).

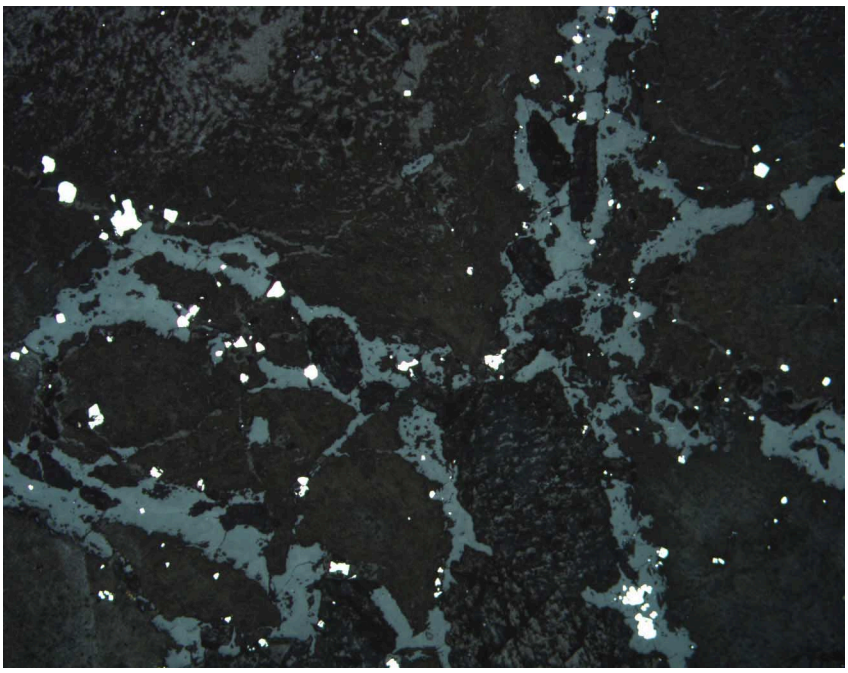

Figure F73. Type 2 anhydrite-quartz-pyrite vein with cockade structure (Sample 193-1189A-3R-1 [Piece 16A]); width of view = 25 mm).

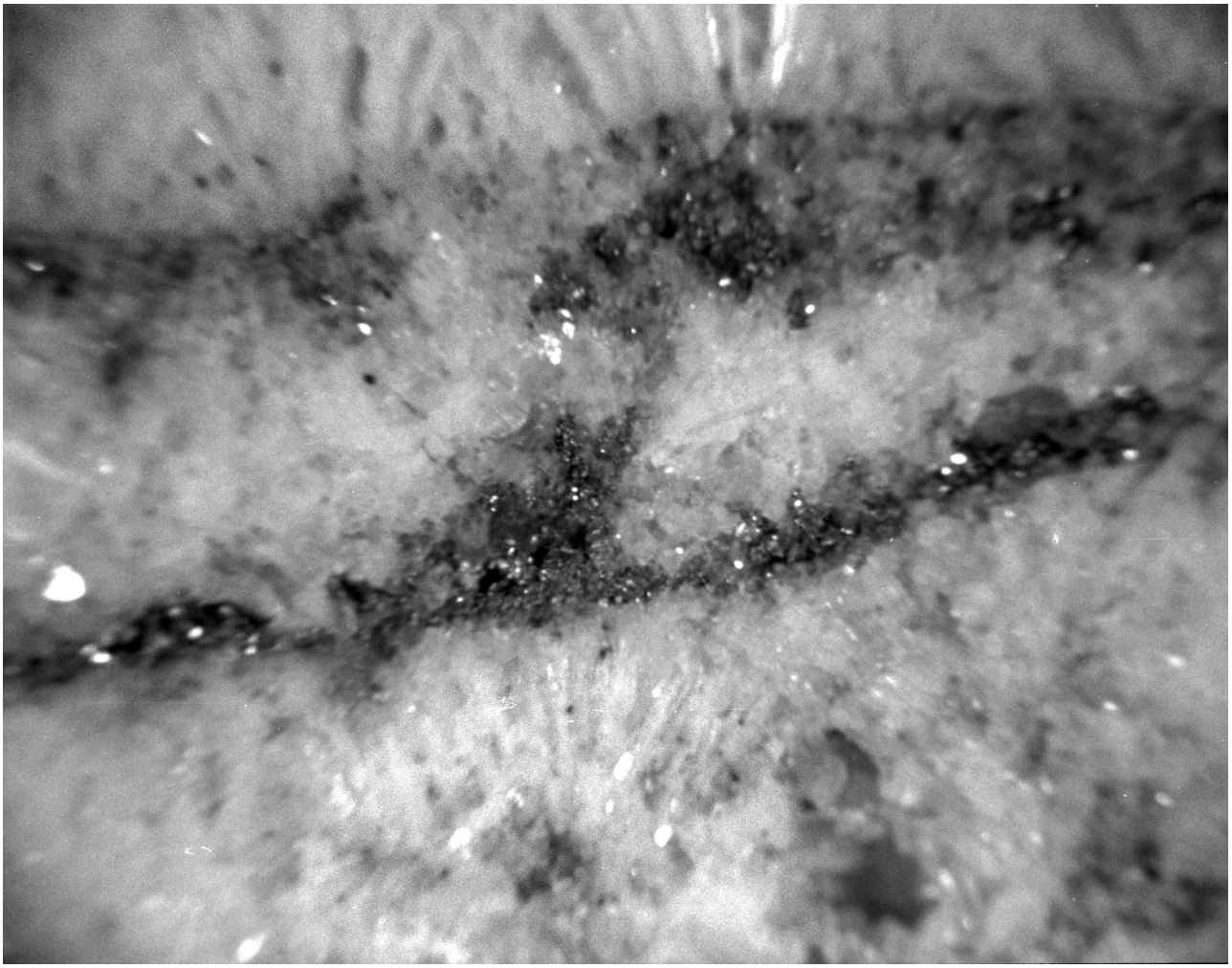

Figure F74. Semimassive sulfide consisting of pyrite and chalcopyrite grains in a quartz-rich matrix. Angular white fragments are altered volcanic rock (Sample 193-1189A-12R-1, 120–128 cm).

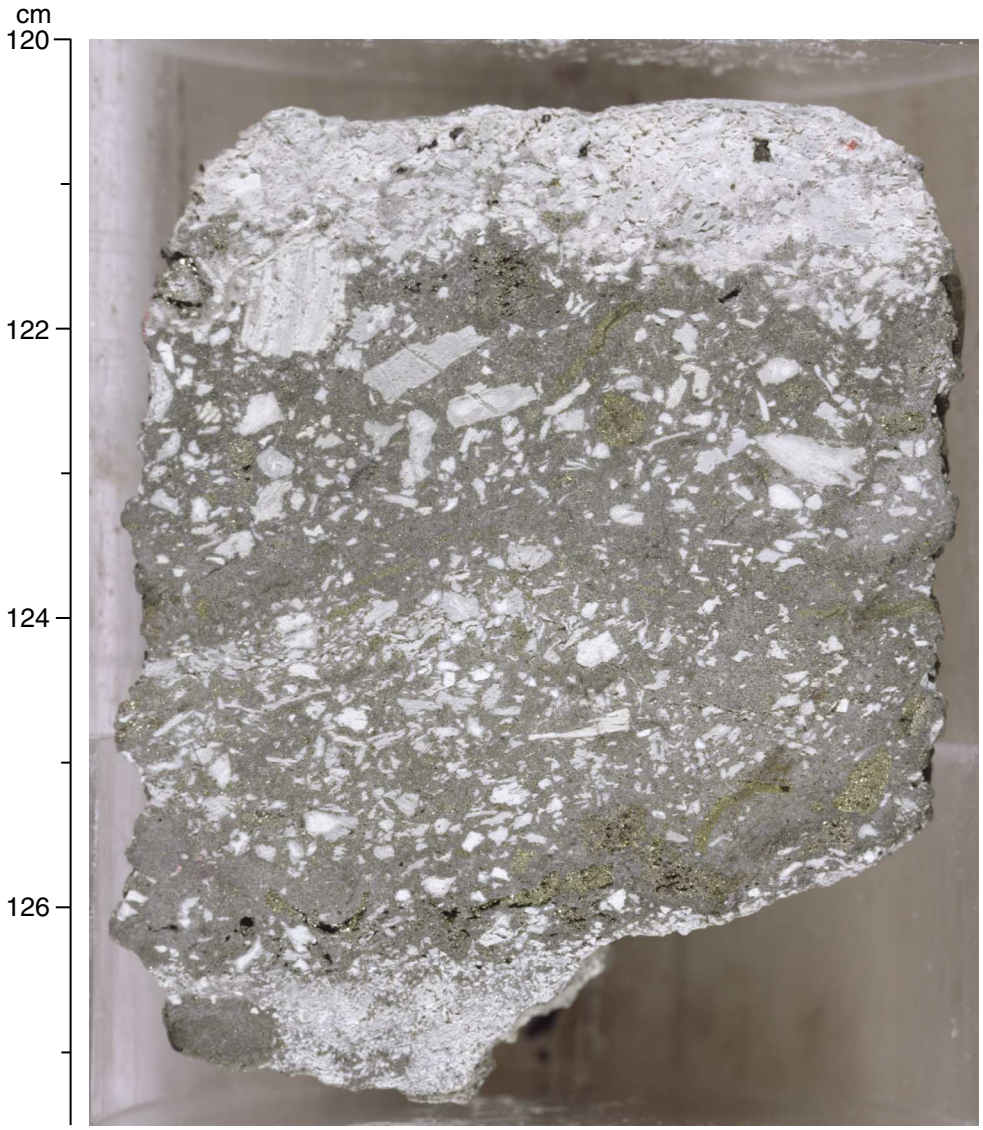

Figure F75. Angular fragment of volcanic rock with stretched vesicles within a quartz-pyrite matrix. Pyrite and chalcopyrite fill some vesicles along the edge of the fragment (Sample 193-1189A-12R-1 [Piece 16, 122–125 cm]; width of view = 1.38 mm. Photomicrograph ID# 1189A_18; **thin section 42**.).

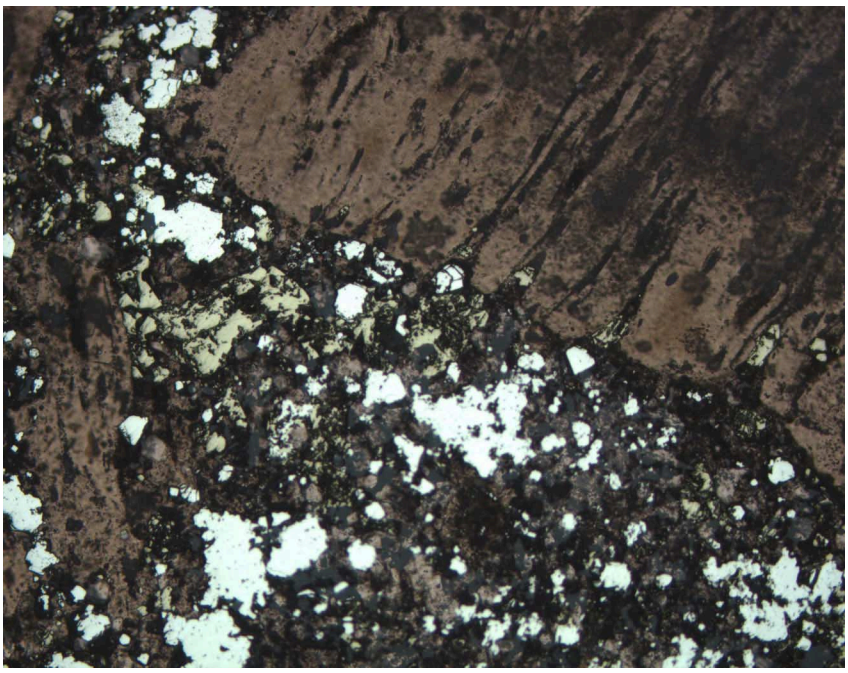

Figure F76. Disseminated Type 1 pyrite in a microlite-rich groundmass of moderately altered rhyodacite (Sample 193-1189A-3R-1 [Piece 2, 6–10 cm]; in plane-polarized transmitted light; width of view = 0.7 mm. Photomicrograph ID# 1189A_06; **thin section 32**).

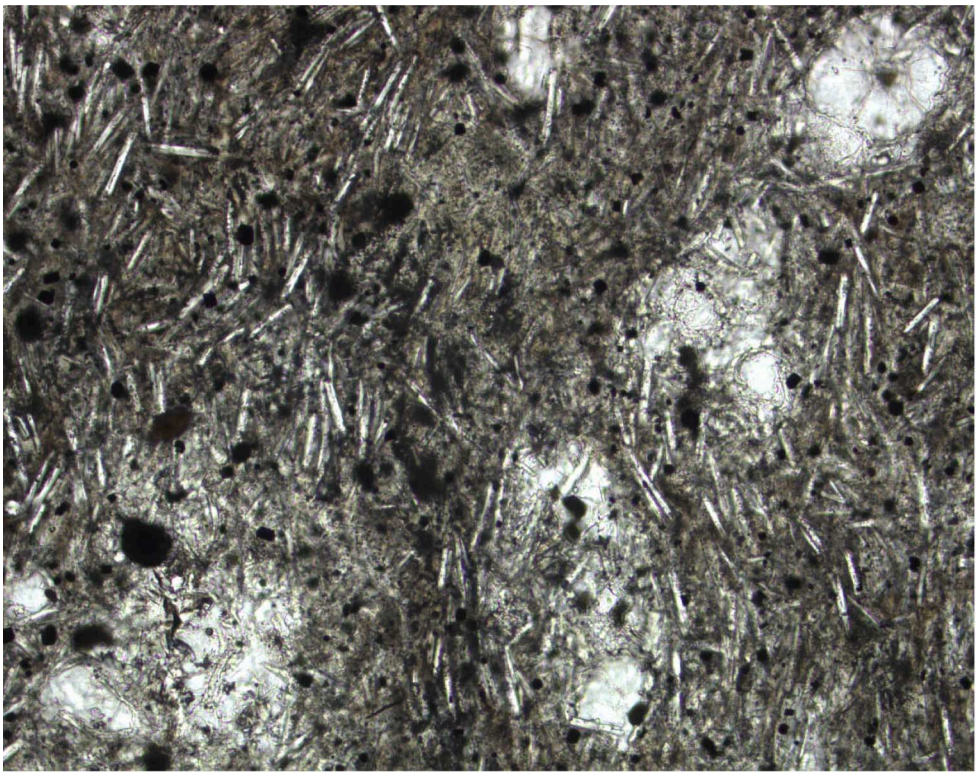

Figure F77. Disseminated euhedral pyrite containing inclusions of groundmass microlites (Sample 193-1189A-7R-1 [Piece 13, 83–86 cm]; in reflected light; width of view = 0.7 mm. Photomicrograph ID# 1189A_10; **thin section 36**).

Figure F78. Pyrite and magnetite occupy the cores of former plagioclase crystals that have been replaced by quartz (Sample 193-1189A-8R-1 [Piece 17, 103–105 cm]; width of view = 0.7 mm. Photomicrograph ID# 1189A_91; **thin section 54**).

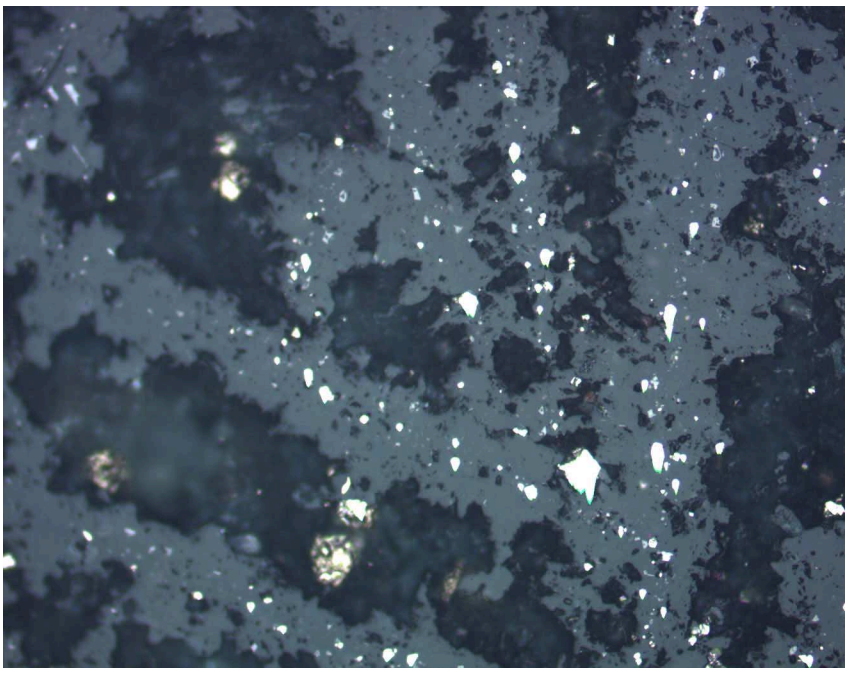

Figure F79. Type 2a quartz and pyrite precipitated on the wall of a vesicle (Sample 193-1189A-11R-1 [Piece 2A]; width of view = 25 mm).

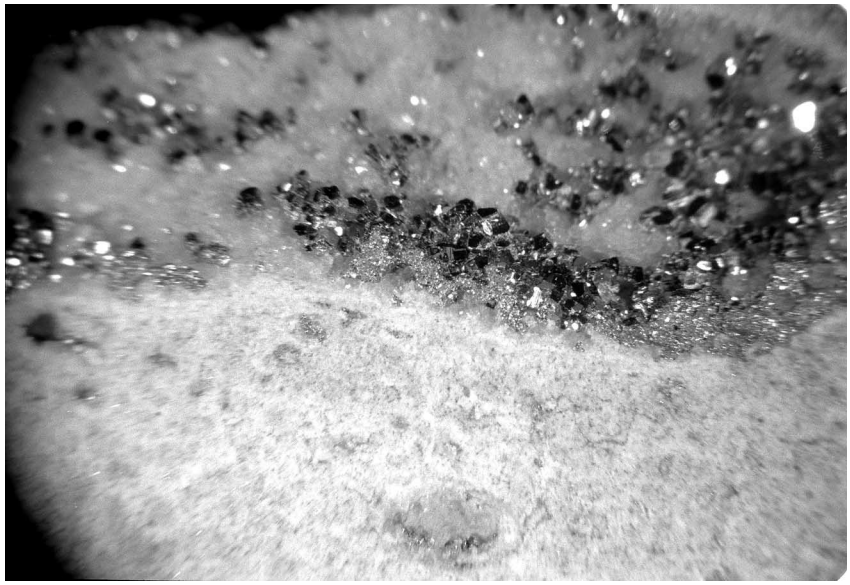

Figure F80. Pyrite crystals (white) in the center, nucleated around quartz, and overgrown by marcasite crystals (light gray) that, in turn, are overgrown by more pyrite (Sample 193-1189A-2R-1 [Piece 15, 113–115 cm]; in reflected light; width of view = 0.28 mm. Photomicrograph ID# 1189A_70; **thin section 33**).

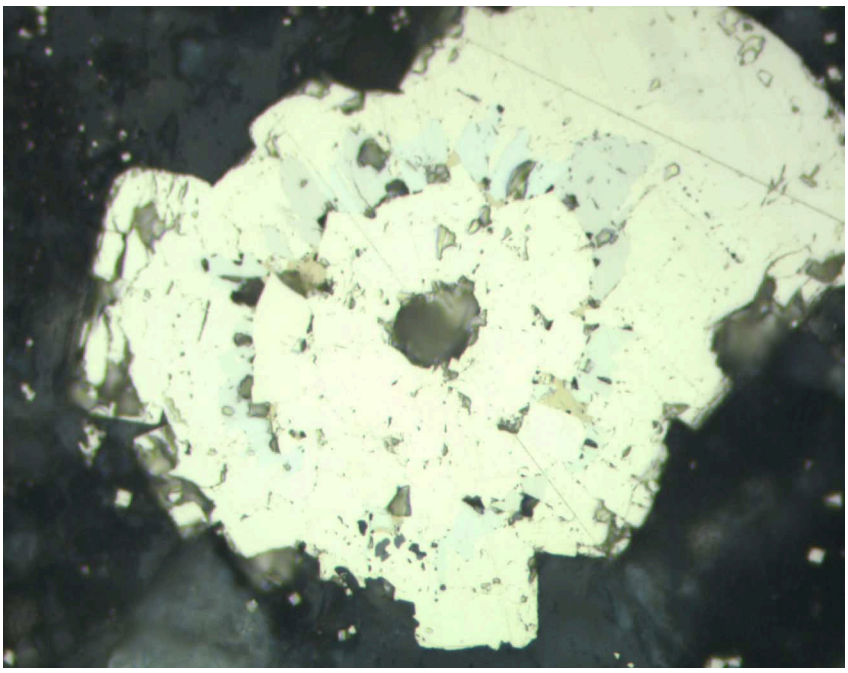

Figure F81. Chalcopyrite (medium gray) in cavity within a quartz mass (dark gray) that fills an amygdule. White mineral is pyrite (see Fig. F77, p. 147) (Sample 193-1189A-7R-1 [Piece 13, 83–86 cm]; in reflected light; width of view = 0.7 mm. Photomicrograph ID# 1189A_44; thin section 36).

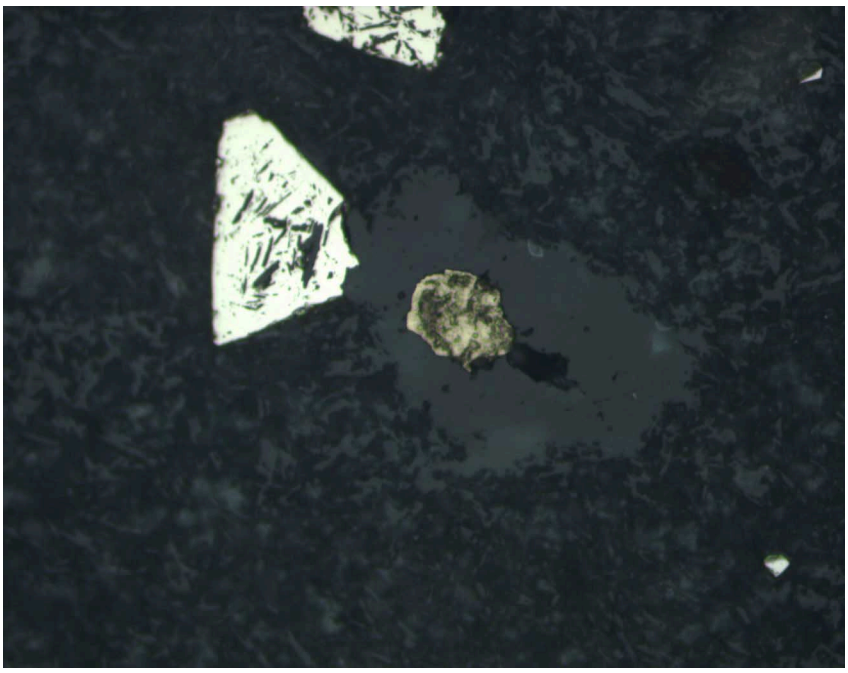

Figure F82. Sphalerite and chalcopyrite intergrown with pyrite (white). Note the galena inclusion in pyrite (Sample 193-1189A-2R [Piece 15, 113–115 cm]; in reflected light; width of view = 0.28 mm. Photomicrograph ID# 1189A_64; **thin section 33**).

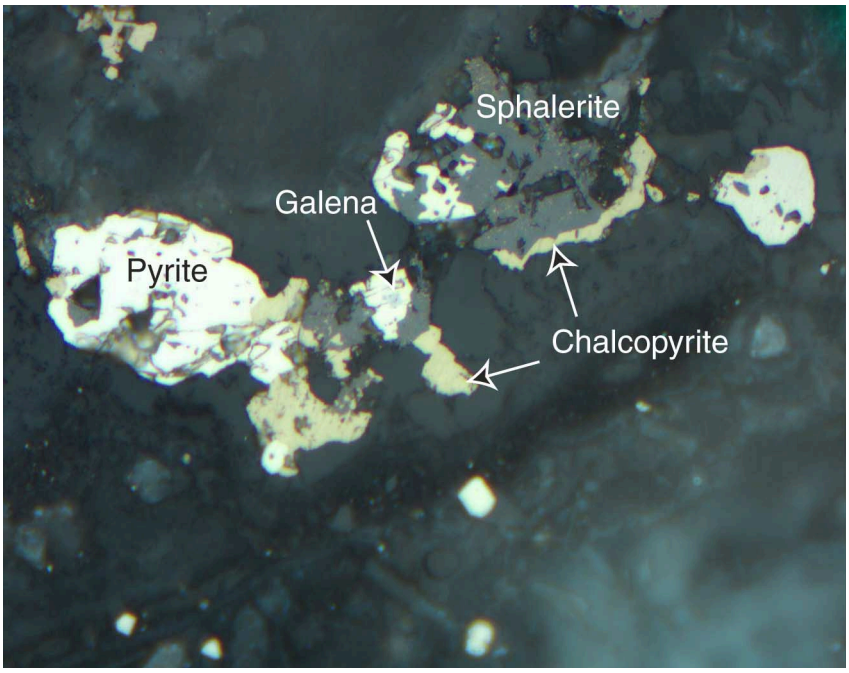

Figure F83. Enlargement of part of Figure F82, p. 152, showing chalcopyrite inclusions ("chalcopyrite disease") in sphalerite. Note the galena inclusion in the small pyrite crystal at the bottom of the photograph (Sample 193-1189A-2R-1 [Piece 15, 113–115 cm]; in reflected light; oil immersion; width of view = 0.14 mm. Photomicrograph ID# 1189A_72; thin section 33).

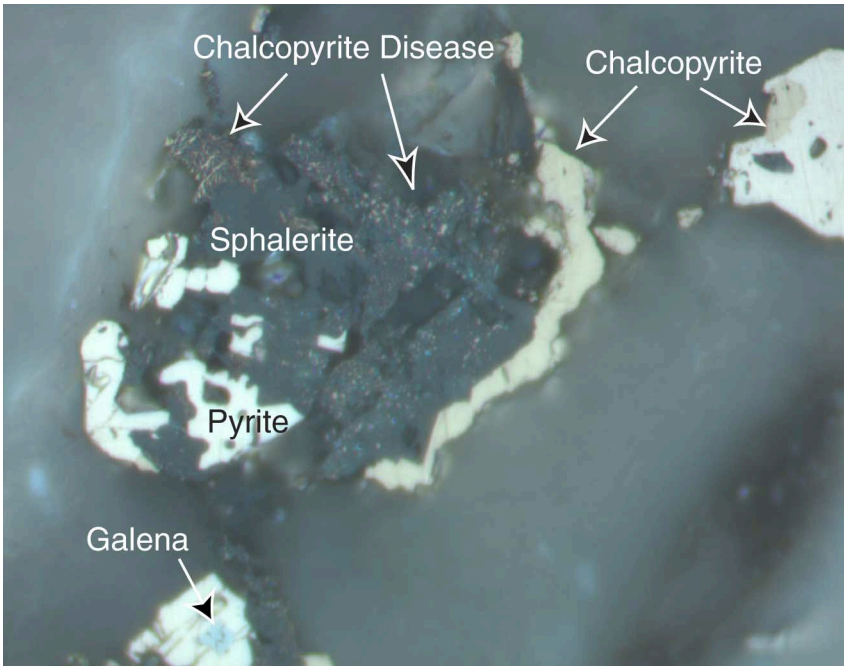

Figure F84. Red hematitic chert (jasper) with disseminated pyrite and chalcopyrite and fragments of highly altered rock (Sample 193-1189A-7R-1, 99–102 cm).

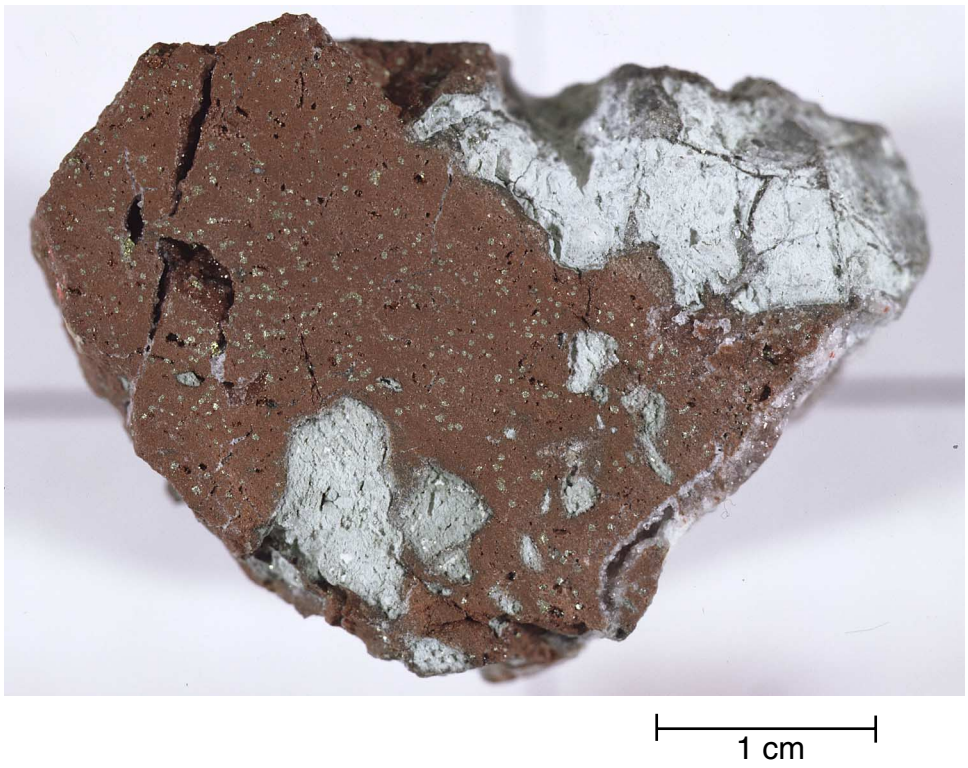

Figure F85. Sphalerite or magnetite (too small to identify in thin section) precipitated on early pyrite and overgrown by later pyrite (Sample 193-1189A-12R-1 [Piece 16, 122–126 cm]; in reflected light, oil immersion; width of view = 0.14 mm. Photomicrograph ID# 1189A_86; **thin section 42**).

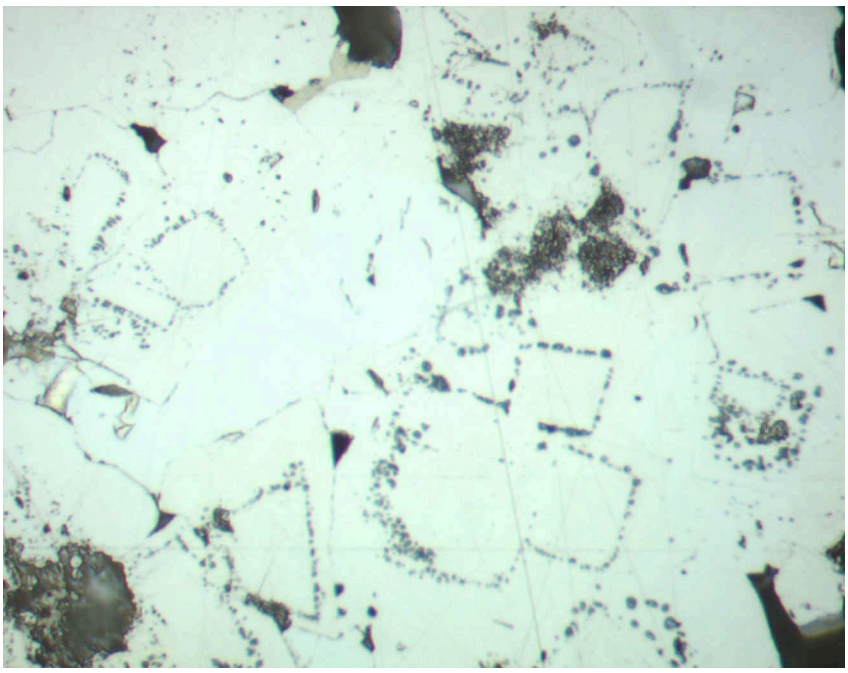

Figure F86. Pyrite containing inclusions of quartz (black) and of sphalerite (gray) with chalcopyrite disease (Sample 193-1189A-3R-1 [Piece 10, 59–63 cm]; in reflected light; width of view = 0.28 mm. Photomicrograph ID# 1189A_68; **thin section 31**).

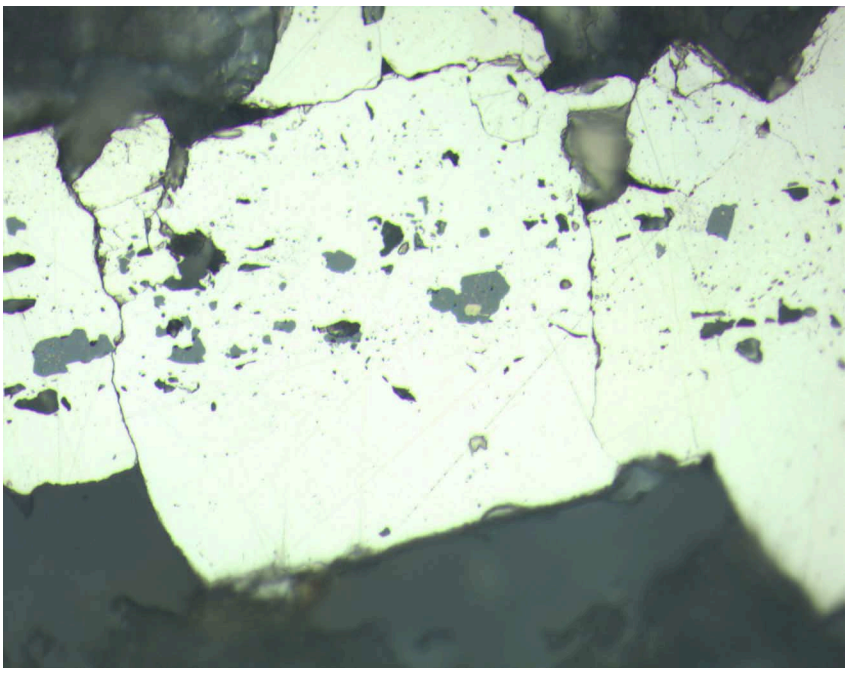

Figure F87. Quartz vein with chalcopyrite diseased sphalerite (medium gray) and chalcopyrite (yellow) intergrown with pyrite (white) (Sample 193-1189A-2R-1 [Piece 15, 113–115 cm]; in reflected light; width of view = 0.28 mm. Photomicrograph ID# 1189A_65; **thin section 33**).

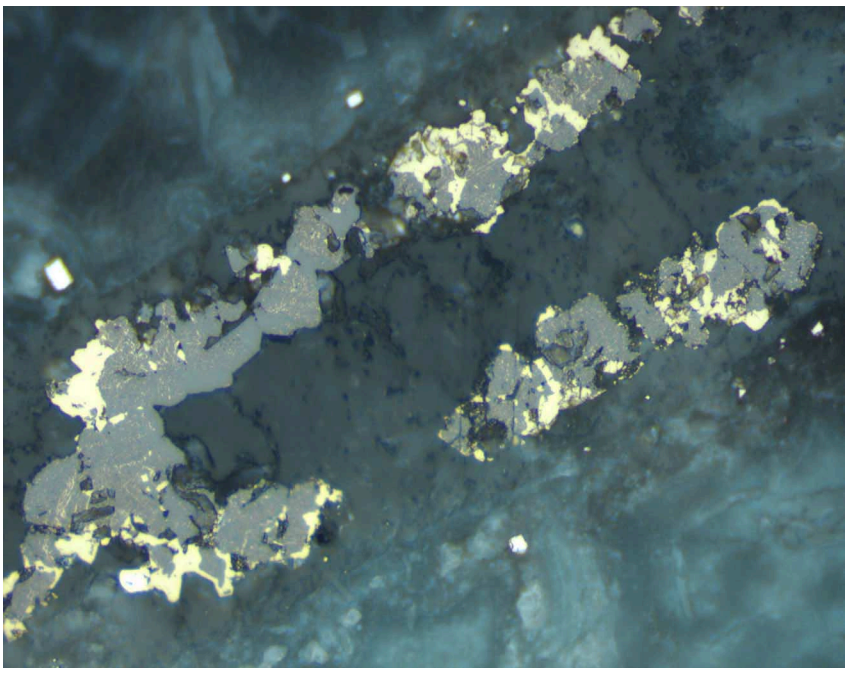

Figure F88. Apparent pseudomorphous replacement of magnetite (dark gray) by pyrite (white) and hematite (medium blue gray) (Sample 193-1189A-8R-1 [Piece 17, 103–105 cm] in reflected light; width of view = 0.14 mm; oil immersion. Photomicrograph ID# 1189A_95; **thin section 54**).

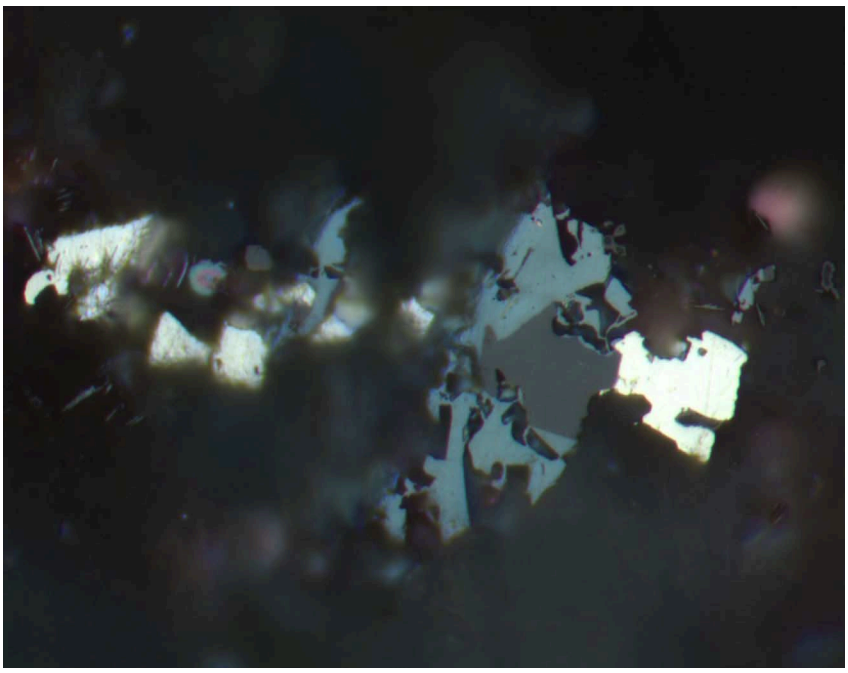

Figure F89. Paragenetic sequence for sulfide and oxide minerals from Hole 1189A. The timing of formation of framboidal pyrite, galena, and hematite is poorly constrained, so they are not included on the figure. See "Parageneses," p. 36, in "Sulfide and Oxide Petrology" for details.

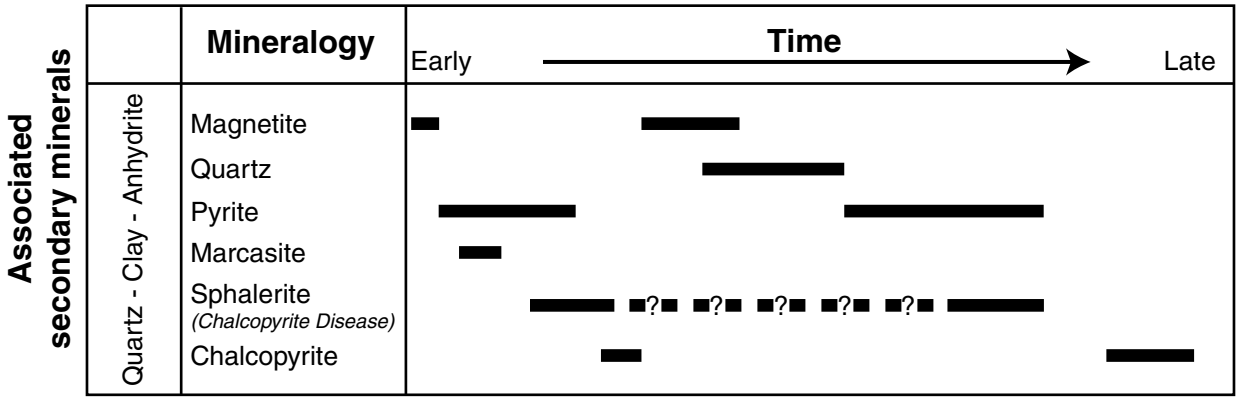

Figure F90. Ovoid structure, 6 mm long in total, with a thin pyrite rim (white) and chalcopyrite fill (yellow, poor polish) (in reflected light; width of view = 11 mm).]

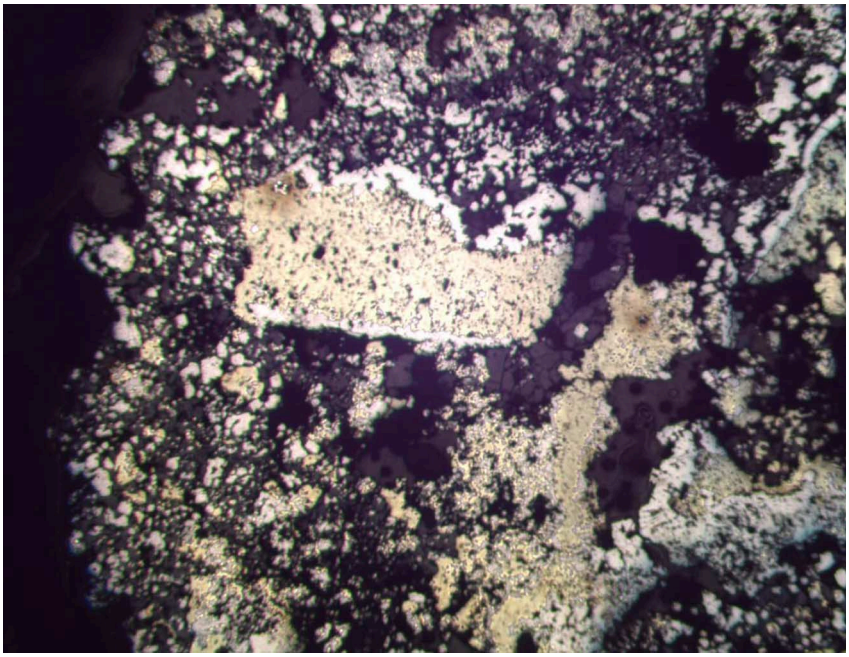

Figure F91. Possibly dismembered ovoid structure filling the center of the field of view. A thin rind of pyrite (white) encloses chalcopyrite (yellow) and coarse anhydrite (black). The structure in the upper left corner is shown in Figure F90, p. 160 (in reflected light; width of view = 11 mm. Photomicrograph ID# 1189B_36; thin section 113).

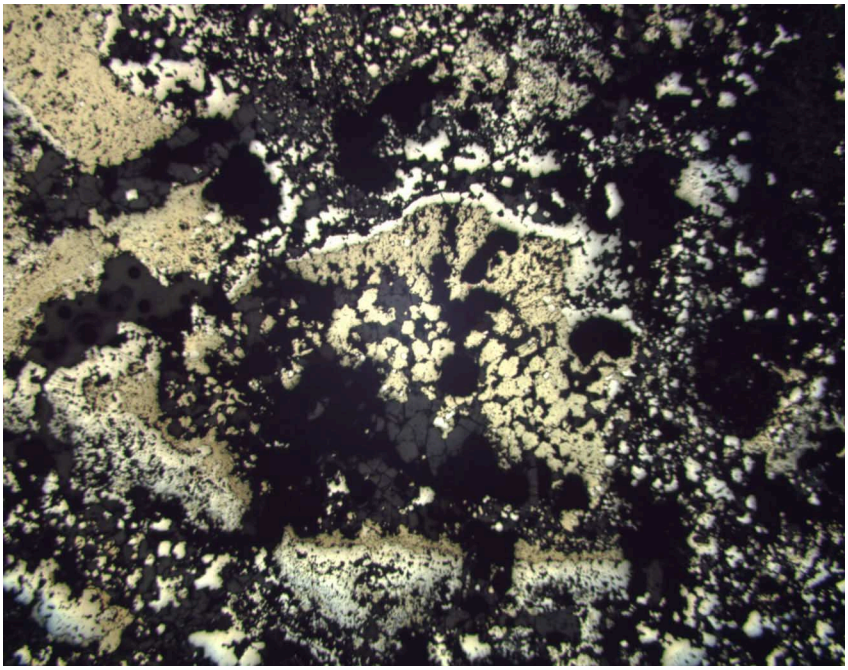

Figure F92. Framboids of pyrite in quartz (width of view = 0.14 mm. Photomicrograph ID# 1189B_68; **thin section 135**).

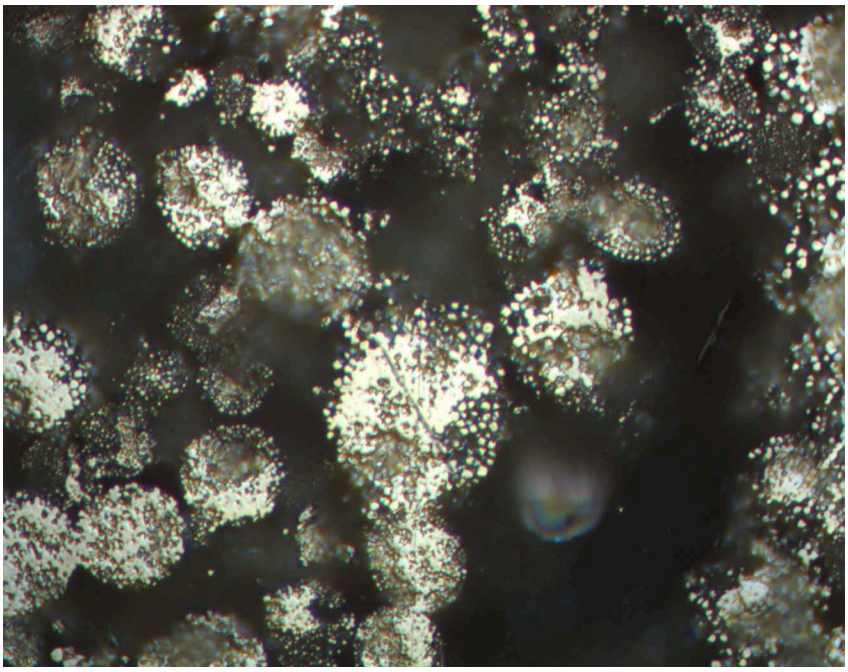

Figure F93. Amygdule filled with quartz and sphalerite (in plane-polarized transmitted light; width of view = 1.38 mm. Photomicrograph ID# 1189B_51; **thin section 136**).

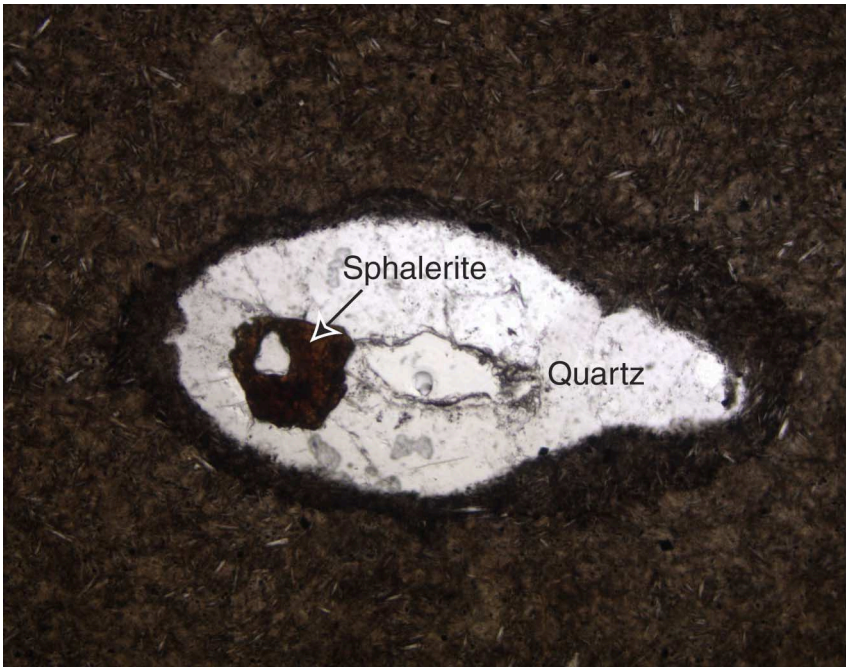

Figure F94. Zoned sphalerite, with chalcopyrite disease in its outer portion, surrounded by anhydrite (in reflected light; width of view = 1.38 mm. Photomicrograph ID# 1189B_27; **thin section 131**).

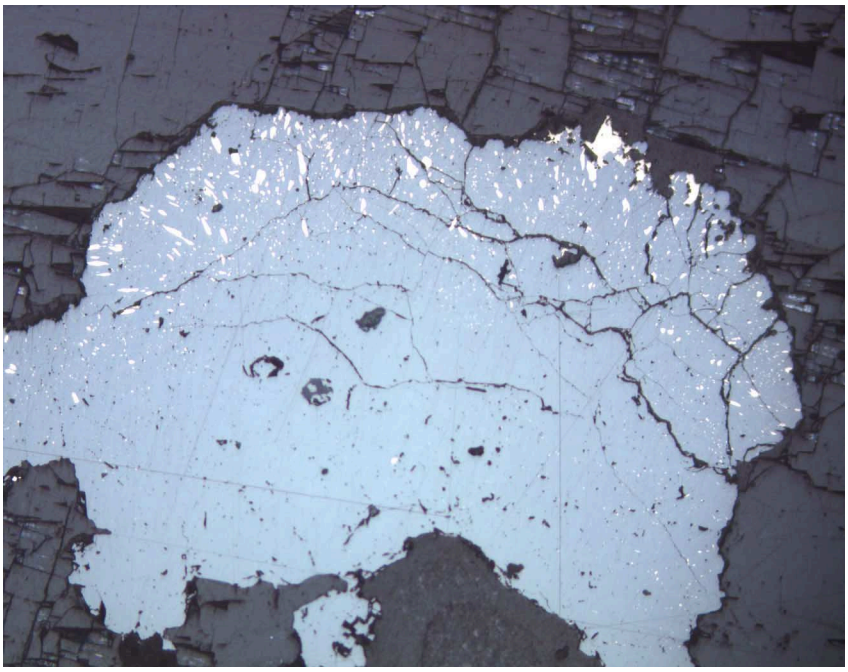

Figure F95. Pyrite (yellow) replacing magnetite (gray) (in reflected light; width of view = 0.28 mm. Photomicrograph ID# 1189B_37; **thin section 140**).

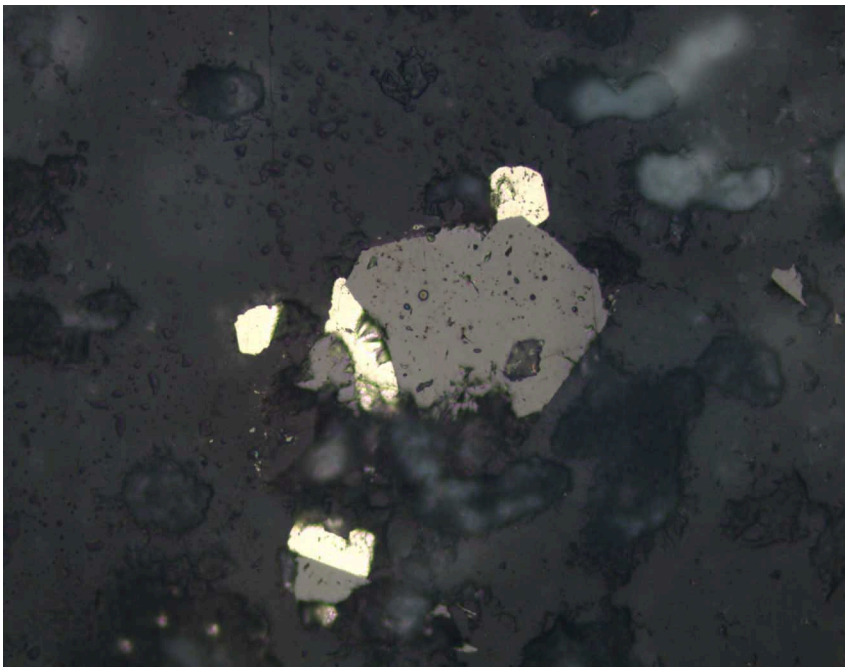

Figure F96. Bladed hematite (light bluish gray) embedded in quartz (dark gray) together with pyrite (white), chalcopyrite (yellow), and magnetite (medium gray) (in reflected light; width of view = 0.7 mm. Photomicrograph ID# 1189B_48; **thin section 140**).

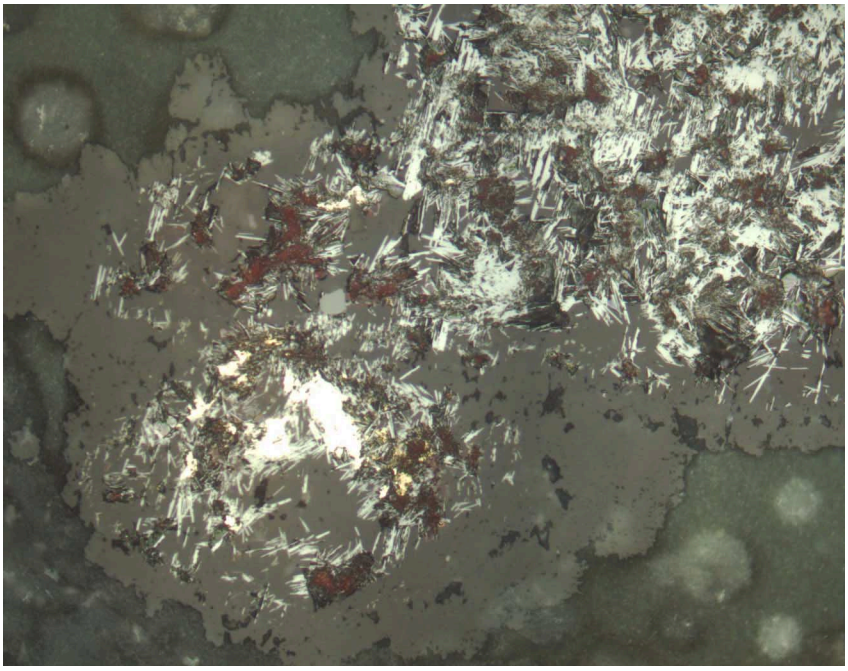

Figure F97. Magnetite (medium gray), hematite (light bluish gray), and pyrite (yellow) assemblage in groundmass (in reflected light; width of view = 0.28. Photomicrograph ID# 1189B_50; **thin section 138**).

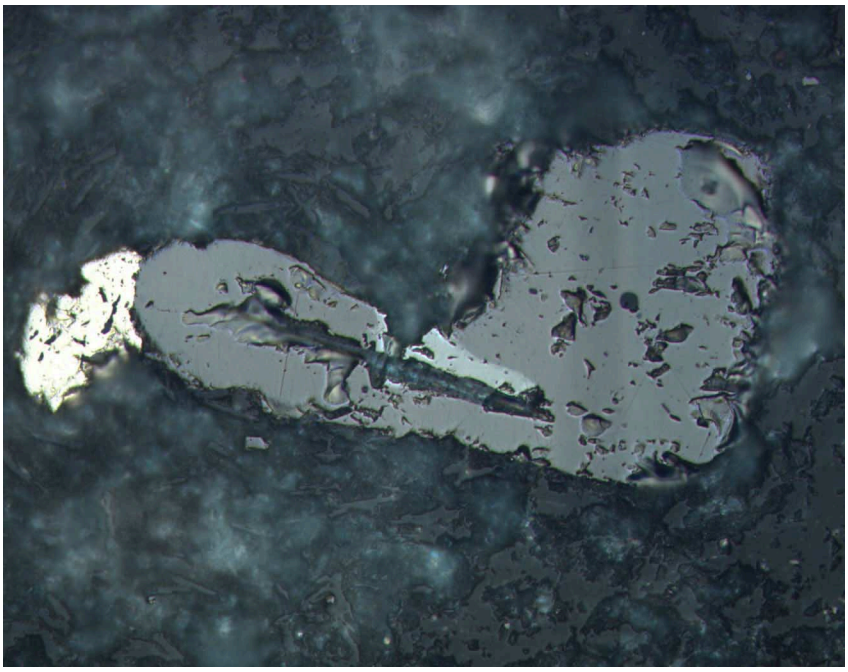

Figure F98. Paragenetic diagram for sulfide and oxide minerals in Site 1189. See **"Concluding Remarks for Site 1189,"** p. 40, in "Sulfide and Oxide Petrology" for details.

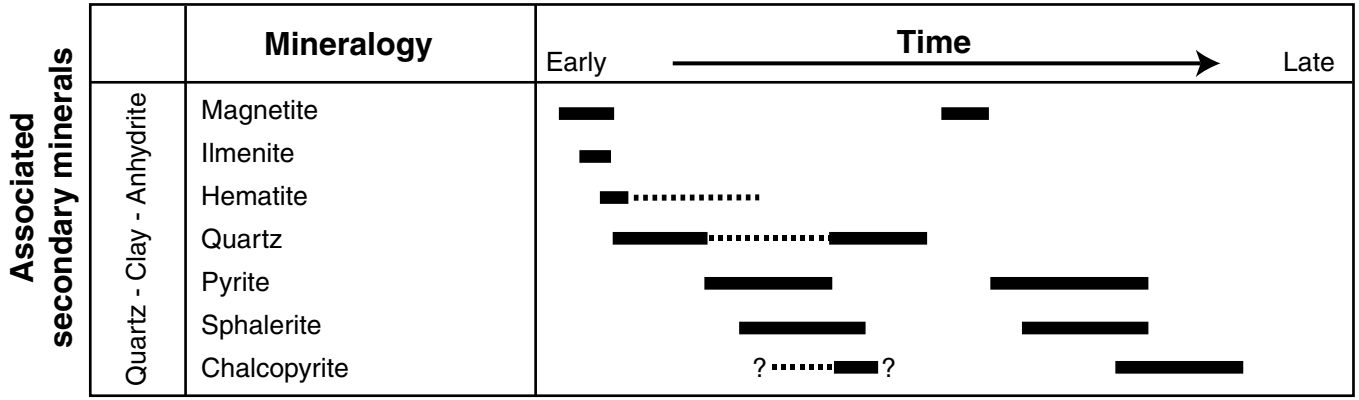

Figure F99. Dip of primary volcanic layering vs. depth, Hole 1189A.

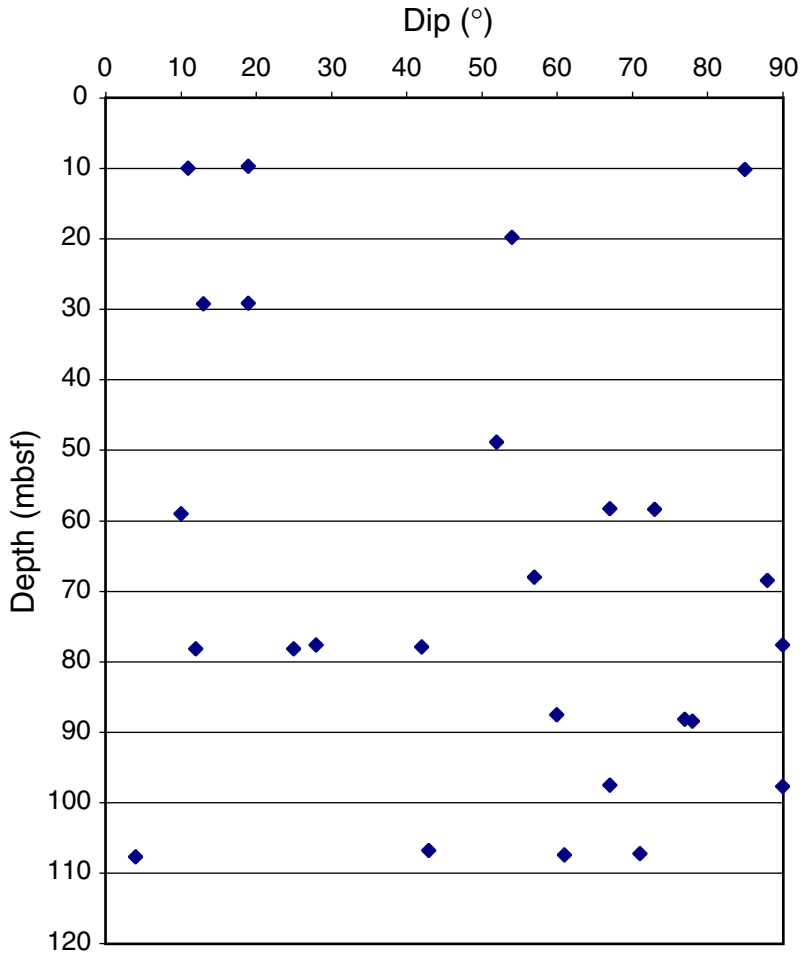

Figure F100. Breccia with fragments of pervasively altered volcanic rock, cemented by coarse anhydrite, quartz and minor pyrite. Note the different colors and the sharp boundaries of the fragments. (cf. Fig. F102, p. 172).

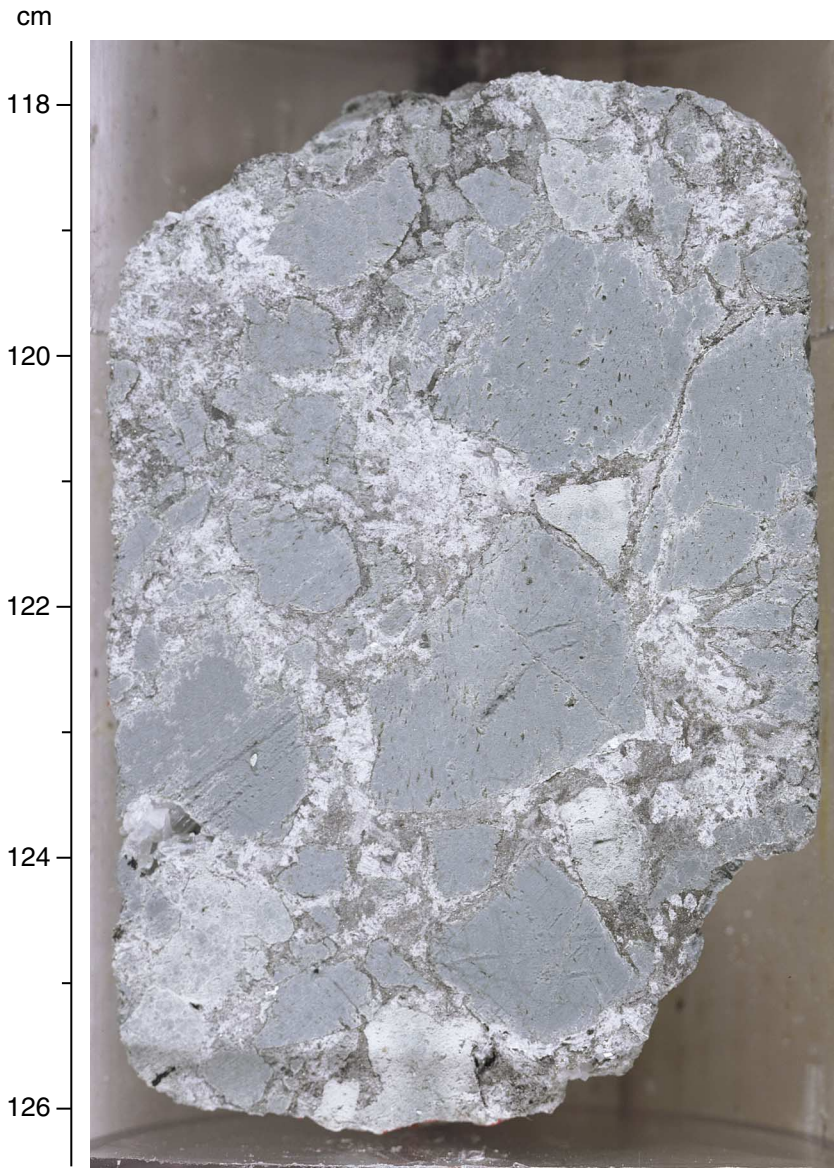

Figure F101. Fragments of flow-banded altered volcanic rock cemented by coarse anhydrite and crosscut by quartz-pyrite veins (Unit 6; Sample 193-1189A-3R-1 [Piece 10, 59–63 cm] in cross-polarized light; width of view = 5.5 mm. Photomicrograph ID# 1189A_22; **thin section 31**).

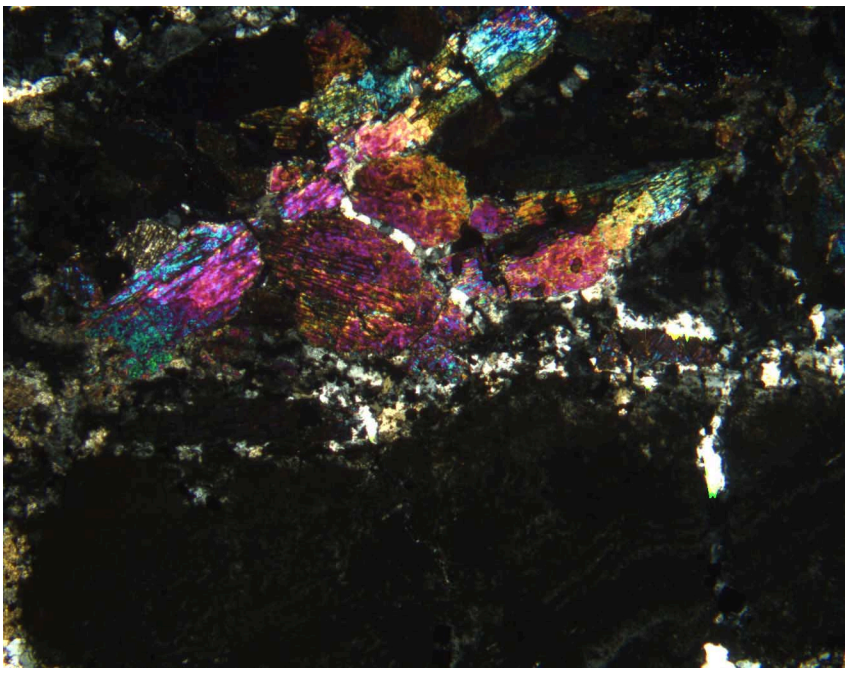

Figure F102. Brecciation, alteration, and quartz-pyrite veining of completely altered volcanic rock. Note that alteration associated with the veining overprints earlier alteration of many of the fragments and that several of the fragments fit together (jigsaw-fit breccia) (cf. Fig. F100, p. 170) (Unit 9; interval 193-1189A-5R-1, 42–50 cm).

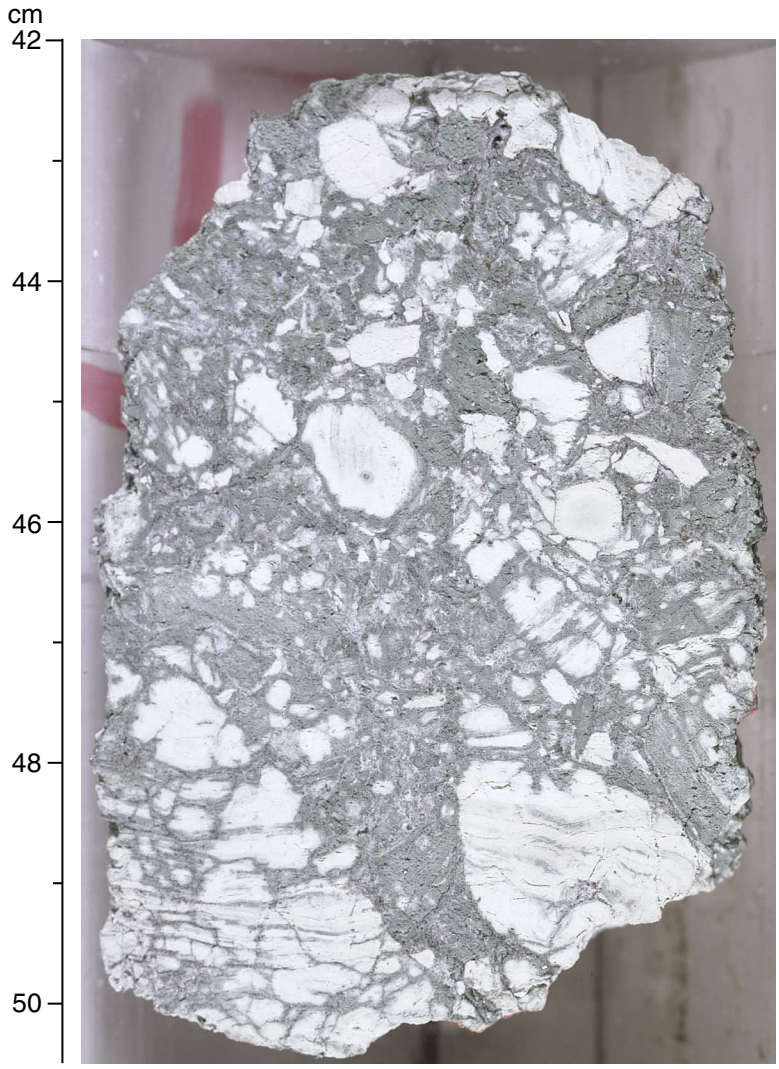

Figure F103. Distribution of veins according to mineralogy vs. lithologic units, Hole 1189A.

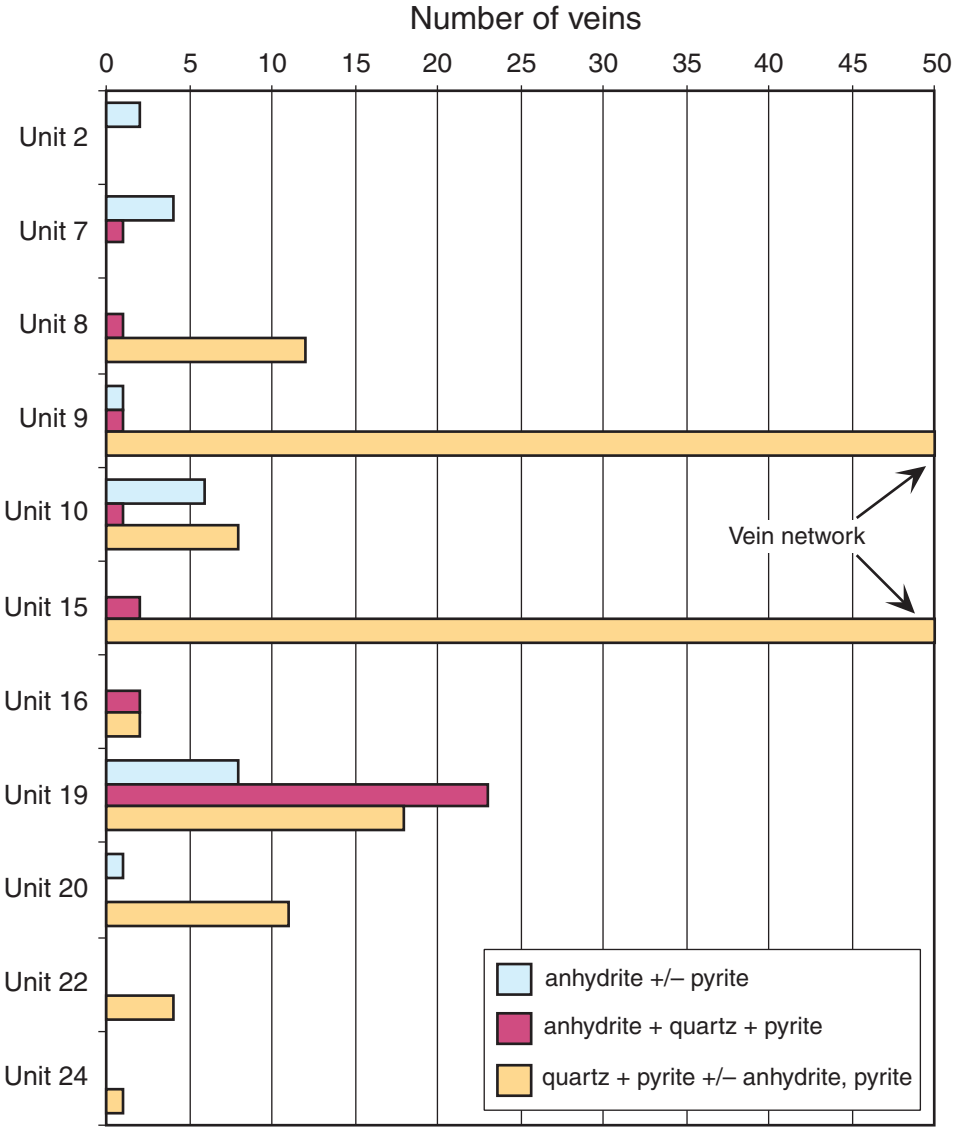

Figure F104. Photograph of a network of quartz-pyrite veins (dark gray) crosscutting earlier patchy silica-sulfate alteration (light gray) (Section 193-1189A-10R-1 [Piece 10, 88.5–100 cm]).

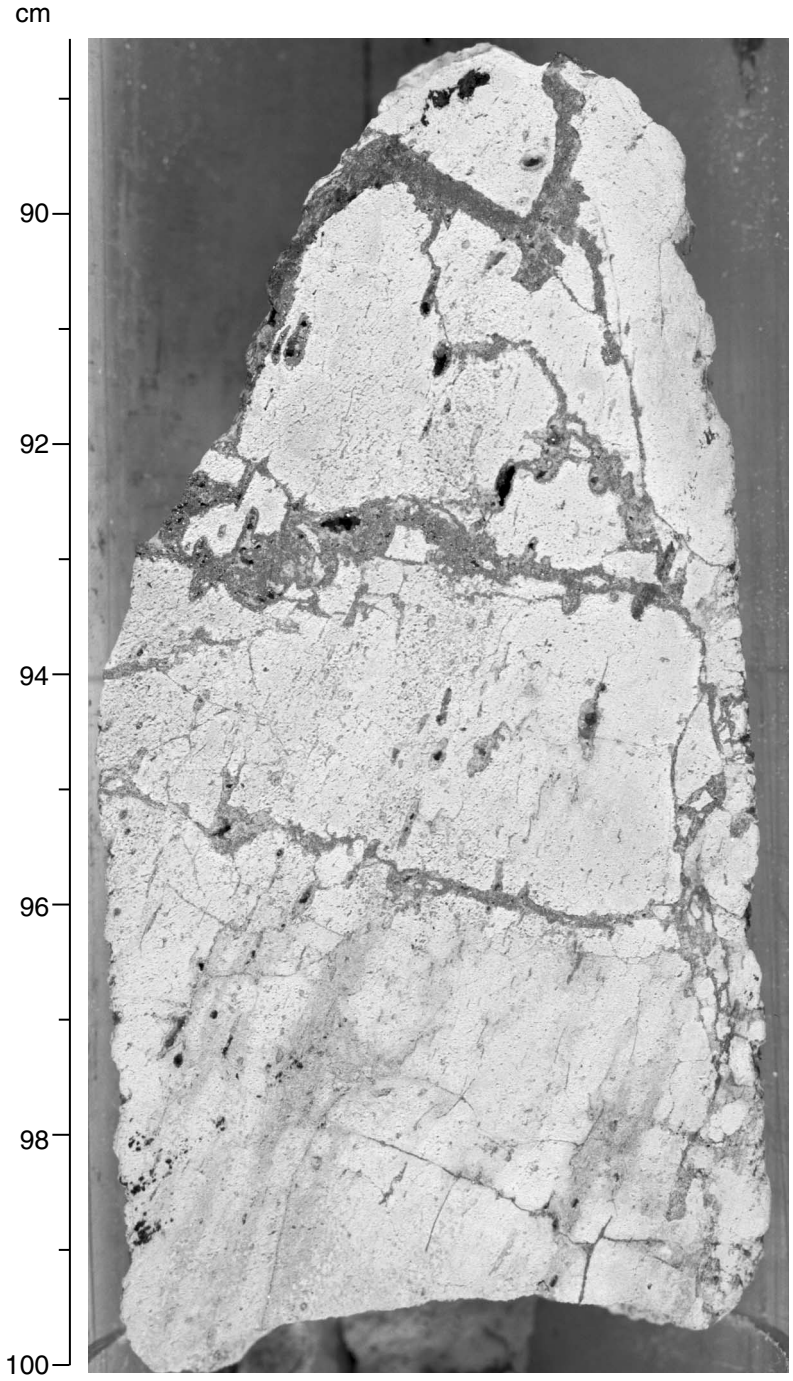

Figure F105. Site 1189 photomicrographs. **A.** Quartz-pyrite veins with halos of poikiloblastic quartz cross-cut by later fractures filled with quartz. Note pyrite along rims in the vein in the lower part of the image (Unit 15; Sample 193-1189A-8R-1 [Piece 6, 42–44 cm] in plane-polarized transmitted light; width of view = 5.5 mm. Photomicrograph ID# 1189A_92; **thin section 38**). **B.** Quartz-pyrite vein with halo of poikiloblastic quartz (Unit 15; Sample 193-1189A-8R-1 [Piece 6, 42–44 cm] in cross-polarized transmitted light; width of view = 2.75 mm. Photomicrograph ID# 1189A_52; **thin section 38**). **C.** Anastomosing quartz-anhydrite-pyrite vein. Note that anhydrite occupies the center of the vein and that pyrite is present along the rims of the altered volcanic clast (Unit 8; Sample 193-1189A-4R-1 [Piece 3, 21–24 cm] in plane-polarized transmitted light; width of view = 5.5 mm. Photomicrograph ID# 1189A_104; **thin section 29**). **D.** Zoned quartz-anhydrite vein with quartz rims around central anhydrite. Note the association of pyrite and chalcopyrite with the anhydrite (Unit 7; Sample 193-1189A-3R-1 [Piece 12, 70–73 cm] in reflected light; width of view = 1.40 mm. Photomicrograph ID# 1189A_8; **thin section 30**). (**Figure shown on next page.**)

Figure F105 (continued). (Caption shown on previous page.)

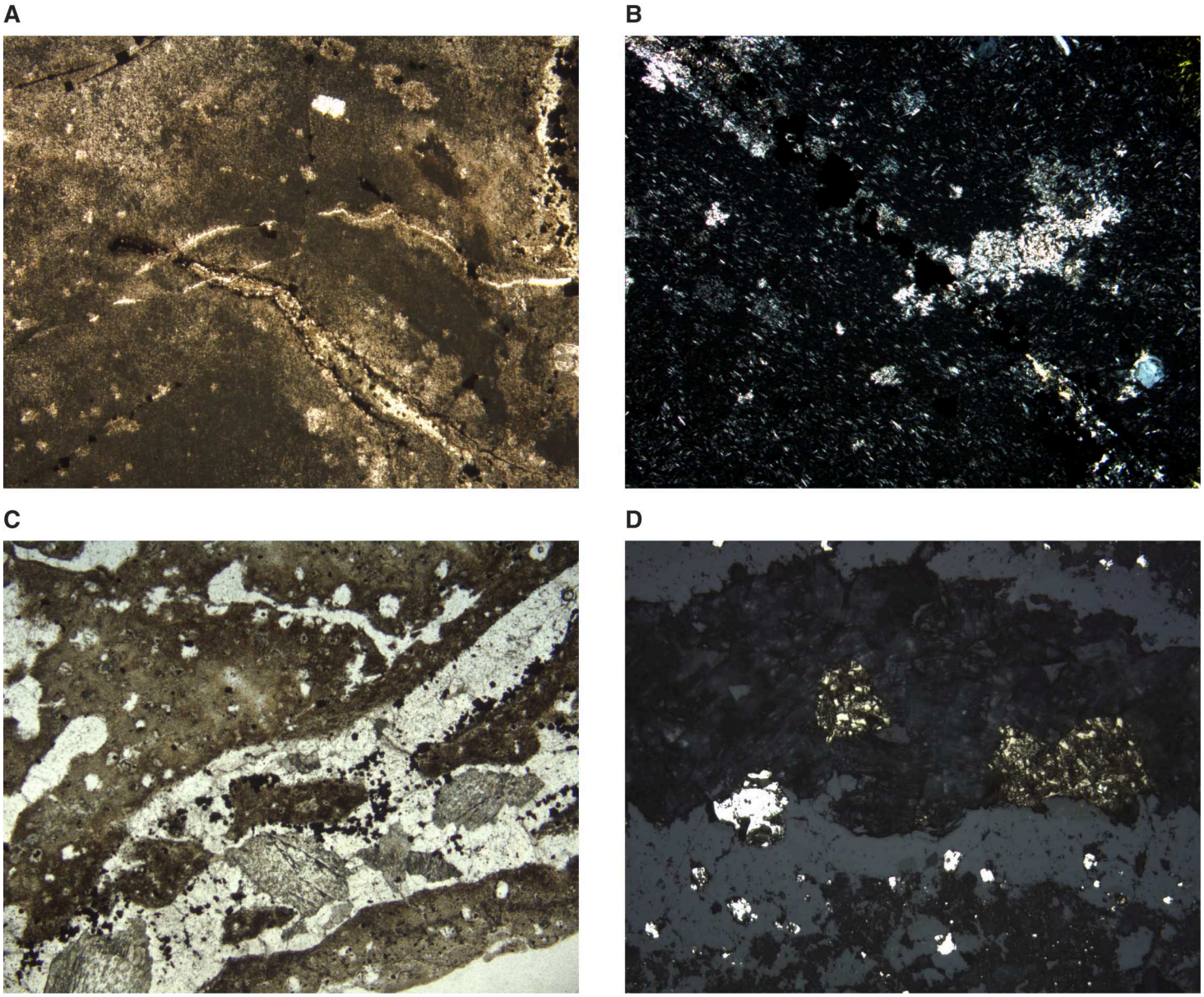

Figure F106. A. Distribution of vein thicknesses in Hole 1189A. **B.** Distribution of veins in different intervals of dip in Hole 1189A. (Continued on next page.)

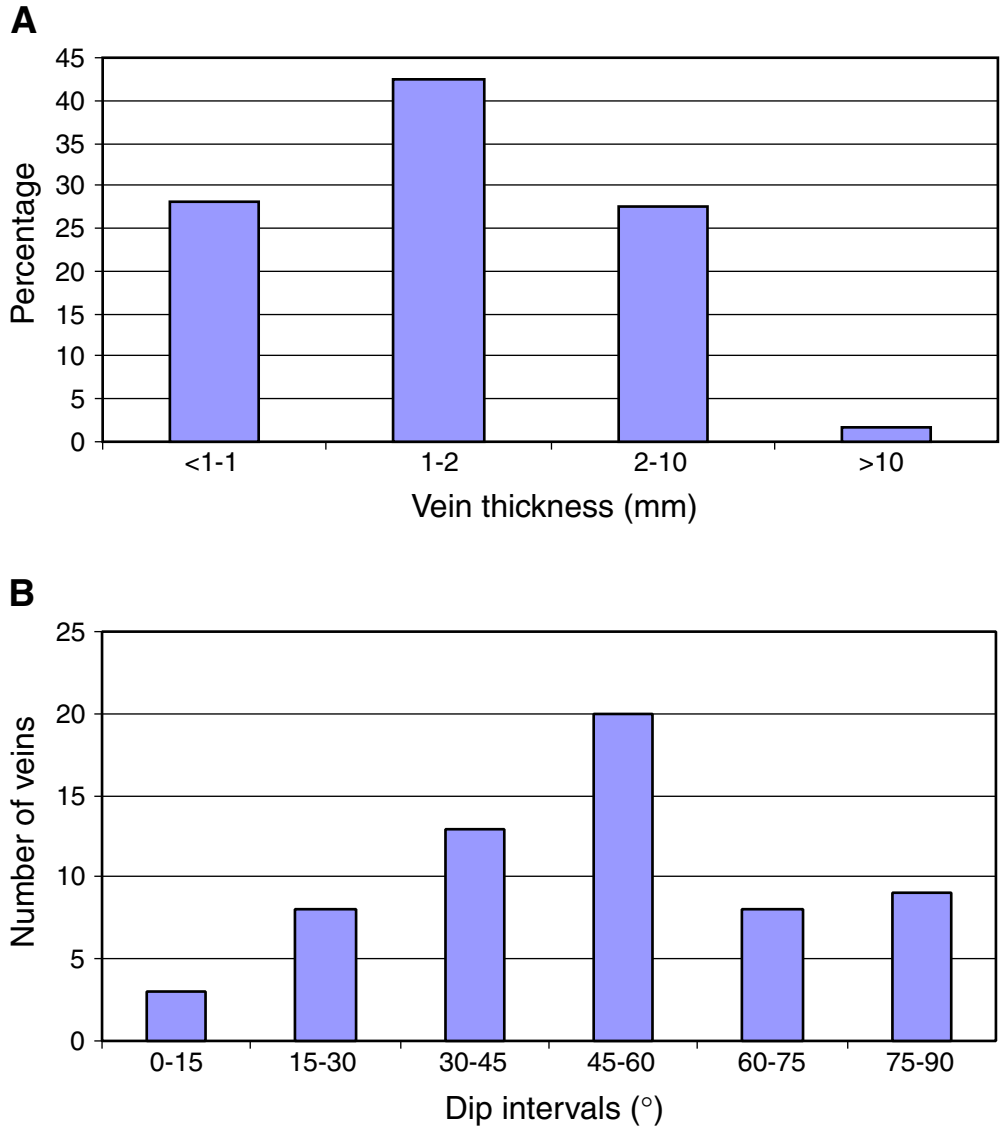

Figure F106 (continued). C. Dip of veins vs. depth in Hole 1189A.

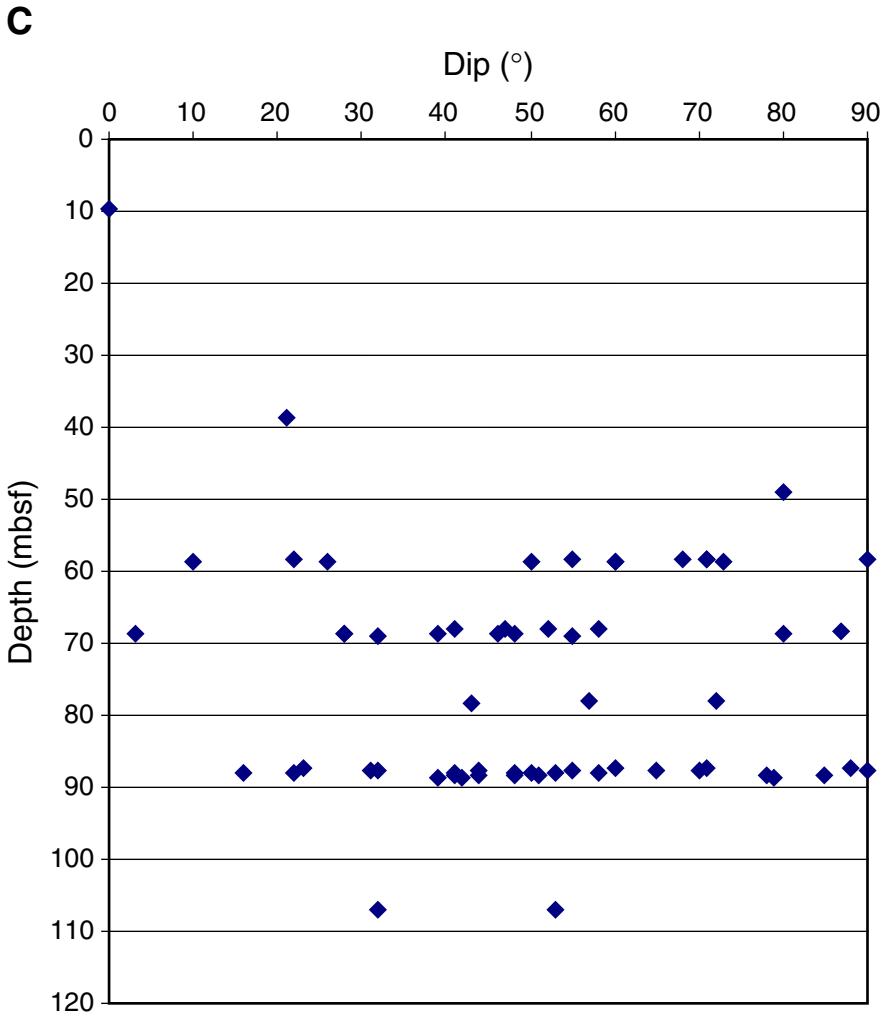

Figure F107. Dip of primary volcanic layering (solid diamonds) and plunge of stretched vesicles (open squares) vs. depth in Hole 1189B.

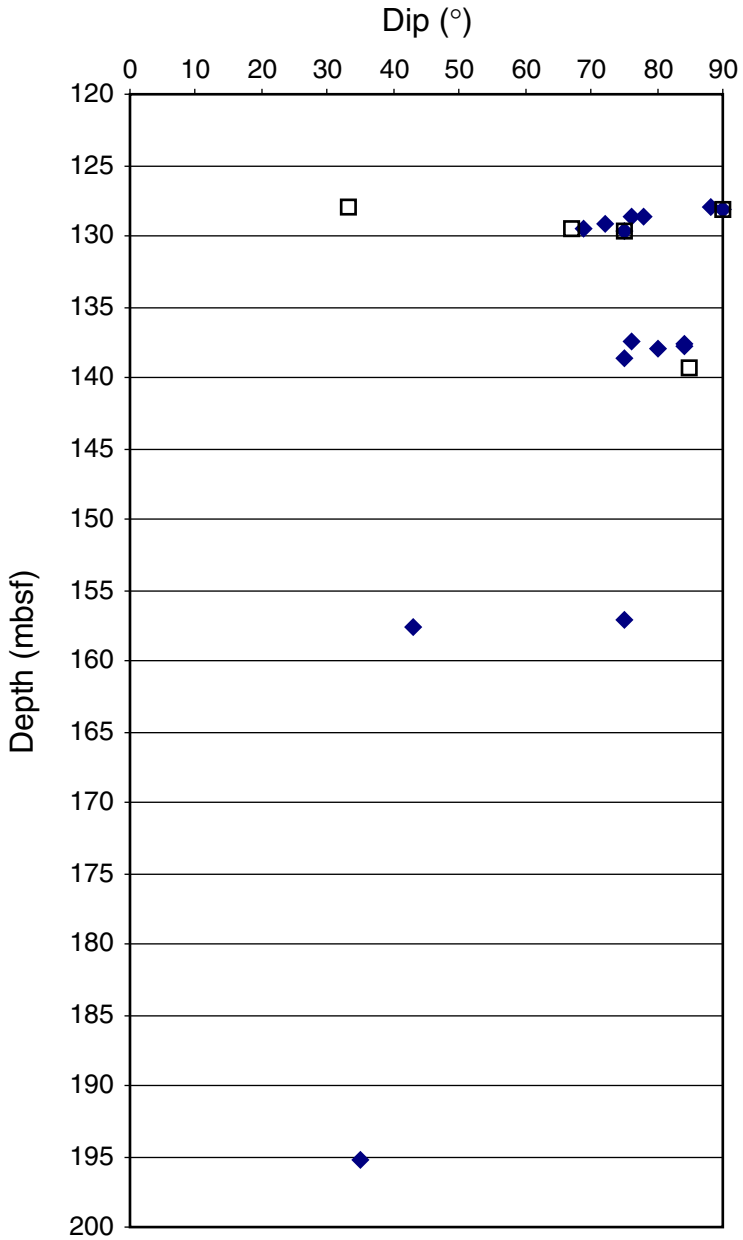

Figure F108. Breccia with highly altered volcanic fragments in a dark matrix of quartz and anhydrite with minor pyrite. Note that breccia is matrix-supported (cf. Fig. F109, p. 181) (Section 193-1189B-7R-1 [Piece 1, 0–5 cm]; 88.70 mbsf).

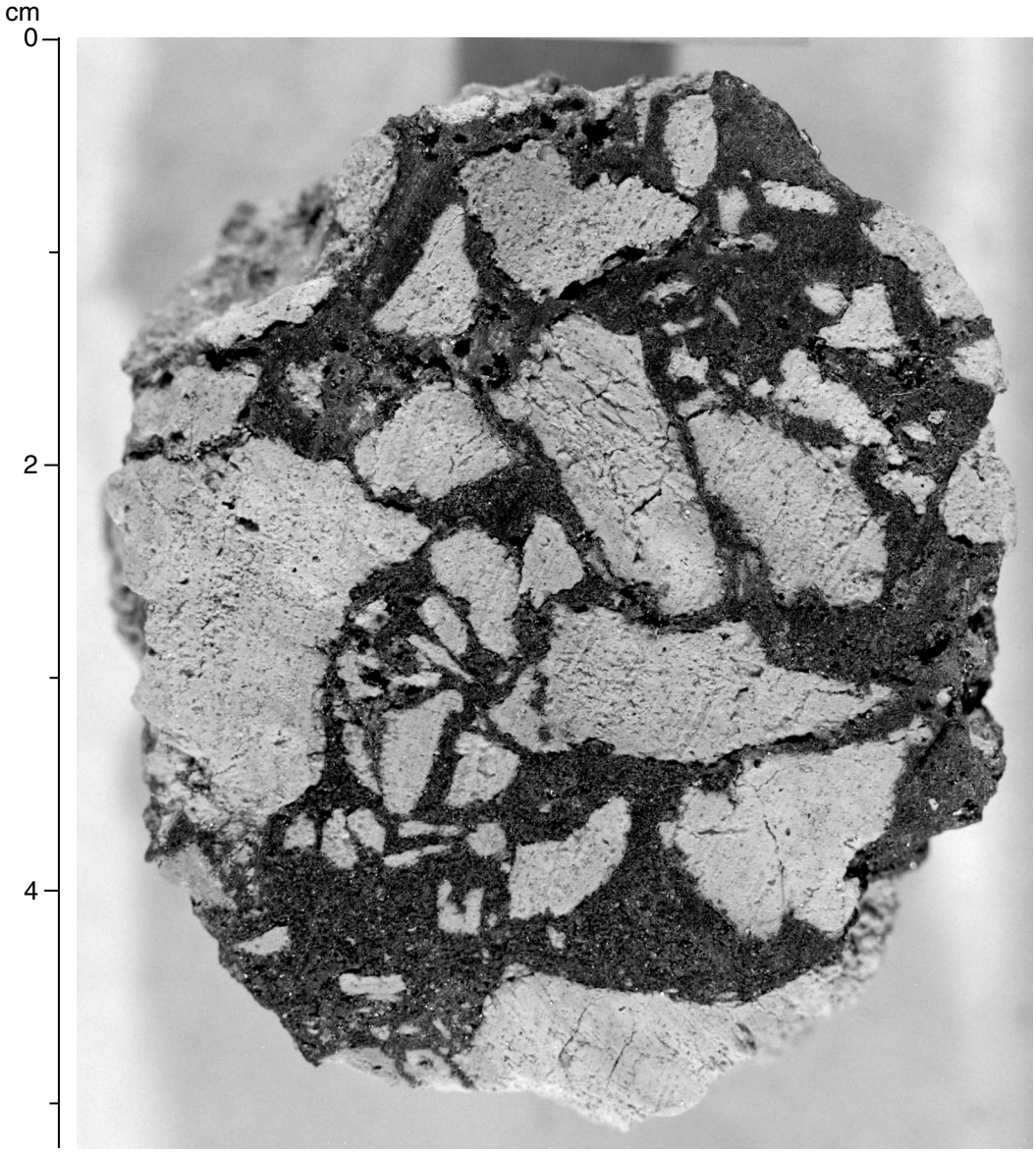

Figure F109. Breccia with fragments of altered, flow banded volcanic rock. The breccia is clast-supported (cf. Fig. F108, p. 180). The brecciated rock is crosscut by a feeble but dense silica vein network. Note also the late anhydrite vein (arrow), crosscutting the vein network in the fragments, running downward from right to left at 29 cm (Section 193-1189B-15R-1 [Piece 4, 25–34 cm]; 166.35 mbsf).

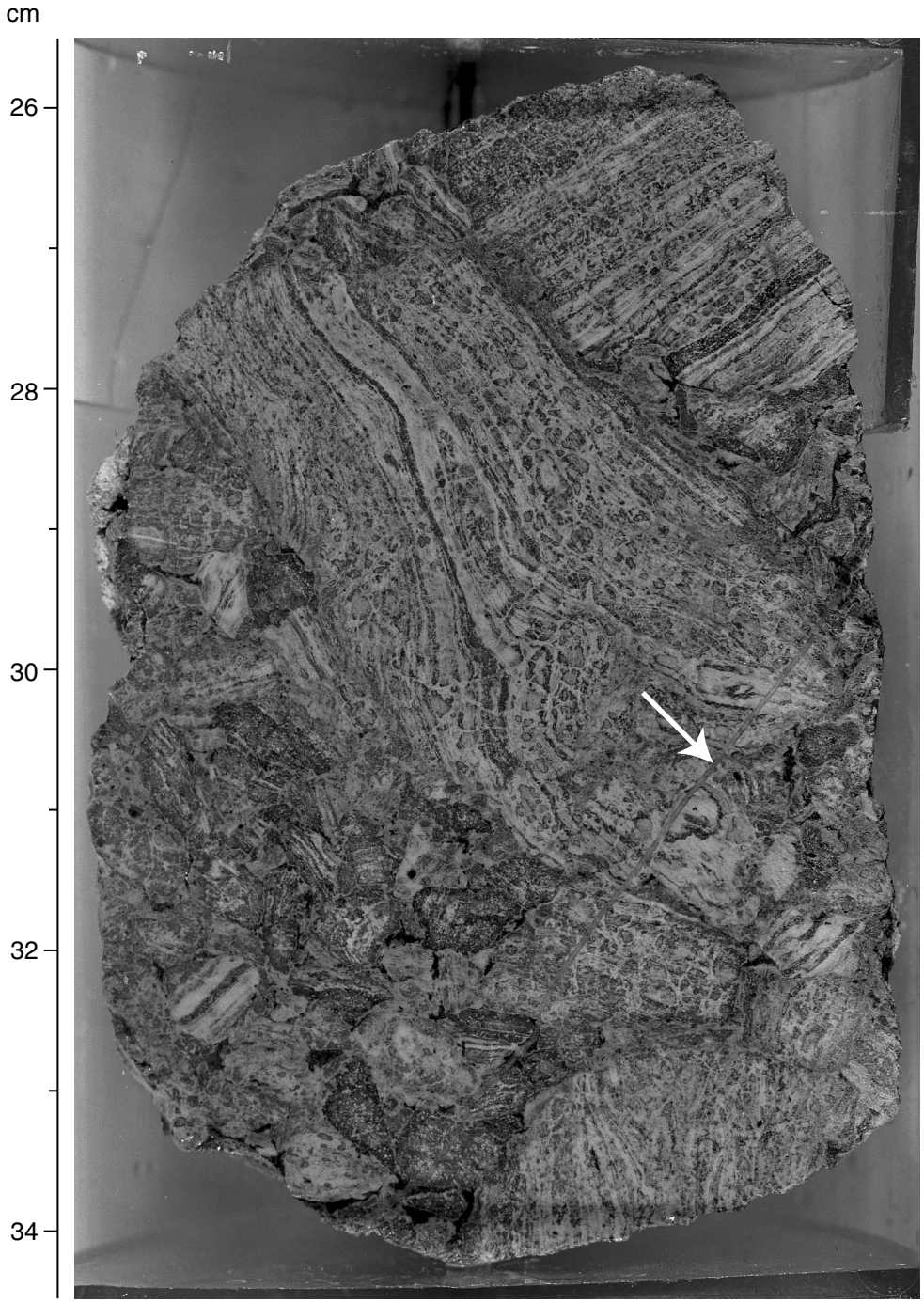

Figure F110. A. Photomicrograph of vein network and jigsaw-fit breccia in altered, flow-banded volcanic rock. The veins contain quartz, anhydrite, sphalerite and pyrite (Unit 23; Sample 193-1189B-14R-1 [Piece 15, 106–118 cm] at 157.57 mbsf). (Continued on next page.)

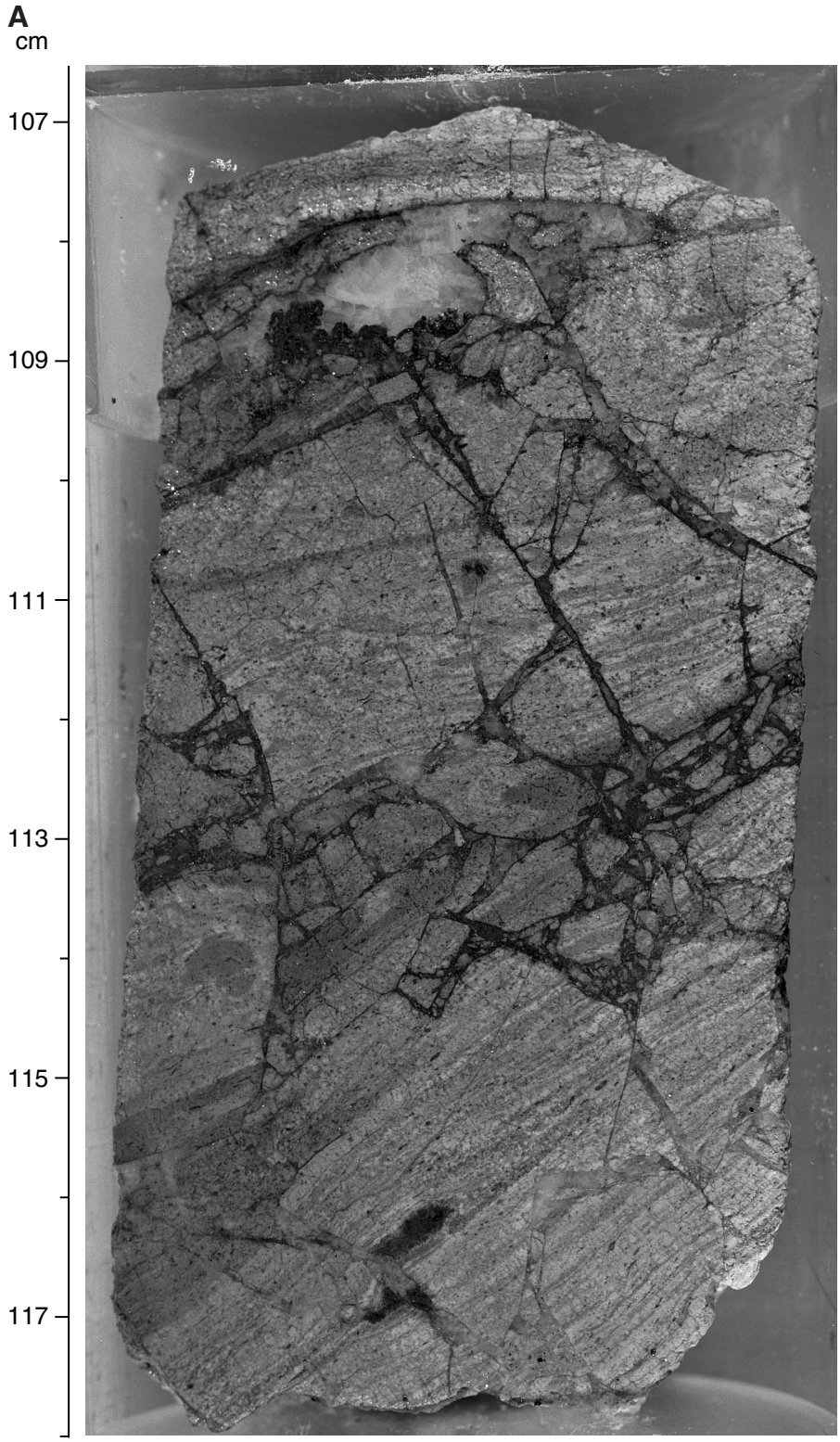

Figure F110 (continued). B. Sketch of A. Black = sulfides and gray = anhydrite and quartz. Prominent flow bands are marked A to G. For explanation, see **"Breccias and Vein Network Structures,"** p. 43.

B

Sample 193-1189B-14R-1 (Piece 14, 107-118 cm)

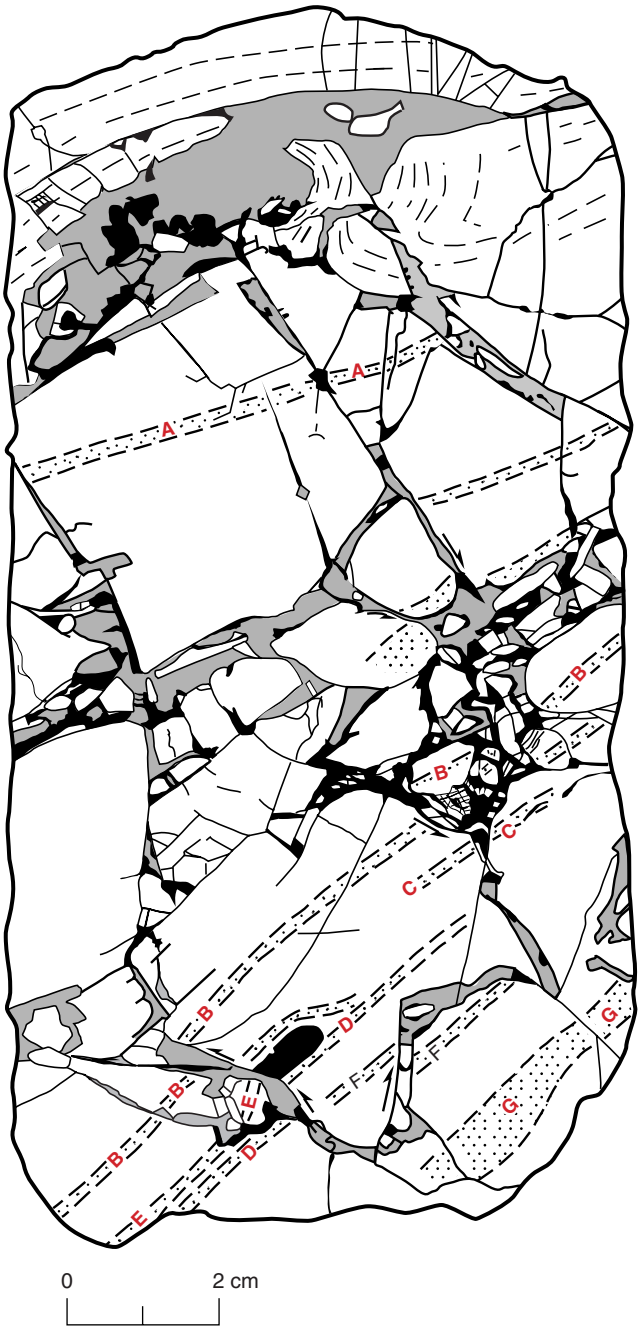

Figure F111. Vein network and brecciated, highly silicified volcanic rock. The veins consist of quartz, magnetite, and pyrite. In the right upper part of the piece, at 19 cm, a thin anhydrite vein (white) can be seen crosscutting the quartz-magnetic-pyrite vein network (Section 193-1189B-16R-1 [Piece 3, 16–26 cm]; 175.85 mbsf).

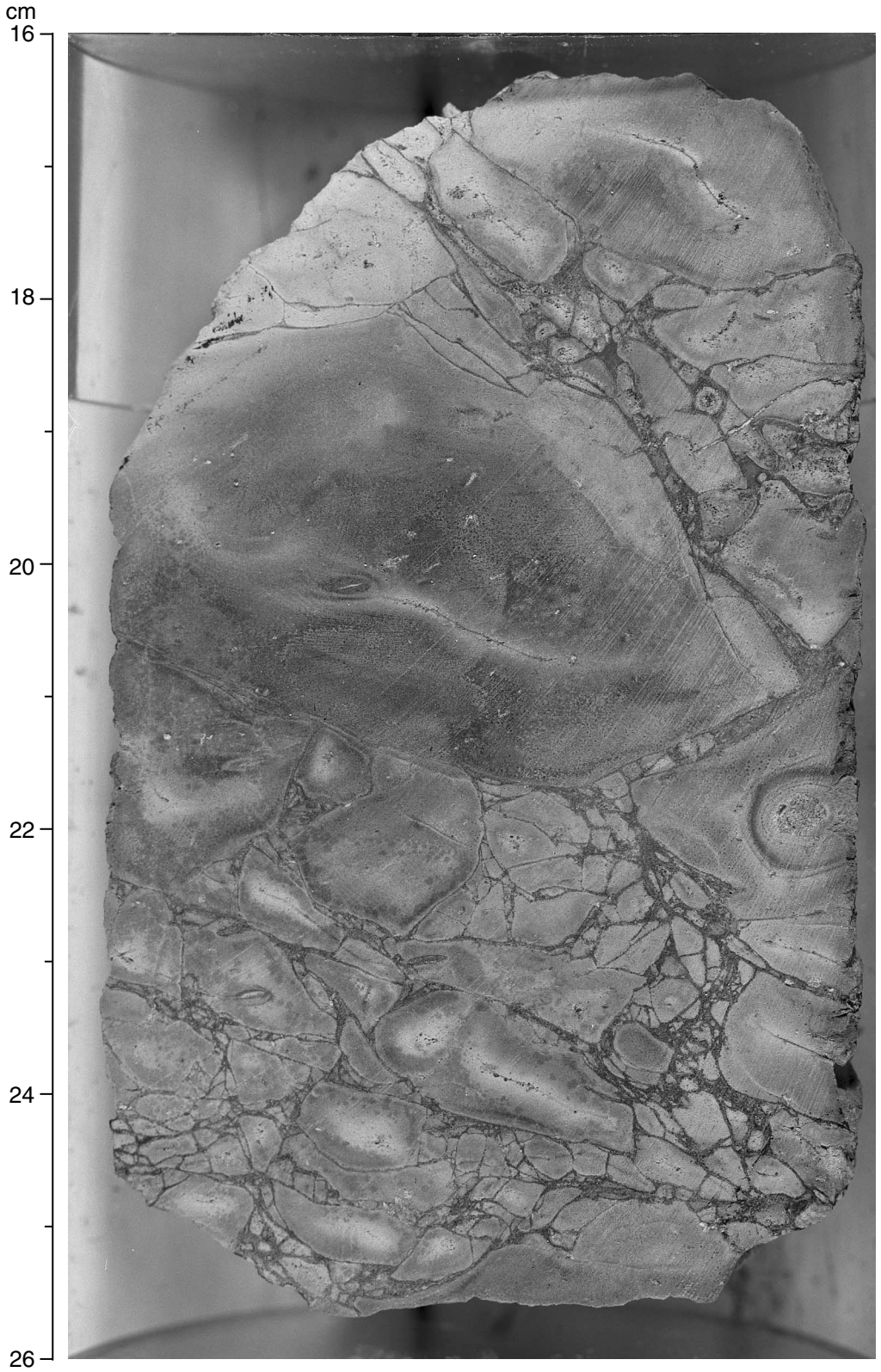

Figure F112. Photograph of coherent flow-banded core piece, with a pseudobreccia appearance created by silica-clay alteration halos around a feeble network of silica veins (interval 193-1189B-15R-1, 130–135 cm)

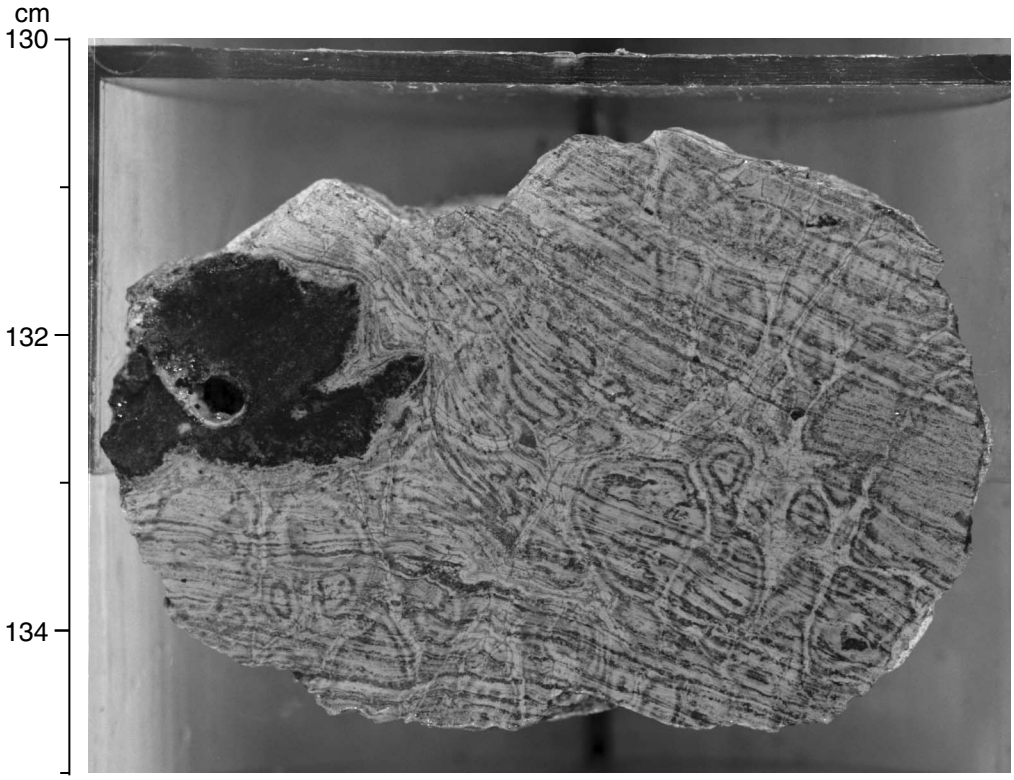

Figure F113. Distribution of veins according to mineralogy in Hole 1189B.

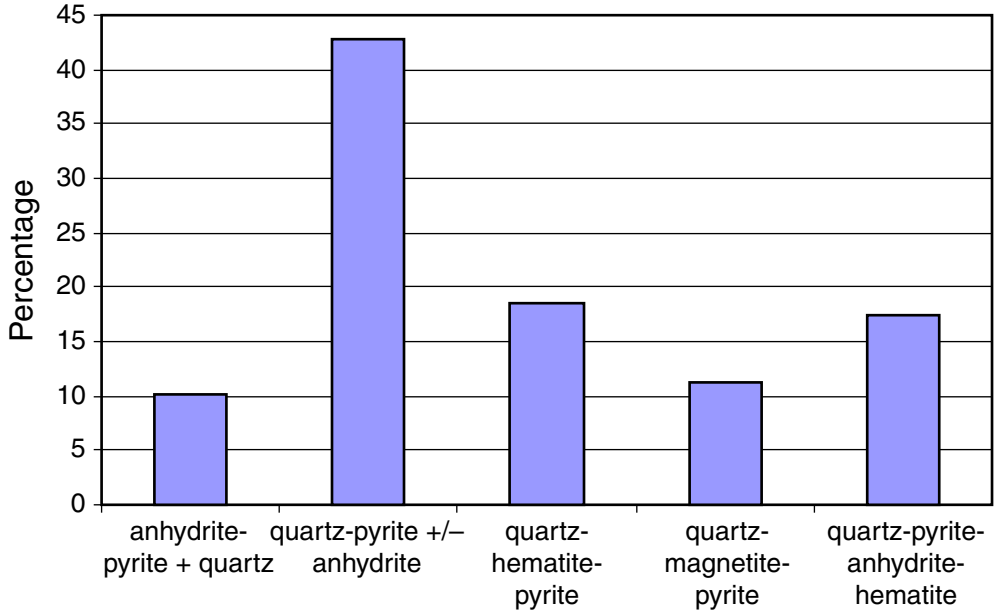

Figure F114. Distribution of veins according to mineralogy vs. lithologic units in Hole 1189B.

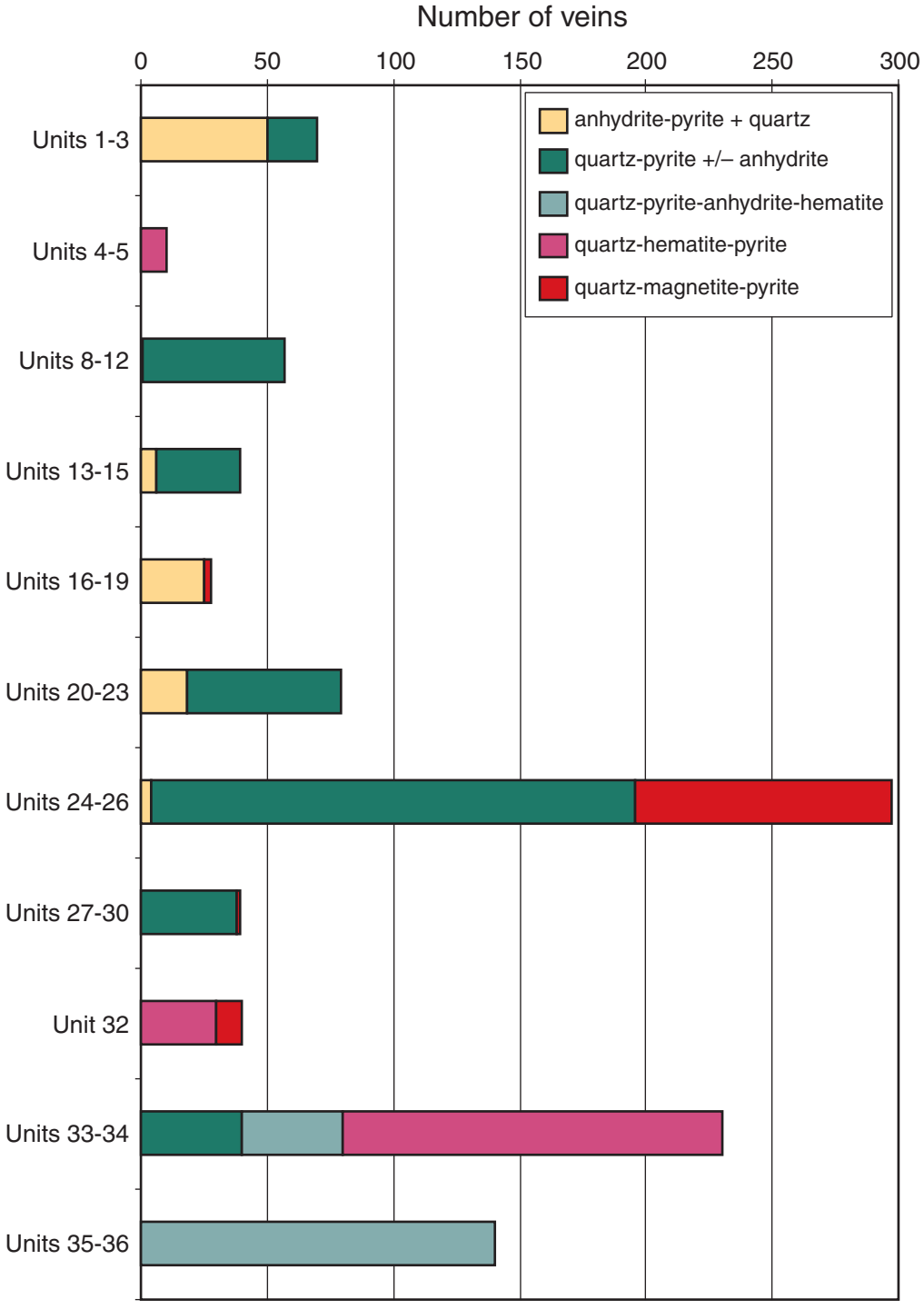

Figure F115. Quartz-anhydrite vein network crosscutting highly altered volcanic rock. The vein running up the center of the piece acted as a feeder for thin veins that run subparallel to the primary layering in the rock. In the right side of the piece is a thick vein of coarse anhydrite that crosscuts the vein network (Unit 13; Sample 193-1189B-10R-1 [Piece 3, 23–33 cm] at 118.13 mbsf).

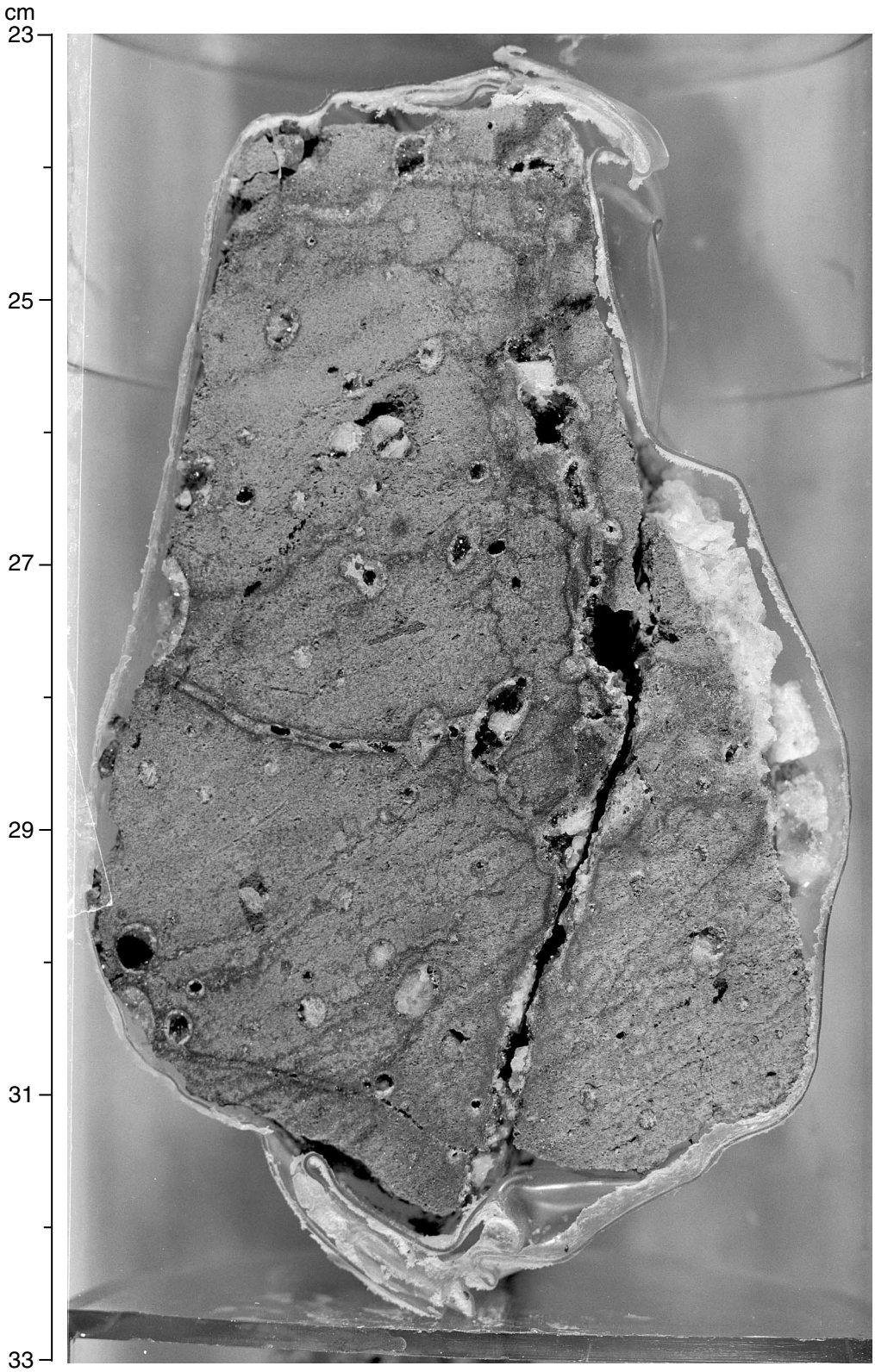

Figure F116. A. Distribution of vein thicknesses in Hole 1189B. **B.** Distribution of veins in different intervals of dip in Hole 1189B. (Continued on next page.)

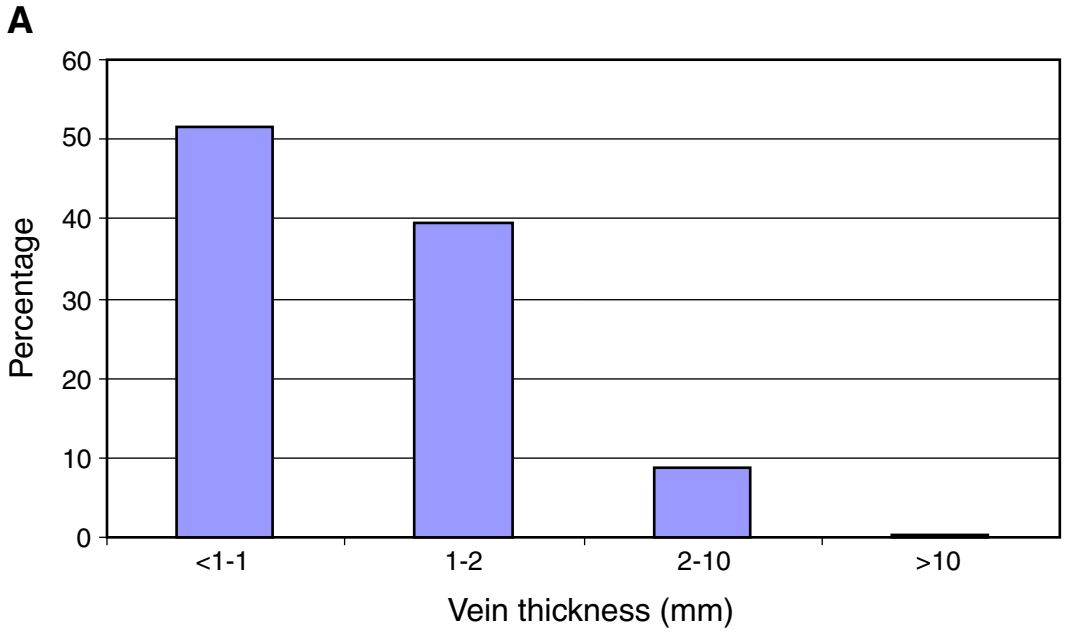

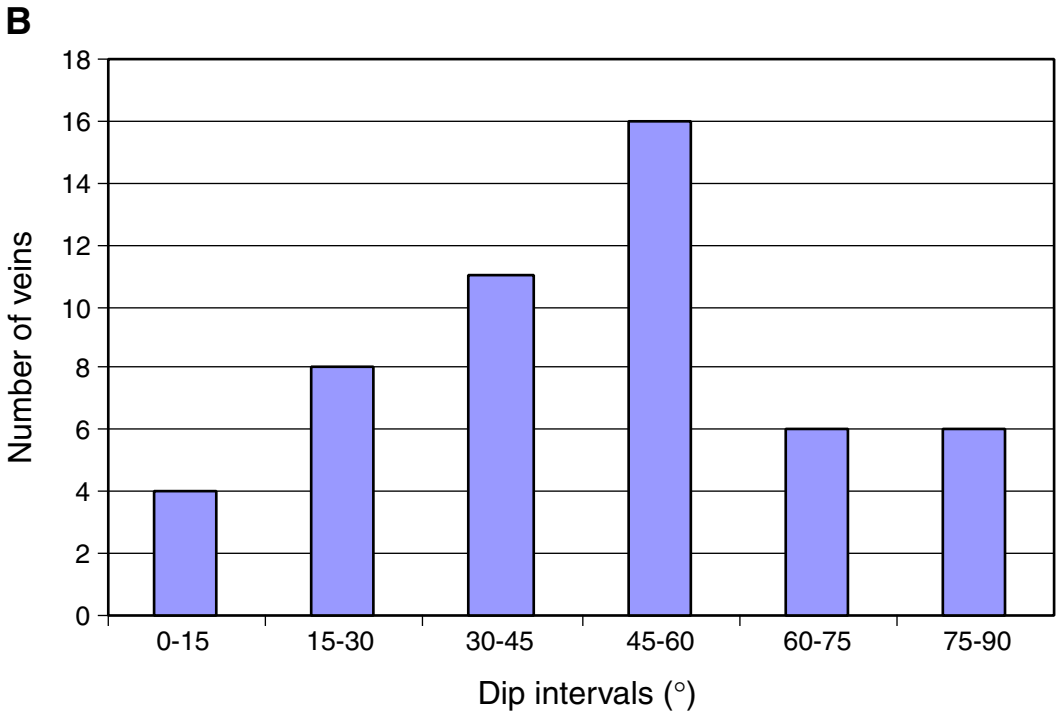

Figure F116 (continued). C. Dip of veins vs. depth in Hole 1189B.

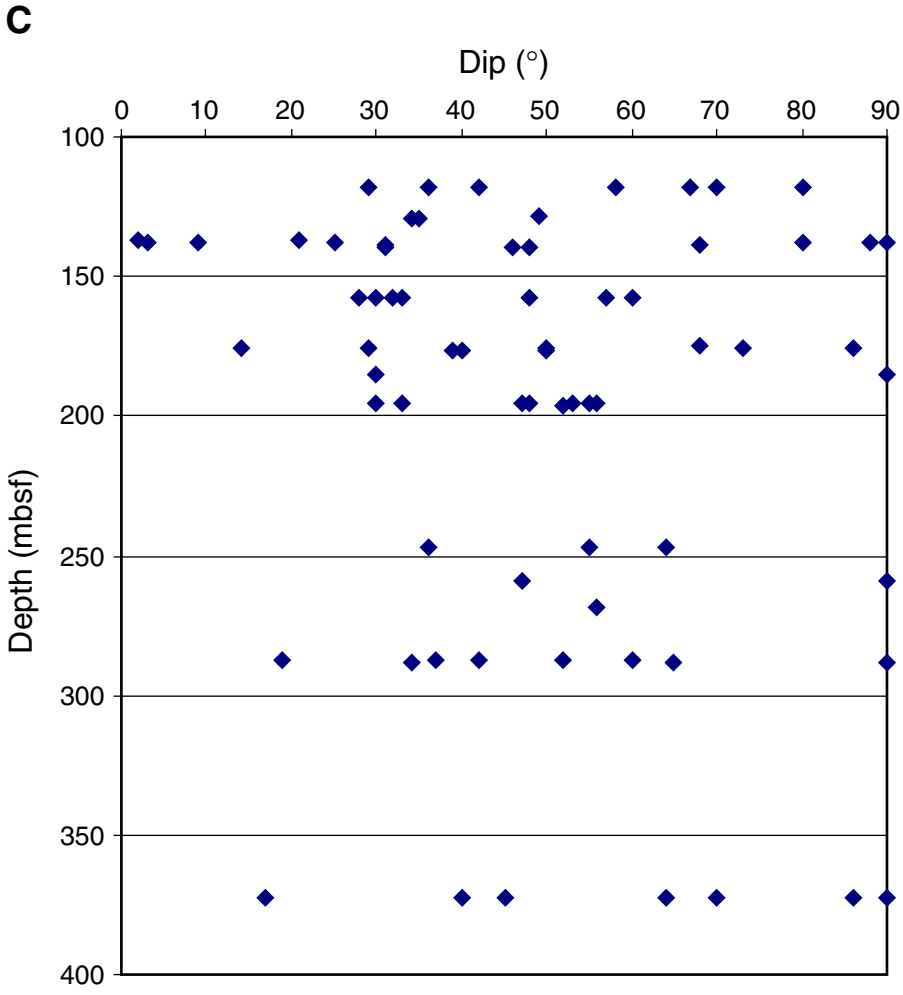

Figure F117. A. Downhole chemical variations of selected major element oxides, plotted with the significant mineral phases from X-ray diffraction, and the alteration and unit logs, Hole 1189A. (Continued on next page.)

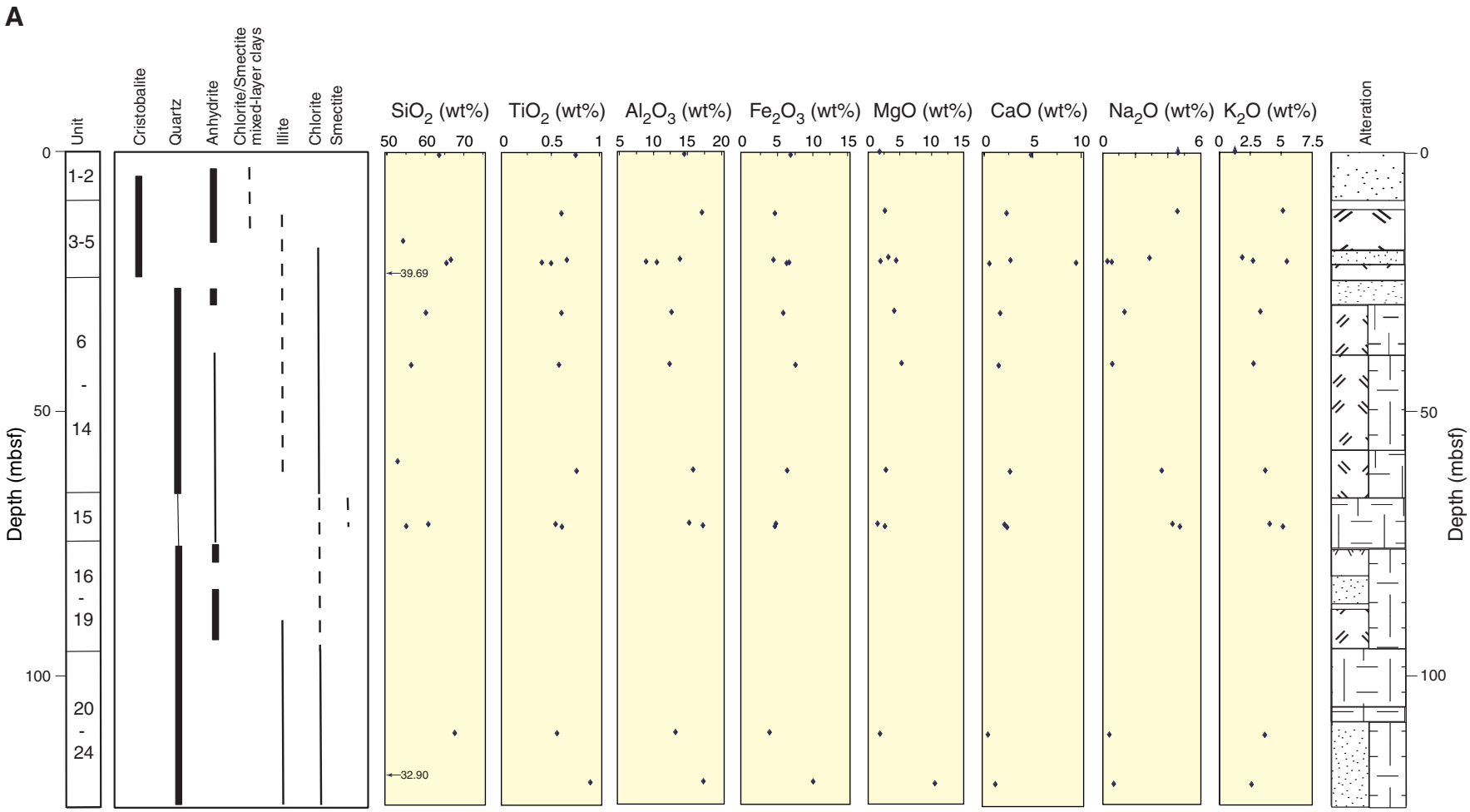

Figure F117 (continued). B. Downhole chemical variations of selected trace elements (in parts per million), plotted with the significant mineral phases from X-ray diffraction, and the alteration logs, Hole 1189A.

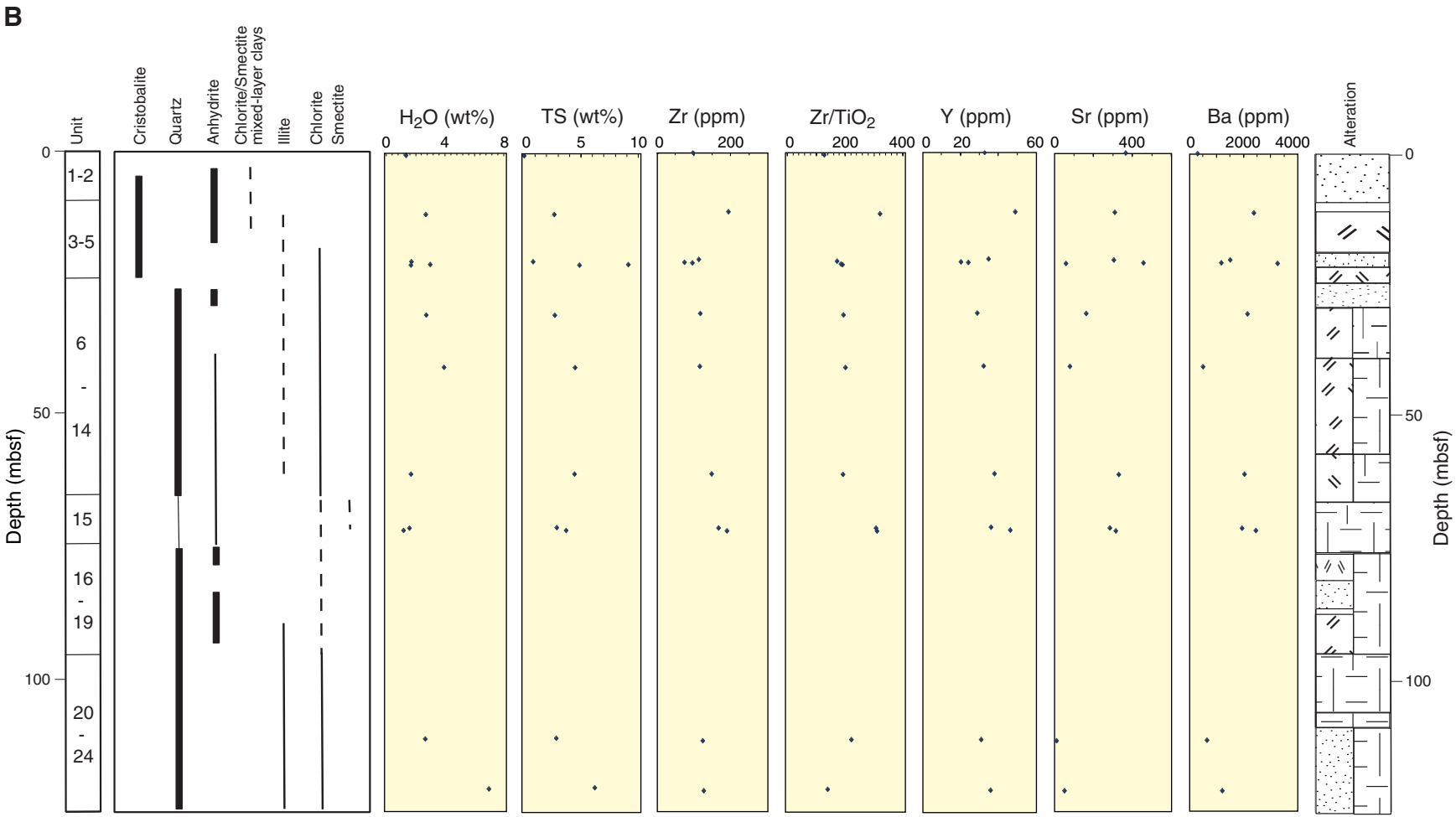

Figure F118. A. Downhole chemical variations of selected major element oxides, plotted with the significant mineral phases from X-ray diffraction, and the alteration and unit logs, Hole 1189B. (Continued on next page.)

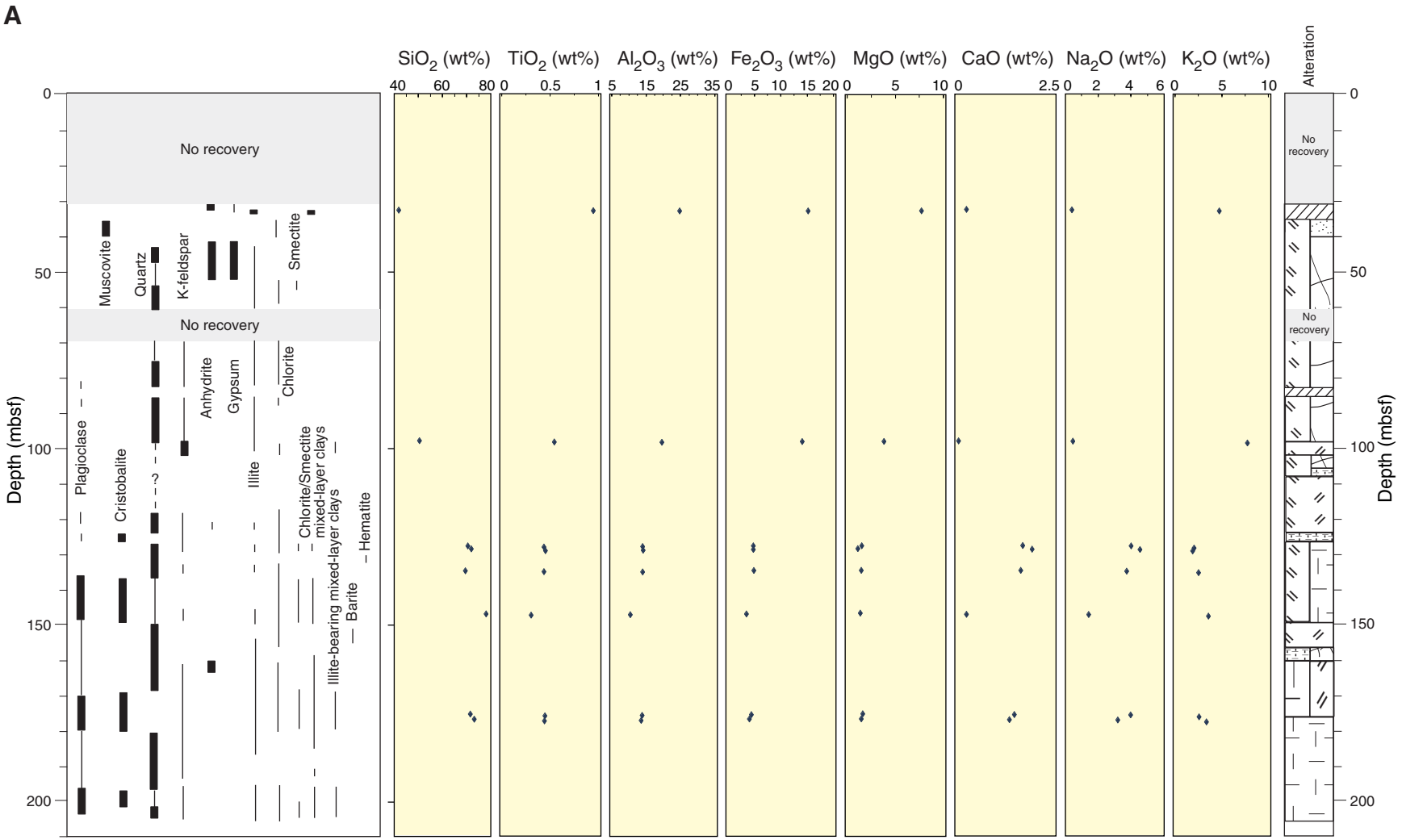

Figure F118 (continued). B. Downhole chemical variations of selected trace elements (as ppm), plotted with the significant mineral phases from X-ray diffraction, and the alteration log, Hole 1189B.

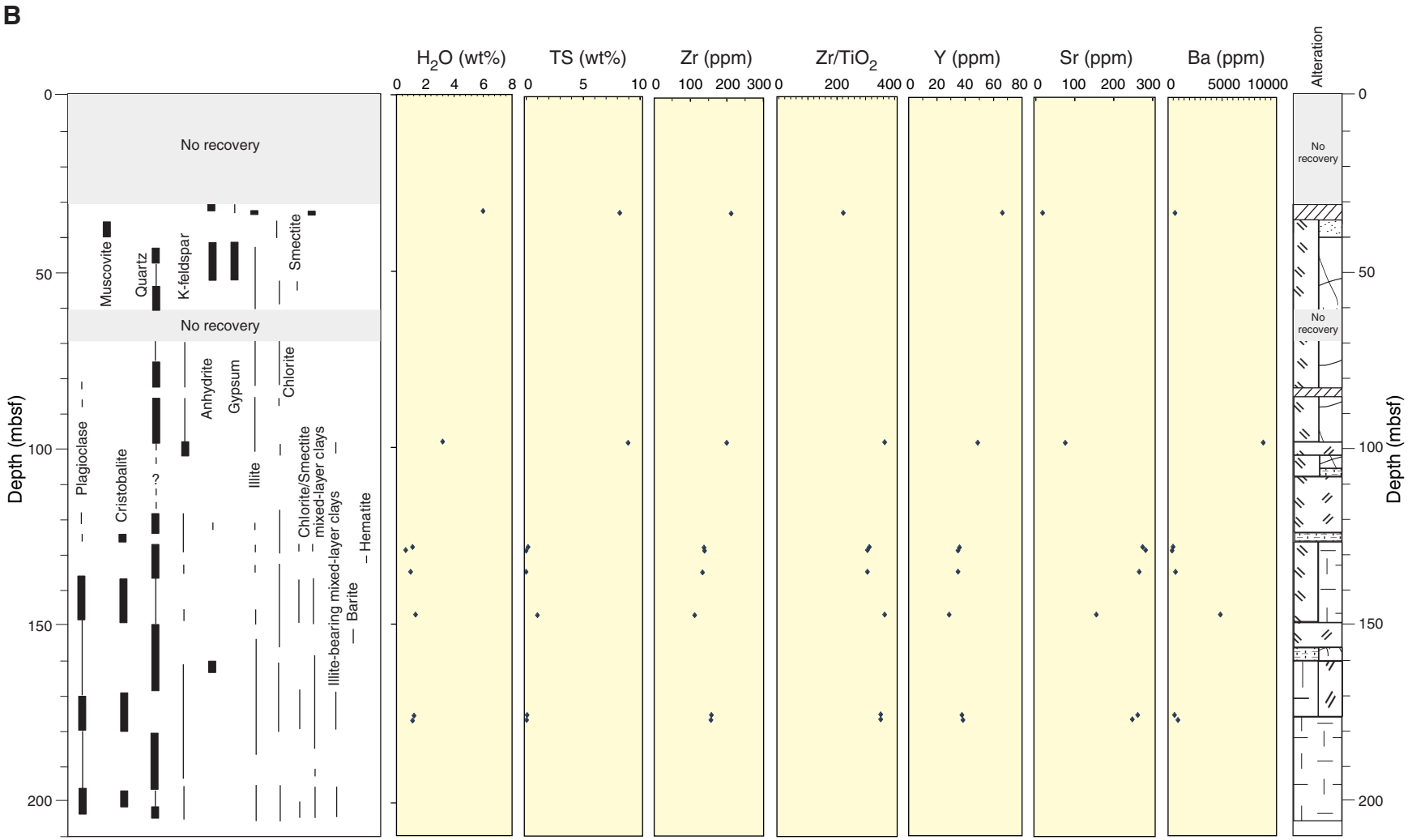

Figure F119. Observations of cultivation experiment.

Culture Conditions	Culture Media Descriptions		Bacterial Observations		pH	
	25°C	60°C	25°C	60°C	25°C	60°C
A	—	■	+++	+	7.92	7.79
B	—	—*	+	+	8.05	8.00
C	▒	▒	++	+	6.21	6.48
D	—	—*	ND	ND	6.32	6.41
E	■	■	+++	+	6.52	6.60
F	—	—	ND	ND	6.43	6.68

■ cloudy
▒ slightly cloudy
— clear
* gypsum deposits

+++ high bacterial growth
++ moderate bacterial growth
+ low bacterial growth
ND not detected

Figure F120. Photomicrographs and schematic images of epifluorescence observations of aerobic culture after 2 weeks of incubation. **A-1, A-2.** DAPI-stained natural seawater bacteria fluoresce blue in the suspensions of clay minerals, which fluoresce yellow-orange. **B-1, C-1.** The bacterial mass forms exopolymeric clusters. **B-2, C-2.** Within these clusters, seawater bacteria of various sizes can be distinguished.

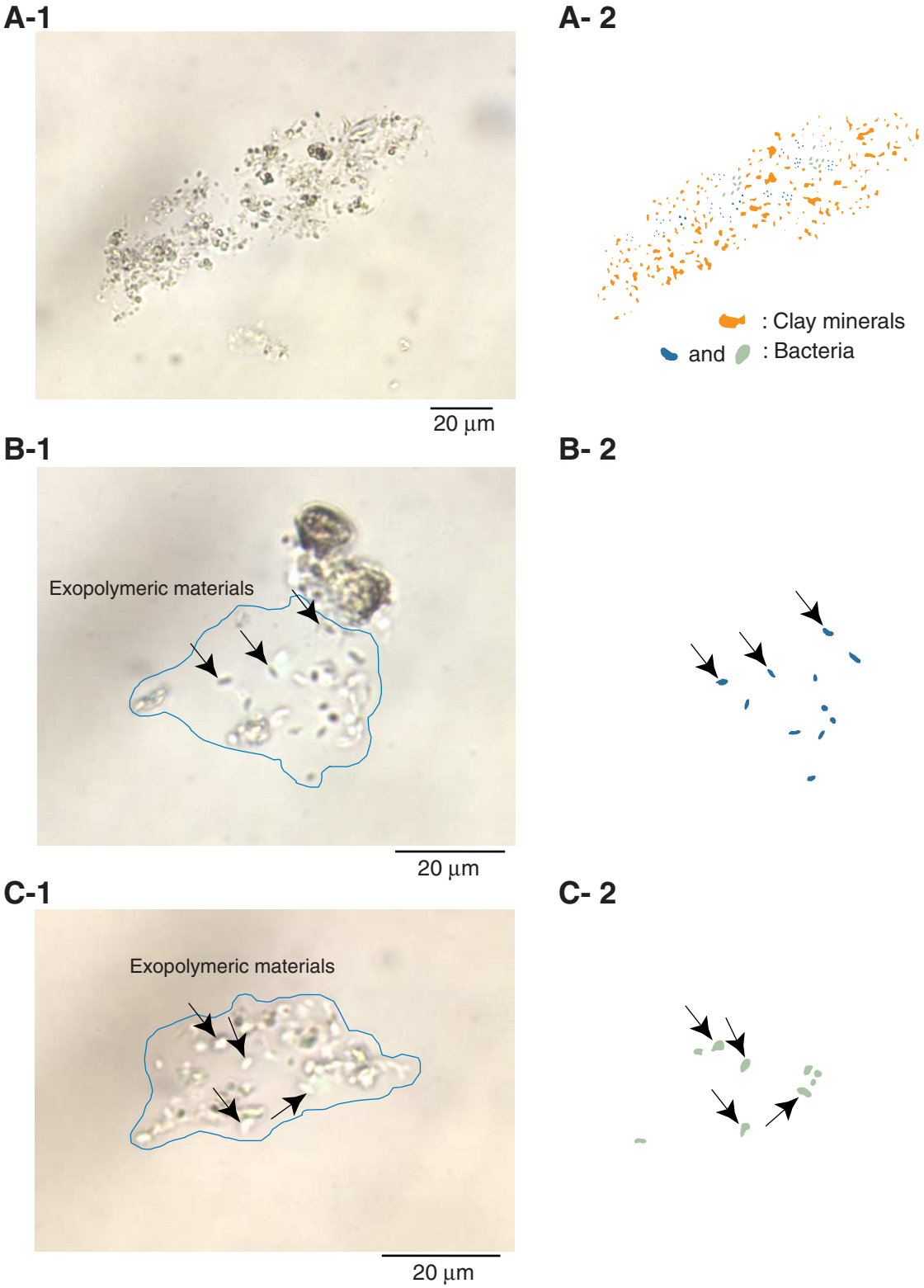

FigFure F121. Photomicrographs and schematic images of epifluorescence observations of anaerobic cultures after 4 weeks of incubation. **A-1, A-2.** DAPI-stained bacteria (blue) in suspensions of clay minerals (orange) from sterilized seawater culture at 25°C. **B-1, B-2.** DAPI-stained bacterial colonies (blue) and clay mineral assemblage (orange) from sterile synthetic seawater at 25°C. **C.** Rod-shaped bacteria found in sterilized synthetic seawater.

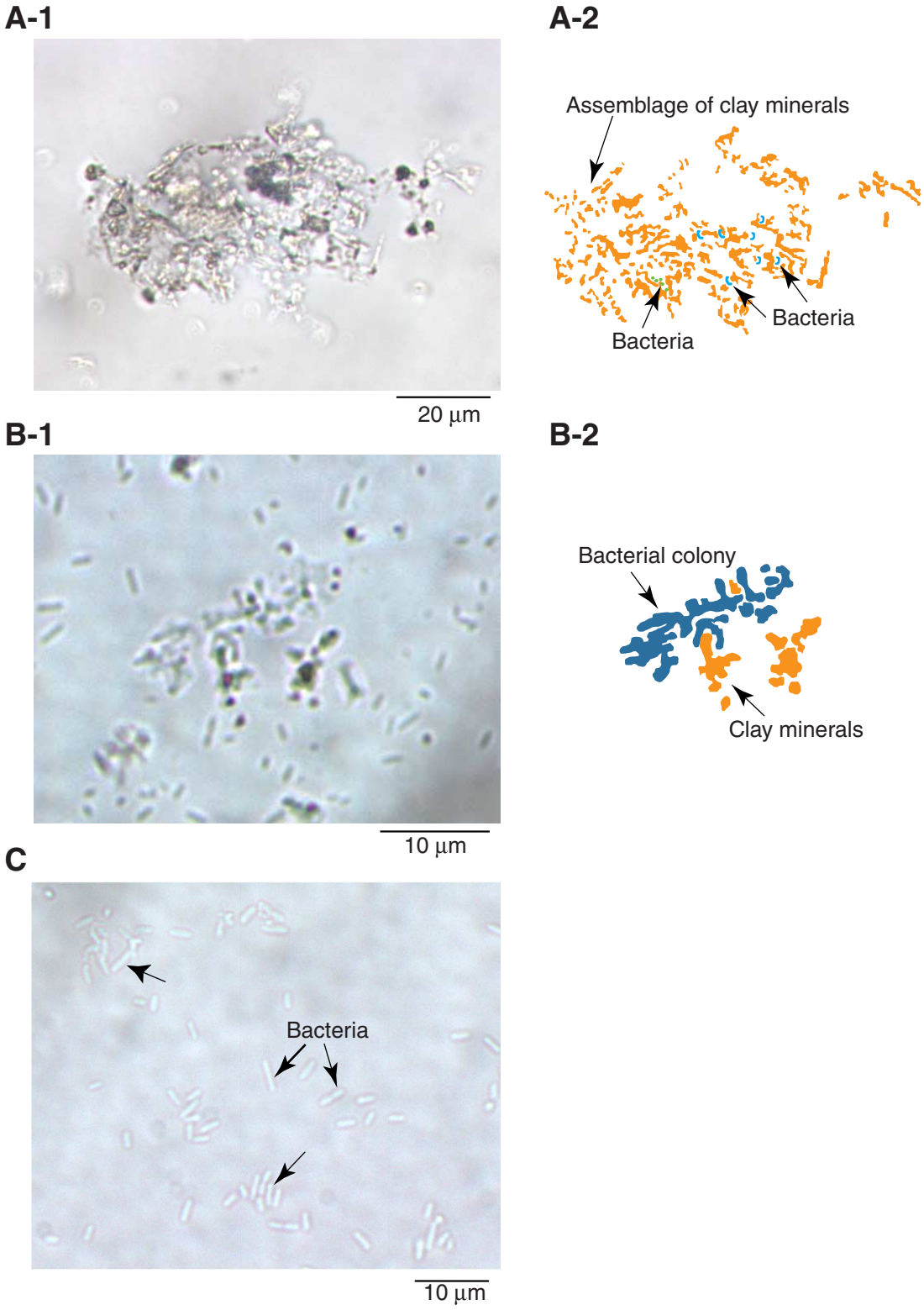

Figure F122. Photomicrographs of transparent rectangular crystals (anhydrite) and flaky brown translucent clusters from Sample 193-1189A-6R-1, 35–38 cm (48.6 mbsf); showing bacterial habitation. **A.** Bacterial spots on surfaces of some flaky clusters. **B.** Bacterial colonies on surfaces. **C.** Rectangular anhydrite crystals with no bacteria.

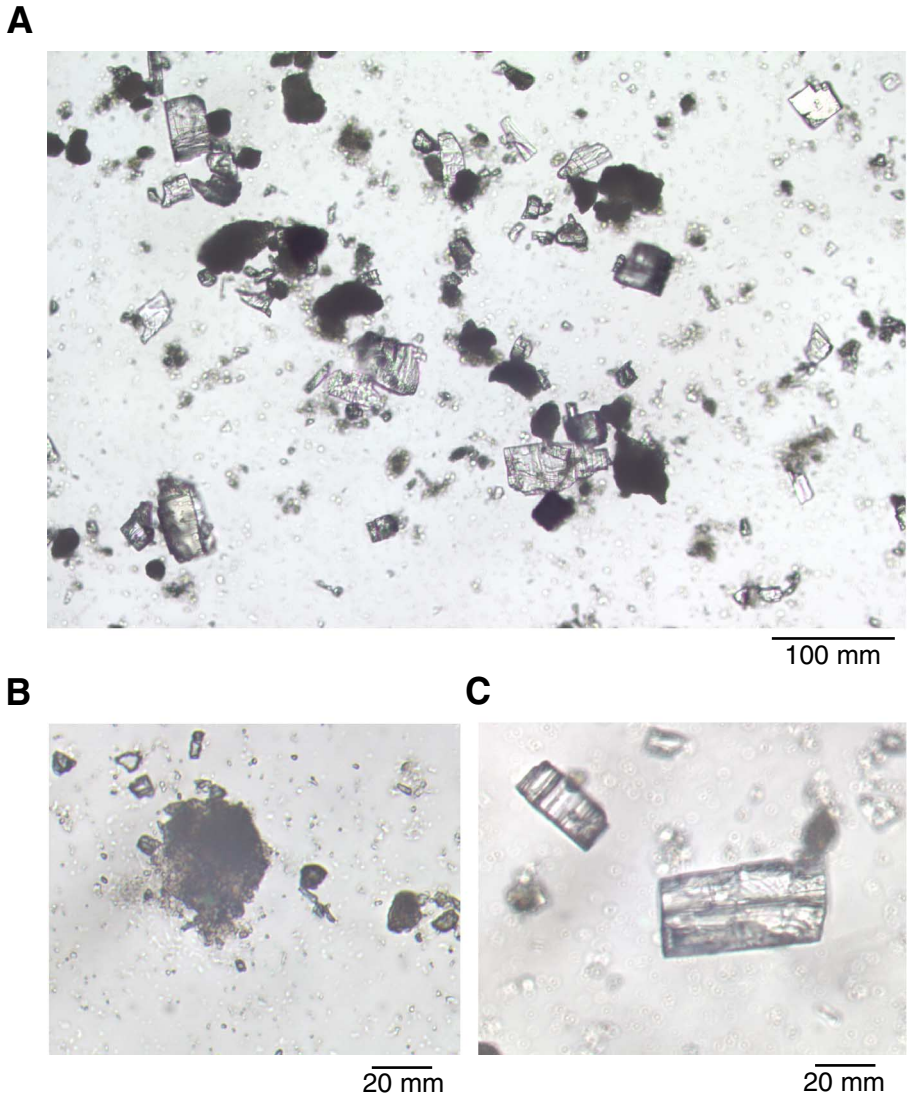

Figure F123. Photomicrographs of Sample 193-1189A-12R-1, 41–50 cm (106.91 mbsf), showing possible bacterial habitation. **A.** Exopolymeric clusters containing transparent, translucent, and opaque particles. **B.** Mineralized bacteria in chains of three to six bacteria.

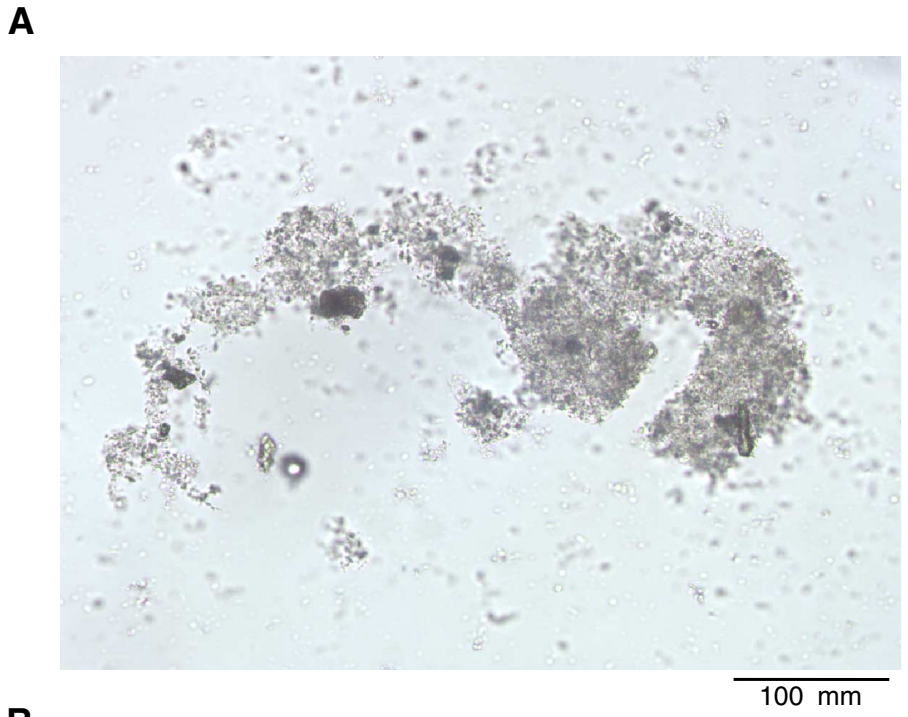

Figure F124. Magnetic susceptibility profile for Site 1189. Solid circles = Hole 1189A, open circles = Hole 1189B.

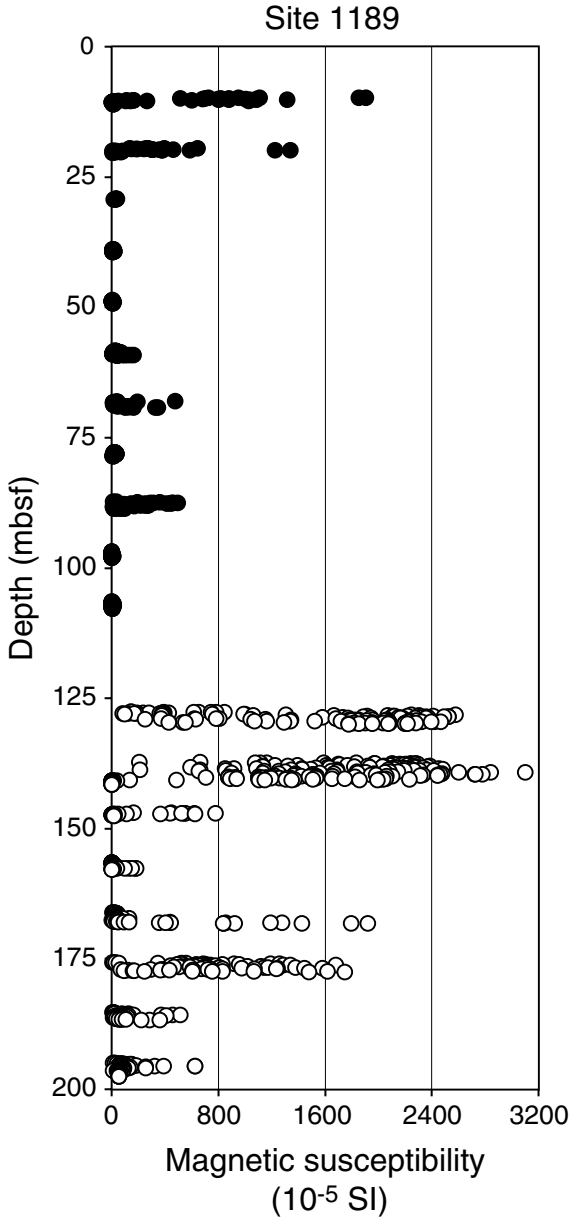

Figure F125. Natural gamma radiation (NGR) profile for Site 1189. Solid circles = Hole 1189A, open circles = Hole 1189B.

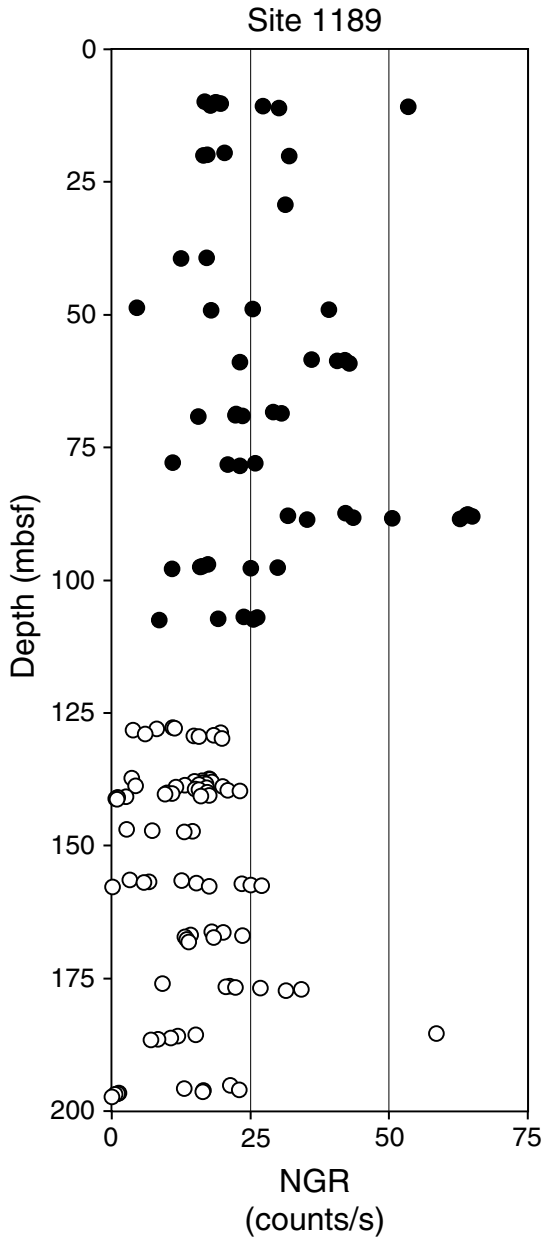

Figure F126. Compressional wave velocity profile for Site 1189. Solid circles = Hole 1189A, open circles = Hole 1189B.

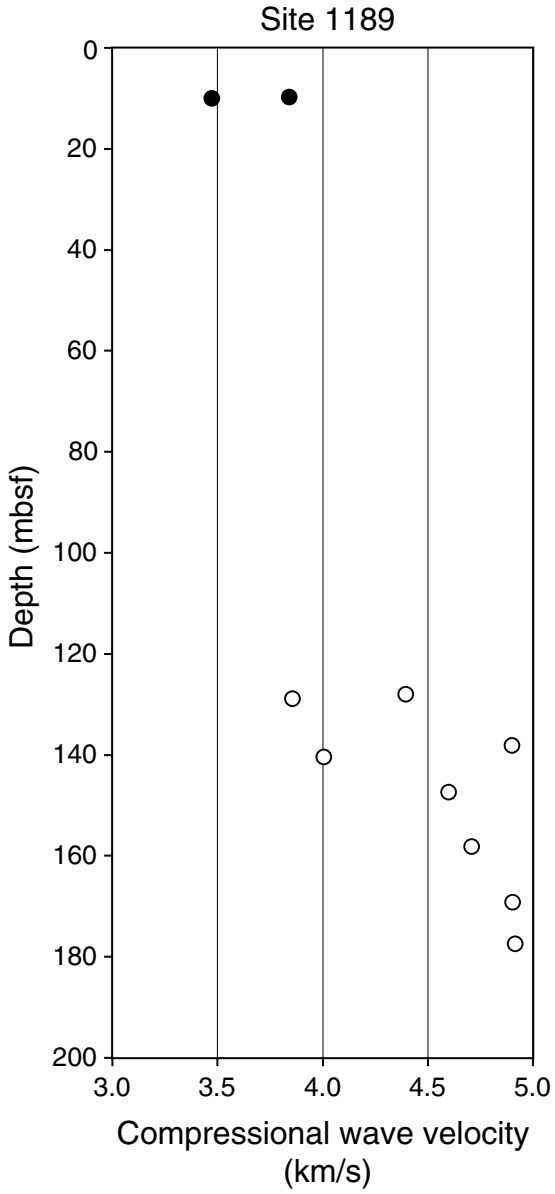

Figure F127. Thermal conductivity profile for Site 1189. Solid circles = Hole 1189A, open circles = Hole 1189B.

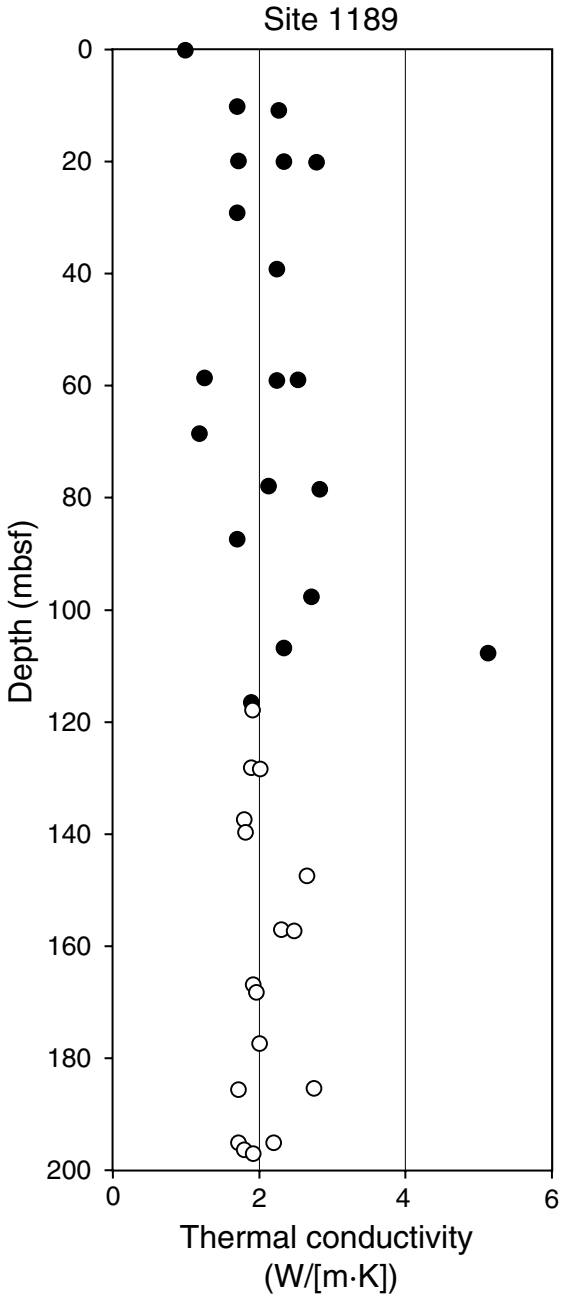

Figure F128. Grain density profile for Site 1189. Solid circles = Hole 1189A, open circles = Hole 1189B.

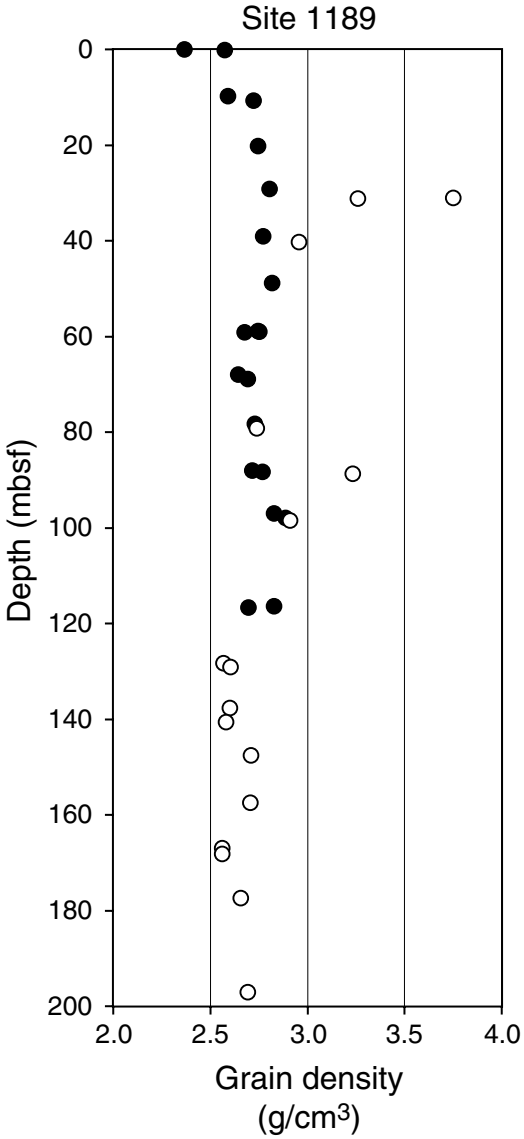

Figure F129. Porosity profile for Site 1189. Solid circles = Hole 1189A, open circles = Hole 1189B.

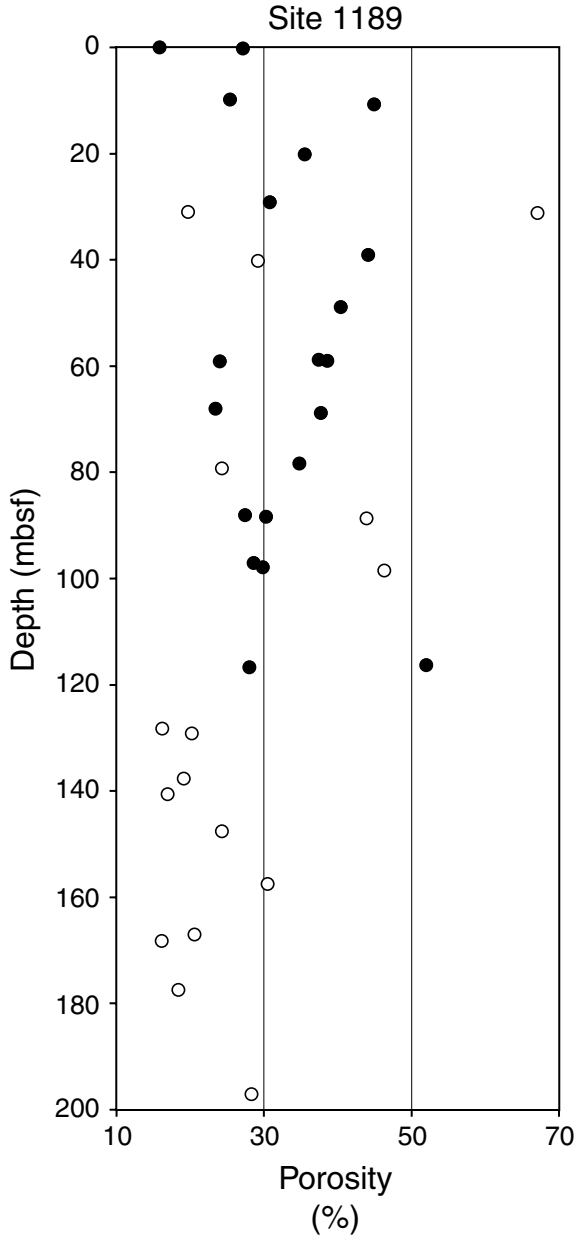

Figure F130. Profile of volume susceptibility vs. depth of archive-half samples, combining data from Hole 1189A with the lower sequence of Hole 1189B. The susceptibility represents point measurements taken using the archive multisensor track in manual mode.

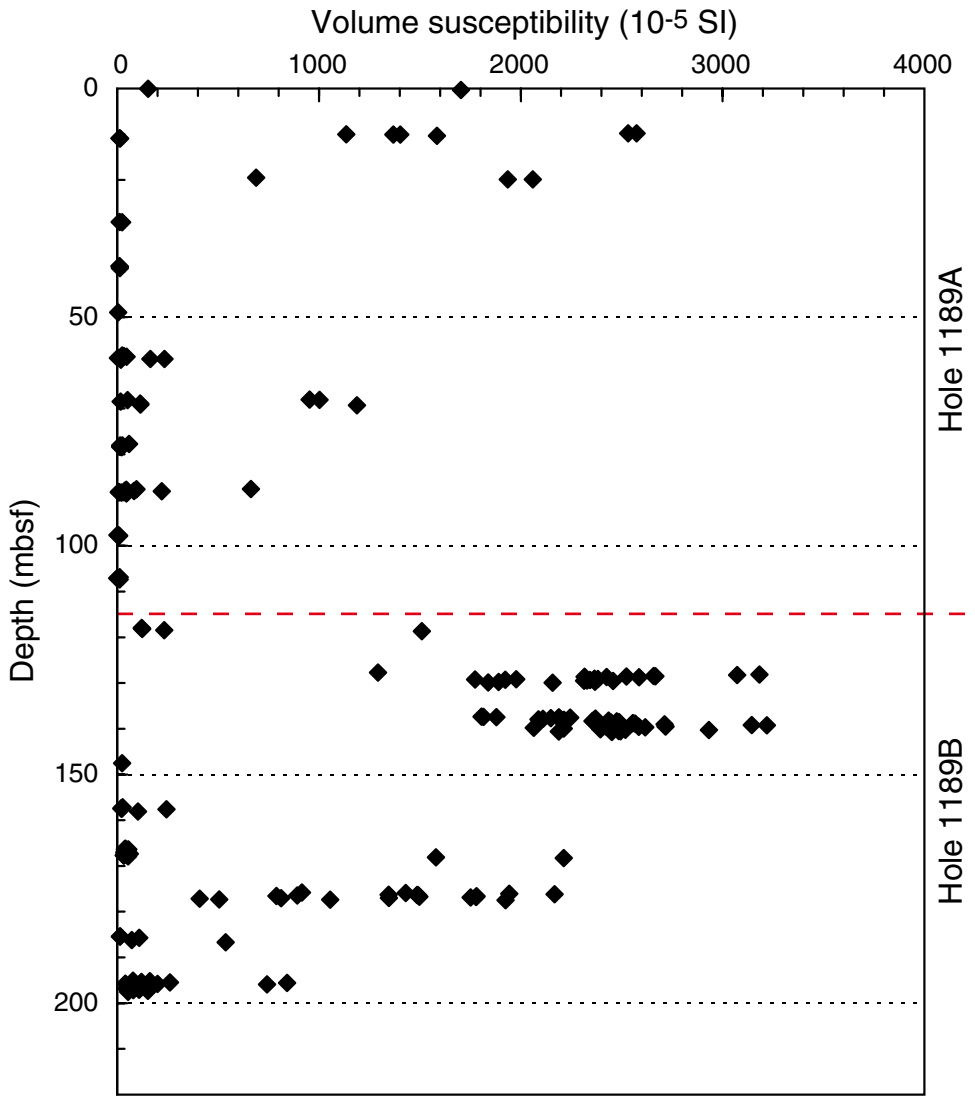

Figure F131. Uncorrected remanent intensity vs. depth of archive-half samples, combined profile for Site 1189.

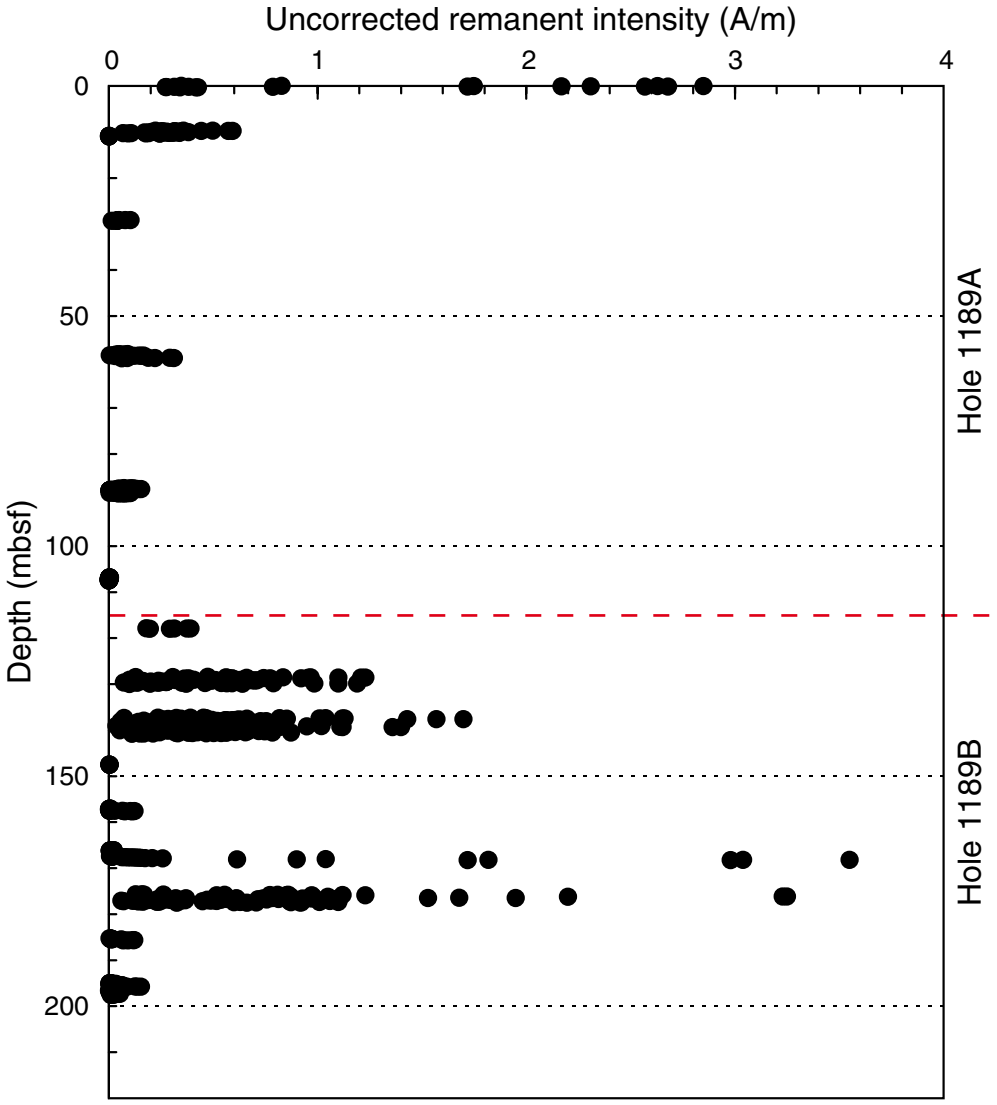

Figure F132. Magnetic susceptibility vs. depth of minicore samples, combined profile for Site 1189.

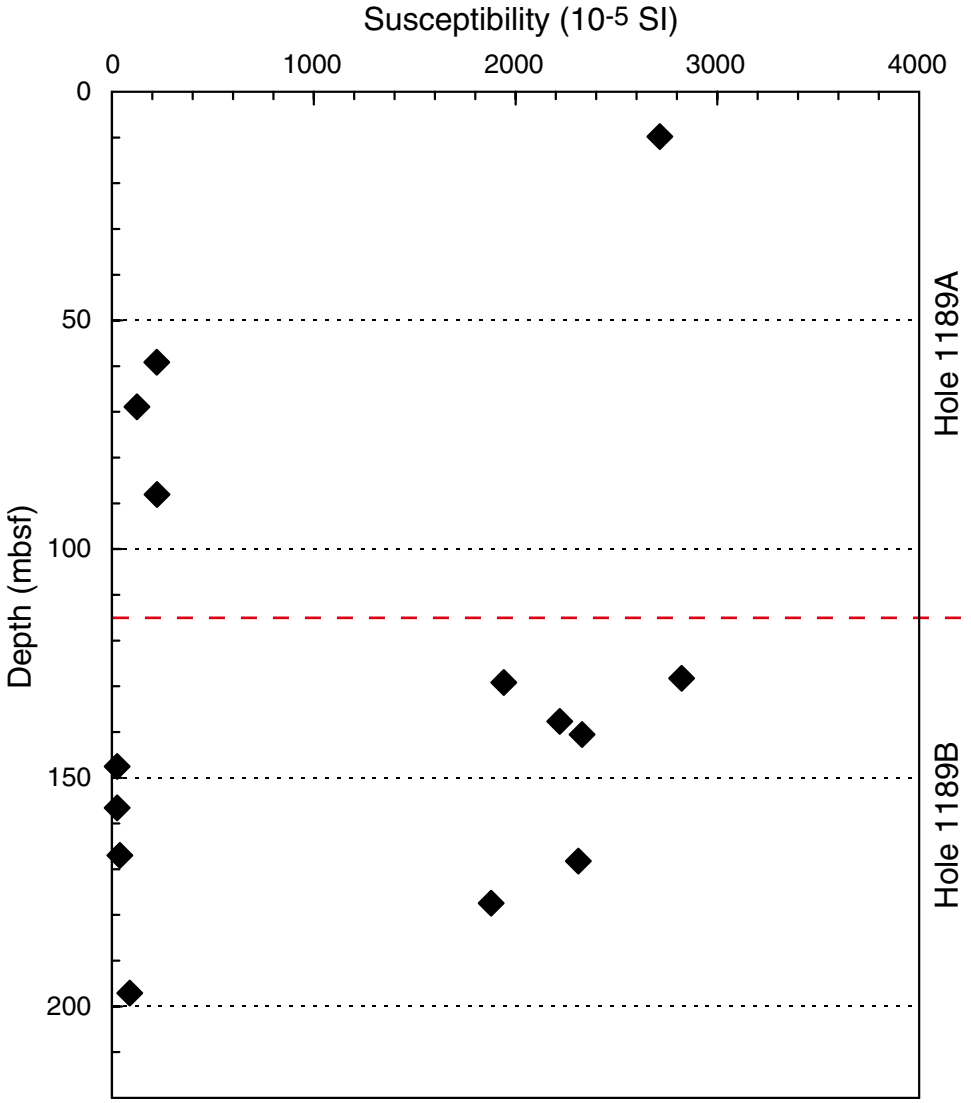

Figure F133. Flinn-type diagram showing the foliation (F) and lineation (L) of the anisotropy of the magnetic susceptibility ellipsoid. Data are divided into two groups: prolate and oblate.

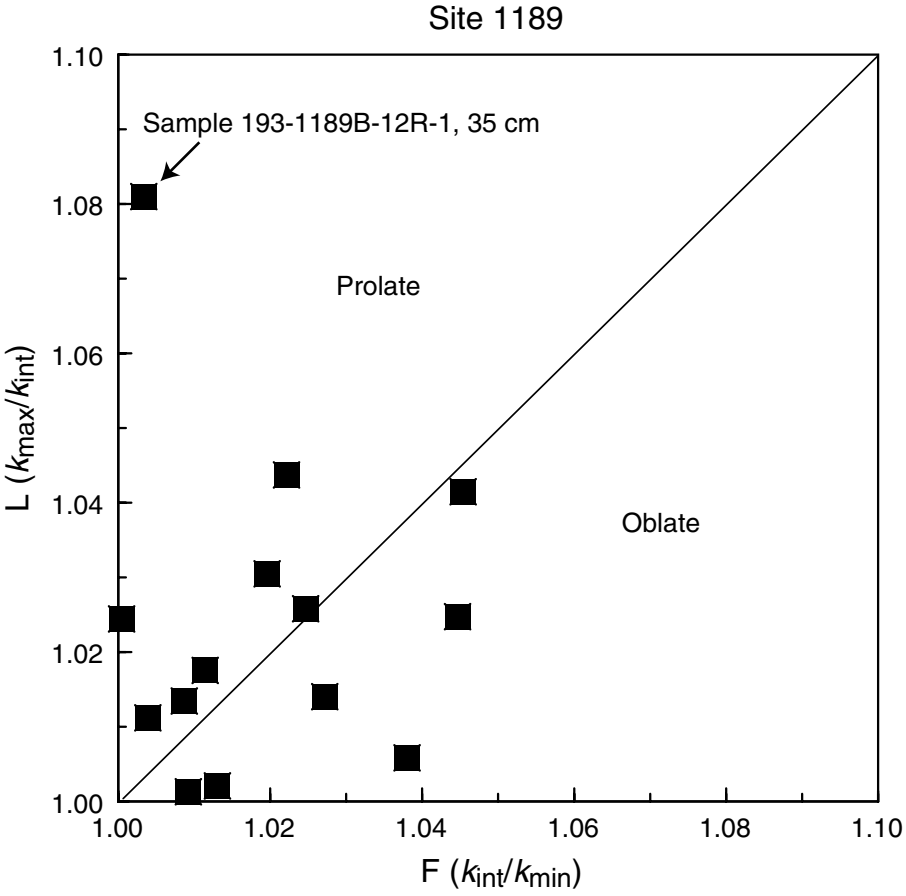

Figure F134. Natural remanent magnetization (NRM) intensity vs. depth of minicore samples, combined profile for Site 1189.

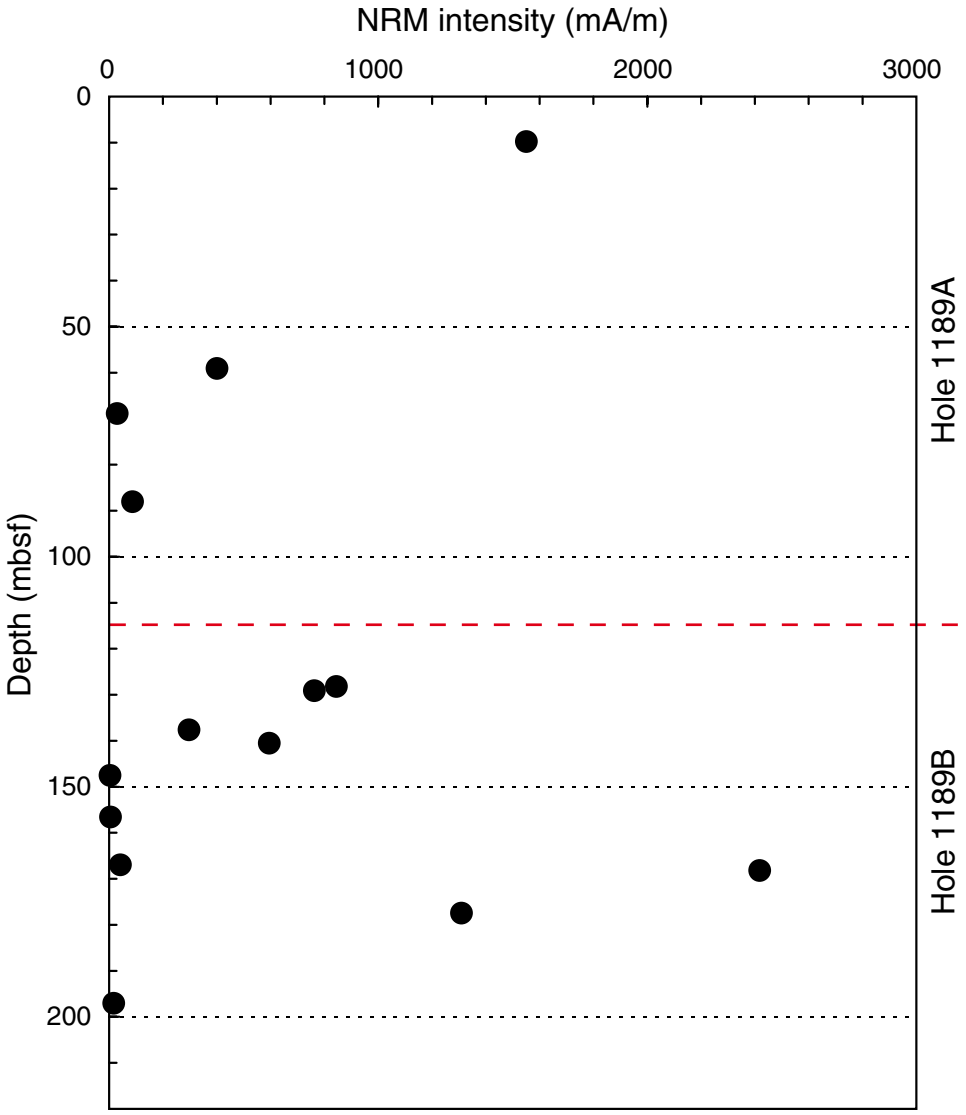

Figure F135. Stable inclination vs. depth of minicore samples, combined profile for Site 1189.

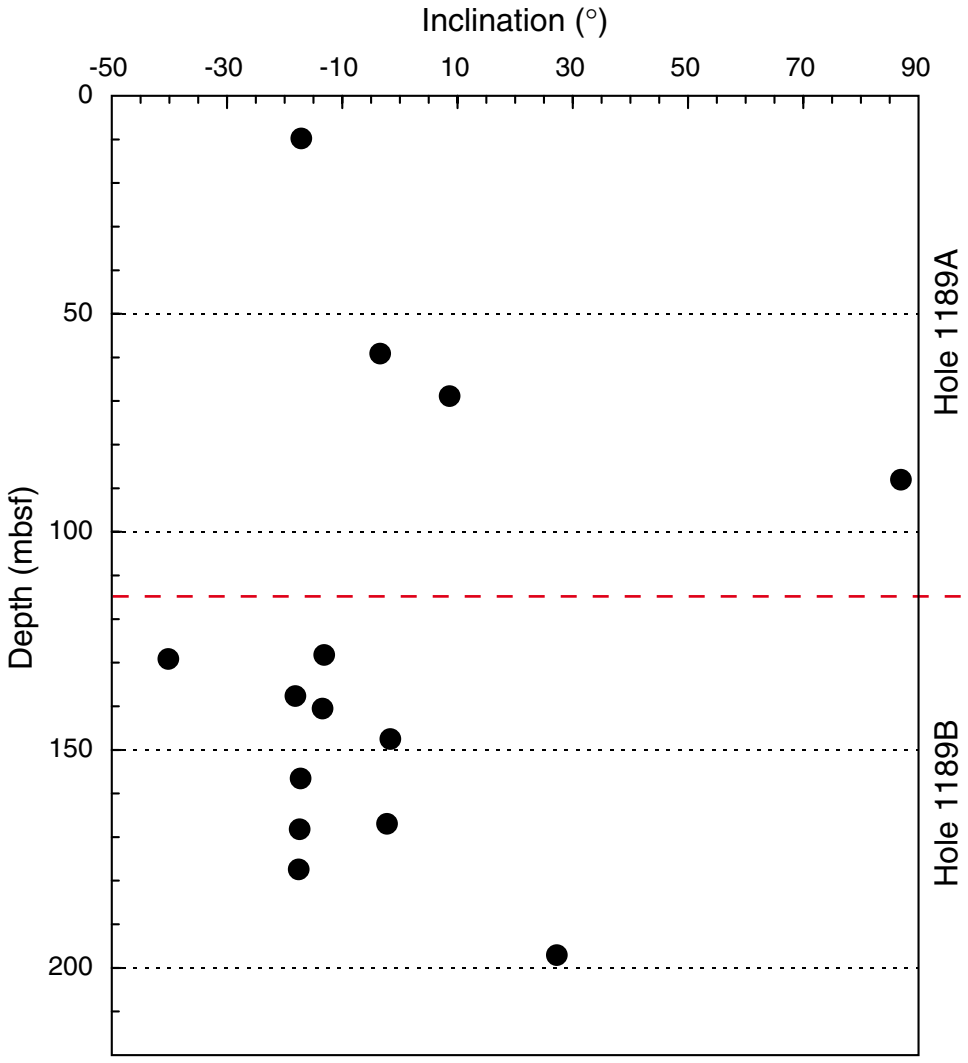

Figure F136. Zijderveld plot and intensity decay curve of Sample 193-1189B-18R-2, 66 cm, showing irregular behavior during progressive alternating-field demagnetization.

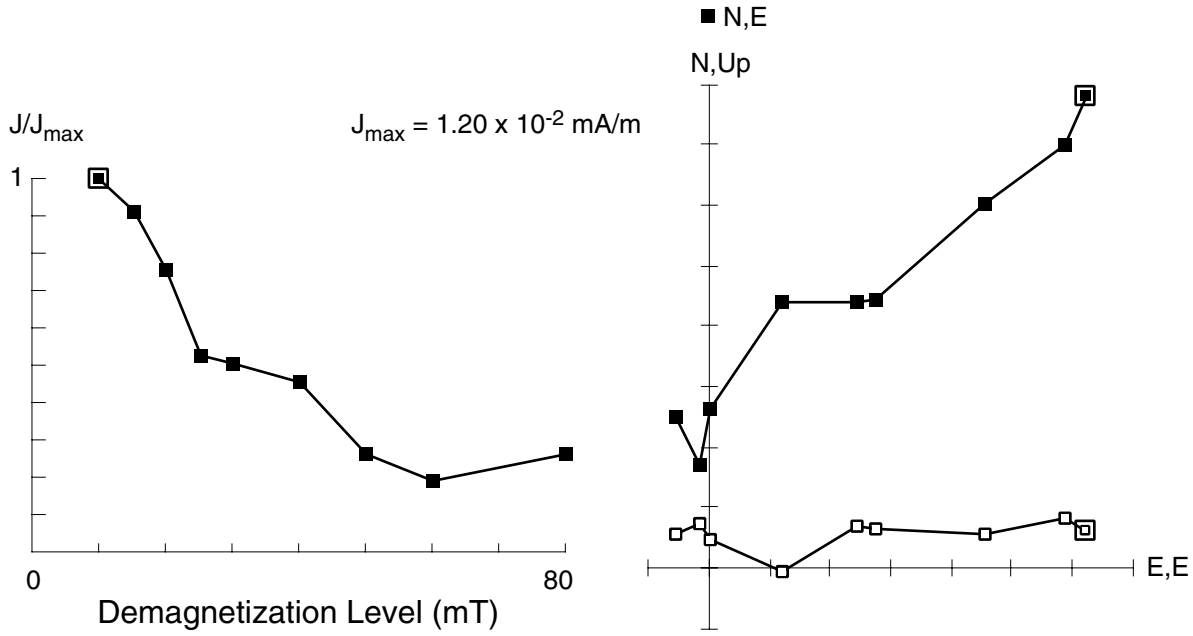

Figure F137. Intensity of isothermal remanent magnetization (IRM) as a function of applied impulse field for four minicores from Hole 1189A.

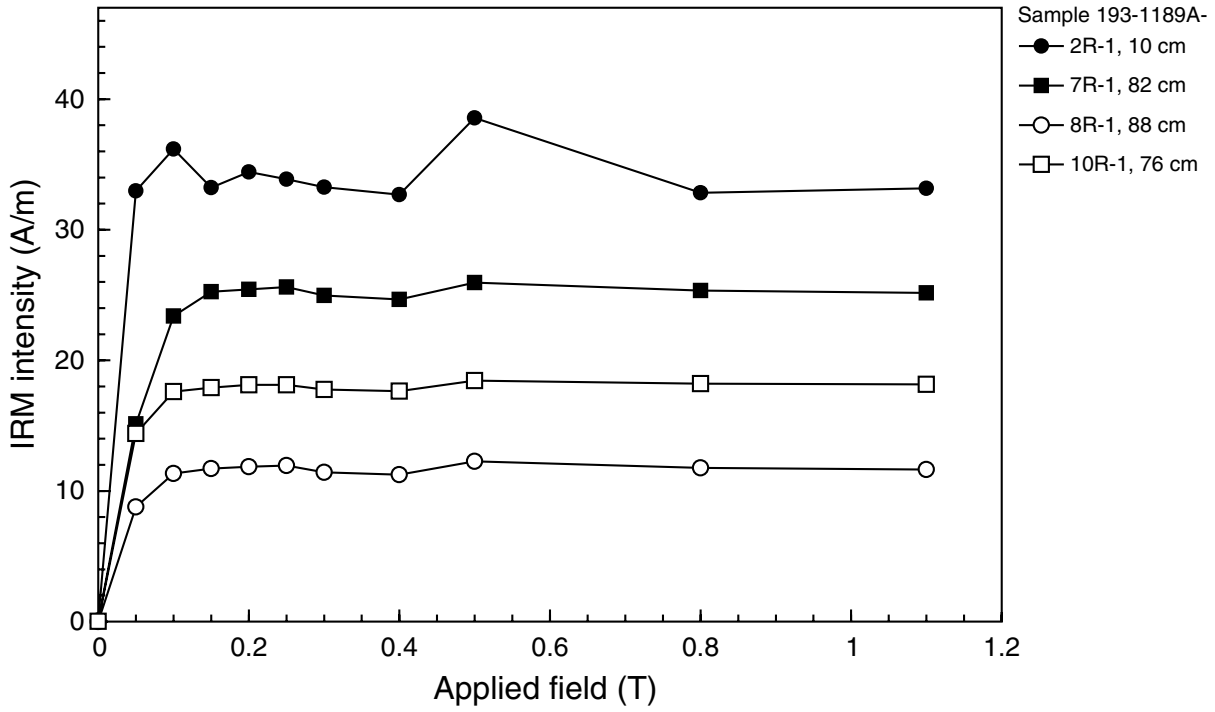

Figure F138. Intensity of isothermal remanent magnetization (IRM) as a function of applied impulse field for 10 minicores from Hole 1189B. The high variability in IRM is a result of instrumental effects.

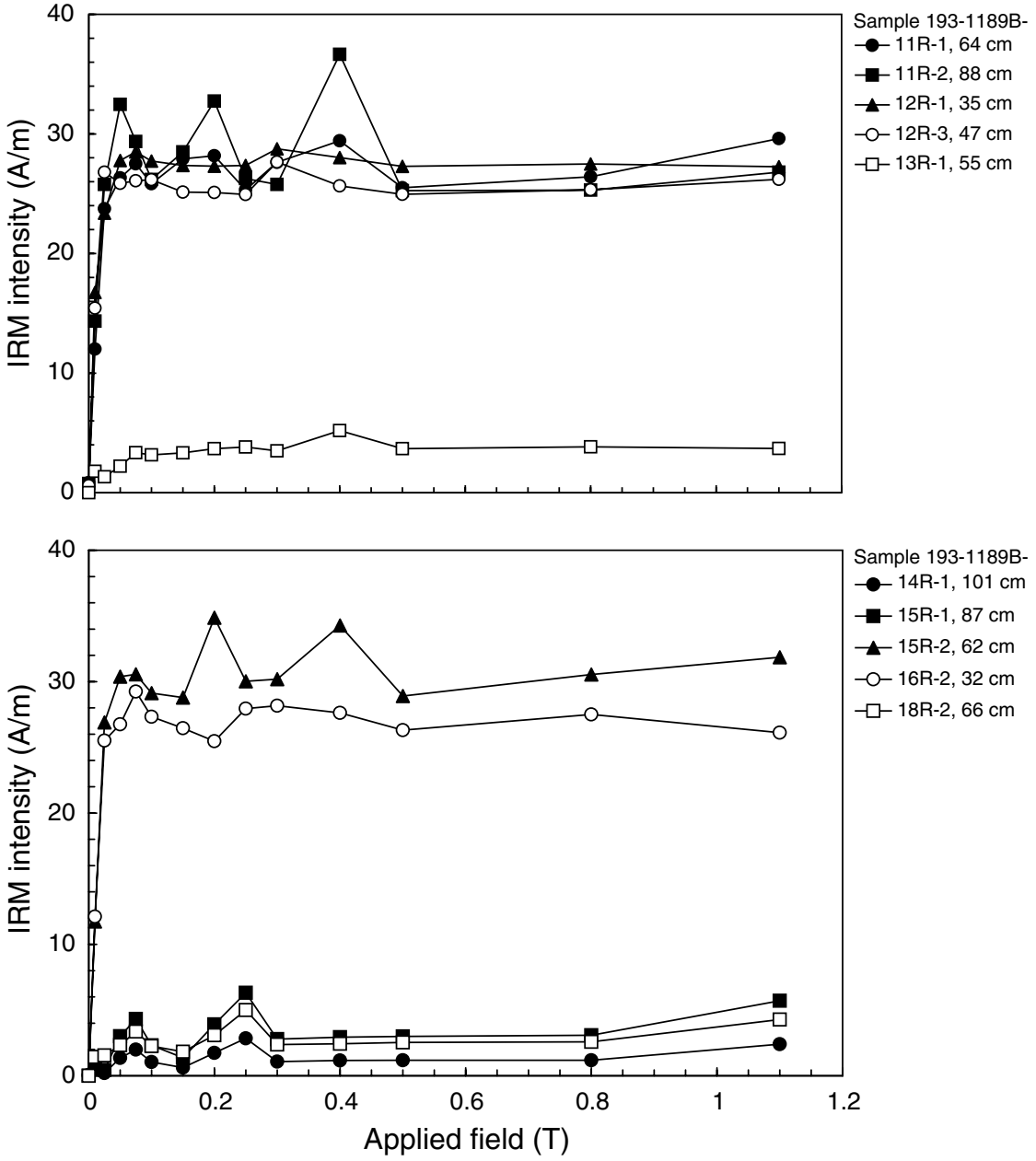

Figure F139. Thermal demagnetization curves of two samples from Hole 1189A. The samples were imparted with an isothermal remanent magnetization (IRM) at an impulse field of 1.1 T.

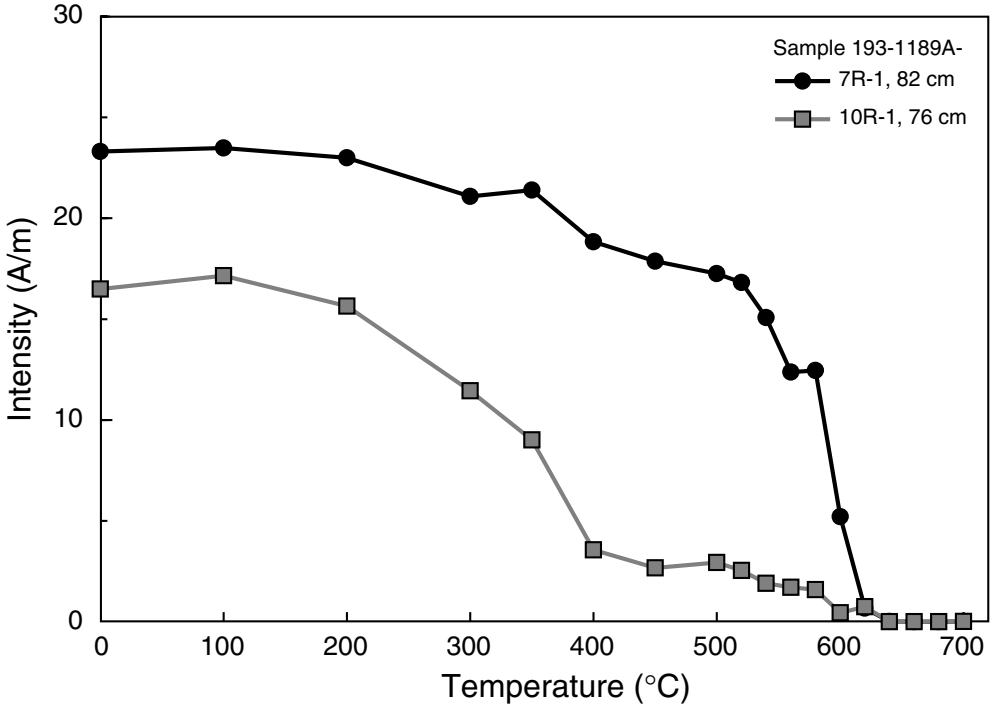

Figure F140. Heave records for the second and third wireline logging runs, Hole 1189B. MTEM = wireline cable sensor, HNGS = hostile-environment natural gamma-ray sonde, APS = accelerator porosity sonde, HLDS = hostile-environment lithodensity sonde, DIT-E = dual induction resistivity tool, NGT = natural gamma-ray tool, DSI = dipole sonic imager, FMS = Formation MicroScanner.

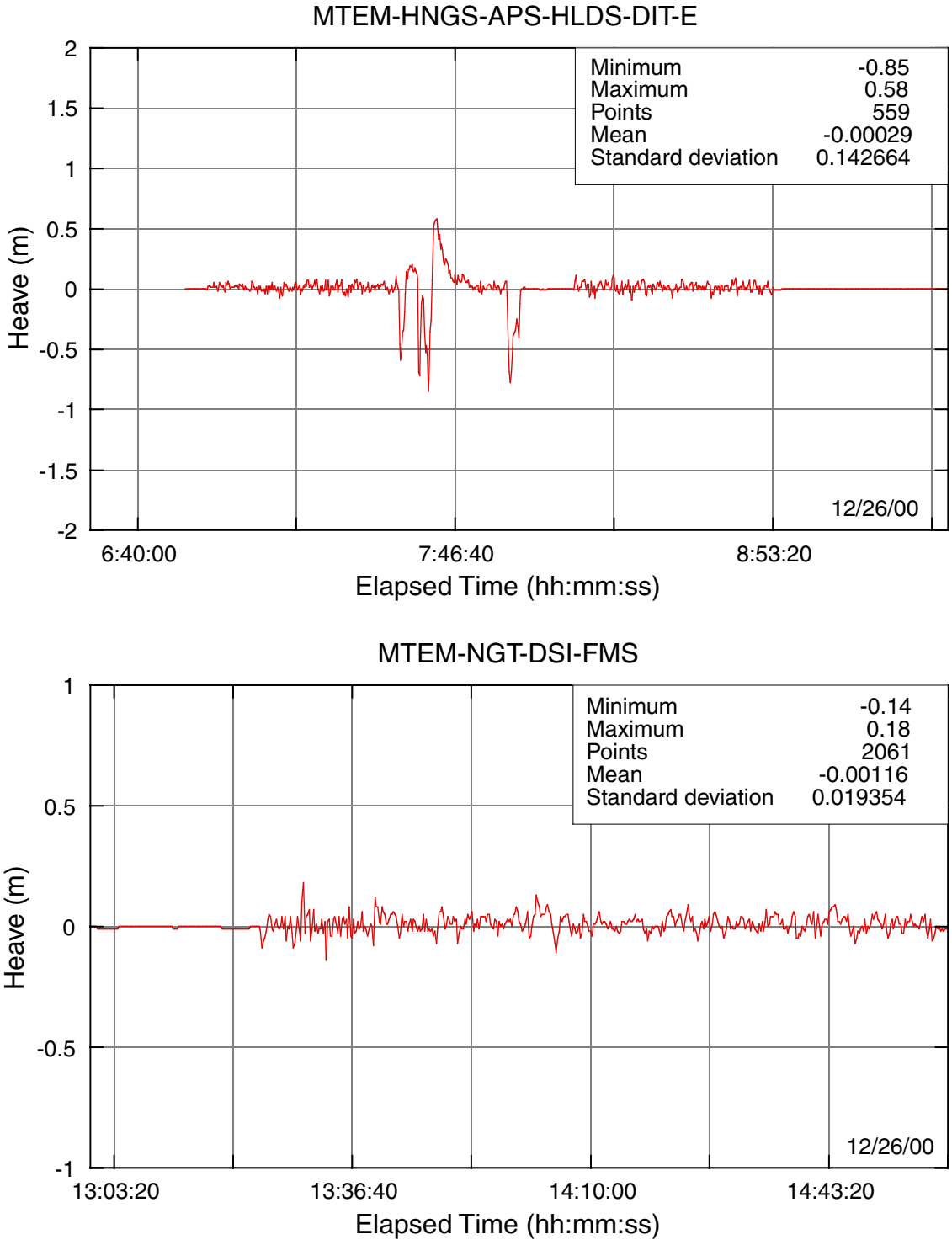

Figure F141. Downhole wireline logs of Hole 1189B. A total of 8 logging units were identified from the changes observed with depth. FMS = Formation MicroScanner, IMPH = medium induction phasor-processed resistivity, IDPH = deep induction phasor-processed resistivity, HCGR = computed gamma-ray headspace, HSGR = total spectral gamma ray.

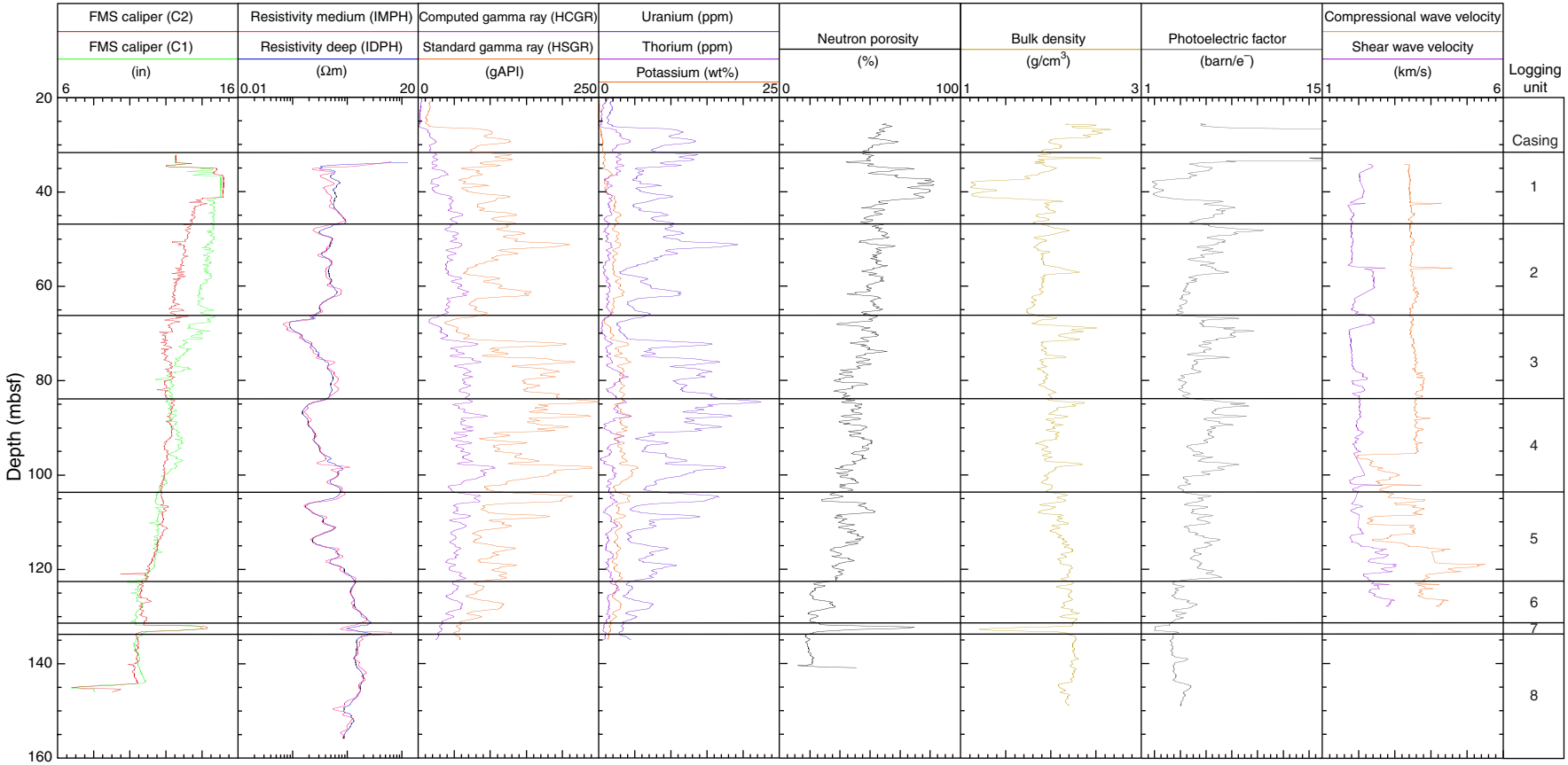

Figure F142. Temperature records obtained with the wireline cable sensor (MTEM) during all the logging runs, Hole 1189B.

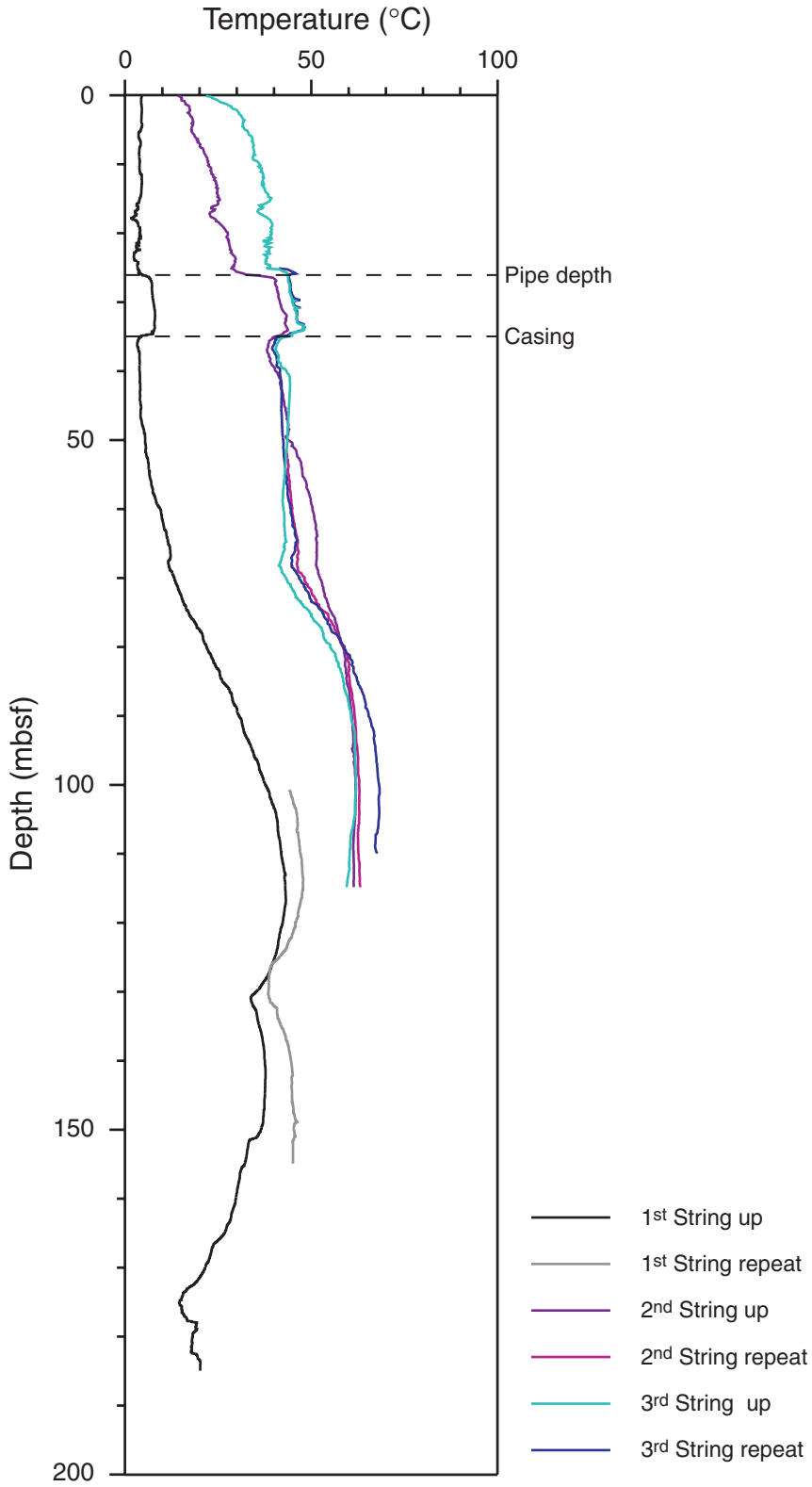

Figure F143. Water sampling temperature probe temperature record of a deployment to 132 mbsf, Hole 1189B.

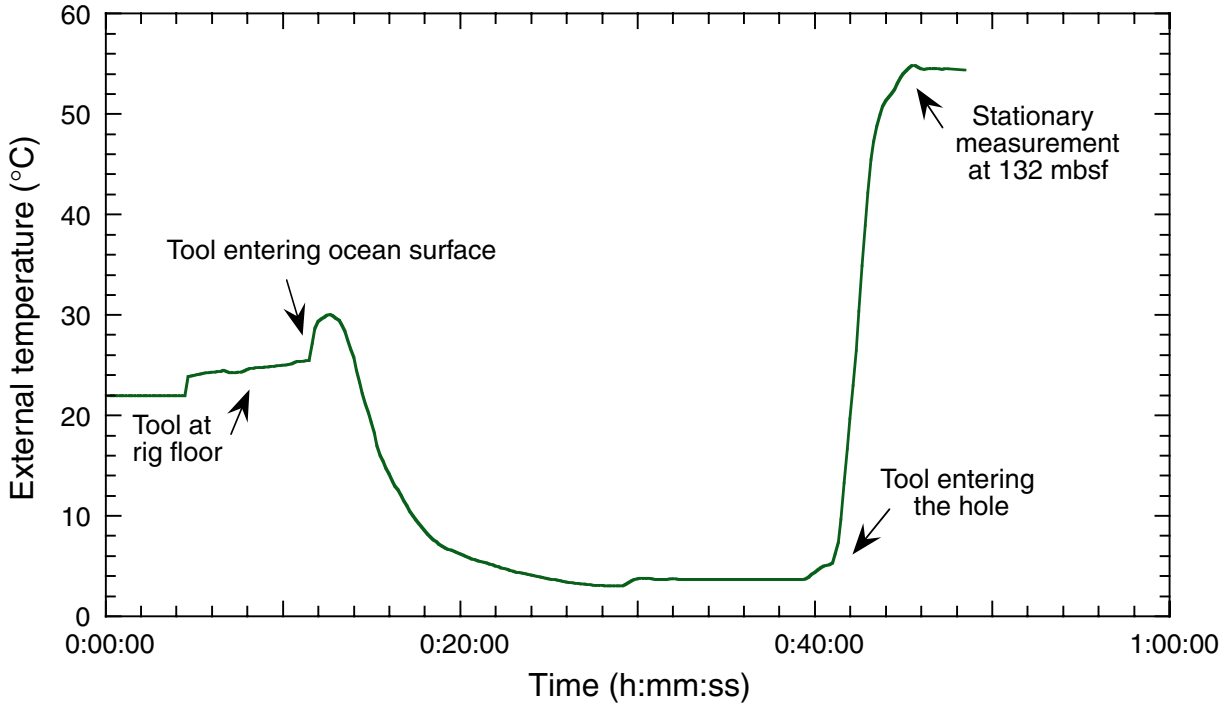

Figure F144. FMS images of the topmost logged section of Hole 1189B showing the presence of conductive minerals. Both static and dynamic types of processing are shown.

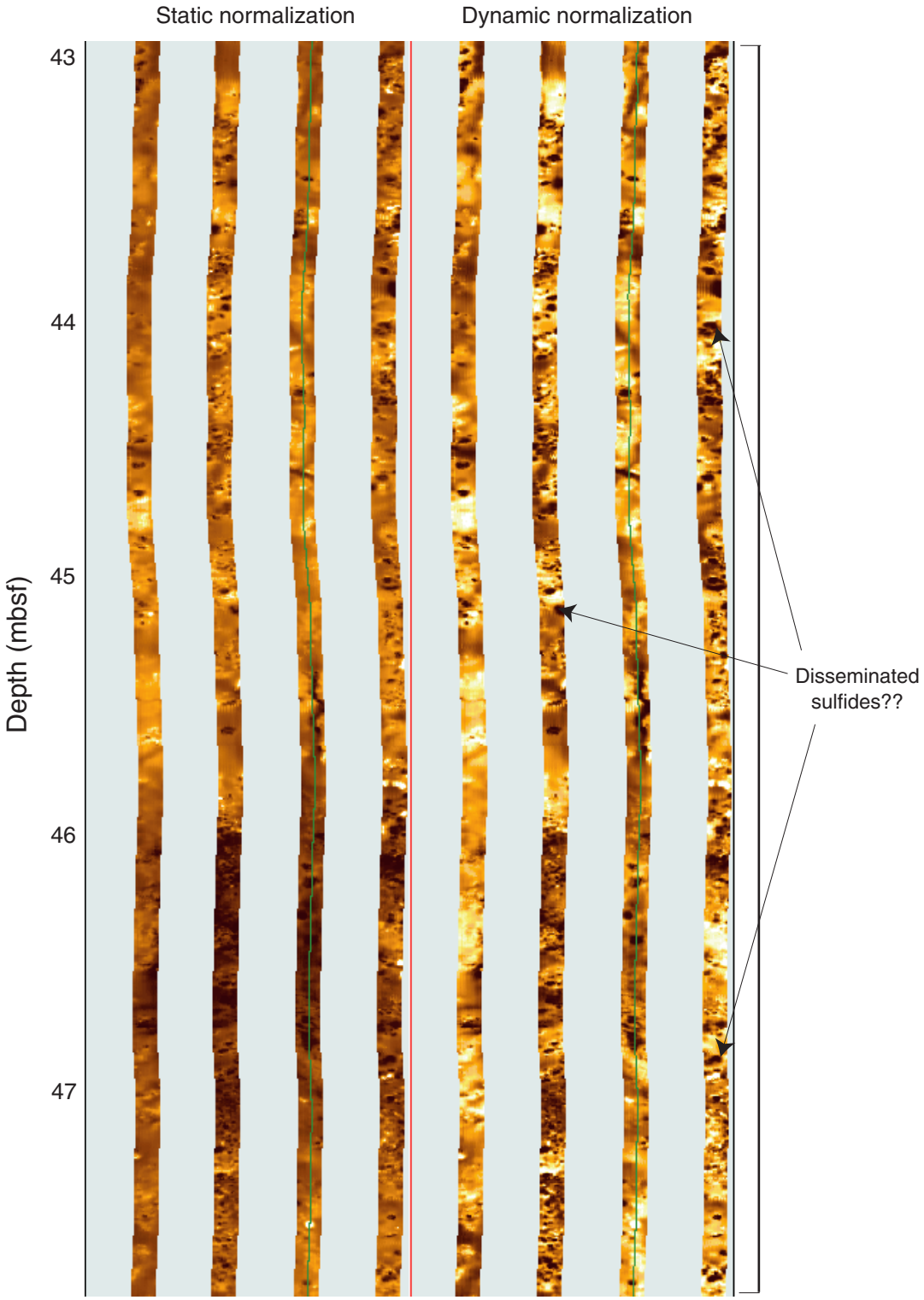

Figure F145. A change in alteration as seen in the FMS images, Hole 1189B. Several fractures are also visible.

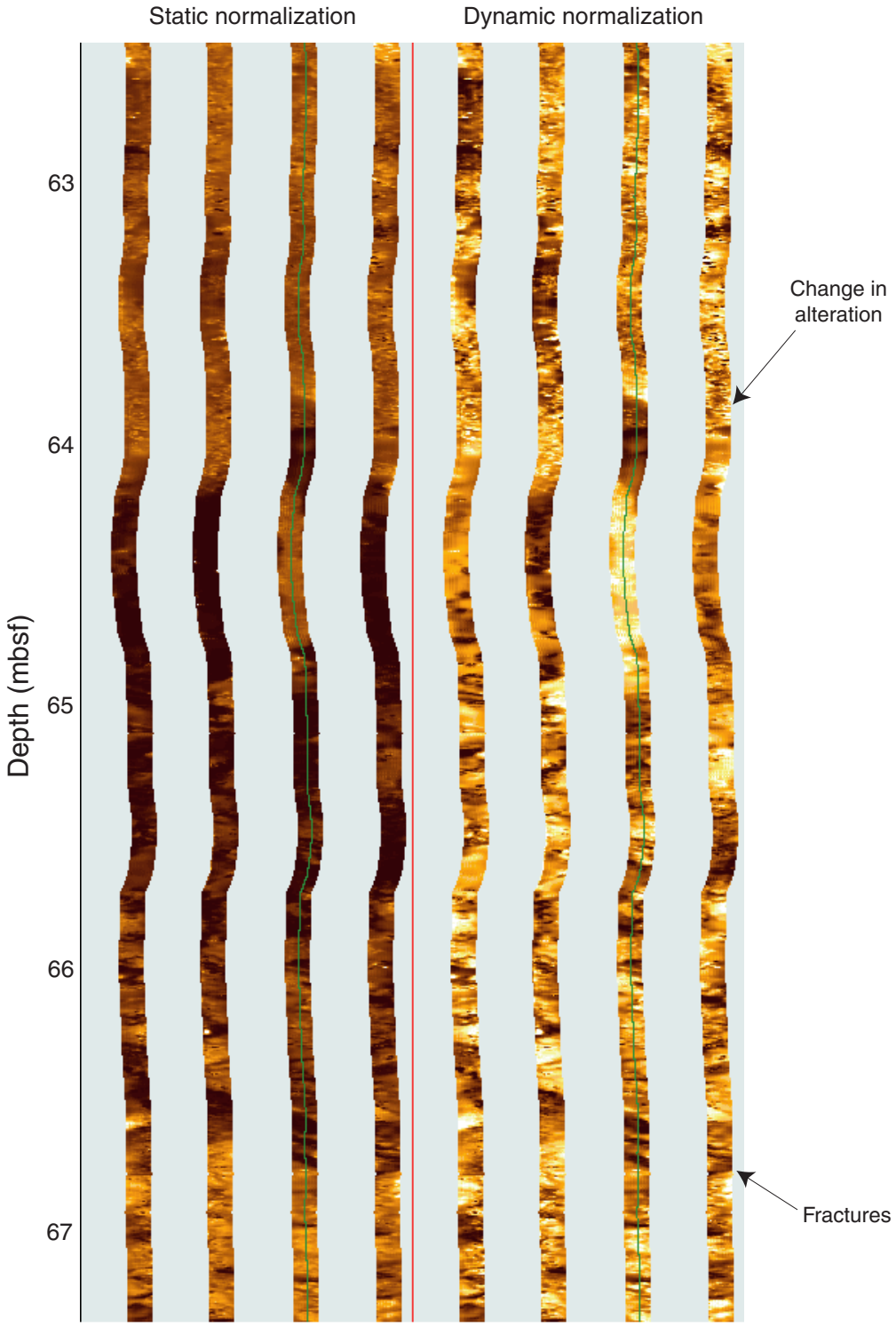

Figure F146. Alternating conductive and resistive thin and shallowly dipping units, Hole 1189B.

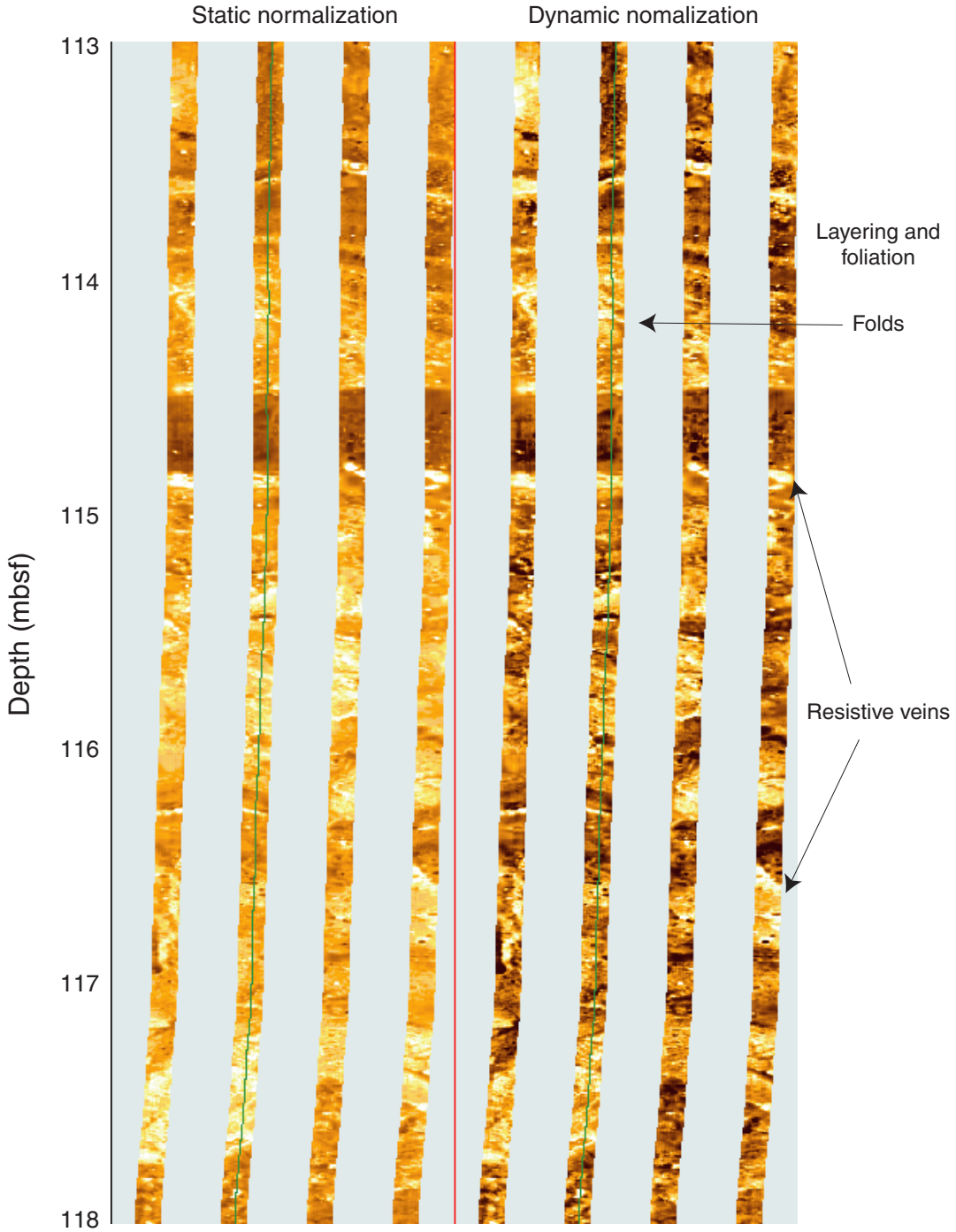

Figure F147. Steep fractures in the vicinity of a cavernous section of borehole at 133 mbsf in Hole 1189B. This may represent a fault zone.

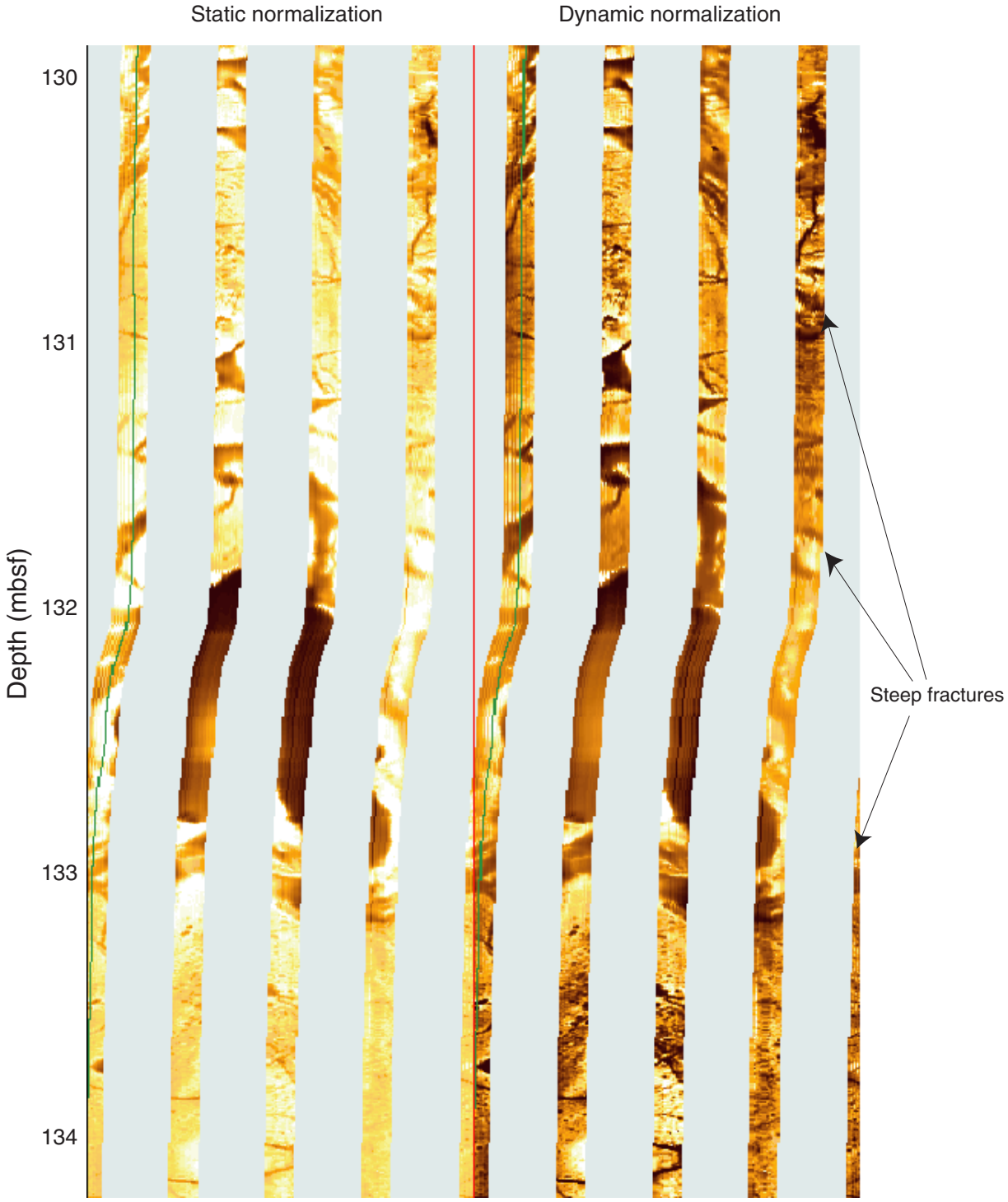

Figure F148. FMS images showing the bottom of the logged interval of Hole 1189B. Numerous conductive subhorizontal and subvertical fractures are present in this resistive unit.

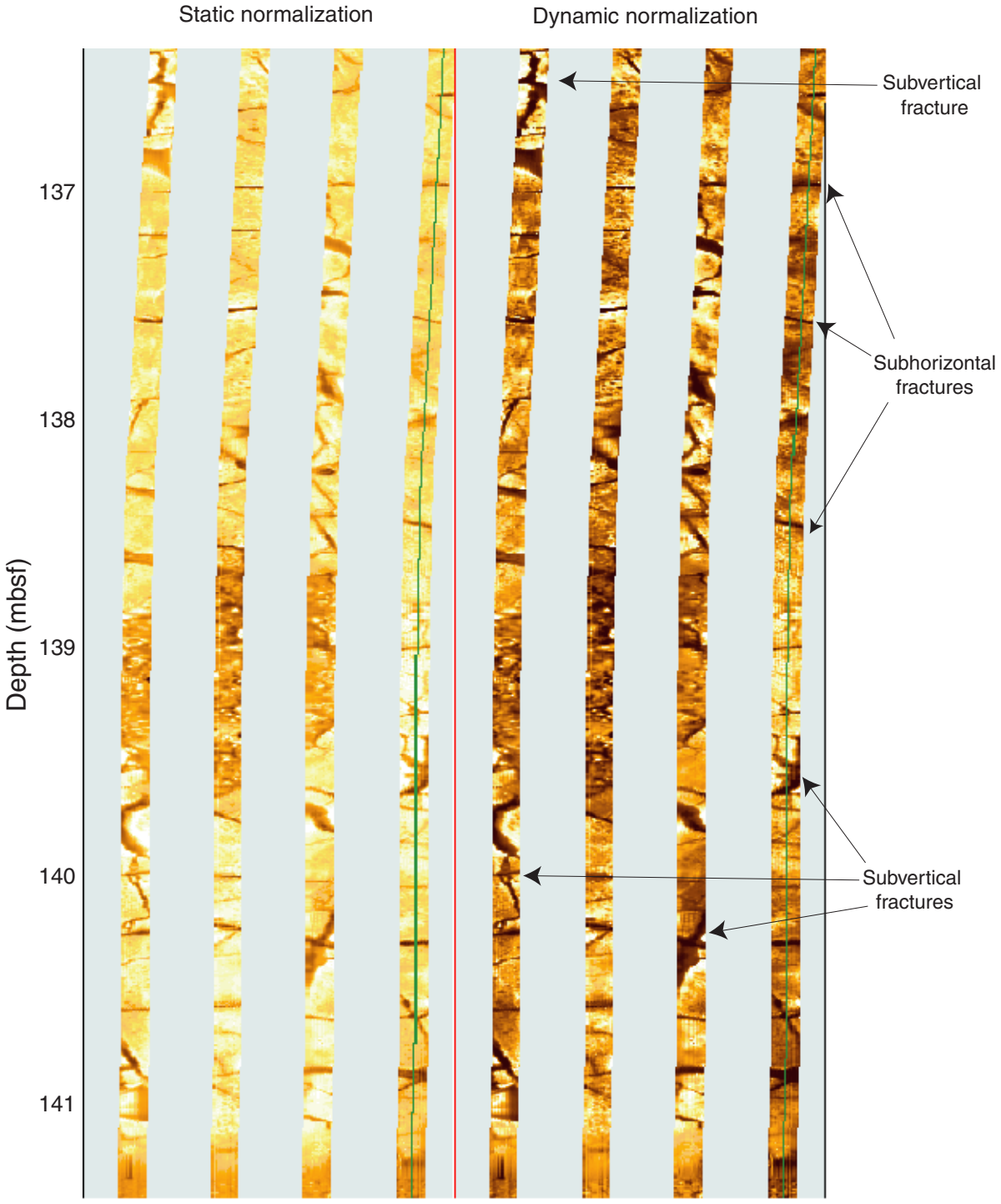

Figure F149. Heave records for the two wireline runs made at Hole 1189C. HNGS = hostile-environment natural gamma-ray sonde, HLDS = hostile-environment lithodensity sonde, DIT-E = dual induction resistivity tool, NGT = natural gamma-ray tool, FMS = Formation MicroScanner.

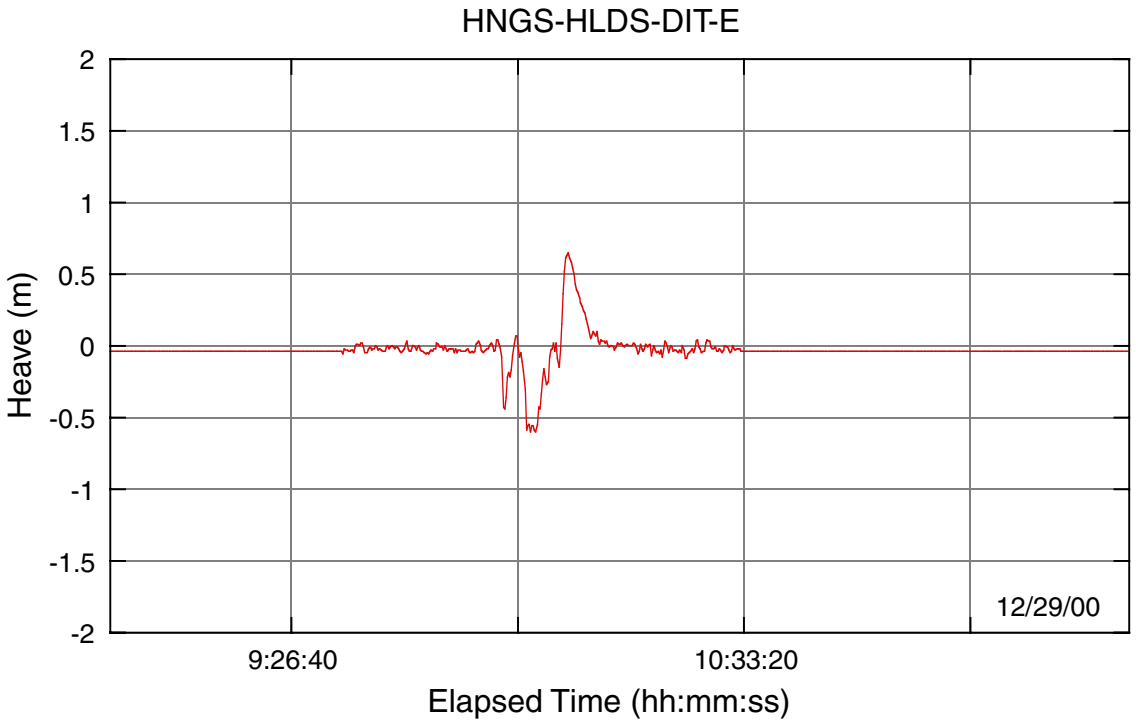

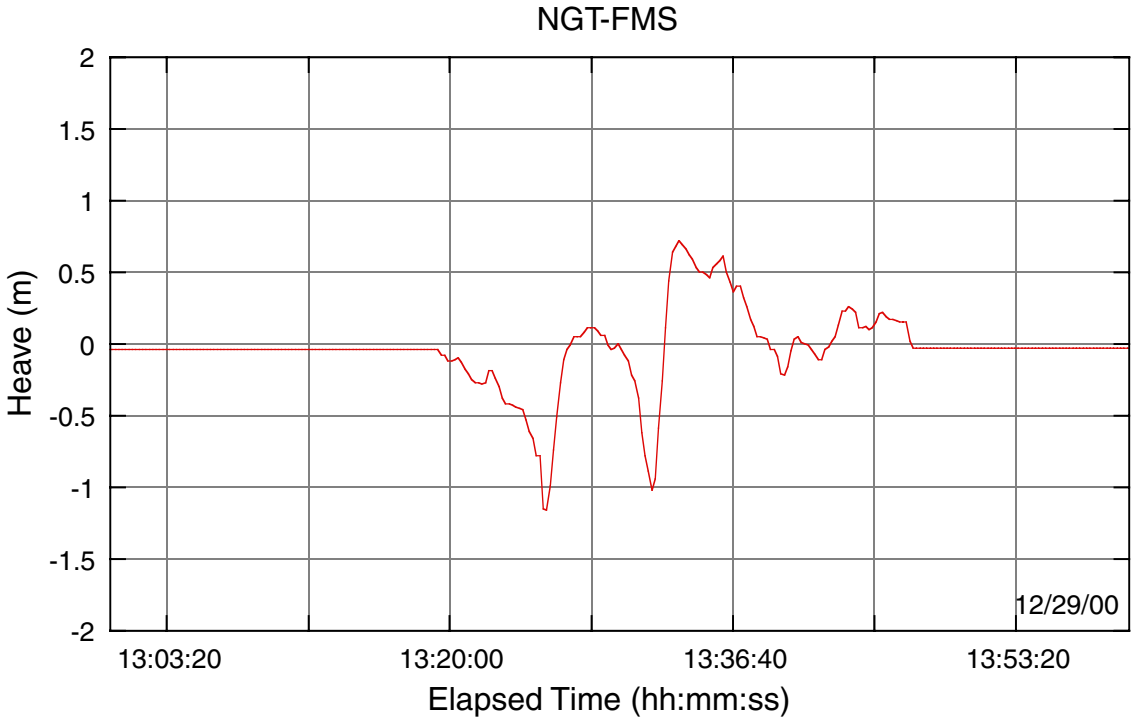

Figure F150. Wireline and logging-while-drilling logs for Hole 1189C. Only the spectral data from the hostile-environment natural gamma-ray sonde (HNGS) are plotted for clarity of presentation. FMS = Formation MicroScanner, RAB = resistivity at the bit, IMPH = medium induction phasor-processed resistivity, IDPH = deep induction phasor-processed resistivity, NGT = natural gamma-ray tool, HSGR = total spectral gamma ray. Arrows = trends within logging units.

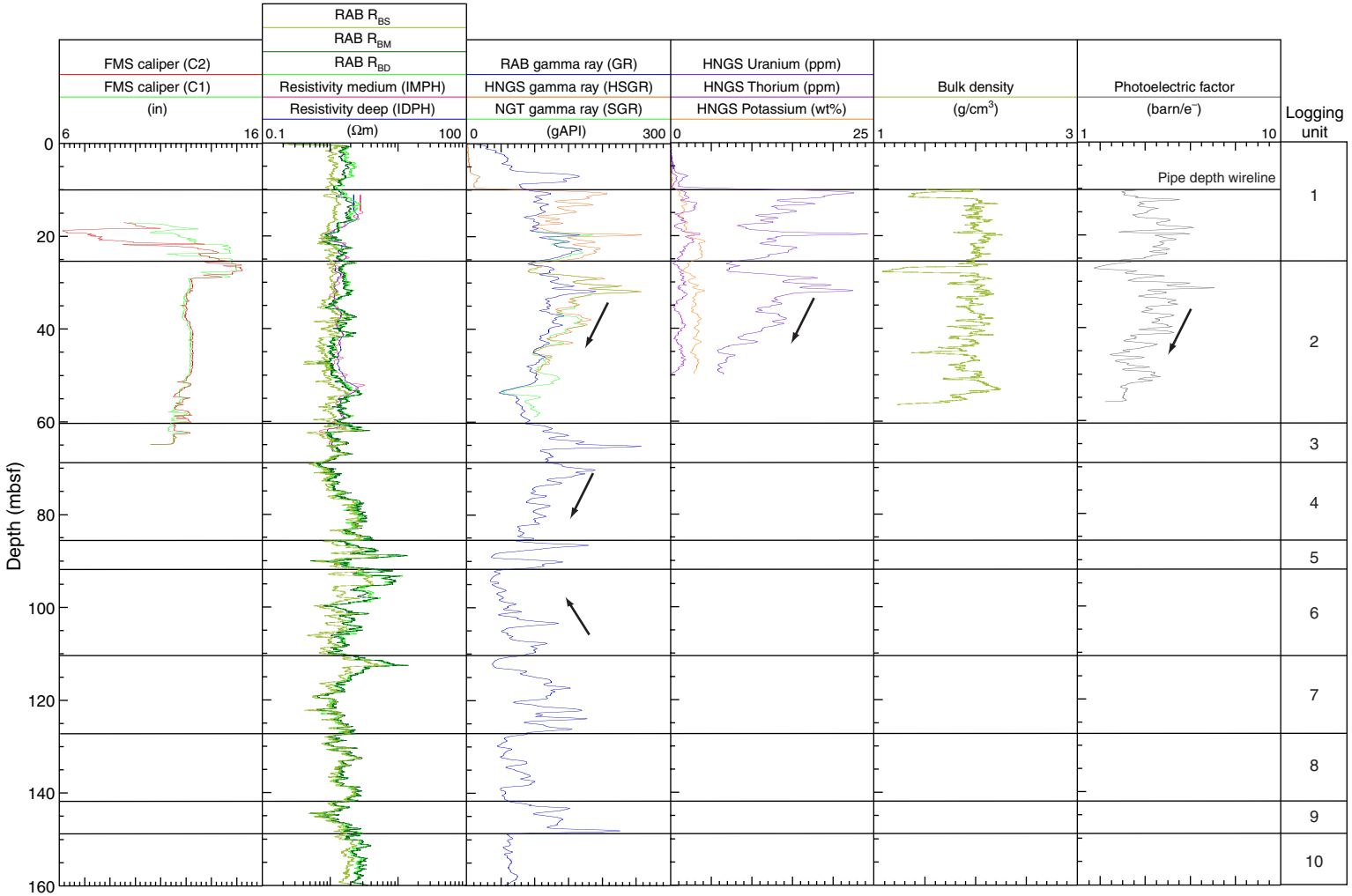

Figure F151. Temperature (blue) and pressure (red) records for the temperature log obtained with the UHT-MSM probe in Hole 1189C.

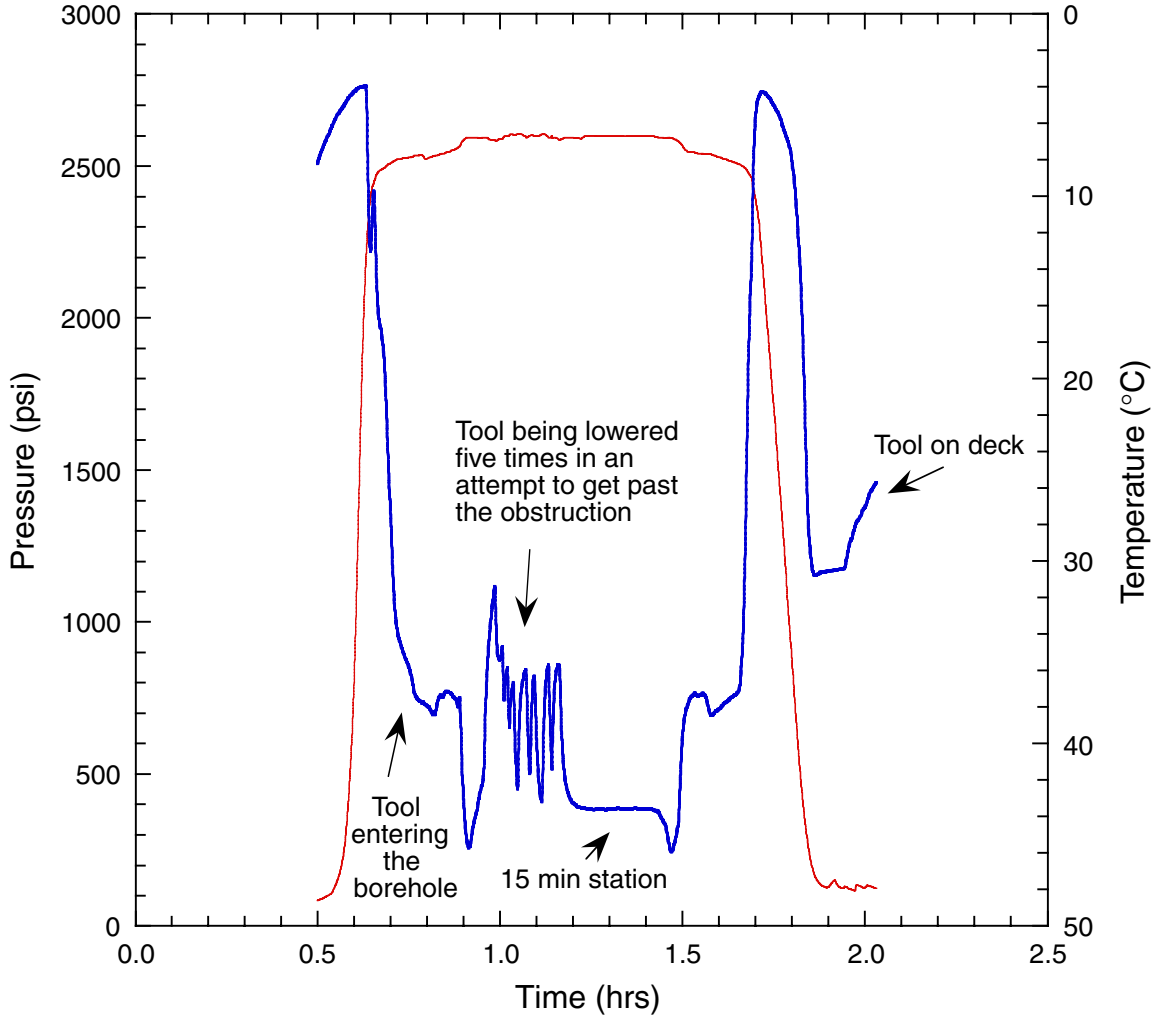

Figure F152. Resistivity-at-the-bit static and dynamic images of Hole 1189C showing subhorizontal fractures and various resistive features. The green line (low-frequency fluctuation) in the static column is the gamma-ray log. The pink line (high-frequency fluctuation) is the bit-rotation speed log.

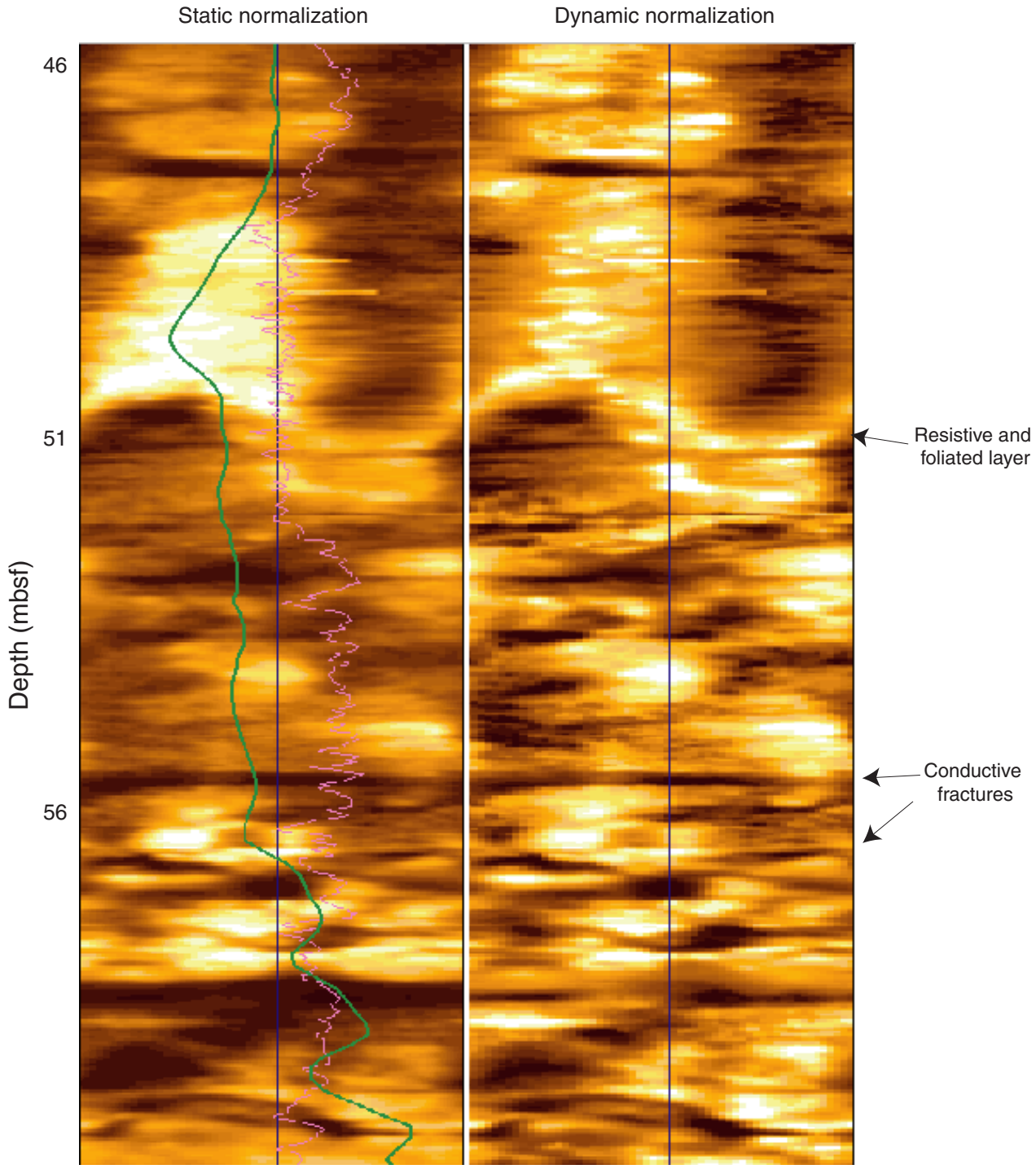

Figure F153. Resistivity-at-the-bit images showing a deeper section of Hole 1189C with more resistive features and conductive fractures. The green line (low-frequency fluctuation) in the static column is the gamma-ray log. The pink line (high-frequency fluctuation) is the bit-rotation speed log.

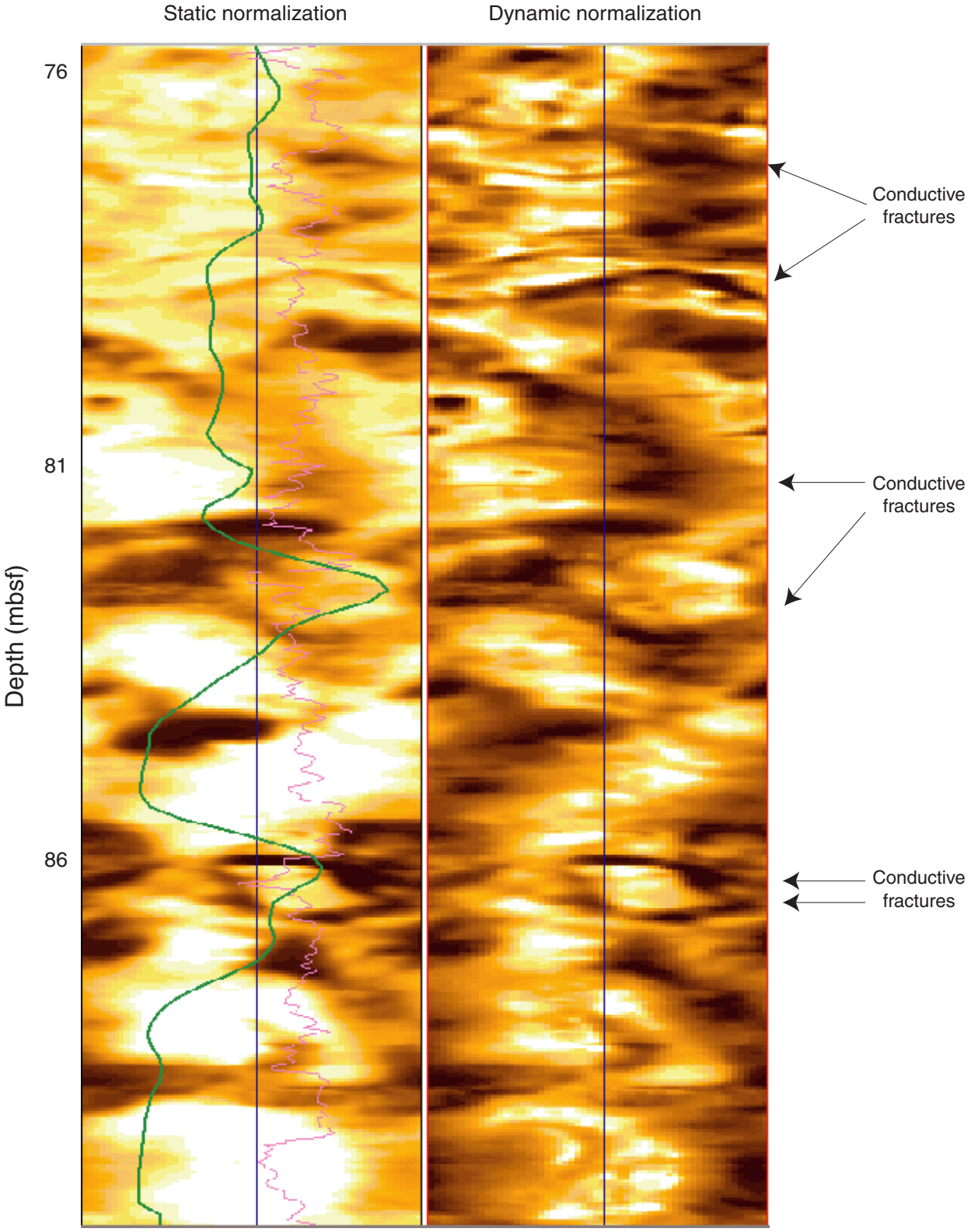

Figure F154. Comparison between resistivity at the bit (RAB) and Formation MicroScanner (FMS) images in Hole 1189C.

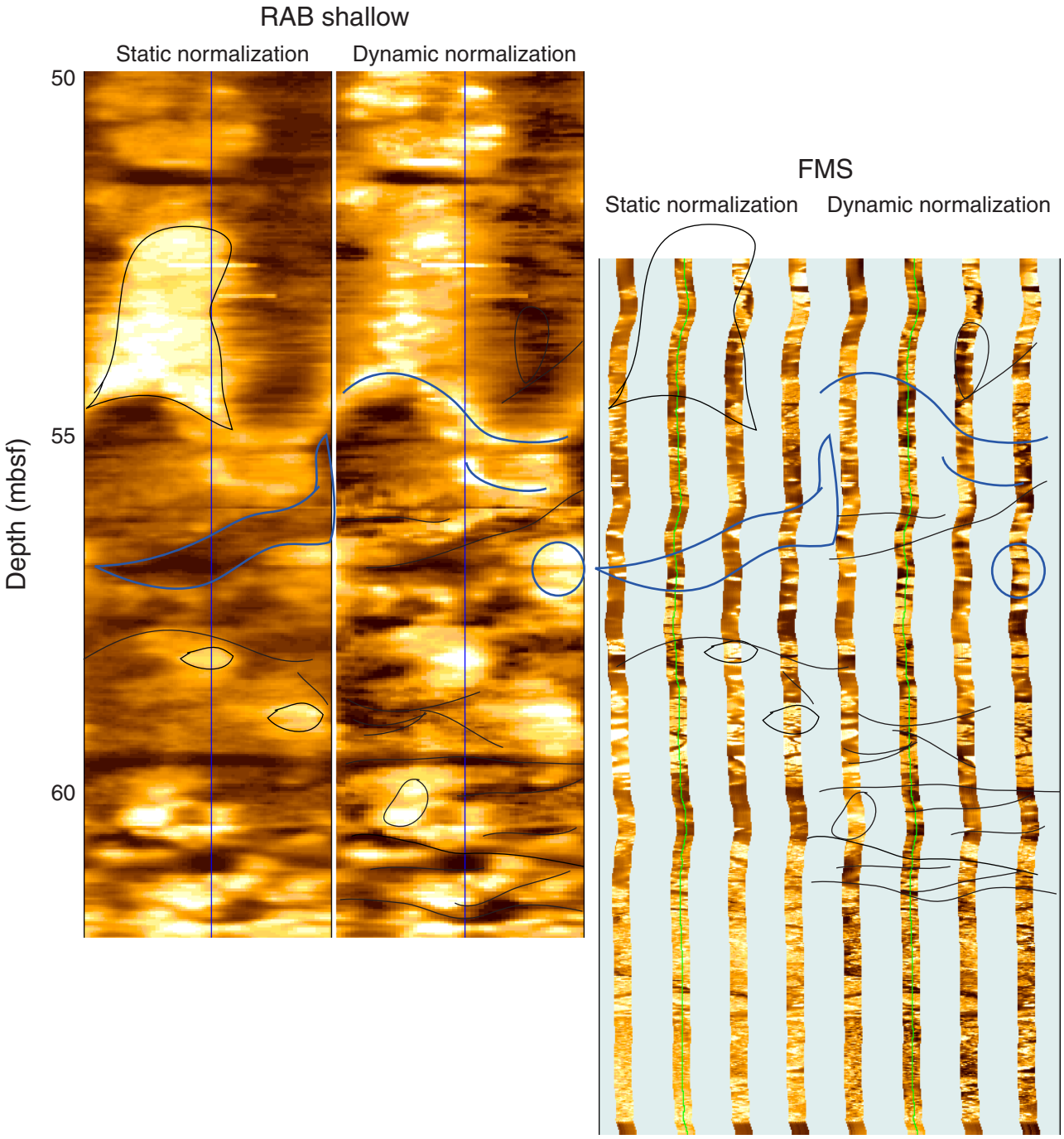

Table T1. Coring summary, Site 1189. (See table note. Continued on next page.)

Hole 1189A
Latitude: 3°43.244′S
Longitude: 151°40.493′E
Time on site (hr, min): 159, 45 (0830 hr, 22 Nov 2000–2045 hr, 23 Nov 2000; 0745 hr, 22 Dec 2000–1700 hr, 26 Dec 2000 1200 hr, 27 Dec 2000–1515 hr, 29 Dec 2000)
Time on hole (hr, min): 36, 15 (0830 hr, 22 Nov 2000–2045 hr, 23 Nov 2000)
Seafloor (drill pipe measurement from rig floor, mbrf): 1701.0
Distance between rig floor and sea level (m): 10.8
Water depth (drill pipe measurement from sea level, m): 1690.2
Total depth (from rig floor, mbrf): 1826.8
Total penetration (mbsf): 125.8
Total length of cored section (m): 125.8
Total length of drilled intervals (m): 0.0
Total core recovered (m): 8.58
Core recovery (%): 6.8
Total number of cores: 13

Hole 1189B
Latitude: 3°43.236′S
Longitude: 151°40.508′E
Time on hole (hr, min): 105, 15 (0745 hr, 22 Dec 2000–1700 hr, 26 Dec 2000)
Seafloor (drill pipe measurement from rig floor, mbrf): 1693.0
Distance between rig floor and sea level (m): 11.0
Water depth (drill pipe measurement from sea level, m): 1683.0
Total depth (from rig floor, mbrf): 1899.0
Total penetration (mbsf): 206.0
Total length of cored section (m): 175.0
Total length of drilled intervals (m): 31.0
Total core recovered (m): 13.69
Core recovery (%): 7.8
Total number of cores: 18

Hole 1189C
Latitude: 3°43.242′S
Longitude: 151°40.524′E
Time on hole (hr, min): 51, 15 (1200 hr, 27 Dec 2000–1515 hr, 29 Dec 2000)
Seafloor (drill pipe measurement from rig floor, mbrf): 1700.0
Distance between rig floor and sea level (m): 11.0
Water depth (drill pipe measurement from sea level, m): 1689.0
Total depth (from rig floor, mbrf): 1866.0
Total penetration (mbsf): 166.0
Total length of cored section (m): 0.0
Total length of drilled intervals (m): 166.0
Comments: LWD and RAB only

Core	Date (2000)	Time (local)	Top depth (mbsf)	Length (m) Cored	Length (m) Recovered	Recovery (%)
193-1189A-						
1R	22 Nov	1800	0.0	9.7	0.22	2.3
2R	22 Nov	1935	9.7	9.7	0.88	9.1
3R	22 Nov	2045	19.4	9.7	0.68	7.0
4R	22 Nov	2200	29.1	9.7	0.19	2.0
5R	22 Nov	2310	38.8	9.8	0.48	4.9
6R	23 Nov	0030	48.6	9.7	0.39	4.0
7R	23 Nov	0210	58.3	9.7	0.80	8.2
8R	23 Nov	0340	68.0	9.7	0.92	9.5
9R	23 Nov	0500	77.7	9.6	0.71	7.4
10R	23 Nov	0620	87.3	9.6	1.11	11.6
11R	23 Nov	0715	96.9	9.6	0.76	7.9
12R	23 Nov	0815	106.5	9.6	0.94	9.8
13R	23 Nov	1110	116.1	9.7	0.50	5.2
193-1189B-						
1R	24 Dec	0910	31.0	9.1	0.10	1.1
2R	24 Dec	1000	40.1	9.6	0.10	1.0
3R	24 Dec	1050	49.7	9.8	0.10	1.0
4R	24 Dec	1145	59.5	9.8	0.00	0.0
5R	24 Dec	1300	69.3	9.7	0.05	0.5
6R	24 Dec	1420	79.0	9.7	0.15	1.5
7R	24 Dec	1545	88.7	9.7	0.05	0.5

Table T1 (continued).

Core	Date (2000)	Time (local)	Top depth (mbsf)	Length (m)		Recovery (%)
				Cored	Recovered	
8R	24 Dec	1635	98.4	9.7	0.20	2.1
9R	24 Dec	1720	108.1	9.8	0.05	0.5
10R	24 Dec	1915	117.9	9.7	0.64	6.6
11R	24 Dec	2135	127.6	9.7	1.72	17.7
12R	25 Dec	0045	137.3	9.7	2.80	28.9
13R	25 Dec	0210	147.0	9.5	0.41	4.3
14R	25 Dec	0400	156.5	9.6	1.16	12.1
15R	25 Dec	0555	166.1	9.6	1.81	18.9
16R	25 Dec	0830	175.7	9.6	1.41	14.7
17R	25 Dec	1010	185.3	9.7	0.83	8.6
18R	25 Dec	1240	195.0	11.0	2.11	19.2

Note: LWD = logging while drilling, RAB = resistivity at bit.

Table T2. Summary of lithologic and alteration features of units described in Hole 1189A. (See table note. Continued on next page.)

Unit	Core, section (Piece)	Curated depth (mbsf) Top	Base	Curated length (m)	Lithology	Alteration
	193-1189A-					
1	1R-1 (1-4)	0.00	0.17	0.17	Fresh, moderately vesicular, aphyric dacite.	Fresh unit. Minor sulfate films coat vesicles. XRD mineralogy: plagioclase and opaline silica dominant, minor augite, quartz, and spinel.
2	1R-1 (5-8) 2R-1 (1-13)	0.17 9.70	0.34 10.63	0.17 0.93	Moderately to completely altered, moderately vesicular, aphyric dacite.	Bleached unit. Vesicles are filled with anhydrite. Rare Fe oxide films. XRD mineralogy: plagioclase, cristobalite, anhydrite dominant, minor pyrite, chlorite/smectite-mixed–layer clays, and traces of chlorite and illite.
3	2R-1 (14)	10.63	10.71	0.08	Coarse-grained quartz-sulfate vein.	Gray silica-sulfate-clay-pyrite vein. Coarse-grained sulfate occurs as vuggy cavity fill. Very fine grained pyrite is disseminated throughout and is concentrated in vugs.
4	2R-1 (15-17)	10.71	11.07	0.36	Hydrothermal breccia with completely altered, perlitic volcanic clasts.	Volcanic rock with remnant perlitic texture altered pervasively to silica clay and fractured by an anhydrite-silica-pyrite stockwork. Fragments are cut by fine anastomosing networks of sulfate veinlets. Anhydrite occurs as vesicle fill. Pyrite occurs in veins and as vesicle fill. XRD mineralogy: anhydrite, cristobalite dominant, minor pyrite and chlorite, and traces of illite.
5	3R-1 (1-9)	19.40	19.96	0.56	Highly to completely bleached, moderately vesicular, aphyric dacite.	Pervasively bleached unit. Pyrite occurs as fine disseminations, as vesicle fill with anhydrite and on fracture surfaces. Veins also contain scattered, coarse-grained anhydrite. XRD mineralogy: plagioclase, cristobalite dominant, minor pyrite, and chlorite.
6	3R-1 (10)	19.96	20.03	0.07	Hydrothermal breccia.	White sulfate-rich volcanic clasts cemented in bluish green sulfate-clay-silica altered material. Pyrite is disseminated throughout. A single blue clay altered rounded fragment contains anhydrite laths that do not extend into the body of the rock, implying earlier alteration. XRD mineralogy: anhydrite, quartz dominant, minor pyrite, and traces of illite.
7	3R-1 (11-16)	20.03	20.36	0.33	Variably bleached and silicified, sparsely to moderately vesicular, intensely veined volcanic rock.	Silicified bleached vesicular volcanic rock. Medium-grained anhydrite-quartz-pyrite veins with silica-pyrite halos cut the rock. Pyrite occurs in vein halos, but also scattered throughout the rock. XRD mineralogy: quartz dominant, minor orthoclase, pyrite, and traces of illite.
8	4R-1 (1-3)	29.10	29.34	0.24	Completely altered, moderately vesicular dacite.	Pervasive green silica-clay alteration, cut by irregular quartz-pyrite veins. Silicate fills vesicles, implying silica flooding of the rock. Rock cut by late anhydrite vein. XRD mineralogy: quartz dominant, minor plagioclase, chlorite, pyrite, and illite.
9	5R-1 (1-9) 6R-1 (1-10)	38.80 48.60	39.42 49.29	0.62 0.69	Completely altered, hydrothermal breccia with flow-laminated volcanic clasts.	Patchy to pervasive multiphase alteration. Stage 1: alteration of volcanics to white clay-anhydrite-silica (locally preserving flow banding). Stage 2: hydraulic brecciation with chlorite alteration associated with anhydrite veining. Stage 3: quartz-pyrite veining with associated chlorite alteration. XRD mineralogy: quartz dominant, minor anhydrite, chlorite, pyrite, and illite.
10	7R-1 (1-8)	58.30	58.88	0.58	Completely altered, nonvesicular to slightly vesicular volcanic rock.	Pervasive green silica-clay alteration overprinted by silicification, which is most intense along quartz-pyrite veins. Anhydrite in the centers of some veins. Elongate vesicles sometimes form tube-like structures that are lined with quartz and pyrite and rare late anhydrite. XRD mineralogy: quartz, plagioclase dominant, minor anhydrite, pyrite, chlorite, and illite.
11	7R-1 (9-10)	58.88	59.02	0.14	Completely altered breccia with possible evidence of clast rotation of flow-laminated fragments.	Clasts show silica-sulfate-chlorite alteration and are cemented in fine grained silica.
12	7R-1 (11-14)	59.02	59.22	0.20	Completely altered sparsely vesicular volcanic rock.	Extensive pervasive silicification overprinting silica-clay alteration. Vesicles are lined with large euhedral quartz and pyrite crystals.
13	7R-1 (15-16)	59.22	59.29	0.07	Completely altered breccia with possible evidence of clast rotation of flow-laminated fragments.	Clasts show green silica-clay alteration and are cemented in fine grained silica. XRD mineralogy: quartz dominant, minor plagioclase, chlorite, and traces of pyrite.
14	7R-1 (17)	59.29	59.32	0.03	Massive silica-Fe oxide-pyrite with minor pale green altered clasts.	Rare, whitish green altered clasts and fine pyrite euhedra are cemented in a red jasperoid cement.
15	8R-1 (1-20)	68.00	69.28	1.28	Plagioclase-rich sparsely vesicular volcanic rock with patchy poikiliblastic silicification associated with a fine network of silica-pyrite veins.	Plagioclase-rich rock overprinted by patchy poikiloblastic silicification. Veins are abundant and are filled with quartz and pyrite in approximately equal proportions. XRD mineralogy: plagioclase dominant, minor quartz, K-feldspar, pyrite, traces of smectite, chlorite, and illite.

Table T2 (continued).

Unit	Core, section (Piece)	Curated depth (mbsf) Top	Curated depth (mbsf) Base	Curated length (m)	Lithology	Alteration
	193-1189A-					
16	9R-1 (1-12)	77.70	78.56	0.86	Completely altered hydrothermal breccia with abundant flow-banded clasts.	Rocks are composed of green silica-clay altered material, which is cut by a network of quartz and pyrite veins with heavily silicified in halos along the veins. XRD mineralogy: anhydrite, quartz dominant, minor plagioclase, pyrite, and traces of chlorite.
17	9R-1 (13)	78.56	78.59	0.03	Completely bleached moderately vesicular volcanic rock.	Completely bleached and slightly silicified. XRD mineralogy: quartz dominant, minor plagioclase, pyrite and traces of chlorite.
	10R-1 (1-2)	87.30	87.37	0.07		
18	10R-1 (3)	87.37	87.41	0.04	Completely altered and mineralized breccia.	Clasts of glassy volcanic rock and sulfide (pyrite + chalcopyrite) in a very fine grained silica-pyrite cement.
19	10R-1 (4-14)	87.41	88.72	1.31	Completely altered hydrothermal breccia with medium- to fine-grained clasts hosted in a network of silica-sulfide veins with late anhydrite vug fill.	Silica-clay alteration overprinted by silicification. Bluish gray domains in the core are heavily silicified, while greenish domains are soft (clayey). Quartz and pyrite veins often have anhydrite vug fill. XRD mineralogy: quartz and anhydrite dominant, minor plagioclase and pyrite, traces of chlorite and illite.
20	11R-1 (1-13)	96.90	98.07	1.17	Completely silicified, massive, moderately vesicular volcanic rock.	Intense silicification overprinting patchily preserved green clay alteration. Vugs and vesicles are commonly lined with quartz and pyrite. Pyrite veins commonly have silicified halos. XRD mineralogy: quartz dominant, minor pyrite, illite, and chlorite.
	12R-1 (1-15)	106.50	107.70	1.20		
21	12R-1 (16)	107.70	107.78	0.08	Completely altered and mineralized volcaniclastic breccia.	Clasts of glassy volcanic rock and sulfide (pyrite + minor chalcopyrite) in a very fine grained silica-pyrite cement.
22	12R-1 (17-18)	107.78	107.88	0.10	Pervasively bleached moderately vesicular volcanic rock with a patchy silica overprint.	Vesicular intensely bleached volcanic unit with patchily developed indurated silicification. Widespread pyrite as vesicle lining. XRD mineralogy: quartz dominant, minor chlorite, pyrite, illite.
	13R-1 (1-7)	116.10	116.61	0.51		
23	13R-1 (8)	116.61	116.69	0.08	Polymict volcaniclastic breccia, with rounded green clay, altered gray silicified and bleached clasts cemented in silica.	Three distinct clast types, all showing differing alteration types, suggesting a polymict nature. Most of the more clay-rich pieces have silicified rims adjacent to the silceous cement. Traces of disseminated pyrite. XRD mineralogy: quartz dominant, minor plagioclase, pyrite and chlorite, and traces of illite.
24	13R-1 (9-10)	116.69	116.82	0.13	Pervasively bleached sparsely vesicular volcanic rock with a patchy silica overprint.	Vesicular intensely bleached volcanic unit with patchily developed indurated silicification. XRD mineralogy: quartz dominant, minor pyrite and, traces of chlorite and illite.

Note: XRD = X-ray diffraction.

Table T3. Results of point counts on volcanic rock thin sections, Hole 1189A.

Core, section, interval (cm)	Unit	Rock type	Number of points	Groundmass (%)	Vesicles (%)	Phenocrysts (%)		
						Plagioclase	Clinopyroxene	Opaques
193-1189A-								
1R-1 (Piece 1, 0-4)	1	Aphyric dacite	750	80.4	19.6	0.0	0.0	0.0
3R-1 (Piece 2, 6-10)	5	Aphyric dacite	750	85.4	14.5	0.0	0.0	0.0
7R-1 (Piece 5, 27-31)	10	Volcanic rock	750	83.4	16.5	0.0	0.0	0.0
7R-1 (Piece 13, 83-86)	12	Volcanic rock	750	96.0	4.0	0.0	0.0	0.0
8R-1 (Piece 6, 42-44)	15	Volcanic rock	500	99.0	0.0	1.0	0.0	0.0
8R-1 (Piece 14, 90-92)	15	Volcanic rock	500	98.2	0.8	1.0	0.0	0.0

Note: Point counts were measured using a rectangular grid with a = 0.667 mm and b = 0.8 mm.

Table T4. Summary of lithologic and alteration features of units, Hole 1189B. (See table notes. Continued on next three pages.)

Unit	Core, section (Piece)	Curated depth (mbsf) Top	Base	Curated length (m)	Lithology	Alteration
	193-1189B-					
1	1R-1 (1)	31.00	31.29	0.29	Semimassive sulfide with sparse volcanic rock clasts.	Fragmental textured massive sulfide and rare soft (GSC altered) vesicular volcanic fragments (2–3 mm in size). Some white apparently anhydrite-replaced samples and chalcopyrite fragments are also present. All cemented in a fine grained pyrite-anhydrite-(quartz) matrix. XRD mineralogy: pyrite, anhydrite, illite, and chlorite/smectite-mixed layer dominant, minor gypsum and chalcopyrite, and traces of sphalerite.
2	1R-1 (2)	31.29	31.39	0.10	Completely altered, moderately vesicular, aphyric rock.	Greenish, soft GSC altered moderately vesicular (10% vesicles) volcanic rock with aligned stretched vesicles up to 4 mm × 2 mm in size. Trace pyrite occurs as vesicle lining. XRD mineralogy: pyrite and muscovite dominant and minor chlorite.
3	2R-1 (1-5) 3R-1 (1-8)	40.10 49.70	40.60 50.54	0.50 0.84	Breccia of completely altered volcanic rock clasts in a pyrite-anhydrite stockwork matrix. Flow banded, vesicular (submillimeter scale), and perlitic clasts. Some clasts show evidence of rotation.	Soft, greenish blue volcanic fragments and rubble cemented in and cut by pyrite-anhydrite-silica stockwork veinlets show ladder textures that parallel and crosscut flow banding in several pieces. Core 3R contains completely altered, clayey, light blue-green clasts with disseminated pyrite (possibly with some amorphous silica) cemented by pyrite + anhydrite – silica. XRD mineralogy: pyrite, gypsum and anhydrite dominant, minor quartz, chlorite, illite, and kaolinite?, and traces of smectite.
4	5R-1 (1-5)	69.30	69.85	0.55	Breccia of completely altered volcanic rock clasts in a pyrite-quartz matrix.	Complete GSC alteration and disseminated pyrite in volcanic rock clasts. Minor anhydrite lining vugs in Piece 2. Euhedral quartz crystals line vugs in Piece 5. XRD mineralogy: pyrite dominant, minor quartz, K-feldspar, and illite, and traces of chlorite.
5	6R-1 (1-5)	79.00	79.56	0.56	Breccia of completely altered volcanic rock clasts in quartz-hematite-pyrite matrix. Some clasts are perlitic. Locally, rare plagioclase phenocrysts and amygdules are truncated at clast margins.	Volcanic rock clasts show stockwork of red quartz-hematite and minor gray quartz-pyrite-hematite veins. Rocks are mostly gray, very fine grained and soft, but few clasts are light gray and slightly silicified. XRD mineralogy: quartz dominant, minor K-feldspar, plagioclase, pyrite, and chlorite, and traces of illite.
6	6R-1 (6)	79.56	79.67	0.11	Massive sulfide.	Massive sulfide rock with 90% pyrite, 9% quartz, and 1% anhydrite.
7	6R-1 (7)	79.67	79.78	0.11	Completely altered, moderately amygdaloidal, aphyric volcanic rock.	Soft clayey rock with spotty texture owing to dark gray quartz amygdules. XRD mineralogy: quartz dominant, minor plagioclase, K-feldspar, pyrite, and chlorite, and traces of illite.
8	7R-1 (1-2)	88.70	88.92	0.22	Breccia of completely altered volcanic rock clasts in an anhydrite-pyrite-quartz matrix. Clasts (maximum diameter 4 cm) are clay altered and some are flow banded or contain submillimeter quartz amygdules.	Breccia of soft clayey clasts with 2% disseminated pyrite. Late anhydrite fills vugs. XRD mineralogy: quartz and pyrite dominant, minor k-feldspar, and traces of illite.
9	8R-1 (1-5)	98.40	98.64	0.24	Completely altered, slightly vesicular, aphyric volcanic rock. Contains fine, submillimeter quartz amygdules.	Completely GSC altered with patchy silicification. Quartz is a common vesicle fill. Piece 5 has 5% pyrite lining vugs, which also have silicified dark gray halos. The vugs also contain solitary anhydrite crystals. XRD mineralogy: K-feldspar dominant, minor pyrite, chlorite, and illite, and traces of illite-bearing mixed-layer clays.
10	8R-1 (6-8)	98.64	98.75	0.11	Breccia of completely altered volcanic rock clasts in a pyrite-quartz matrix.	Breccia contains greenish gray very soft and light greenish gray silicified clasts in a pyrite-quartz stockwork.
11	8R-1 (9-16)	98.75	99.15	0.40	Completely altered, silicified, moderately vesicular volcanic rock.	Moderately silicified rock with quartz-pyrite-anhydrite amygdules. Vesicles are lined with very fine grained euhedral quartz that is overgrown by pyrite.
12	9R-1 (1-2)	108.10	108.19	0.09	Breccia of completely altered volcanic rock clasts in a pyrite-quartz matrix. Clasts (2 cm maximum diameter) are light blue-green and clay rich. Some show remnant flow banding.	Very soft clayey rock fragments dissected by pyrite microveinlets. Pyrite is also disseminated.
13	10R-1 (1-3)	117.90	118.23	0.33	Silica-clay altered, moderately amygdaloidal, aphyric volcanic rock. Green silicified rock with vesicles up to 5 mm in size, mostly filled with quartz.	Some vesicles are lined by anhydrite-pyrite. Several hairline veins of quartz-anhydrite-pyrite with 1–2 mm dark gray siliceous halos are present. Traces of honey-yellow sphalerite occur around the edges of quartz amygdules. The matrix contains trace chalcopyrite. Quartz dominant, minor chlorite, K-feldspar, plagioclase, and pyrite.

Table T4 (continued).

Unit	Core, section (Piece)	Curated depth (mbsf) Top	Base	Curated length (m)	Lithology	Alteration
	193-1189B-					
14	10R-1 (4-7)	118.23	118.53	0.30	Silica-chlorite altered, spherulitic, flow banded aphyric volcanic rock.	Rocks contains up to 50% white, (clay-altered?) isolated and coalesced spherulites (up to 1 mm), which locally contain silica-pyrite kernels. The groundmass consists of dark green (chloritic?) domains with patches of dark gray silica pyrite and minor wispy domains of anhydrite-quartz. XRD mineralogy: quartz dominant, minor chlorite, K-feldspar, anhydrite, pyrite, and illite.
15	10R-1 (8)	118.53	118.67	0.14	Completely altered, silicified, massive, moderately vesicular, aphyric volcanic rock.	Pervasive silica-pyrite alteration. Light gray domain in one fragment contains abundant, <1-mm, round, quartz crystal aggregates of uncertain origin. XRD mineralogy: cristobalite and plagioclase dominant, minor K-feldspar and chlorite, and traces of pyrite.
16	11R-1 (1-2)	127.60	127.74	0.14	Breccia of completely altered volcanic clasts. Clasts are up to 1 cm in maximum diameter; some are flow-banded and rotated.	Soft, light green (chlorite-rich) clasts are completely altered and hosted in a dark gray siliceous matrix. Locally, the matrix also contains very fine grained magnetite. XRD mineralogy: quartz dominant, minor anhydrite, k-feldspar, chlorite, chlorite/smectite-mixed layer, smectite, illite, and pyrite.
17	11R-1 (3)	127.74	127.77	0.03	Jasperoidal breccia of completely altered volcanic clasts.	Porous, vuggy jasperlitic silica-Fe-oxide with very fine grained disseminated magnetite in patches. Drusy pyrite and shaded anhydrite occur as vug fill. Volcanic clasts are completely altered and green clay (chlorite?) rich. XRD mineralogy: quartz dominant, minor anhydrite and pyrite, and traces of hematite.
18	11R-1 (4-8)	127.77	128.03	0.26	Polymict breccia of completely altered volcanic clasts. Clasts (blocky, 50% to 70% of rock, up to 1 cm in maximum diameter) are green, clay-rich, and locally flow-banded, white clay altered, or light gray and siliceous.	Complete alteration of volcanic clasts. Green clasts are rich in green clay (chlorite), white, soft clasts are rich in white clay, and gray clasts are silicified (locally with minor magnetite). The dark gray matrix is silica with minor magnetite and pyrite. XRD mineralogy: quartz dominant, minor K-feldspar, illite, chlorite, and pyrite, and traces of plagioclase.
19	11R-1 (9-10)	128.03	128.28	0.25	Completely altered, moderately vesicular, aphyric volcanic rock. Vesicles are elongate and subvertically aligned. Contains black xenoliths (1 to 2 cm).	Silicified groundmass with fine (up to 0.1 mm) spots of clay. Vesicles are generally lined or partially filled with green clay (chlorite) and/or anhydrite and traces of pyrite. Exceptionally large vug in Piece 5 of Section 12R-1 contains green clay, pyrite, barite lining. XRD mineralogy: cristobalite and plagioclase dominant, minor k-feldspar, quartz, chlorite/smectite-mixed layer, smectite, illite, and chlorite.
	11R-2 (1-11)	128.28	129.68	1.40		
	11R-3 (1)	129.68	129.97	0.29		
	12R-1 (1-11)	137.30	138.71	1.41		
	12R-2 (1-14)	138.71	140.09	1.38		
	12R-3 (1-10)	140.09	140.82	0.73		
	13R-1 (1-3)	147.00	147.20	0.20		
20	13R-1 (4-9)	147.20	147.49	0.29	Breccia with completely altered volcanic clasts. Locally polymictic in composition (perlitic, flow-banded, amygdaloidal, and glassy clasts). Perlitic clasts are common. Some perlitic clasts have fine, submillimeter stretched amygdules.	Light green and light gray clasts are completely clay altered. There are some dark gray silicified clasts. Matrix is quartz-anhydrite with minor pyrite. XRD mineralogy: quartz dominant, minor plagioclase and pyrite, and traces of chlorite and barite.
21	13R-1 (10)	147.49	147.59	0.07	Completely altered, massive, aphyric volcanic rock. Parts of the groundmass are perlitic.	Green clay (chlorite) rich, pervasive GSC alteration cut by a fine network of silica-pyrite veinlets. XRD mineralogy: quartz dominant, minor plagioclase, and traces of chlorite, illite, and pyrite.
22	14R-1 (1)	156.50	156.60	0.10	Silicified and mineralized, sparsely vesicular, aphyric volcanic rock.	Highly silicified and mineralized volcanic rock. Alternating irregular hematite-bearing and hematite-free bands create a layered structure that mimics flow banding. Pyrite abundance (up to 10%) varies between different bands. XRD mineralogy: quartz dominant, minor pyrite, and traces of illite.
23	14R-1 (2-17)	156.60	157.80	1.20	Breccia of completely altered volcanic rock fragments. Flow banded and perlitic clasts, locally grading into coherent facies. Local evidence for synvolcanic intrusion of molten lava into brecciated facies. This unit is an autoclastic breccia.	Completely GSC altered rocks. Flow banding is well preserved in clay-anhydrite rich layers intercalated with rare gray quartz-rich layers. Flow-banded, soft, white to light greenish gray, incipiently silicified clasts (clay > anhydrite > quartz) are set in a quartz-rich gray cement (quartz > clay > anhydrite). Large anhydrite crystals in clasts and matrix, probably late vug fill. Sphalerite in vugs with quartz and pyrite in Pieces 6 and 15 of Section 14R-1. XRD mineralogy: anhydrite and quartz dominant, minor K-feldspar, plagioclase, chlorite, and pyrite.
	14R-2 (1-6)	157.80	158.09	0.29		
24	14R-2 (7-8)	158.09	158.30	0.21	Completely altered, brecciated, silicified, sparsely vesicular, aphyric volcanic rock.	Highly silicified. Narrow bleached halos along pyrite veinlets. Vugs and vesicles are lined with quartz and pyrite and are overgrown by anhydrite. XRD mineralogy: quartz dominant, minor pyrite, plagioclase, and K-feldspar.
	15R-1 (1)	166.10	166.16	0.06		

Table T4 (continued).

Unit	Core, section (Piece)	Curated depth (mbsf) Top	Base	Curated length (m)	Lithology	Alteration
	193-1189B-					
25	15R-1 (2-17) 15R-2 (1-5) 16R-1 (1)	166.16 167.59 175.70	167.59 167.97 175.77	1.43 0.38	Brecciated completely altered and silicified, flow banded volcanic rock. Clast supported, with abundant flow-banded clasts (maximum diameter >6 cm).	The unit is in parts autoclastic and shows areas of pseudobrecciated texture owing to alteration to light greenish gray material along microcracks associated with virtual loss of flow-banded texture. It is similar to Unit 23, but much more silicified. Overall, the pieces from Section 15R-1 are similar to each other. Flow banding wraps around a black, irregular, vesicular xenolith (Piece 16 in Section 15R-1). Locally, flow banding is overprinted by alteration along fine fractures generating a nodular pseudoclastic texture. (Piece 1 in Section 16R-1 is interpreted as fall back). Rare fine (<0.5 mm) ovoid spots filled with sugary quartz and hematite. XRD mineralogy: cristobalite and plagioclase dominant, minor k-feldspar, illite, and chlorite, and traces of smectite, chlorite/smectite-mixed layer, illite-bearing mixed-layer, and pyrite.
26	15R-2 (6-10) 16R-1 (2-10)	167.97 175.77	168.28 176.44	0.31 0.67	Silicified, sparsely vesicular, sparsely plagioclase-phyric volcanic rock with prominent quartz-(pyrite-magnetite) vein network locally fit generating a jigsaw-fit texture. Plagioclase, (generally 1 vol%), phenocrysts are up to 2 mm (laths or tabular to rounded shapes). Contains rare mafic xenoliths.	Silicified rock cut by a fine network of quartz-pyrite and quartz magnetite veins. Siliceous alteration halos (millimeter scale) along veins. Magnetite occurs in halos of quartz-pyrite veins. XRD mineralogy: cristobalite and plagioclase dominant, minor k-feldspar and illite, and traces of illite-bearing mixed-layer, chlorite, smectite, and chlorite/smectite-mixed layer.
27	16R-1 (11-19) 16R-2 (1-4)	176.44 177.12	177.12 177.52	0.68 0.40	Very highly altered, moderately vesicular, aphyric volcanic rock with hieroglyphic groundmass texture. Angular to irregular, shardlike shaped white groundmass domains (up to 3 mm) are embedded in dark gray groundmass. Trace of plagioclase phenocryst laths (up to 2 mm). Vesicles are round to lensoidal (up to 2 cm in maximum dimension) and typically lined by quartz.	Very highly altered, silicified rock with fine, white anhydrite/white clay-rich domains (angular irregular shapes, maximum diameters are 1 to 3 mm). Vesicles are lined/filled by drusy quartz and/or anhydrite. Locally chalcopyrite, pyrite, and/or covellite occur in quartz-lined vesicles and on fracture surfaces. XRD mineralogy: quartz dominant, minor plagioclase, K-feldspar, chlorite/smectite-mixed layer, and pyrite, and traces of illite.
28	17R-1 (1-3)	185.30	185.58	0.28	Silicified, moderately vesicular, aphyric volcanic rock.	Highly silicified rocks cut by a fine quartz-pyrite vein with a pale halo (silification overprinting silification). Vesicles are lined by quartz ± traces of pyrite. Some vesicles are filled with quartz-pyrite in the vein halo. XRD mineralogy: quartz dominant, minor plagioclase, K-feldspar, and pyrite.
29	17R-1 (4-6)	185.58	185.74	0.16	Breccia of completely altered, flow banded volcanic clasts (maximum diameter >5 cm). There are clasts with folded flow banding, which is truncated at the margins. In one clast, flow banding is wrapping around a black, siliceous xenolith.	Flow-banded gray-green silicified volcanic rock with rare dark spots that contain magnetite, hematite, and chlorite. XRD mineralogy: quartz dominant, minor plagioclase, K-feldspar, pyrite, and chlorite/smectite-mixed layer.
30	17R-1 (7-18)	185.74	186.26	0.52	Silicified, flow-banded volcanic rock.	Strongly silicified volcanic rock. Drusy quartz lined and filled vugs in Pieces 7, 10, and 14. Green clay layers occur in flow-banded pieces. Trace of fresh plagioclase phenocrysts are present in Piece 7. XRD mineralogy: quartz dominant, minor plagioclase, K-feldspar, pyrite, and chlorite/smectite-mixed layer.
31	17R-1 (19-20)	186.26	186.34	0.08	Graded, thinly bedded, volcaniclastic sandstone. Contains a variety of fragments including perlitic, porphyritic, and glassy clasts.	White, green, and blue clay fragments are hosted in a hard silicified matrix. Pyrite occurs as fine drusy crystals in voids and as fine disseminated crystals. Trace disseminated chalcopyrite. XRD mineralogy: quartz dominant, minor plagioclase, pyrite, and illite.
32	17R-1 (21-28) 18R-1 (1-2)	186.34 195.00	186.75 195.12	0.41 0.12	Flow-banded silicified volcanic rock.	Flow banding defined by green clay-rich layers. Trace of disseminated magnetite and pyrite. Magnetite occurs in patches of reddish brown clay and as disseminations in Piece 28 of Section 17R-1. XRD mineralogy: quartz dominant, minor plagioclase, K-feldspar, pyrite, and chlorite, and traces of illite, illite-bearing mixed layer, and chlorite/smectite-mixed layer.
33	18R-1 (3-6)	195.12	195.45	0.33	Breccia of completely altered, flow-banded volcanic rock.	GSC altered clasts, with moderate silicification, set in a dark gray matrix of quartz, hematite, and pyrite. XRD mineralogy: cristobalite and plagioclase dominant, minor quartz, K-feldspar, illite, and chlorite, and traces of illite-bearing mixed layer and pyrite.
34	18R-1 (7-21) 18R-2 (1-4)	195.45 196.42	196.42 196.78	0.97 0.36	Breccia of completely altered flow banded volcanic rock which is locally overprinted by silicification along a fine vein network generating a pseudoclastic texture.	GSC altered clasts, with gray silicified blebs and silicification along quartz-hematite vein network. XRD mineralogy: cristobalite and plagioclase dominant, minor quartz, K-feldspar, pyrite, illite, chlorite, and chlorite/smectite-mixed layer, and traces of smectite, illite-bearing mixed layer, talc?, and actinolite?.

Table T4 (continued).

Unit	Core, section (Piece)	Curated depth (mbsf) Top	Curated depth (mbsf) Base	Curated length (m)	Lithology	Alteration
35	193-1189B-18R-2 (5-8)	196.78	197.16	0.38	Completely altered, clast-supported polymict breccia with spherulitic and flow-banded clasts (>5 cm in maximum diameter). Abundant evidence for clastic transport including truncated folded flow banding and rotated flow-banded clasts.	Various types of silica-sulfate-clay-altered clasts, with quartz-hematite-sulfide-bearing matrix. XRD mineralogy: quartz dominant, minor plagioclase, K-feldspar, and chlorite, and traces of illite and pyrite.
36	18R-2 (9-15)	197.16	197.57	0.41	Breccia of completely altered, flow-banded volcanic rock.	GSC altered clasts with quartz-pyrite-bearing matrix.

Notes: GSC = green silica-clay, XRD = X-ray diffraction.

Table T5. Minerals identified by X-ray diffraction analysis, Hole 1189A.

Core, section, interval (cm)	Unit	Description	XRD identification: major (minor, "trace") minerals*	Anhydrite (wt%)
193-1189A-				
1R-1, 0-4	1	Fresh, moderately vesicular, aphyric dacite	Plagioclase, opaline silica (augite, quartz, spinel)	
2R-1, 34-35	2	Moderately to completely altered, vesicular aphyric dacite	Plagioclase, cristobalite (K-feldspar, pyrite, chl/sm mixed-layer clays)	
2R-1, 77-78	2	Moderately to completely altered, vesicular aphyric dacite	Anhydrite (cristobalite, plagioclase, pyrite, "chlorite")	
2R-1, 113-115	4	Hydrothermal breccia with completely altered volcanic clasts	Anhydrite, cristobalite (pyrite, chl/sm mixed-layer clays, "illite")	
3R-1, 6-10	5	Highly to completely bleached, vesicular aphyric dacite	Plagioclase, cristobalite (pyrite, chlorite)	
3R-1, 20-22	5	Highly to completely bleached, vesicular aphyric dacite	Cristobalite, plagioclase (K-feldspar, pyrite, chlorite, illite)	
3R-1, 59-63	6	Hydrothermally fractured volcaniclastic breccia	Quartz, anhydrite (pyrite, "illite")	20-25
3R-1, 70-73	7	Bleached and silicified, intensely veined dacite	Quartz (K-feldspar, pyrite, "chlorite, illite")	
4R-1, 17-20	8	Completely altered dacite	Quartz (plagioclase, pyrite, chlorite, illite)	
4R-1, 21-24	8	Completely altered dacite	Quartz (plagioclase, chlorite, pyrite, "illite")	
5R-1, 14-16	9	Completely altered, hydraulic breccia with flow laminated clasts	Quartz (anhydrite, chlorite, pyrite, illite)	2-5
7R-1, 27-28	10	Completely altered, slightly vesicular volcanic rock	Quartz, plagioclase (pyrite, anhydrite, chlorite, illite)	2-5
7R-1, 58-59	11	Completely altered hydrothermal(?) breccia	Quartz (anhydrite, pyrite, "illite, chlorite")	5-10
7R-1, 95-96	13	Completely altered hydrothermal(?) breccia	Quartz (plagioclase, chlorite, "pyrite, anhydrite")	<2
8R-1, 31-32	15	Poikiloblastically silicified plagioclase-rich volcanic rock	Plagioclase (quartz, pyrite, "anhydrite, chlorite")	<2
8R-1, 42-44	15	Poikiloblastically silicified plagioclase-rich volcanic rock	Plagioclase (quartz, K-feldspar, pyrite, "anhydrite, smectite, chlorite")	<2
8R-1, 90-92	15	Poikiloblastically silicified plagioclase-rich volcanic rock	Plagioclase, quartz (pyrite, K-feldspar, "anhydrite, chlorite, illite")	<2
8R-1, 113-114	15	Poikiloblastically silicified plagioclase-rich volcanic rock	Quartz, plagioclase ("chlorite, pyrite")	
9R-1, 16-17	16	Completely altered hydrothermal breccia	Quartz, anhydrite (plagioclase, pyrite, "chlorite")	15-20
10R-1, 0-1	17	Completely bleached moderately vesicular volcanic rock	Quartz (plagioclase, pyrite, "chlorite")	
10R-1, 50-51	19	Completely altered hydrothermal breccia	Quartz, anhydrite (plagioclase, pyrite, "chlorite, illite")	10-15
11R-1, 37-38	20	Completely silicified, massive, vesicular volcanic rock	Quartz (pyrite, illite, chlorite, "anhydrite")	<2
12R-1, 69-70	20	Completely silicified, massive, vesicular volcanic rock	Quartz (illite, pyrite)	
13R-1, 24-33	22	Pervasively bleached moderately vesicular volcanic rock	Quartz (chlorite, pyrite, illite)	
13R-1, 51-53	23	Polymict volcaniclastic breccia	Quartz (plagioclase, pyrite, chlorite, "illite")	
13R-1, 62-71	24	Pervasively bleached sparsely vesicular volcanic rock	Quartz (pyrite, "chlorite, illite")	

Notes: chl/sm mixed-layer clays = chlorite/smectite-mixed-layer clays. * = the terms major, minor, and trace are applied to X-ray diffraction (XRD) analyses as explained in **"Hydrothermal Alteration,"** p. 8, in the "Explanatory Notes" chapter and do not imply quantitative abundances. Anhydrite abundances are estimated for quartz-bearing assemblages as described in **"Hydrothermal Alteration,"** p. 8, in the "Explanatory Notes" chapter. This procedure probably results in an overestimation of the anhydrite abundance, because the effect of clays is ignored. In the absence of a suitable calibration, it is not possible to estimate anhydrite abundance from XRD spectra for cristobalite-dominated assemblages.

Table T6. Minerals identified by X-ray diffraction analysis, Hole 1189B. (See table notes. Continued on next page.)

Core, section, interval (cm)	Unit	Description	XRD identification: major (minor, "trace") minerals*	Anhydrite (wt%)
193-1189B-				
1R-1, 0		Hammer sample (for further explanation see "Variation of Alteration with Depth," p. 24 in "Hydrothermal Alteration," in the "Site 1189" chapter)	Pyrite (chalcopyrite, illite, "sphalerite")	
1R-1, 0-2	1	Semimassive sulfide with sparse volcanic rock clasts	Anhydrite (pyrite, chalcopyrite, gypsum)	
1R-1, 20-30	1	Semimassive sulfide with sparse volcanic rock clasts	Pyrite, illite, chl/sm mixed-layer clays ("sphalerite")	
1R-1, 30-31	2	Completely altered, moderately vesicular, aphyric rock	Pyrite, muscovite (chlorite)	
2R-1, 11-20	3	Breccia of completely altered volcanic rock clasts in a pyrite-anhydrite stockwork matrix	Anhydrite (gypsum, pyrite)	
2R-1, 11-20	3	Breccia of completely altered volcanic rock clasts in a pyrite-anhydrite stockwork matrix	Gypsum, pyrite (anhydrite, illite)	
2R-1, 40-50	3	Pyrite-anhydrite stockwork matrix	Pyrite, anhydrite, quartz (gypsum)	
2R-1, 40-50	3	Wallrock sample	Pyrite (illite, chlorite, kaolinite?, "smectite, quartz")	
3R-1, 0-10	3	Breccia of completely altered volcanic rock clasts in a pyrite-anhydrite stockwork matrix	Quartz, pyrite ("illite")	
5R-1, 11-22	4	Breccia of completely altered volcanic rock clasts in a pyrite-quartz matrix	Pyrite (quartz, K-feldspar, illite, "chlorite")	
6R-1, 23-33	5	Breccia of completely altered volcanic rock clasts in quartz-hematite-pyrite matrix	Quartz (K-feldspar, plagioclase, pyrite, chlorite, "illite")	
6R-1, 64-74	7	Completely altered, aphyric volcanic rock	Quartz (plagioclase, K-feldspar, pyrite, chlorite, "illite")	
7R-1, 0-10	8	Breccia of completely altered volcanic rock clasts	Quartz, pyrite (K-feldspar, "illite")	
8R-1, 7-9	9	Completely altered, slightly vesicular, aphyric volcanic rock	K-feldspar (pyrite, chlorite, illite, "illite-bearing mixed-layer clays")	
10R-1, 26-27	13	Silica-clay altered, aphyric volcanic rock	Quartz (chlorite, K-feldspar, plagioclase, pyrite)	
10R-1, 57-60	14	Silica-chlorite altered, spherulitic, aphyric volcanic rock	Quartz (chlorite, K-feldspar, anhydrite, pyrite, illite)	
10R-1, 67-69	15	Completely altered, silicified, massive, aphyric volcanic rock	Cristobalite, plagioclase (K-feldspar, chlorite, "pyrite")	
11R-1, 0-7	16	Breccia of completely altered volcanic clasts	Quartz (anhydrite, K-feldspar, chlorite, chl/sm mixed-layer clays, smectite, illite, pyrite)	
11R-1, 14-16	17	Jasperoidal breccia of completely altered volcanic clasts	Quartz (anhydrite, pyrite, "hematite")	
11R-1, 19-20	18	Polymict breccia of completely altered green volcanic clasts	Quartz (K-feldspar, illite, chlorite, pyrite, "plagioclase")	
11R-1, 63-65	19	Completely altered, moderately vesicular, aphyric volcanic rock	Cristobalite, plagioclase (quartz, "pyrite, chlorite, chl/sm mixed-layer clays, smectite")	
11R-2, 46-47	19	Completely altered, moderately vesicular, aphyric volcanic rock	Cristobalite, plagioclase (quartz, chlorite, "chl/sm mixed-layer clays, smectite")	
11R-2, 89-91	19	Completely altered, moderately vesicular, aphyric volcanic rock	Cristobalite, plagioclase (quartz, smectite, "chlorite")	
12R-1, 114-115	19	Completely altered, moderately vesicular, aphyric volcanic rock	Plagioclase (K-feldspar, quartz, chlorite, "illite, pyrite")	
12R-2, 55-57	19	Completely altered, moderately vesicular, aphyric volcanic rock	Cristobalite, plagioclase (K-feldspar, quartz, chl/sm mixed-layer clays, "smectite, illite")	
13R-1, 22-24	20	Breccia with completely altered volcanic clasts	Quartz (plagioclase, pyrite, "chlorite")	
13R-1, 34-36	20	Breccia with completely altered volcanic clasts	Quartz (pyrite, "barite")	
13R-1, 52-54	21	Completely altered, massive, aphyric volcanic rock	Quartz (plagioclase, "chlorite, illite, pyrite")	
14R-1, 0-10	22	Silicified and mineralized, aphyric volcanic rock	Quartz (pyrite, "illite")	
14R-1, 57-58	23	Breccia of completely altered volcanic rock fragments	Anhydrite, quartz ("plagioclase, chlorite")	60
14R-1, 117-119	23	Breccia of completely altered volcanic rock fragments	Anhydrite, quartz (K-feldspar, plagioclase, chlorite)	50
14R-2, 10-11	23	Breccia of completely altered volcanic rock fragments	Quartz (plagioclase, pyrite, "chlorite")	
14R-2, 29-35	24	Completely altered, brecciated, silicified, aphyric volcanic rock	Quartz (pyrite, plagioclase, K-feldspar)	
15R-1, 16-17	25	Breccia completely altered and silicified volcanic rock	Cristobalite, plagioclase (K-feldspar, illite, chlorite, "smectite, chl/sm mixed-layer clays, illite-bearing mixed-layer clays, pyrite")	
15R-1, 128-129	25	Breccia completely altered and silicified volcanic rock	Cristobalite, plagioclase (K-feldspar, illite, chlorite, "smectite, chl/sm mixed-layer clays, illite-bearing mixed-layer clays, pyrite")	
15R-2, 61-64	26	Silicified, sparsely vesicular, aphyric volcanic rock	Cristobalite, plagioclase (K-feldspar, illite, "chlorite, smectite, chl-sm-mixed-layer clays, pyrite")	
16R-1, 36-39	26	Silicified, sparsely vesicular, aphyric volcanic rock	Cristobalite, plagioclase (K-feldspar, "illite, illite-bearing mixed-layer clays, chlorite, smectite, chl/sm mixed-layer clays")	
16R-1, 130-131	27	Very highly altered, moderately vesicular, aphyric volcanic rock	Quartz (plagioclase, pyrite, chl/sm mixed-layer clays)	
16R-2, 9-10	27	Very highly altered, moderately vesicular, aphyric volcanic rock	Quartz (plagioclase, K-feldspar, chl/sm mixed-layer clays, "pyrite, illite")	
17R-1, 19-20	28	Silicified, moderately vesicular, aphyric volcanic rock	Quartz (plagioclase, K-feldspar, pyrite)	
17R-1, 60-63	30	Silicified, flow-banded volcanic rock	Quartz (plagioclase, K-feldspar, pyrite, chl/sm mixed-layer clays)	
17R-1, 65-66	30	Silicified, flow-banded volcanic rock	Quartz (plagioclase, K-feldspar, pyrite, chl/sm mixed-layer clays)	
17R-1, 96-98	31	Normal graded, thinly bedded, volcaniclastic sandstone	Quartz (plagioclase, pyrite, illite)	

Table T6 (continued).

Core, section, interval (cm)	Unit	Description	XRD identification: major (minor, "trace") minerals*	Anhydrite (wt%)
17R-1, 118-122	32	Flow-banded silicified volcanic rock	Quartz (plagioclase, K-feldspar, pyrite, chlorite, "illite, illite-bearing mixed-layer clays, chl/sm mixed-layer clays")	
18R-1, 24-25	33	Breccia of completely altered, flow-banded volcanic rock	Cristobalite, plagioclase (quartz, K-feldspar, illite, chlorite, "illite-bearing mixed-layer clays, pyrite")	
18R-1, 70-71	34	Breccia of completely altered flow-banded volcanic rock	Cristobalite, plagioclase (quartz, K-feldspar, pyrite, illite, chlorite, chl/sm mixed-layer clays, "illite-bearing mixed-layer clays, talc?")	
18R-1, 107-108	34	Breccia of completely altered flow-banded volcanic rock	Cristobalite, plagioclase (quartz, K-feldspar, pyrite, illite, chl/sm mixed-layer clays, "smectite, illite-bearing mixed-layer clays, actinolite?")	
18R-2, 23-24	34	Breccia of completely altered flow-banded volcanic rock	Cristobalite, plagioclase (quartz, K-feldspar, pyrite, illite, chlorite, chl/sm mixed-layer clays, "smectite, illite-bearing mixed-layer clays, actinolite?")	
18R-2, 42-43	35	Completely altered, clast-supported polymict breccia	Quartz (plagioclase, K-feldspar, chlorite, "illite, pyrite")	

Notes: chl/sm mixed-layer clays = chlorite/smectite-mixed-layer clays. * = the terms major, minor, and trace are applied to X-ray diffraction (XRD) analyses as explained in "Hydrothermal Alteration," p. 8, in the "Explanatory Notes" chapter and do not imply quantitative abundances. Anhydrite abundances are estimated for quartz-bearing assemblages as described in "Hydrothermal Alteration," p. 8, in the "Explanatory Notes" chapter. This procedure probably results in an overestimation of the anhydrite abundance, because the effect of clays is ignored. In the absence of a suitable calibration, it is not possible to estimate anhydrite abundance from XRD spectra for cristobalite-dominated assemblages.

Table T7. Major element oxides with selected trace elements, Hole 1189A.

Core, section: 193-1189A-:	1R-1	2R-1	3R-1	3R-1	3R-1*	3R-1*	3R-1	3R-1	4R-1*	4R-1	5R-1	7R-1	8R-1	8R-1	12R-1	13R-1
Interval (cm):	0-4	113-115	6-10	6-10	6-10	20-22	59-63	70-73	17-20	21-24	14-16	27-31	42-44	90-92	67-69	24-33
Curated depth (mbsf):	0.02	10.83	19.46	19.46†	19.46	19.60	19.99	20.10	29.27	29.31	38.94	58.57	68.42	68.90	107.17	116.34
Rock type:	FD	BR	AD	AD		BR	AD	AD	AD	AD	BR	AD	AD	BR	AD	AD
Alteration style:	F	GSC	BL	BL		GSC	GSC	Sil	GSC	GSC	GSC	GSC	Sil	Sil	Sil	GSC
Ignited rock powder composition:																
Major element oxide (wt%):																
SiO_2	64.25	56.32	68.08	68.08	67.62	65.59	42.22	68.51	67.66	62.93	60.16	55.18	62.83	56.89	70.54	36.23
TiO_2	0.76	0.63	0.68	0.68	0.79	0.86	0.43	0.52	0.78	0.64	0.62	0.80	0.56	0.63	0.59	1.00
Al_2O_3	14.67	17.80	14.22	14.56	14.71	16.01	9.53	11.00	14.45	13.31	13.25	16.59	15.81	17.85	13.82	19.10
Fe_2O_3	6.92	4.81	4.50	4.62	4.76	5.19	7.05	6.57	6.76	6.08	8.09	6.68	4.96	4.77	4.02	11.13
MnO	0.14	0.02	0.03	0.04	0.05	0.05	0.04	0.02	0.06	0.06	0.07	0.03	0.01	0.02	0.01	0.06
MgO	1.84	2.80	3.33	3.27	3.34	4.61	4.77	2.07	4.61	4.33	5.64	3.01	1.58	2.81	1.98	11.58
CaO	4.90	2.40	2.77	3.08	3.20	2.28	10.13	0.59	1.18	1.73	1.62	2.80	2.18	2.46	0.44	1.28
Na_2O	4.68	4.77	2.93	3.11	2.97	2.20	0.32	0.59	1.31	1.42	0.64	3.80	4.43	4.90	0.45	0.75
K_2O	1.26	5.37	1.90	1.98	2.00	3.65	2.91	5.71	3.58	3.49	2.95	3.89	4.22	5.34	3.85	2.88
P_2O_5	0.27	0.15	0.12	0.17	BD	BD	0.08	0.15	BD	0.20	0.18	0.25	0.15	0.16	0.39	0.72
Total (wt%):	99.68	95.08	98.55	99.57	99.44	100.43	77.49	95.73	100.39	94.18	93.23	93.03	96.74	95.83	96.08	84.74
LOI (wt%):	1.07	3.95	2.09	2.09	2.94	3.54	6.00	4.36	4.25	4.50	6.42	4.52	3.39	3.33	4.05	9.20
Trace element (ppm):																
Zr	97	196	116	115	123	128	76	97	123	120	118	150	169	192	126	128
Y	33	50	35	35	32	37	21	24	35	29	33	39	37	47	31	37
Sr	367	314	309	309	323	248	464	61	138	167	82	335	290	320	14	55
Zn	104	BD	42	44	63	51	BD	19	37	BD	BD	BD	BD	BD	BD	BD
Cu	143	BD	225	210	821	247	BD	BD	12	BD	BD	BD	BD	BD	1480	BD
Ba	307	2418	1535	1515	1478	2769	1204	3311	2374	2179	525	2073	1974	2487	669	1237
Whole rock composition:																
Major element oxide (wt%):																
SiO_2	63.56	54.10	66.65	66.65	65.63	63.26	39.69	65.52	64.78	60.09	56.29	52.69	60.70	55.00	67.69	32.90
TiO_2	0.76	0.60	0.67	0.67	0.77	0.83	0.40	0.50	0.75	0.61	0.58	0.77	0.54	0.61	0.56	0.91
Al_2O_3	14.51	17.09	13.92	14.25	14.28	15.44	8.96	10.52	13.83	12.71	12.40	15.84	15.28	17.26	13.26	17.35
Fe_2O_3	6.84	4.62	4.40	4.52	4.62	5.01	6.63	6.28	6.47	5.80	7.57	6.38	4.79	4.61	3.85	10.11
MnO	0.14	0.02	0.03	0.04	0.04	0.05	0.04	0.02	0.06	0.05	0.06	0.03	0.01	0.02	0.01	0.05
MgO	1.82	2.69	3.26	3.20	3.25	4.45	4.48	1.98	4.42	4.14	5.28	2.87	1.52	2.71	1.90	10.52
CaO	4.85	2.30	2.71	3.02	3.11	2.20	9.52	0.57	1.13	1.65	1.51	2.68	2.11	2.38	0.42	1.16
Na_2O	4.63	4.58	2.87	3.05	2.88	2.12	0.30	0.56	1.25	1.35	0.60	3.63	4.28	4.74	0.43	0.69
K_2O	1.25	5.16	1.86	1.94	1.94	3.52	2.74	5.46	3.43	3.33	2.76	3.72	4.08	5.16	3.69	2.61
P_2O_5	0.27	0.15	0.11	0.16	BD	BD	0.08	0.14	BD	0.19	0.17	0.24	0.14	0.15	0.37	0.65
Total S (wt%):	0.04	2.66	0.83	0.83	1.31	1.22	9.15	4.89	2.42	2.73	4.50	4.42	2.89	3.70	2.86	6.19
Total H_2O^+ (wt%):	1.35	2.69	1.71	1.71	2.23	3.27	3.00	1.67	3.13	2.74	3.92	1.68	1.59	1.17	2.65	7.00
$S_{water\text{-}soluble\ sulfate}$ (wt%):	0.00	2.98	0.25	ND	ND	ND	6.71	0.62	ND	0.69	1.17	0.03	1.60	0.07	0.01	0.21

Notes: Upper portion of the table gives analyses of the ignited powders, while the lower portion is the original rock compositions. Water, total sulfur, and loss on ignition (LOI) are reported in weight percent of the unignited powders for Hole 1189A. The analyses of samples containing >1 wt% total S should be used as general compositional guides and not as absolute values. Rock types: FD = fresh dacite; BR = breccia; AD = altered dacite. Alteration types: F = fresh; GSC = green silica-clay; BL = bleached; Sil = silicified. * = samples ignited for 6 hr at 600°C followed by 4 hr at 1050°C; all other samples were roasted only for 1 hr at 1050°C. BD = below detection; ND = not determined. † = duplicate.

Table T8. Major element oxides with selected trace elements, Hole 1189B.

Core, section: 193-1189B-:	1R-1	8R-1	11R-1	11R-2	12R-2	13R-1	16R-1	16R-2
Interval (cm):	20-30	7-9	63-65	89-91	55-57	52-54	36-39	31-33
Curated depth (mbsf):	31.20	98.47	128.23	129.17	139.26	147.52	176.06	177.44
Rock type:	AD	AD	AD	AD	AD	AD	AD	AD
Alteration style:	GSC	GSC	GSC/Sil	GSC/Sil	GSC/Sil	GSC	Sil	Sil
Ignited rock powder composition*:								
Major element oxide (wt%):								
SiO_2	41.99	50.54	70.59	72.00	69.51	78.07	71.56	73.23
TiO_2	0.95	0.55	0.44	0.45	0.44	0.31	0.45	0.45
Al_2O_3	24.76	19.71	14.11	14.20	14.06	10.40	13.88	13.56
Fe_2O_3	15.25	14.08	4.87	4.85	4.94	3.58	4.48	4.11
MnO	0.04	0.03	0.10	0.14	0.10	0.07	0.10	0.14
MgO	7.73	3.87	1.56	1.13	1.48	1.40	1.65	1.49
CaO	0.26	0.05	1.71	1.95	1.66	0.25	1.49	1.37
Na_2O	0.42	0.48	4.03	4.56	3.76	1.45	3.98	3.21
K_2O	4.75	7.79	2.05	1.92	2.55	3.59	2.59	3.37
P_2O_5	0.40	0.38	0.34	0.36	0.35	0.34	0.36	0.36
Total (wt%):	96.55	97.48	99.79	101.57	98.85	99.45	100.54	101.28
LOI (wt%):	4.77	9.00	1.42	0.99	0.88	2.03	1.09	1.22
Trace element (ppm):								
Zr	212	200	138	139	134	113	158	157
Y	66	49	36	35	35	29	38	39
Sr	18	76	274	283	266	155	263	248
Zn	105	20	76	135	52	1416	204	152
Cu	114	13	13	23	83	681	43	315
Ba	685	8835	508	425	726	4881	646	949
Whole rock composition:								
Major element oxide (wt%):								
SiO_2	39.98	45.99	69.58	71.29	68.89	76.49	70.78	72.33
TiO_2	0.90	0.50	0.43	0.45	0.43	0.30	0.44	0.44
Al_2O_3	23.58	17.94	13.91	14.06	13.94	10.19	13.73	13.40
Fe_2O_3	14.52	12.82	4.80	4.81	4.90	3.51	4.43	4.06
MnO	0.04	0.03	0.10	0.14	0.10	0.07	0.10	0.14
MgO	7.37	3.52	1.54	1.12	1.47	1.37	1.63	1.47
CaO	0.25	0.04	1.68	1.93	1.65	0.24	1.47	1.35
Na_2O	0.40	0.44	3.97	4.52	3.73	1.42	3.94	3.17
K_2O	4.52	7.09	2.02	1.90	2.53	3.52	2.56	3.33
P_2O_5	0.39	0.35	0.33	0.36	0.35	0.33	0.36	0.35
Total S (wt%):	8.23	8.95	0.16	0.01	0.02	1.00	0.10	0.03
Total H_2O^+ (wt%):	6.03	3.23	1.12	0.64	0.98	1.34	1.23	1.12
$S_{water\text{-}soluble\ sulfate}$ (wt%):	2.33	0.05	0.02	0.02	0.02	0.00	0.00	0.04

Notes: Rock type: AD = altered dacite. Alteration type: GSC = green silica-clay, Sil = silicified. * = all samples ignited for 6 hr at 600°C and then for 4 hr at 1050°C. The upper portion of the table gives abundances in the ignited powder, whereas the lower portion contains original rock compositions. Water, total sulfur, and loss on ignition (LOI) are reported in weight percent of unignited powder. Analyses of samples containing more than 1 wt% total S should be used as general compositional guides, and not as absolute values. LOI was conducted at 1050°C for 4 hr.

Table T9. Total sulfur and water measurements on powdered samples used for ICP-AES and XRD analysis, Hole 1189A.

Core, section, interval (cm)	Curated depth (mbsf)	TS unignited (wt%)	TS ignited* (wt%)	TS ignited† (wt%)	H_2O^+ unignited (%)
193-1189A-					
1R-1, 0-4	0.02	0.04	BD	ND	1.35
2R-1, 34-35	10.04	0.51	ND	ND	2.44
2R-1, 77-78	10.47	9.39	ND	ND	2.34
2R-1, 113-115	10.83	2.66	1.79	0.41	2.69
3R-1, 6-10	19.46	0.83	0.03	ND	1.71
3R1, 20-22	19.60	1.22	ND	BD	3.27
3R-1, 59-63	19.99	9.15	5.99	1.20	3.00
3R-1, 70-73	20.10	4.89	0.16	ND	1.67
4R1, 17-20	29.27	2.42	ND	0.02	3.13
4R-1, 21-24	29.31	2.73	0.24	ND	2.74
5R-1, 14-16	38.94	4.50	0.56	ND	3.92
7R-1, 27-28	58.57	4.42	BD	ND	1.68
7R-1, 58-59	58.88	7.61	ND	ND	2.07
7R-1, 95-96	59.25	1.11	ND	ND	1.37
8R-1, 31-32	68.31	3.05	ND	ND	1.62
8R-1, 42-44	68.42	2.89	BD	ND	1.59
8R-1, 90-92	68.90	3.70	BD	ND	1.17
8R-1, 113-114	69.13	2.12	ND	ND	1.42
9R-1, 16-17	77.86	7.26	ND	ND	1.24
10R-1, 0-1	87.30	2.71	ND	ND	1.83
10R-1, 50-51	87.80	4.41	ND	ND	2.36
11R-1, 37-38	97.27	3.12	ND	ND	3.19
12R-1, 69-70	107.17	2.86	0.14	ND	2.65
13R-1, 24-33	116.34	6.19	0.36	ND	7.00

Notes: TS = total sulfur. * = powder ignited at 600°C for 6 hr and then at 1050°C for 1 hr, † = powder ignited at 600°C for 6 hr and then at 1050°C for 4 hr. Detection limit = 0.01. Instrument precision = ±0.04%. ND = not determined. BD = below detection.

Table T10. Total sulfur and water measurements on powdered samples used for ICP-AES and XRD analyses, Hole 1189B.

Core, section, interval (cm)	Curated depth (mbsf)	TS unignited (wt%)	H_2O^+ unignited (wt%)
193-1189B-			
1R-1, 0-2	31.02	45.49	1.40
1R-1, 20-30	31.20	8.23	6.03
2R-1, 11-20	40.21	23.92	9.50
2R-1, 40-50	40.50	31.78	6.11
2R-1, 40-50	40.50	14.92	4.66
5R-1, 11-22	69.41	32.65	0.91
6R-1, 23-33	79.23	2.16	1.46
8R-1, 7-9	98.47	8.95	3.23
11R-1, 19-20	127.79	1.58	2.35
11R-1, 63-65	128.23	0.16	1.12
11R-2, 46-47	128.74	0.42	1.70
11R-2, 89-91	129.17	0.01	0.64
12R-2, 55-57	139.26	0.02	0.98
13R-1, 22-24	147.22	1.75	1.38
13R-1, 34-36	147.34	8.36	0.88
13R-1, 52-54	147.52	1.00	1.34
14R-1, 57-58	157.07	5.03	1.51
14R-1, 117-119	157.67	4.05	3.06
15R-1, 16-17	166.26	0.44	2.02
15R-1, 128-129	167.38	0.17	1.33
15R-2, 61-64	168.21	0.00	1.23
16R-1, 36-39	176.06	0.10	1.23
16R-1,130-131	177.00	1.00	1.28
16R-2, 9-10	177.22	0.68	1.50
16R-2, 31-33	177.44	0.03	1.12
17R-1, 19-20	185.49	2.13	0.63
17R-1, 65-66	185.95	1.81	1.12
18R-1, 24-25	195.24	0.29	1.43
18R-1, 70-71	195.70	1.05	2.44
18R-1, 107-108	196.07	0.10	2.14
18R-2, 23-24	196.65	0.65	1.96
18R-2, 42-43	196.84	0.46	1.82

Note: TS = total sulfur, ICP-AES = inductively coupled plasma-atomic emission spectroscopy, XRD = X-ray diffraction.

Table T11. ICP-AES analyses of the composite sample from Hole 1189A*.

Analyte	Result	Detection limit
Oxide (wt%):		
TiO_2	0.504	
Al_2O_3	12.87	
Fe_2O_3	8.75	
MnO	0.020	
MgO	1.83	
CaO	1.59	
Na_2O	1.90	
K_2O	2.21	
P_2O_5	0.167	
S(tot)	5.95	
Trace element (ppm):		
Li	BD	5
Be	BD	2
Sc	10	
V	41	
Cr	12	
Co†	28	
Ni	BD	10
Cu	2610	
Zn	34	
As	BD	20
Sr	140	
Y	20	
Zr	91	
Mo	BD	5
Ag	BD	5
Sb	BD	20
Ba	497	
La	10	
Yb	3	2
Lu	BD	5
Pb	BD	50
Au (ppb)	BD	200

Notes: ICP-AES = inductively coupled plasma-atomic emission spectroscopy. * = sample sent to Commonwealth and Industrial Research Organization (CSIRO) for midcruise shore-based analyses (shipment number 1189A-(1); CSIRO number 142646D). † = contamination from tungsten carbide mill. BD = below detection limit. Analyst: L. Dotter, CSIRO, Australia.

Table T12. NAA analyses of the composite bulk sample from Hole 1189A*.

Element	Unit	Result	Detection limit
Sb	ppm	0.5	0.1
As	ppm	22.4	0.5
Ba	ppm	581	100
Br	ppm	17.7	0.5
Cd	ppm	BD	5
Ca	%	1.25	0.5
Ce	ppm	24.8	2
Cs	ppm	BD	0.5
Cr	ppm	19.2	2
Co	ppm	31.4	0.5
Eu	ppm	0.97	0.5
Au	ppb	20.2	2
Hf	ppm	3.26	0.5
Ir	ppb	BD	5
Fe	%	5.81	0.02
La	ppm	9.64	0.5
Lu	ppm	0.51	0.2
Hg	ppm	BD	1
Mo	ppm	BD	5
K	%	1.56	0.2
Rb	ppm	21.7	10
Sm	ppm	3.69	0.2
Sc	ppm	11.5	0.1
Se	ppm	BD	2
Ag	ppm	BD	2
Na	%	1.41	0.01
Ta	ppm	BD	1
Te	ppm	BD	2
Tb	ppm	0.74	0.5
Th	ppm	1.17	0.5
Sn	ppm	BD	200
W	ppm	53.5	1
U	ppm	1.12	1
Yb	ppm	3.25	0.5
Zn	ppm	BD	50
Zr	ppm	BD	200

Notes: NAA = neutron activation analysis. * = sample sent to Commonwealth and Industrial Research Organization (CSIRO) for midcruise shore-based analyses (shipment number 1189A; CSIRO number 142646), with an activation time of 1 week. BD = below detection. Analyst: L. Dotter, CSIRO, Australia.

Table T13. Water chemistry data from downhole water sampler, temperature, and pressure probe sampling of borehole fluid, Hole 1189B surface seawater, and IAPSO standard.

Hole:	1189B	Seawater
	27 Dec 2001	22 Dec 2001
Water depth (mbsf):	130	Surface
Temperature (°C):	55	30
pH:	7.0	8.4
Alkalinity (mmol/L):	2.04	2.18
Salinity (‰):	35	34
		IAPSO
Na^+ (mmol/L)	479.3	480
K^+ (mmol/L)	16.3	10.4
Mg^{2+} (mmol/L)	48.1	54
Ca^{2+} (mmol/L)	18.6	10.5
Cl^- (mmol/L)	563	559
SO_4^{2-} (mmol/L)	33.8	28.9
B^{3+} (µmol/L)	531	450
Mn^+ (µmol/L)	236	—
Fe tot (µmol/L)	72	—
Sr^{2+} (µmol/L)	123	87
Ba^{2+} (µmol/L)	7	—
Li^+ (µmol/L)	131	27

Notes: Fe tot = total iron. Na, K, Mg, Ca, Cl, and SO_4 were measured by ion chromatography. B, Mn, Fe, Sr, Ba, and Li were measured by inductively coupled plasma–atomic emission spectroscopy. IAPSO = seawater standard. — = not analyzed.

Table T14. Total bacterial count and ATP measurements, Hole 1189A.

Hole, core	Depth (mbsf)	Direct count (cells/cm^3)*	ATP (pg/cm^3)†	Active bacterial cells based on ATP content (cells/cm^3)‡
193-1189A-				
2R	9.70	1.3×10^7	18.2	3.6×10^5
5R	39.13	4.6×10^6	4.8	9.6×10^4
6R	48.60	9.8×10^5	ND	1×10^4
7R	58.84	ND	ND	1×10^4
9R	77.70	ND	ND	1×10^4
10R	88.33	ND	ND	1×10^4
12R	106.91	ND	ND	1×10^4

Notes: * = detection limit of 1×10^5 cells/cm^3. ATP = adenosine triphosphate. † = detection limit of 0.5 pg/cm^3 (1×10^4 cells/cm^3). ‡ = ATP content of a bacteria is ~1×10^{-19} mol/cell. ND = not detected (below detection).

Table T15. Total bacterial count, Hole 1189B.

Hole, core	Depth (mbsf)	Direct count (cells/cm^3)*
193-1189B-		
1R	31.00	3.1 x 10^6
6R	79.07	ND
12R	140.01	ND
14R	156.88	ND
16R	175.95	ND

Notes: * = detection limit: 1 x 10^5 cells/cm^3. ND = not detected (below detection).

Table T16. Enrichment cultivation at different culture conditions, Hole 1189A.

Hole, core	Depth (mbsf)	Aerobic cultivation			Anaerobic cultivation		
		4°C	25°C	60°C	25°C	60°C	90°C
193-1189A-							
2R	9.70	+	+	—	+	—	—
5R	39.13	—	+	—	+	+	+
6R	48.60	—	++	—	+	+	+
8R	68.39	—	—	—	—	+	+
12R	106.91	—	—	—	—	—	—

Note: — = no growth, + = growth, ++ = more growth.

Table T17. Enrichment cultivation at different culture conditions, Hole 1189B.

Hole, core	Depth (mbsf)	Anaerobic cultivation	
		60°C	90°C
193-1189B-			
1R	31.00	—	—
2R	40.50	—	—
3R	51.30	—	—
5R	69.80	—	—
6R	79.07	+	+
8R	98.40	++	+
10R	118.10	—	++
11R	128.94	—	+
12R	140.01	—	—
14R	156.88	—	—
16R	175.95	—	—

Note: — = no growth, + = growth, ++ = more growth.

Table T18. Cultivation experiments with different seawater types.

Microbe source	Media (150mL)	Temperature 25°C	Temperature 60°C	Conditions
Core sample* (5 g)	Natural seawater (pH 8.3)	A	A	Aerobic
No sample	Natural seawater (pH 8.3)	B	B	Aerobic
Core sample* (5 g)	Sterilized seawater (pH 6.9)	C	C	Anaerobic
No sample	Sterilized seawater (pH 6.9)	D	D	Anaerobic
Core sample* (5 g)	Sterile artificial seawater (pH 6.1)	E	E	Anaerobic
No sample	Sterile artificial seawater (pH 6.1)	F	F	Anaerobic

Notes: * = core sample used in these experiments was from Sample 193-1189A-5R-1, 33–35 cm; 39.13 mbsf. A, C, E = medium inoculated with core. B, D, F = corresponding controls (no core), respectively.

Table T19. Compressional velocity data, Holes 1189A and 1189B.

Core, section, Interval (cm)	Piece	Depth (mbsf)	Velocity (km/s)	Sil/Qtz (%)	Px (%)	Cl (%)	Py (%)	Plag (%)	Mt (%)	Vesicles (%)	Alteration	Comments
193-1189A-												
2R-1, 9	2	9.79	3.84	50	0	50	0	0	0	15	Cm	Aphyric, vesicular volcanic rock.
2R-1, 37	6	10.07	3.47	50	0	50	0	0	0	7	Cm	Aphyric, vesicular volcanic rock.
193-1189B-												
11R-1, 63	10	127.97	4.39	40	0	20	Tr	40	Tr	4	Hi	Aphyric, vesicular volcanic rock.
11R-2, 88	8	128.91	3.85	40	0	25	Tr	35	Tr	8	Hi	Aphyric, vesicular volcanic rock.
12R-1, 34	3	138.18	4.90	45	0	30	Tr	25	Tr	8	Hi	Trachytic, vesicular volcanic rock.
12R-3, 46	7	140.42	4.00	40	0	40	Tr	20	Tr	10	Hi	Aphyric, vesicular volcanic rock.
13R-1, 55	10	147.46	4.60	50	0	49	1	0	0	5	Cm	Silicified volcanic rock.
15R-1, 87	11	158.15	4.71	15	0	80	Tr	5	Tr	0	Cm	Volcanic rock with relict flow-banding and spherulitic texture.
15R-2, 62	10	169.15	4.90	48	5	10	Tr	37	Tr	0	Hi	Moderately plagioclase-phyric, xenolith-bearing volcanic rock.
16R-2, 31	4	177.44	4.92	49	0	30	Tr	20	Tr	5	Hi	Vesicular volcanic rock.

Notes: Sil/Qtz = silica/quartz, Px = pyroxene, Cl = clay, Py = pyrite, Plag = plagioclase, Mt = magnetite. Cm = complete, Hi = high, Tr = trace.

Table T20. Index properties, Holes 1189A and 1189B.

Core, section interval (cm)	Piece	Type	Depth (mbsf)	Bulk water content (%)	Density (g/cm³)			Porosity (%)	Void ratio
					Bulk	Dry	Grain		
193-1189A-									
1R-1, 0-5	1	Rock fragment	0.00	7.5	2.153	1.992	2.365	15.8	0.187
1R-1, 17-22	5	Rock fragment	0.17	12.9	2.153	1.876	2.572	27.1	0.371
2R-1, 8-10	2	Minicore	9.78	11.9	2.193	1.932	2.590	25.4	0.340
2R-1, 102-117	15	Rock fragment	10.72	23.5	1.958	1.498	2.720	44.9	0.816
3R-1, 76-80	13	Rock fragment	20.16	17.1	2.134	1.770	2.746	35.5	0.551
4R-1, 0-5	1	Rock fragment	29.10	14.0	2.257	1.941	2.805	30.8	0.445
5R-1, 30-34	5	Rock fragment	39.10	22.6	1.999	1.547	2.770	44.1	0.790
6R-1, 26-32	5	Rock fragment	48.86	19.8	2.092	1.678	2.818	40.4	0.679
7R-1, 55-58	8	Rock fragment	58.85	18.3	2.100	1.717	2.744	37.4	0.598
7R-1, 72-75	11	Rock fragment	59.02	18.9	2.085	1.690	2.750	38.6	0.627
7R-1, 81-83	13	Minicore	59.11	10.8	2.278	2.032	2.675	24.0	0.316
8R-1, 0-3	1	Rock fragment	68.00	10.6	2.264	2.024	2.642	23.4	0.305
8R-1, 87-89	14	Minicore	68.87	18.7	2.063	1.677	2.691	37.7	0.605
9R-1, 59-62	9	Rock fragment	78.29	16.7	2.134	1.777	2.727	34.8	0.535
10R-1, 75-77	9	Minicore	88.05	12.5	2.250	1.969	2.714	27.4	0.378
10R-1, 103-115	11	Rock fragment	88.33	13.9	2.240	1.929	2.768	30.3	0.435
11R-1, 13-18	3	Rock fragment	97.03	12.7	2.312	2.019	2.828	28.6	0.401
11R-1, 97-116	13	Rock fragment	97.87	13.1	2.331	2.025	2.886	29.8	0.425
13R-1, 24-33	4	Rock fragment	116.34	28.2	1.888	1.355	2.827	52.0	1.085
13R-1, 57-62	9	Rock fragment	116.67	12.9	2.228	1.942	2.696	28.0	0.388
193-1189B-									
1R-1, 0-2	1	Rock fragment	31.00	6.3	3.214	3.012	3.751	19.7	0.245
1R-1, 20-30	2	Rock fragment	31.20	39.1	1.759	1.071	3.259	67.1	2.043
2R-1, 11-20	2	Rock fragment	40.21	12.5	2.391	2.092	2.956	29.2	0.413
6R-1, 23-33	3	Rock fragment	79.23	10.7	2.321	2.072	2.737	24.3	0.321
7R-1, 0-10	1	Rock fragment	88.70	19.9	2.262	1.813	3.231	43.9	0.782
8R-1, 10-14	4	Rock fragment	98.50	23.3	2.037	1.563	2.910	46.3	0.862
11R-1, 63-65	10	Minicore	128.23	7.2	2.316	2.149	2.566	16.2	0.194
11R-2, 87-89	8	Minicore	129.15	9.1	2.285	2.078	2.604	20.2	0.253
12R-1, 34-36	3	Minicore	137.64	8.5	2.298	2.103	2.599	19.1	0.236
12R-3, 46-48	7	Minicore	140.54	7.5	2.317	2.144	2.581	16.9	0.204
13R-1, 52-54	10	Minicore	147.54	10.8	2.299	2.051	2.708	24.3	0.321
14R-1, 100-102	14	Minicore	157.50	14.2	2.193	1.881	2.705	30.5	0.438
15R-1, 86-88	10	Minicore	166.96	9.4	2.244	2.033	2.560	20.6	0.260
15R-2, 61-63	11	Minicore	168.21	7.2	2.312	2.146	2.560	16.1	0.193
16R-2, 31-33	4	Minicore	177.44	8.0	2.357	2.169	2.657	18.4	0.225
18R-2, 65-67	8	Minicore	197.07	13.0	2.221	1.932	2.693	28.3	0.394

Table T21. Grain density of powders analyzed by inductively coupled plasma spectroscopy, Holes 1189A and 1189B.

Core, section, interval (cm)	Depth (mbsf)	Grain density (g/cm^3)
193-1189A-		
1R-1, 0-4	0.02	2.72
2R-1, 113-115	10.83	2.66
3R-1, 6-10	19.46	2.63
3R-1, 6-10	19.46	2.66
3R-1, 20-22	19.60	5.75
3R-1, 59-63	19.99	3.31
3R-1, 70-73	20.10	2.86
4R-1, 17-20	29.27	2.79
4R-1, 21-24	29.31	2.89
5R-1, 14-16	38.94	3.00
7R-1, 27-31	58.57	2.96
8R-1, 42-44	68.42	2.95
8R-1, 90-92	68.90	2.86
12R-1, 67-69	107.17	2.91
13R-1, 24-33	116.34	3.01
193-1189B-		
1R-1, 20-30	31.20	5.56
8R-1, 7-9	98.47	4.89
11R-1, 63-65	128.23	2.85
11R-2, 89-91	129.17	2.76
12R-2, 55-57	139.26	2.70
13R-1, 52-54	147.52	2.83
16R-1, 36-39	176.06	2.74
16R-2, 31-33	177.44	2.84

Table T22. Magnetic properties of minicores, Holes 1189A and 1189B.

Number	Core, section, interval (cm)	Depth (mbsf)	Vertically oriented	Volume (cm^3)	NRM (mA/m)	Susceptibility (10^{-5} SI)	Koenigsberger ratio	Stable inclination (°)	Stable declination (°)	Brief description
	193-1189A-									
1	2R-1, 10	9.8	Yes	14.1	1551	2715	19.7	–17	239	Black–dark gray, vesicular
2	7R-1, 82	59.12	Yes	12.8	401	222	62.2	–3	315	Gray, massive, slightly vesicular
3	8R-1, 88	68.88	Yes	12.1	30	124	8.3	9	143	Light gray with fine dark gray veins
4	10R-1, 76	88.06	Yes	7.6	88	223	13.5	87	244	Light–dark green, brecciated
	193-1189B-									
5	11R-1, 64	128.24	Yes	11.0	845	2823	10.3	–13	333	Dark gray, massive, hard
6	11R-2, 88	129.16	Yes	10.5	763	1942	13.5	–40	85	Dark gray, massive, hard
7	12R-1, 35	137.65	Yes	10.1	297	2219	4.6	–18	348	Dark gray, massive, hard
8	12R-3, 47	140.55	Yes	10.8	596	2330	8.8	–13	92	Dark gray, massive, hard
9	13R-1, 55	147.55	Yes	10.5	4	26	5.5	–2	175	Dark gray-green, small veins, hard
10	14R-1, 101	156.6	Yes	11.0	5	25	7.0	–17	285	Green, brecciated, hard
11	15R-1, 87	166.97	Yes	9.4	42	39	37.0	–2	279	Green, brecciated, hard
12	15R-2, 62	168.22	Yes	9.8	2418	2311	36.0	–17	106	Black, massive, very hard
13	16R-2, 32	177.45	Yes	10.6	1310	1879	24.0	–18	255	Black, massive, vesicular, very hard
14	18R-2, 66	197.08	Yes	10.6	18	89	6.9	27	15	Dark green, white clasts, brecciated

Note: NRM = natural remanent magnetization.

Table T23. Anisotropy of magnetic susceptibility values for the normalized principal susceptibility values and directions, Holes 1189A and 1189B.

Core, section, interval (cm)	Depth (mbsf)	k (10^{-5} SI)	k_{max} Magnitude	k_{max} Declination (°)	k_{max} Inclination (°)	k_{int} Magnitude	k_{int} Declination (°)	k_{int} Inclination (°)	k_{min} Magnitude	k_{min} Declination (°)	k_{min} Inclination (°)	Error (10^{-5})	P
193-1189A-													
2R-1, 10	9.80	2715	1.0266	360	1	0.9963	270	31	0.9771	90	59	12.0	1.0507
7R-1, 82	59.12	222	1.0154	209	14	0.9979	117	8	0.9866	360	74	1.6	1.0292
8R-1, 88	68.88	124	1.0039	360	68	1.0026	106	6	0.9935	198	21	0.1	1.0105
10R-1, 76	88.06	223	1.0163	318	57	0.9921	180	26	0.9916	80	19	1.0	1.0249
193-1189B-													
11R-1, 64	128.24	2823	1.0421	348	28	1.0006	210	54	0.9572	90	20	51.2	1.0887
11R-2, 88	129.16	1942	1.0309	90	59	1.0060	284	30	0.9630	190	7	10.6	1.0705
12R-1, 35	137.65	2219	1.0537	221	54	0.9748	101	20	0.9715	180	28	39.6	1.0846
12R-3, 47	140.55	2330	1.0163	360	81	1.0104	98	1	0.9734	188	9	6.6	1.0441
13R-1, 55	147.55	26	1.0087	324	28	0.9976	64	16	0.9937	180	57	0.1	1.0151
14R-1, 10	156.60	25	1.0182	90	54	1.0042	292	34	0.9776	195	11	0.1	1.0416
15R-1, 87	166.97	39	1.0361	328	15	0.9927	232	22	0.9712	90	63	0.3	1.0668
15R-2, 62	168.22	2311	1.0057	90	20	1.0036	187	21	0.9907	320	61	8.0	1.0152
16R-2, 32	177.45	1879	1.0252	270	53	0.9994	360	1	0.9754	90	37	11.8	1.0511
18R-2, 66	197.08	89	1.0118	182	0	0.9984	272	5	0.9898	90	85	0.4	1.0223

Notes: Axes of susceptibility ellipsoid: k = volume susceptibility, k_{max} = maximum, k_{int} = intermediate, and k_{min} = minimum. P = degree of magnetic anisotropy.